Therapeutic Benefit of Scaffolds That Capture Metastatic Tumor Cells *in vivo*

by

Grace G. Bushnell

A dissertation submitted in partial fulfillment
of the requirements for the degree of
Doctor of Philosophy
(Biomedical Engineering)
in The University of Michigan
2019

Doctoral Committee:

Professor Lonnie Shea, Chair
Professor Jacqueline Jeruss
Associate Professor Ariella Shikanov
Professor Max Wicha

Grace G. Bushnell

ggb@umich.edu

ORCID iD: 0000-0002-8891-803X

This dissertation is dedicated to my family and fiance, with love

ACKNOWLEDGEMENTS

This page will not do justice to the gratitude I feel for each and every person provided the support that carried me through this phase of my career, I hope to express a fraction of that thankfulness here.

To my family and friends, thank you for your unconditional support and love. Everything I do is because you have inspired me. To my mom, dad, brother, grandparents and fiance - thank you for believing in me, I love you all. To my fiance, thank you for lifting me up, pushing me, and always supporting me. I don't think I could have made it through these past few years without your constant love and support. To the best named Snapchat and GroupMe groups of this century, thank you for keeping me sane and listening to me complain about mice and insane experiments.

To my PhD advisor, Dr. Lonnie Shea, thank you for giving me the opportunity to do the following work and supporting me every step of the way. Thank you for pushing me, supporting me, and inspiring me in equal measure. Thank you for being a model of calm, collected intensity and excitement and providing a wonderful environment in which to work. I feel incredibly fortunate to have had your mentorship these years. To Dr. Jacqueline Jeruss, thank you for being such a great surgeon and doctor - without you taking the time to talk to your patients as well as treat them, I would not have had the opportunity to work on the research described here. In that one simple conversation you took the first step to opening a door for me to a project that has not only been scientifically rich and interesting but has the potential for real positive impact on patients. I would also like to thank the members of my dissertation

committee: Dr. Max Wicha and Dr. Ariella Shikanov. Thank you for challenging me and having a wealth of advice and ideas always. Dr. Thomas Moore thank you for the best class that I took in my graduate career and patiently answering all of my immunology questions - no matter how far out of left field. Dr. Phillip Messersmith, thank you for supporting me past my years in your lab at Northwestern. You were instrumental in motivating me to pursue graduate school. Dr. Devin Barrett, thank you for giving me the opportunity to do research with you in the Messersmith Lab and for encouraging me to consider graduate school as a real option. Dr. Rohit Kolhatkar, thank you for taking a young engineer under your wing and teaching her to do science - your kindness and support sparked an interest and drive to do research that otherwise would not have developed.

To the members of the Shea Lab, thank you for your camaraderie, moral and scientific support, and general antics. Presumably no lab has as much cake as the Shea Lab - I will miss future -paloozas. To members of Team Tumor both past and present, working with you has been a privilege and a joy. Thank you for making 22 hour flow days bearable - there's no one I would rather look at flow plots (i.e. Rorschach tests) with. I wish you all the best in your future endeavors.

The research in this dissertation would not have been possible without financial support from the National Science Foundation Graduate Research Fellowship Program, the NIH F31 National Research Service Award CA224982-01, and the NIH Transformative Research Program (R01 CA173745). Thank you to P.E.O. Plymouth Chapter EA for the support and nomination and P.E.O. International for the P.E.O. Scholar Award. Thank you to the Biomedical Engineering departments at both Northwestern University and University of Michigan for financial and administrative support.

Thank you to everyone, I could not have completed this work without your support.

TABLE OF CONTENTS

LIST OF FIGURES

Figure

LIST OF TABLES

ABSTRACT

For most cancers, the formation of distant metastasis is the point at which clinical treatment shifts from curative intent to extending progression free survival. Physicians are currently unable to diagnose metastasis until disseminated tumor cells affect the function of a target organ as a secondary tumor. This dissertation describes a novel approach where implantable biomaterial scaffolds are used to recruit metastatic tumor cells for early detection prior to colonization of solid organs. This recruitment of tumor cells to a defined site can not only serve as a platform for detection, but can also have therapeutic effects and be used as a platform to study metastatic processes. This dissertation describes work in each of these three areas including using an implantable biomaterial scaffold for early detection, therapeutic benefit, and a platform to study metastasis. The therapeutic benefit of scaffolds was demonstrated by scaffold implantation significantly enhancing disease-free survival in a murine model of triple negative breast cancer. Myeloid derived suppressor cells were the key population of immune cells whose capture at the scaffold and reduction in the spleen and primary tumor lead to enhanced survival. In an effort to probe the contributions of various immune cell types to the formation and maintenance of the pre-metastatic and metastatic niche *in vivo*, a gene delivery approach was utilized to alter the immune microenvironment of the scaffold and investigate the recruitment of tumor cells, finding reduced immune and tumor cell recruitment with IL-10 delivery and developing a model of tumor cell recruitment that is dependent upon the proportion of each immune cell type in the niche. Additional efforts to use the scaffold to study metastasis included studying scaffold captured tumor cells relative to tumor cells derived from

other locations. Scaffold captured tumor cells were a highly aggressive population of metastatic tumor cells similar to those found in a metastatic lung, underscoring the use of the scaffold as a sampling location for metastatic disease that is reflective of tumor cell phenotype in solid organs. Next, biomaterial scaffolds were also validated in transgenic models of both breast and pancreatic cancer to identify immune dysregulation as a function of tumor burden, recruit tumor cells, and to reduce tumor burden. Finally, non-invasive ultrasound imaging and subsequent spectral analysis techniques were applied to identify changes in the scaffold associated with tumor burden and tumor cell recruitment. Taken together, this body of work supports that the implantable biomaterial scaffold technology provides a robust and novel approach for the early detection of metastatic disease in both breast and pancreatic cancer, therapy to divert both pre-metastatic niche forming immune cells and tumor cells themselves to an ectopic site and away from solid organs, and as a platform to study mechanisms of the pre-metastatic niche and metastasis.

CHAPTER I

Introduction

1.1 Opening

Cancer metastasis is responsible for 90% of cancer related deaths. As the second most common cause of death in the United States, an estimated 1.7 million new cases will be diagnosed in 2018 and 610,000 patients will die from the disease. Metastasis is deadly, not only because tumor cells colonize a vital organ and prevent normal function, but also because there are no proven detection methods to identify either an increased risk for metastasis or metastasis at it's earliest stages before organ function is compromised. The research presented in this dissertation exists at the intersection of biomaterials, tissue engineering, immunoengineering, and cancer biology and aims to develop novel detection strategies for metastasis, use the biomaterial platform to study metastasis and the pre-metastatic niche, and to investigate the use of biomaterials as a therapeutic for metastasis.

1.2 Contents

Chapter 1 provides a general introduction to the concept of engineering the pre-metastatic niche and the research topics explored in this dissertation.

Chapter 2 establishes an intellectual framework for the dissertation and sum-

marizes the relevant history of the pre-metastatic niche, cancer metastasis, and engineering approaches to study these phenomena.

Chapter 3 introduces the concept of using implantable biomaterial scaffolds for early detection of metastasis and therapeutic benefit in combination with a resection of the primary tumor. The central goal of this work was to develop a slowly degrading biomaterial scaffold that is capable of recruiting metastatic tumor cells in a chronic implantation setting. The scaffold microenvironment was found to be dynamic with primary tumor progression, demonstrating an increase in myeloid derived suppressor cells with concordant with metastasis development in the scaffold. We demonstrate that in combination with resection of the primary tumor after detection of tumor cells in the implant, scaffold implantation enhances survival relative to a mock surgery.

Chapter 4 discusses the use of the scaffold technology as a platform to investigate the role of various cytokines and immune cell populations in tumor cell recruitment to a metastatic site. Lentivirus encoding for immunomodulatory factors including CXCL12, Il10, and CCL2 was delivered from the scaffold and investigated for its ability to alter the immune cell populations present within the scaffold and subsequently alter tumor cell recruitment. Delivery of CXCL12 was found to enhance immune cell recruitment while delivery of IL10 reduced immune cell recruitment. Tumor cell recruitment to the engineered niche was also investigated and IL10 was found to significantly reduce tumor cell recruitment to the scaffold. The role of individual immune cell populations was investigated by developing a multiple linear regression model for tumor cell recruitment across all lentiviral conditions. Finally, the effect of immunomodulated microenvironments were evaluated by treating tumor cells with conditioned media generated from explanted scaffolds with the lentivirus of interest. This chapter demonstrates that the scaffold may be used as a platform to validate key contributors to tumor cell recruitment and phenotype at a metastatic site.

Chapter 5 describes the investigation of the tumor cells recruited to biomaterial

scaffolds *in vivo* and comparison to the primary tumor and lung metastasis. Tumor cells were isolated from various metastatic locations *in vivo* and expanded into cell lines. These locations included the primary tumor (PT), scaffold (SCAF), and lung (LUNG). Following the generation of cell lines from each location, the phenotype of these tumor cell lines were compared both *in vitro* and *in vivo*. SCAF cells were found to be more aggressive *in vitro* including higher migration, mammosphere formation, cancer stem cell surface marker and 30 times more metastatic to the lung compared to the PT line when inoculated *in vivo*. The molecular differences accounting for differential metastatic behavior and phenotype were investigated using RNAseq and Hi-C techniques for function and structure of the genome respectively. RNAseq identified key differentially expressed pathways including TNFα signaling via NFκB which was enriched in SCAF relative to PT. This finding was supported by an alteration in both structure (Hi-C) and function (RNAseq) in genes with NFκB binding sites between SCAF and PT cells. Additionally TNFα via NFκB was also enriched in LUNG relative to PT indicating this may be a common mechanism of metastatic phenotype between these two cell lines. This chapter demonstrates that the scaffold may be used as a sampling location for metastatic tumor cells that are reflective of those found in the lung.

Chapter 6 describes the use of biomaterial scaffolds in spontaneous models of tumorigenesis and metastasis. All previous models of metastasis described in this dissertation relied upon orthotopic injection of tumor cells into the mammary fat pad of healthy mice. In this chapter we investigated the ability of the scaffold to recruit metastatic cancer cells in two models of spontaneous tumorigenesis and metastasis. We first started with the spontaneous breast cancer model MMTV-RFP-PyMT. We found the scaffold recruits tumor cells and displays tumor-burden dependent immune dynamics. We next investigated the spontaneous model of pancreatic cancer KPCY. In this model we again found that the scaffold recruits tumor cells and displays tumor-

burden dependent immune dynamics. We also found a reduction in metastatic burden in the KPCY model with scaffold implantation relative to mock surgery. Finally, we investigated the ability of the immune signature in the scaffold to differentiate between these two tumor types and found differential tumor-dependent immune modulation in these two cancers. The recruitment of tumor cells and tumor-dependent immune dynamics by biomaterial scaffolds in two very different tumor models in two cancers with very different clinical outcomes highlights the versatility and translatability of this platform technology.

Chapter 7 discusses the use of high frequency spectral ultrasound imaging or SUSI to detect metastasis to biomaterial scaffolds. Biomaterial scaffolds that recruit tumor cells *in vivo* are a promising platform technology for the early detection of metastasis in patients with breast cancer. However, a key need for this platform to be implemented in patients is a non-invasive monitoring system. In this chapter the use of SUSI as a non-invasive monitoring tool is detailed in both human xenograft and mouse syngeneic models of breast cancer metastasis. Tissue parameters identifying alterations associated with metastasis were discovered that are consistent across both human and mouse tumors. The biological mechanism of these alterations was also investigated via SUSI analysis of decellularized scaffolds from tumor free and tumor bearing mice as well as analysis of scaffold infiltrating cells from tumor free and tumor bearing mice. Finally, classification algorithms were designed and applied to the data to stratify SUSI signatures from tumor free and tumor bearing mice. This chapter highlights the potential avenues for translation of the scaffold not only as a site to collect tumor cells but also as a site to monitor both non-invasively and longitudinally to identify tissue parameter alterations associated with development of metastasis.

Chapter 8 concludes the dissertation and summarizes the presented findings. The significance and impact of the work described herein are discussed and proposed future directions are detailed.

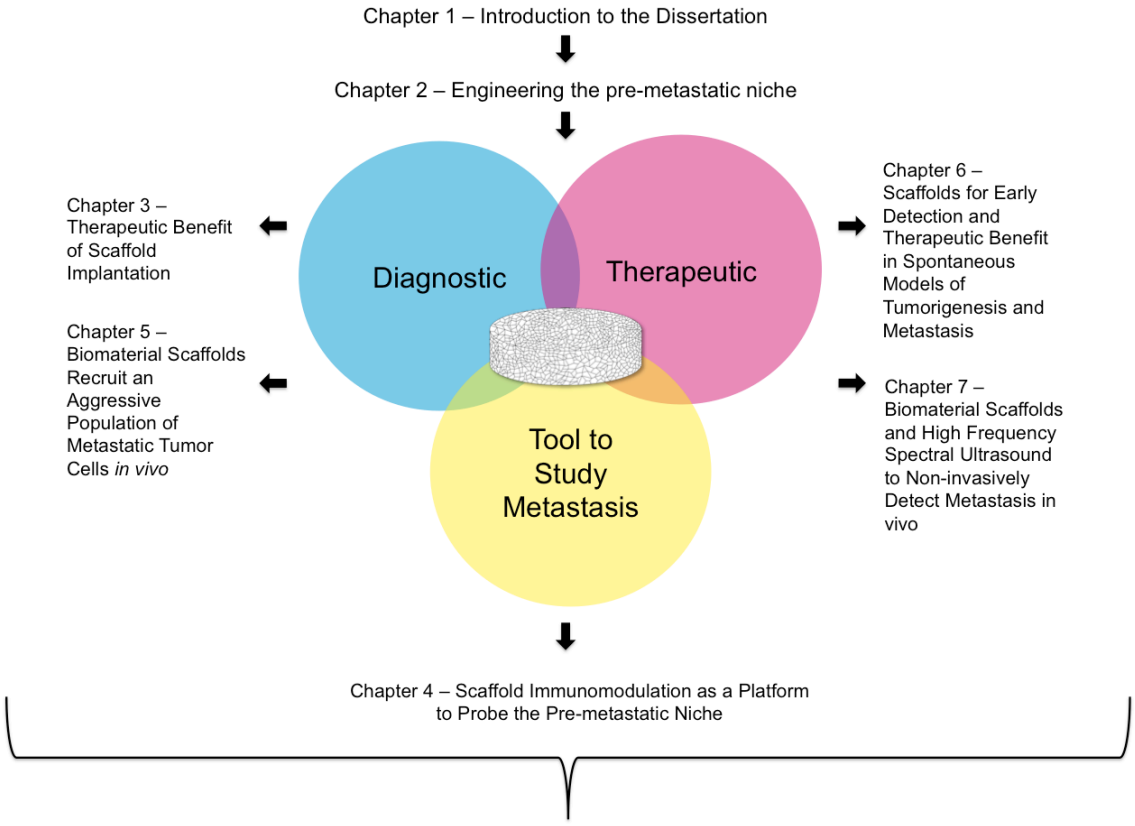

Figure 1.1: **Overview of dissertation contents.**

CHAPTER II

Engineering the Pre-metastatic Niche

2.1 Authors

Brian A Aguado*, Grace G Bushnell*, Shreyas S Rao, Jacqueline S Jeruss, Lonnie D Shea * These authors contributed equally to this work

2.2 Abstract

The pre-metastatic niche forms during metastatic progression, in which the primary tumor drives the aberrant accumulation of immune cells in target organs to prime the microenvironment for tumor cell colonization. Since the discovery of the pre-metastatic niche, there has been great interest in deconstructing the complexity of the niche and identifying the roles of individual niche components in mediating tumor cell homing, colonization, and proliferation. Technological advances in biomaterials engineering have enabled various iterations of pre-metastatic niche mimics, in which the immune response, soluble factors, extracellular matrix proteins, and other niche cells have been used to mimic the niche both *in vitro* and *in vivo* with user-defined parameters. Given the newfound ability to manipulate metastatic cell trafficking *in vivo*, engineered pre-metastatic niche mimics have also been used as oncomaterials, demonstrating both diagnostic and therapeutic capabilities. In sum,

the juxtaposition of pre-metastatic niche biology and biomaterials engineering have enabled unique discoveries of how tumor cells interact with pre-metastatic niches, which may offer insights for future strategies to block pre-metastatic niche formation and cellular interactions in metastatic cancer patients.

2.3 Introduction

Diagnosing a patient with metastasis often indicates the disease has become increasingly difficult to treat effectively, since metastasis is responsible for 90% of cancer-associated deaths [1, 2]. The journey of a metastatic cell from a primary tumor to a secondary target organ is a progressive cascade of multiple events, involving numerous microenvironmental signals at each stage of disease progression [3–5]. Briefly, the metastatic cascade begins with invasion, where primary tumor cells undergo a phenotypic change termed the epithelial-mesenchymal transition (EMT) to degrade the tumor basement membrane and move into the surrounding tumor vasculature to become a circulating tumor cell (CTC). CTCs are attracted via chemokine gradients to organ microenvironments through a process known as homing. Once a CTC encounters the target organ microenvironment, the CTC escapes the vasculature via extravasation and is then classified as a disseminated tumor cell. During colonization, the disseminated tumor cell encounters an attractive and permissible niche at a target organ, where the tumor cell adheres, proliferates, and begins to form a secondary tumor. At this point in the cascade, secondary tumors begin to negatively affect organ function and dramatically decrease chances of survival. In 1889, Steven Paget developed the seed and soil hypothesis, positing that the spread of tumors is not random but governed by regulated processes where the metastatic tumor cell, or seed, grows more optimally in organ soils primed for tumor cell arrival [6]. Pagets observations were the first to describe cancer cell dissemination as pre-determined, and that cancer cells tend to colonize specific tissue types. For example, in the case

of breast cancer, metastases tend to form primarily in bone tissues, liver, lung, and brain, indicating a tropism for specific microenvironments [3]. This primed microenvironment located at target organs has been termed the pre-metastatic niche (**Figure 2.1**) and is involved in promoting tumor cell homing, colonization, and growth at a target organ. The pre-metastatic niche is a complex microenvironment, which includes inflammatory immune cells, stromal cells, extracellular matrix (ECM) proteins, tumor-secreted exosomes, and homing factors. In brief, niche formation is a function of primary tumor microenvironment formation and evolution. Tumor secreted factors and tumor-derived exosomes (**Figure 2.1A**) mobilize and recruit bone marrow derived cells (BMDCs) to niches in secondary organs (**Figure 2.1B**) where they interact with the local stroma to create permissive and attractive sites for metastatic cells (**Figure 2.1C, 2.1D**) [7]. The niche was first described by Kaplan et al. through the arrival of VEGFR1+ BMDCs to the metastatic site, which preceded and predicted the arrival of tumor cells [8]. Additional BMDC populations have been implicated in the formation of the pre-metastatic niche including CD11b+ myeloid cells, myeloid derived suppressor cells (MDSCs), neutrophils, tumor-associated macrophages, and regulatory T cells [9–16]. Tumor-secreted factors and exosomes can also directly modify the host stroma to establish a supportive microenvironment [17, 18]. Additionally, fibroblasts, endothelial cells, and lung epithelial cells have been associated with the establishment of the pre-metastatic niche via secretion of inflammatory cytokines and chemokines [10, 13, 19]. Though there is evidence that pre-metastatic niche formation leads to metastases, there is an urgent need to further elucidate the individual and combinatorial cues that promote tumor cell homing, colonization, and proliferation at the pre-metastatic niche, with the goal of developing novel therapeutic interventions. Due to biological complexity and commonalities with primary tumor progression, the contributions of individual components leading to metastasis have been challenging to study *in vivo*. Biomaterial-based strategies have been developed to deconstruct

these complex environments and focus on distinct metastatic processes, including primary tumor formation [20–22], invasion [23], and extravasation [24, 25], as well as metastatic cell homing [26], colonization [27], and proliferation [28]. Tissue engineering principles are being applied to model the pre-metastatic niche environment as a means to identify and study the key factors driving tumor cell activity at an organ site. Compared to more traditional genetic or transgenic animal models for evaluating metastatic progression, studying these processes using an engineered ectopic site *in vivo* avoids the need for biologically modifying the tumor or host (**Table 2.1**). As a result, the progression of the tumor, formation of metastases, and phenotype of the host are kept constant, thus reducing numerous confounding biological factors. The design of artificial, user-defined niches using biomaterials may facilitate the identification of components of the pre-metastatic niche *in vivo*, which may lead to strategies that efficiently prevent niche formation, divert metastatic cells away from target organs, or develop early detection strategies [29, 30]. Several factors should be considered when implementing biomaterials to engineer a pre-metastatic niche, including choice of material (synthetic and/or natural), fabrication method, inclusion of bioactive cues, degradability, and porosity (**Table 2.2**). Furthermore, biomaterials-based tools that mimic the pre-metastatic niche have recently been shown to have translational opportunities, enabling novel detection and therapeutic strategies in animal models that have been previously unattainable using conventional approaches [31]. The strategies for engineering mimics of the pre-metastatic niche are described in this review, with a focus on (i) how biomaterials have been used to probe questions regarding tumor cell recruitment to an engineered niche, (ii) tumor cell behavior upon arrival to a niche, and iii) how engineered niches may be used for detection and therapeutic strategies.

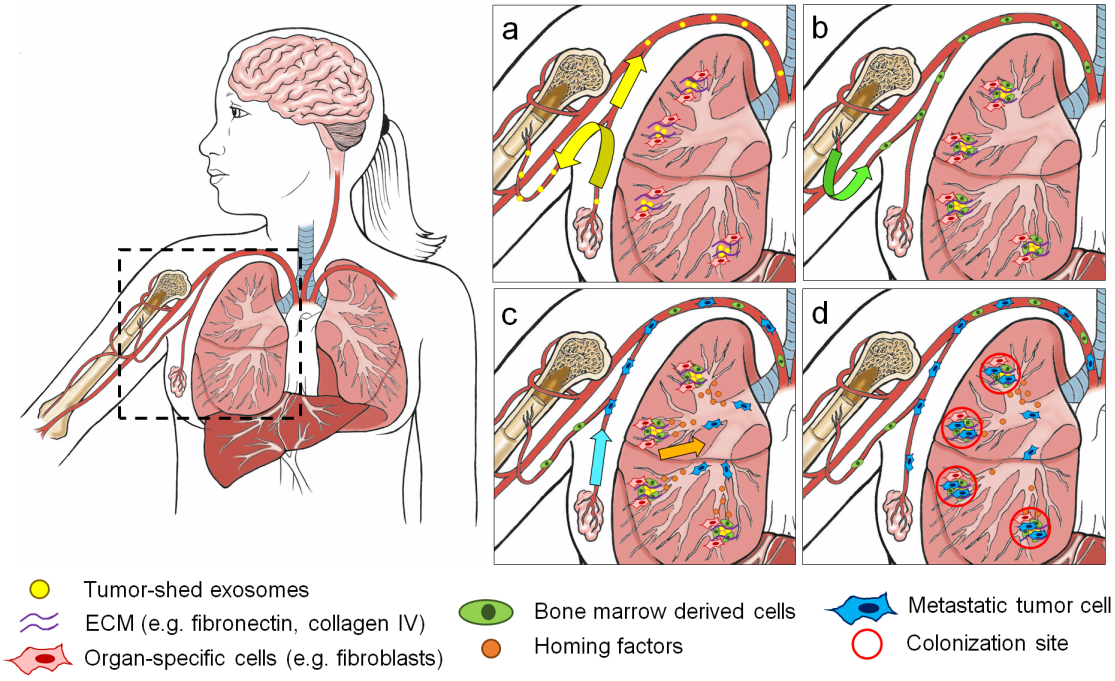

Figure 2.1: **Formation of the pre-metastatic niche.** (A) Hypoxic tumor sheds exosomes (yellow dots) to simultaneously prepare the niche at a target organ and to stimulate mobilization of BMDCs. Other tumor-secreted factors (e.g. lysyl oxidase) crosslink ECM proteins (purple curves). (B) BMDCs (green cells) accumulate at prepared sites, adhering to accumulated ECM. (C) BMDCs and other immune cells (e.g. myeloid derived suppressor cells) secrete factors (orange dots) to induce metastatic cell (blue cells) homing to niche sites. (D) Metastatic cells colonize and proliferate at metastatic niche sites. Illustrations courtesy of Katie Aguado.

Strategy	Advantages	Disadvantages
Biomaterial pre-metastatic niche mimic	-Limited off-target effects -Defined location for analysis -Biomaterial properties can be manipulated for different applications -Ease of evaluating multiple niche cues in one device -Large number of cells can be retrieved from the device	-Does not recapitulate all elements of the native pre-metastatic niche -The foreign-body response may influence the biomaterial environment and differ from a natural pre-metastatic niche
High-risk tissue-bed biopsy	-Enables determination of cues leading to organ-specific metastasis -Captures heterogeneity between metastatic foci	-Variability between samples may confound discovery of critical signals -The identification of pre-metastatic sites is limited
Genetically engineered mouse models	-Direct evidence for the role of a factor or cell type in metastasis -Ability to knock-out and knock-in specific genes	-Costly and time intensive -Potential for off-target effects on health of the animal or on tumor progression

Table 2.1: **Strategies for characterizing the pre-metastatic niche and the formation of metastasis**

2.4 Cancer Cell Recruitment to an Engineered Niche

Numerous tissue engineering approaches have been utilized to create biomaterial platforms to mimic properties of the pre-metastatic niche (**Table 2.2**). Material options include synthetic degradable materials (e.g. poly(lactic-co-glycolic acid), PLG), synthetic non-degradable materials (e.g. polyacrylamide), and natural materials (e.g. silk). Each of these substances can be formed into a porous scaffold structure capable of (i) supporting retention of loaded factors or cells, (ii) facilitating integration with a host tissue upon implantation, (iii) facilitating formation of a defined microenvironment *in vivo* and (iv) ultimately providing an ectopic site for the recruitment of metastatic tumor cells. The choice of material depends on the desired application and feature of the pre-metastatic niche to mimic. For example, in applications where the desired goal is to simulate the bone microenvironment, relatively stiff biomaterials with similar mechanical properties to bone may be advantageous [32]. These

Source	Material	Structure	Fabrication Method	Bioactive modifications	Refs
Synthetic	Poly(lactic-co-glycolic acid)	Scaffold	Gas foaming	CCL22, MDSCs	[31]
		Layered scaffold	Microspheres	Haptoglobin	[34]
		Scaffold			
	Poly(ε-caprolactone		Gas foaming	None	[30]
			Microfabrication		
			Electrospinning	Exosomes	[29]
		Microparticles	Precipitation	Osteoblasts	[32]
	Poly-L-lactic acid			EPO, SDF-1	[26]
		Nanoparticles	Precipitation		
	Hydroxyapatite	Porous gel	Microfabrication	Serum	[35]
	Polyacrylamide	Scaffold	Commercial	Collagen/BMSCs	[27,
	Polyurethane	Microparticles	Layer-by-layer	MSCs	36]
	Polyallyamine		coating	CAFs	[37]
					[38]
Natural	Bone fragments	Human/mouse	Direct harvest	None	[39,
	Silk	Scaffold	Salt leaching	BMP-2	40]
	Lung/liver matrix	Coatings	Decellularization	None	[33,
					41]
	Osteoblast matrix	Mineralized sheets	Decellularization	None	[42]
	Collagen	Bulk gel	Embedded in microfluidic chamber	MSCs, ECs	[43]
					[44]

Table 2.2: **Materials and biological modifications for the engineering of the pre-metastatic niche.**

materials can be combined with appropriate factors implicated in organotropism to specific sites to better emulate the properties of the target organ [33]. A platform that provides facile and sustained delivery of the factor or cell type being investigated can serve to examine the contribution of that factor to the homing and colonization of cancer cells [31, 34]. This combination of biomaterials and biological modifications provides a vast toolkit for dissecting the molecular components of the pre-metastatic niche and discovering novel contributors to pre-metastatic niche formation and function *in vivo*.

2.4.1 Immune cell trafficking

Multiple immune cell types are involved in pre-metastatic niche formation, and the complexity of the niche has confounded the analysis of the role for each cell type. In

addition to VEGFR+ BMDCs playing a major role in establishing the pre-metastatic niche, other myeloid cells including MDSCs [45, 46], macrophages [47], and monocytes [15] contribute to niche formation and tumor cell homing. For instance, hypoxic tumor cells secrete lysyl oxidase which crosslinks collagen IV in the lung and facilitates the accumulation of CD11b+ monocytes, ultimately leading to pre-metastatic niche formation [10, 48]. T-cells have also been shown to be involved in assembling the pre-metastatic niche [49, 50]. The role of hematopoetic stem and progenitor cells (HSPCs) has also been elucidated in pre-metastatic niches. Purified populations of HSPCs were tracked *in vivo* using an orthotopic E0771 adenocarcinoma breast tumor model, and HSPCs were shown to differentiate readily into immunosuppressive myeloid cells [11]. Once immune cells accumulate at distal organs, they secrete a multitude of factors facilitating the subsequent recruitment and colonization of disseminated tumor cells [51, 52]. Recent studies have shown the real-time interactions of immune cells and disseminated tumor cells undergoing colonization at target organs using intravital imaging, further elucidating the role of myeloid cell populations in providing a primed harbor for tumor cells at target organs [53]. While these studies identify the importance of immune cells in the pre-metastatic niche, few studies have investigated the interplay between tumor cell and immune cells within the pre-metastatic niche. This lack of investigation is partially due to a lack of tools to probe the pre-metastatic niche without significant off-target effects on tumor, metastatic progression, or immune function. Monitoring and evaluating tumor cell interactions with immune cells at the pre-metastatic niche represents an opportunity to probe the mechanisms governing metastasis.

Understanding cellular interactions at the pre-metastatic niche would lead to opportunities to exploit immune cells to capture metastatic tumor cells for detection and therapy. Upon implantation, biomaterial scaffolds elicit an acute inflammatory response in the host. The host response to an implanted biomaterial includes several

blood-material interactions, including the formation of a fibrous capsule consisting of inflammatory immune cells and fibroblasts around the border of the implant. Although several other reviews discuss the inflammatory response to implanted biomaterials [54–57], more recent studies elucidate a connection between the immune cells recruited to a biomaterial and the immune cells required to establish a pre-metastatic niche site (**Figure 2.2**). For example, in an immune competent Balb/C mouse, a variety of inflammatory immune cell populations are recruited to a subcutaneously implanted poly(ε-caprolactone) (PCL) micro-porous scaffold (**Figure 2.2A, 2.2B**). During a four-week implantation period prior to 4T1 breast tumor cell inoculation, Ly6C+F4/80- inflammatory monocytes and CD11c+F4/80- dendritic cells accumulate at the implant site. However, following tumor inoculation, inflammatory monocytes further increased and Gr1hiCD11b+Ly6C- MDSCs accumulated at the scaffold (**Figure 2.2C**), while dendritic cell and F4/80+CD11b+ macrophage populations decreased, thus recapitulating elements of the pre-metastatic niche [30]. Immune cell dynamics at the scaffold correlate with tumor cell recruitment, indicating the biomaterial implant is able to recapitulate characteristics of a natural pre-metastatic niche. In another approach, poly-L-lactic acid (PLA) microspheres have also been shown to recruit CD11b+ monocytes to the implant location [26]. B1F10 melanoma cells home to implanted PLA microspheres due to the prior arrival of inflammatory immune cells. The recruitment of tumor cells without chemokine delivery indicates that tumor cells can home to an implant due to the local foreign body response alone. Importantly, the composition of the immune cells in the foreign body response may differ in tumor-bearing relative to healthy animals, with the foreign body response in a tumor-bearing host facilitating formation of a pre-metastatic niche at an ectopic location. The emerging concept of immune cells mediating tumor cell recruitment to an implanted biomaterial has significant implications in the study and modulation of metastatic cell trafficking, as well as enabling detection and study of tumor cells at

user-defined, ectopic locations.

2.4.2 Soluble factors and exosomes

The pre-metastatic niche microenvironment also consists of chemokines and cytokines that actively influence immune cell and metastatic cell behavior. Various secreted factors from stromal cells have been implicated in recruiting immune cells associated with the pre-metastatic niche including SDF-1, TGF-β, S100A-8/9, IL-1, and caveolin-1 [13]. Similarly, immune factors including VEGF, IL-6, IL-1, TNF, CCL17, G-CSF, Bv8, S100 proteins, CCL2 and CCL22 were shown to be over-expressed at target organs during metastatic progression, suggesting a role in pre-metastatic niche formation and tumor cell recruitment [14, 52, 58]. The function of each of these factors has been described in detail by Liu et al [59]. In brief, VEGF was found to recruit VEGFR1+ BMDCs [8], TNF induces S100A8/9 expression which attracts Mac1+ myeloid cells and tumor cells to the niche [60, 61], G-CSF mobilizes MDSCs to the lung niche [9], Bv8 promotes angiogenesis and mobilization of myeloid cells to the niche [12], IL-6 is responsible for tumor promoting inflammation [61], and finally CCL2 recruits monocytes and BMDCs and facilitates the extravasation of cancer cells [16]. Immature Gr1+CD11b+ MDSCs are responsible for suppressing IFN-γ and increasing inflammatory cytokine expression, and induce the expression of MMP9 in cells to allow for matrix remodeling at the niche [62]. Additionally, the role of soluble factors in mediating metastasis to bone tissue has been characterized using 3D models, where tumor cells actively prepare the bone tissue for colonization through the release of cytokines such as IL-8 [35, 63]. Colonizing breast tumor cells must produce osteoclast-activating factors including IL-6, IL-11, and TNF to initiate bone resorption in an effort to create space for the metastatic lesion [64]. Additionally, inflammatory Mac1+ monocytes and lung endothelial cells are known to secrete calcium-binding S100A8 and S100A9 factors in the presence of a primary

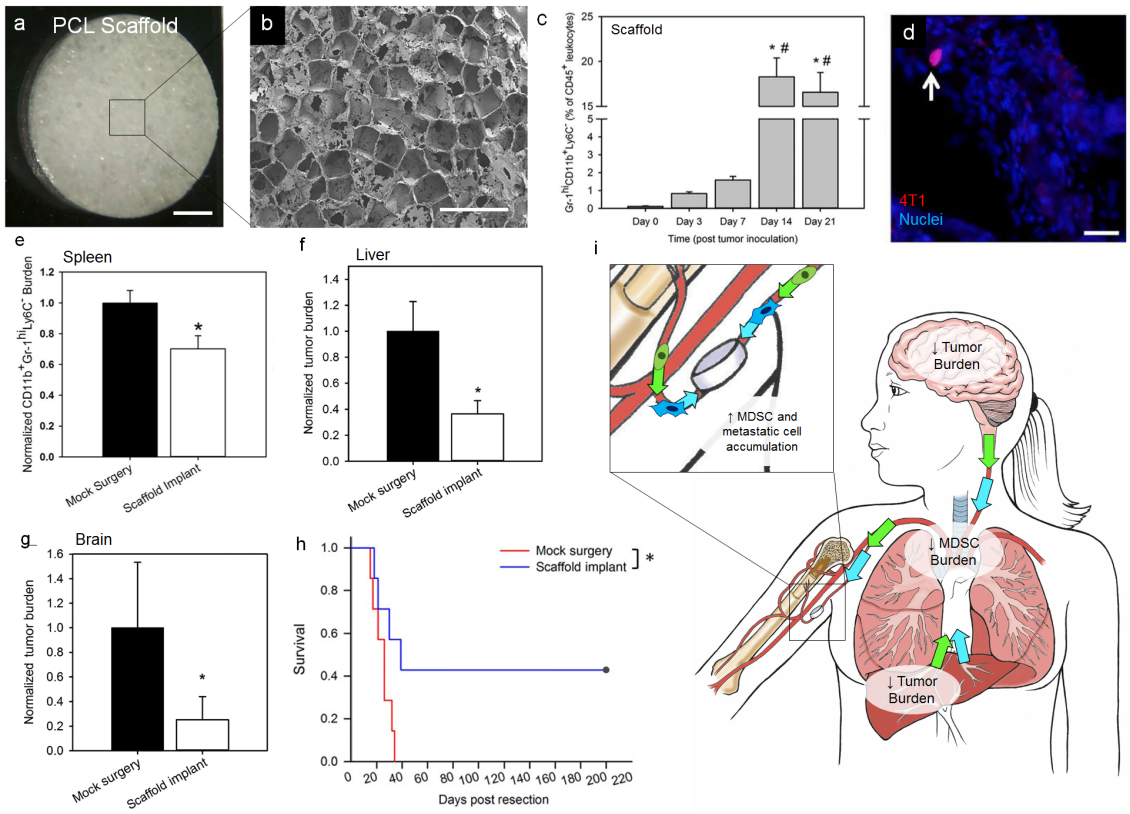

Figure 2.2: **Myeloid derived suppressor cell (MDSC) dynamics in a breast tumor bearing mouse implanted with a biomaterial scaffold.** (A) Photographic (scale = 1 mm between black tick marks) and (B) Scanning electron microscope images (scale = 1 mm) of a microporous PCL scaffold. (C) Tumor progression influences Gr1hiCD11b+Ly6C- MDSCs at the PCL scaffold implanted subcutaneously in a Balb/C mouse inoculated with 4T1 triple negative breast tumor cells. (D) PCL scaffolds reduce MDSC burden in the spleen, which indicates a reduction in systemic MDSC burden.

tumor, which initiates the recruitment of additional monocytes to pre-metastatic sites [19, 60]. S100A8 and S100A9 are also known to increase formation and activation of invadopodia via p38 signaling, which may promote tumor cell adhesion at a pre-metastatic niche [65]. Soluble factors have a clear role in mediating the recruitment of different immune cell populations, which subsequently impact tumor cell recruitment to the niche. While many soluble factors have been implicated in the pre-metastatic niche, these have been difficult to study in a controlled manner due to the commonality of many of these chemokines and cytokines with processes in tumor progression.

The release of chemotactic factors from biomaterials has been used to manipulate immune and tumor cell trafficking to implant sites. Chemokine releasing scaffolds have recruited metastatic melanoma tumor cells [26]. Stromal-derived factor 1 (SDF-1) and erythropoietin (EPO) releasing scaffolds implanted subcutaneously have been compared, with EPO scaffolds having increased tumor cell recruitment (**Figure 2.3A**). The delivery of viruses from biomaterials that encode for chemokines has also been employed to modulate immune cell trafficking [66]. Similarly, PLG scaffolds with an immobilized lentivirus encoding for CCL22 modulated the immune cell composition within the scaffold [31]. An increase in MDSCs at the niche was observed, which enhanced tumor cell recruitment to the scaffold, similar to the mechanism of pre-metastatic niche formation and completion by tumor cells [45, 46]. These factors are thought to modulate the chemokines at the local environment; however, altering the trafficking of immune cells locally may potentially have an impact systemically. Collectively, these studies indicate that individual secreted factors have distinct cell recruitment abilities and direct release from the material may enable studies of immune and metastatic cell trafficking.

Tissue engineered constructs have delivered a variety of soluble factors to investigate their role in tumor cell homing [41]. Silk biomaterial scaffolds have been developed to study the impact of BMP-2 on bone metastasis [67]. BMP-induced

transcriptional pathways are activated during breast and prostate cancer invasion and bone metastasis [68, 69]. Using a layered scaffold system, BMP-2 release stimulates adhesion of PC3 prostate cancer cells to the scaffold and enhanced the attached cells expression of osteogenic markers in response to BMP-2. More recently, the immune cell secretome that may attract MDA-MB-231 breast cancer cells was characterized using systems biology and biomaterial techniques [34]. Using mass spectrometry proteomics, 115 proteins were identified as secreted by the immune cells, and were considered candidate mediators of metastatic cell homing. Using a complementary systems biology approach that measures large-scale transcription factor activity, the list of candidate factors was narrowed to five. Haptoglobin was identified as a critical mediator of homing and PLG scaffolds were engineered to locally release haptoglobin upon implantation in orthotopic breast cancer mouse models. The protein-releasing scaffolds were able to recruit significantly more metastatic tumor cells to the synthetic scaffold site relative to blank scaffolds, indicating a role for haptoglobin in tumor cell homing to a niche. Taken together, elucidation of the ability of EPO [26] and haptoglobin [34] to recruit tumor cells to engineered niches indicates that these platforms can serve to validate components of the pre-metastatic niche, and also facilitate discovery of novel contributors to pre-metastatic niche formation and function. Tumor-shed exosomes, which contain a variety of soluble factors that elicit dramatic changes in immune cell trafficking and the target organ ECM, have similarly been delivered locally as a means to promote tumor cell recruitment. Typically 50-90 nm in diameter, exosomes are small membrane vesicles shed from cells via fusion of multi-vesicular bodies to the cell membrane [70, 71]. The multi-vesicular bodies carry signaling molecules from the cytoplasm, and once secreted from a cell, the newly-formed exosome participates in cell-cell communication after internalization by another cell type [72]. Exosomes were shown to prepare organs for tumor cell colonization and mobilize BMDCs to pre-metastatic niche sites [7, 18]. For pre-

metastatic niche formation in the lung, RNA molecules from tumor-shed exosomes activate TLR3 in alveolar type II cells, which stimulates neutrophil recruitment to a target site [59]. As such, using tumor derived exosomes in engineered pre-metastatic niches may further elucidate their role during metastasis progression [73]. With this concept in mind, de la Fuente et al embedded exosomes in a 3D biomaterial scaffold to serve as a metastatic trap (M-Trap) [29]. The authors found that in both peritoneal and orthotopic models of ovarian cancer, the M-Trap device preferentially captured metastatic cells (**Figure 2.3B**). As a result, mice implanted with M-Trap scaffolds survived significantly longer than those without implants, with a greater survival benefit demonstrated with removal of the implant after focalization of the metastatic disease.

2.4.3 Extracellular matrix

The pre-metastatic niche microenvironment assists with immune cell and tumor cell colonization to a target tissue. As early as 1999, it was demonstrated that intravenously delivered human prostate cancer cells would arrive and engraft to implanted human bone fragments but not implanted human lung or intestinal tissues [39]. Similarly, human SUM1315 cells, derived from a patient bone nodule of metastatic breast cancer, preferentially colonize engrafted human bone sample when co-injected with human bone marrow stem cells and did not metastasize to mouse bone [39]. Further studies using a similar humanized bone metastasis model in SCID mice have shown disparities in gene expression profiles of cell lines that metastasize spontaneously at typical metastatic sites in control mice compared to cells that preferentially metastasized to human bone implants [40]. These studies show the preferential colonization of tumor cells to species-specific microenvironments. More broadly, these early studies pioneered the concept that tumor cell colonization can be controlled with the proper design and presentation of a specific microenvironment primed for

tumor cell recruitment. Tissue engineering strategies have been utilized to model organ-specific colonization *in vitro* using organ ECM mimics. To address this need, a high-throughput strategy to rapidly screen tumor cell adhesion and migration on a biomaterial-screening platform has recently been reported. Specific tumor cell lines have a certain proclivity for ECM protein compositions due to integrin expression [74]. Barney et al. suggest that integrin binding dictates organotropism, with β1, 2, and 6 integrin subunit expression determining cellular adhesion to lung, liver, and brain ECM mimics [75]. By taking advantage of the cell surface receptors expressed on tumor cells, cells can be cultured on tissue-inspired biomaterials, such as bone, brain, and lung ECM. Integrin-mediated phenotypes observed on these ECM materials provided an *in vitro* fingerprint for cell lines with predictable metastatic targets. After identifying these fingerprints, heterogeneous tumor cell lines were cultured on the biomaterial ECMs to accurately predict the *in vivo* metastatic targets. Further studies have determined that tumor-derived exosomes display distinct integrin patterns that preferentially bind to organ-specific cells, thus demonstrating that organotropism is mediated through multiple extracellular signals [18].

Tumor cell adhesion has also been tested using decellularized lung and liver matrix to coat biomaterial scaffolds [42]. Organ decellularization is a commonplace tissue engineering method used to obtain tissue-specific matrix [76], and has been recently used to assess tumor cell activity on primary tumor [77], lung [78], and bone-derived matrices [79]. Using this approach *in vivo*, lung and liver decellularized organ matrix obtained from tumor-bearing mice was used to coat micro-porous PCL scaffolds, and upon subcutaneous implantation, was shown to enhance tumor cell colonization at the scaffold relative to healthy decellularized organ matrix (**Figure 2.4A, 2.4B**). Interestingly, proteomics was used as a technique to evaluate the composition of lung and liver matrix to identify the unique components of organ-specific pre-metastatic niches. In this example, myeloperoxidase was determined using proteomics

and validated as a factor that mediates tumor cell colonization using an engineered myeloperoxidase-coated PCL scaffold. Taubenberger et al. have investigated this with engineered mineralized ECM-based scaffolds seeded with osteoblasts. Scanning electron microscopy was utilized to characterize the myofibrillar network produced by seeded osteoblasts, which was comparable to the assembly of trabecular bone tissue. Atomic force microscopy was also used in this study to measure the detachment force of various breast cancer cells as a measure of tumor cell adhesion to the engineered sites. Tumor cells seeded on the human bone mimic revealed gene expression changes in osteopontin, which are consistent with tumor cells colonizing bone tissue *in vivo*. This study demonstrated the ability of combinatorial approaches to help identify and characterize the interaction between many elements in the *in vivo* niche [43]. Taken together, these results demonstrate the ability of tissue engineered constructs to recapitulate elements of bone-specific colonization, and represent a highly controllable platform to study these interactions for any organ *in vitro*.

2.4.4 Cell delivery

While specific cell types have been implicated in pre-metastatic niche formation, de-convoluting the role of each cell type has been elusive due to the off-target effects of altering a cell population globally via transgenic strategies, antibody depletion, or adoptive transfer. Biomaterials provide a practical strategy to evaluate the function of a specific cell type in recruiting tumor cells to the pre-metastatic niche, as cells can be seeded directly onto a biomaterial scaffold and implanted into a mouse model of metastatic cancer. The most frequently reported approach involving cell transplantation to enhance cancer cell recruitment has attempted to mimic the bone marrow niche through transplantation of human bone marrow stromal cells (**Figure 2.5A**) [33, 36], BMDCs [27, 36], or mesenchymal stem cells [37]. These cells were seeded on a biomaterial scaffold and cultured *in vitro* prior to implantation. Upon

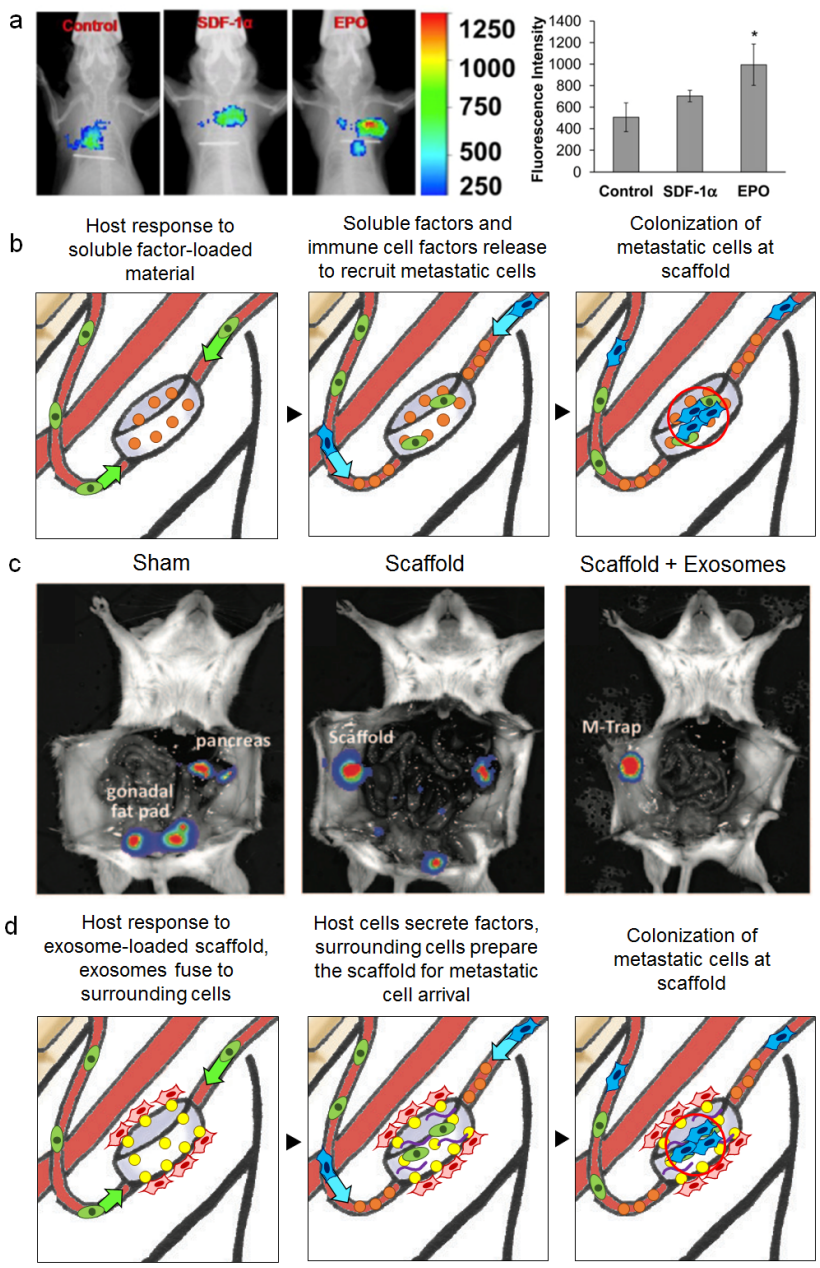

Figure 2.3: **Soluble factors and exosomes mediate tumor cell homing.** (A) Control, EPO and SDF-1α loaded scaffolds recruit labeled B16F10 melanoma cells, quantified using bioluminescence imaging (*P <0.05). (B) Exosome-laden scaffolds (M-trap) capture SKOV3 ovarian cancer cells delivered into the peritoneal cavity. Bioluminescence imaging shows control mice with metastasis to the pancreas and gonadal fat pads 1 week after inoculation. Blank scaffolds were able to redirect tumor cells, although abdominal metastases were still detected. M-trap scaffolds were able to recruit tumor cells with no visible metastases at 1 week after inoculation.

implantation, engineered bone marrow niches were able to recruit human breast cancer [27, 33, 41], erythroleukemia (**Figure 2.5B**, 2.5C) [36], acute myeloid leukemia [37], and prostate cancer cells [27, 80] to the implant site. Interestingly, studies suggest the frequency of capturing tumor cells using scaffolds seeded with BMDCs may correlate with the frequency of CTC capture in the blood [27]. In sum, bone marrow mimics are capable of capturing tumor cells at an ectopic site using animal models of both hematological malignancies and carcinoma metastasis, further demonstrating that cell-laden materials are capable of mimicking metastatic niches.

Aside from bone marrow mimics, tissue engineered constructs have been used to deliver cells found at pre-metastatic niche sites to generate a more accurate model. Stromal cells (e.g. neutrophils, fibroblasts, lymphatic endothelial cells) at target organs provide the microenvironment necessary for human breast tumor cell colonization [81, 82]. Local fibroblasts participate in the formation of pre-metastatic niches and become cancer-supportive through the secretion of growth factors and ECM remodeling proteins [83]. In a model of ovarian and colorectal peritoneal metastasis, De Vlieghere et al. designed cancer-associated fibroblast (CAF) loaded microparticles (MP-CAF) to divert peritoneal metastasis. Human CAFs were encapsulated within alginate/gelatin microparticles (500-700 μm in diameter), and the particles were coated with a membrane composed of polyelectrolytes to retain CAFs within the microparticle and prevent degradation. Once implanted in the intraperitoneal space of nude mice, CAFs and CAF-secreted ECM were found to be key in the formation of peritoneal niches for metastasis, and as a result, can serve as a biomimetic trap for cancer cells [84]. Injection of MP-CAFs into the peritoneal cavity redirected cancer cells to the microparticles and resulted in prolonged animal survival [38]. Similarly, MDSCs have been harvested from spleens of mice and seeded onto PLG scaffolds prior to implantation in an orthotopic model of breast cancer using highly metastatic, brain-tropic MDA-MB-231BR cells [31, 85]. MDSCs were retained

on the scaffold after implantation, and recruited significantly more tumor cells to the implant site relative to blank scaffolds. Collectively, implantable bone marrow niches and other cell-laden scaffolds represent a powerful tool to investigate the contribution of specific cell types to metastatic cell homing and colonization of tissues and organs.

2.5 Tumor cell behavior at engineered niches

Once a disseminated tumor cell adheres to and grows within a niche present in the target organ, the cell is said to have colonized the organ. Colonization has been associated with specific genetic changes, including a mesenchymal-to-epithelial (MET) transition. In contrast to the EMT transition during invasion, MET is the process by which tumor cells return to their epithelial-like state to form a distant tumor mass. MET is typically characterized with gene expression studies, generally showing a return to expressing E-cadherin and down-regulating vimentin [86]. Metastatic colonization is also mediated by the activity of specific transcription factors, including decreased activity of TGFβ/SMAD3 activity and increased PRRX1 activity [87, 88]. As disseminated tumor cells successfully colonize the target organ, proliferation at the metastatic site may occur based on cues received from the pre-metastatic niche [3]. The cues involved in activating dormant metastatic cells to a proliferative state are still largely unknown. However, there is evidence that the perivascular niche and sprouting versus stable endothelial networks are able to regulate dormancy through control of TSP-1, TGF-β, periostin, tenascin, versican, and fibronectin, all factors previously implicated in the pre-metastatic niche [89]. Alternatively, tumor cells may also reside in a dormant state where the tumor cells do not divide or the rate of proliferation is equal to the rate of cell death [90]. The pre-metastatic niche has been shown to be involved in transitioning dormant disseminated tumor cells into an active state and initiating their proliferation [89]. Metastatic inefficiency is defined as the inability of tumor cells to grow at a metastatic site [91–93]. Without proper acti-

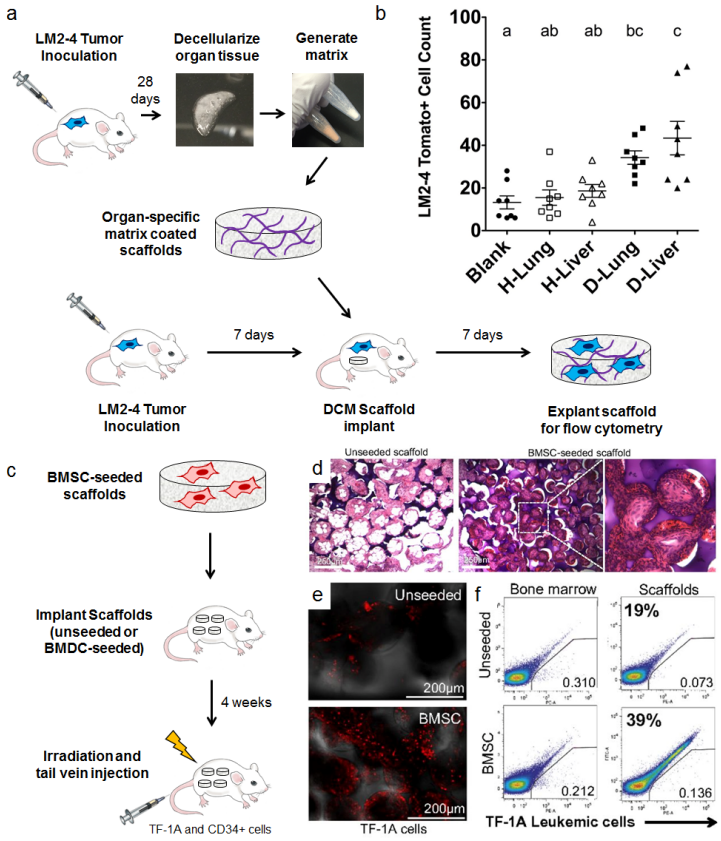

Figure 2.4: **Modeling organotropism using ECM- or BMSC-functionalized scaffolds.** (A) Decellularized lung and liver matrix from healthy and diseased mice inoculated with tdTomato-tagged LM-2 lung/liver targeting breast tumor cells was used to coat PCL scaffolds, and scaffolds were implanted subcutaneously in tumor-inoculated mice to detect differences in tumor cell colonization as a function of matrix coatings. (B) Matrix-coated scaffolds from diseased lungs and livers recruited more cells relative to blank and healthy coating controls as assessed by flow cytometry.(C) Delivery of multipotent BMSCs (CD44+, CD106+, CD14-, CD34-, CD45-, CD73+, and CD105+) on scaffolds recruit leukemia tumor cells to an implant site. (D) Images of hematoxylin and eosin stained tissue sections of subcutaneously implanted 3D microfabricated polyacrylamide scaffolds (unseeded vs. BMSC seeded, scale bars = 250 μm). (E) Homing of intravenously transplanted human TF-1A cells to unseeded vs. BMSC seeded scaffolds. Confocal images of scaffolds show significantly more stained TF-1A cells arriving to BMSC-seeded scaffolds 6 hours after injection (scale bars = 250 μm). (F) Flow cytometric analysis of labeled TF-1A cells at the bone marrow vs. implanted scaffolds. FACS analysis suggests there were approximately twice as many cells at BMSC-seeded scaffolds relative to unseeded scaffolds.

vation, disseminated tumor cells may undergo apoptosis at the target organ, remain dormant at the metastatic site for up to several years, or continue circulating through the body [94–96].

In vitro biomaterial models of colonization, including models of the pre-metastatic niche, have proved to be useful to model critical cues that enable sustained tumor cell proliferation. The accumulation of ECM proteins and inflammatory immune cells have been implicated in their ability to activate dormant CTCs into a proliferative state. These effects have been investigated using materials such as a 3D basement membrane culture model. Barkan et al. demonstrated that solitary tumor cells remain dormant due to cell cycle arrest through elevated p16 and p27 activity [28, 97]. The proliferation rates of multiple cell types in 2D and 3D basement membrane gels have been tested, and a variety of breast tumor cell lines had signs of dormancy in 3D *in vitro* culture with increased activity of p16 and p27 cell cycle regulators. These results were comparable to *in vivo* dormancy typically exhibited by these cell lines. However, the introduction of fibronectin to the 3D culture environment enhanced proliferation rates of dormant cells and increased cytoskeletal rearrangements, indicating a dormant/static to proliferative/dynamic switch in phenotype. These results imply that ECM components typically found in the pre-metastatic niche, i.e. fibronectin, are greatly involved in initiating the dormant-to-proliferative switch.

Metastatic cells at the pre-metastatic niche experience paracrine signals from neighboring cells. Consequently, 3D co-culture systems are currently being utilized to more accurately model the pre-metastatic niche *in vitro* [98]. For instance, to model MDA-MB-231 tumor cell extravasation, the bone pre-metastatic niche was recently modeled in 3D using a microfluidic platform consisting of osteo-differentiated mesenchymal stem cells embedded in a collagen gel lined with endothelial cells [44]. Likewise, 3D collagen gels containing human lung adenocarcinoma cells, lung fibroblasts, and macrophages were used to track MMP-1 and VEGF production in different

culture conditions (e.g. hypoxia) [13]. Co-culture systems in which cancer cells, osteoblast-like cells, and/or mesenchymal stem cells are placed in a matrix are being employed to generate a microenvironment *in vitro* that models elements of the *in vivo* metastatic bone niche. These systems have imparted enhanced migration, adhesion, angiogenicity, and drug resistance to human breast adenocarcinoma cells when co-cultured with osteoblast-like cells and mesenchymal stem cells on a silk scaffold compared to indirect co-culture models [99]. Phenotypic changes were reported for osteoblasts in the metastatic niche including decreased proliferation and mineralization as tumor cell activity was enhanced [99]. A similar study was performed with LNCaP prostate cancer cells and human osteoblasts [100]. However, in this approach the authors were interested in paracrine signaling pathways and instead of direct co-culture, the LNCaP cells were embedded in PEG hydrogels and co-cultured with PCL scaffolds pre-seeded with osteoblasts. Microarray analysis demonstrated that paracrine signaling between cancer cells and osteoblasts in two separate tissue engineering constructs alter gene expression patterns associated with homing and colonization (such as S100A6) compared to mono-culture controls. As *in vitro* strategies continue to evolve the inclusion of multiple cell types in a 3D culture system will be critical for generating more robust niche platforms for study. Engineered biomaterial models that use multiple cell types may allow for a more accurate mimic of the pre-metastatic niche and may provide a platform to evaluate the cues critical for tumor cell behavior decisions within the niche.

2.6 Translational opportunities for pre-metastatic niche mimics

In this section, we demonstrate that implantable niches may serve as oncomaterials, defined as biomaterials that enable detection and/or treatment of cancer. The

juxtaposition of biomaterials and oncology principles to enable detection and treatment of cancer metastasis may provide more effective therapies (**Figure 2.6A, 2.6B**). In a clinical setting, the probability of a tumor spreading to target organs has been shown to correlate with tumor size. Tumors less than 2 cm diameter have a lower risk of metastasis, compared to tumors greater than 2 cm in diameter [101]. Detection strategies for metastasis are often limited to CT and MRI scans, and tumors must be at least 1 cm in size to distinguish from surrounding tissue [101]. These size limitations are particularly problematic for highly aggressive cancers such as pancreatic that disseminate at very early stages of the disease [102]. Technologies for the early detection of metastatic disease combined with an early intervention prior to the spread of metastatic tumor cells to solid organs provide an opportunity to improve patient outcomes.

2.6.1 Materials for metastatic cell detection

The probability of patient survival increases with early detection of rare CTCs in the blood [103], which has motivated the continued development of these technologies. Nanomaterial strategies have been employed to isolate and characterize CTCs for developing personalized therapies for cancer patients [104]. The traditional approach to developing personalized therapies is to analyze the genetic aberrations of tumor biopsy samples from patients. As cancer progresses to metastasis, tumor cells constantly evolve at a molecular level, and the turnover of tumor cell molecular targets and emergence of therapeutic-resistant clones challenges the development of personalized therapies. For these reasons, techniques to capture, characterize, and culture CTCs are being developed to complement primary tumor biopsy analysis and provide a more comprehensive study of tumor genomics for individual patients [104–106]. CellSearch, an FDA approved, commercially available CTC enrichment system, enables reliable detection of CTCs in blood samples from metastatic cancer patients

[107]. Most notably, *ex vivo* culture of CTCs in conjunction with *in vitro* biomaterial mimics of the pre-metastatic niche have facilitated the capture, culture, and study of CTCs [108–110].

CTCs are isolated from blood, whereas cells found within the pre-metastatic niche mimics have left the vasculature and may represent a distinct cell type with distinct prognostic value. Despite advances in *ex vivo* CTC detection, CTCs captured in blood samples may remain in the circulation for years, and may not be representative of tumor cell populations capable of colonization [95, 105, 111]. Additionally, detection of CTCs does not indicate that permissive niches for tumor cells to home, colonize and proliferate exist. Recently, Azarin et al. reported biomaterial scaffolds for the early detection of cancer metastasis [31]. Using an orthotopic mouse model of breast cancer, micro-porous PLG scaffolds were implanted either subcutaneously or in the intraperitoneal fat. Tumor cells populated the scaffolds prior to their colonization at common organ sites (i.e. lung, liver, and brain). Interestingly, using inverse spectroscopic optical coherence tomography (ISOCT) [112], unique microstructural alterations were detected at the scaffold due to tumor cell arrival, allowing for a non-invasive method of metastasizing tumor cell detection. The scaffold technology, coupled with ISOCT or other imaging techniques, may enable a viable method for early metastasis detection while overall metastatic tumor burden remains low (**Figure 2.6C**). In a future clinical setting, these scaffolds, either alone or modified with ECM proteins or cytokine delivery, may provide a practical source of actively colonizing tumor cells for phenotypic and genomic analyses of patient-specific metastatic tumor cells and their heterogeneity.

2.6.2 Early detection, early intervention, and metastatic cell capture can enhance survival

Recently, implantable scaffolds have been shown to significantly impact survival in mouse models of metastasis. For instance, micro-porous PCL scaffolds have recently increased survival of immune competent mice inoculated with 4T1 metastatic breast tumor cells [30]. The scaffold provides a site for early detection and acts as a sink for metastatic tumor cells and pre-metastatic niche immune components. As a result, the scaffold reduced the average tumor burden in the liver and brain. A post-surgical model of breast cancer metastasis was used to investigate the impact of the scaffold on survival. In this model the primary tumor was removed after the time point where tumor cells were detectable in scaffolds. Results show 40% of scaffold-implanted mice survived the tumor resection procedure past 200 days relative to sham controls where survival did not exceed 30 days. The study suggested that increased survival may result from a decreased burden of MDSCs present at the primary tumor and spleen of scaffold-implanted mice (**Figure 2.2D**). Therefore, the study implicates that biomaterials designed to reduce the overall generation of MDSCs during metastatic disease progression or divert them to an ectopic location may impact survival. Similarly, exosome impregnated scaffolds drastically changed the pattern of peritoneal ovarian cancer metastasis by redirecting the vast majority of tumor cells to the implant (**Figure 2.3B**) [29], which resulted in a significant survival benefit for mice that receive an implant versus those that did not (mean survival of 200 days compared to 120 days). Additionally, removal of the implant after focalization of much of the disease to the biomaterial further enhanced survival (310 days mean survival). These studies have demonstrated that by taking advantage of the natural biological cues that form the pre-metastatic niche in distant organs, vast numbers of pre-metastatic niche forming cells and/or metastasizing cancer cells themselves can be captured, which combined with a treatment can provide a substantial survival

advantage.

2.6.3 Opportunities for metastasis detection platforms

Although recent evidence suggests pre-metastatic niche models enable early detection and treatment of metastatic disease, open questions remain regarding the efficacy of these platforms when compared to other emerging metastasis detection technologies. Additional technologies for metastasis detection include exosome detection and CTC enumeration **Table 2.3**. Both of these platforms are part of a larger initiative to utilize liquid biopsies to gain more information about a patients disease state, evolving molecular features, and response to therapy. While liquid biopsies have shown promise in these areas they also have distinct disadvantages that could potentially be circumvented by pre-metastatic niche mimics. For example, exosome detection is likely to be less sensitive than CTC detection due to exosome heterogeneity and the presence of large numbers of exosomes in healthy patients [70, 113]. Similarly, the presence of CTCs indicates the risk for metastasis but does not indicate that there are permissive microenvironments in organs for these cells to home and colonize. These considerations show specific advantages for the use of pre-metastatic niche mimics, however, there are also potential issues associated with the clinical use of these devices. The safety of creating a site for metastatic cells to home will be evaluated in clinical trials, however current preclinical work has demonstrated reduced tumor burden and enhanced survival associated with focalization of disease at an implant [29–31].

In a clinical setting, the choice of material (**Table 2.2**) is critical for designing a functional implantable device for recruiting and detecting metastatic cells. For example, materials such as PLG are susceptible to hydrolytic degradation, thus limiting the amount of time the material can remain in a patient. The scaffold should ideally not degrade rapidly and maintain its structure for several months during the course

of a patients treatment, given that metastasis may occur on a timescale from months to years [114]. Polymer scaffold degradation is desired for many tissue engineering applications where tissue growth eventually replaces the material, but degradation is likely undesirable for long-term implantable metastasis detectors in patients. Non- or semi-degradable materials could be used to fabricate implantable scaffolds less susceptible to hydrolytic degradation [80]. The material must also elicit an appropriate inflammatory response at the implant site in order to initiate the recruitment of metastatic cells, and should be amenable to harvesting intact populations of tumor cells for downstream analysis. Additionally, scaffold porosity increases the interior surface area for blood vessel and immune cell infiltration, in order to provide tumor cells access to the scaffold. In a future clinical setting, material selection will be paramount for successful translation of pre-metastatic niche mimics as oncomaterials.

Thus far, no clinical trials have been initiated for the application of biomaterial pre-metastatic niche mimics as devices to detect metastasis. Although several biomaterials utilized as pre-metastatic niche mimics are already FDA approved for use in human patients (**Table 2.2**), limitations in imaging tumor cell arrival to the implant remain. ISOCT is a practical approach for detecting the nanostructural alterations due to tumor cell arrival [112], however, the penetration depth that is associated with this optical technique will need to be enhanced for translation to a clinical setting. Future iterations of pre-metastatic niche mimics may implement alternative methods for tumor cell detection. Imaging technologies already available in the clinic such as ultrasound may be implemented for tumor cell detection. In order for translation to move forward, the safety of biomaterial devices in large animal and human subjects needs to be assessed. Even though safety remains an open question, the future for pre-metastatic niche mimics as oncomaterials remains promising, given the ability to detect and treat metastasis at early stages of disease in pre-clinical studies.

Platform	Stage	Safety	Sensitivity	Specificity	Therapy	Refs
Exosome detection	Primary	+	-	+	-	[83]
CTC detection	Circulation	+	+	+	-	[107, 115]
Biomaterial mimic	Dissemination	?	+	++	+	[30, 31, 34, 42]

Table 2.3: **Risks and opportunities of detection technologies for metastasis**

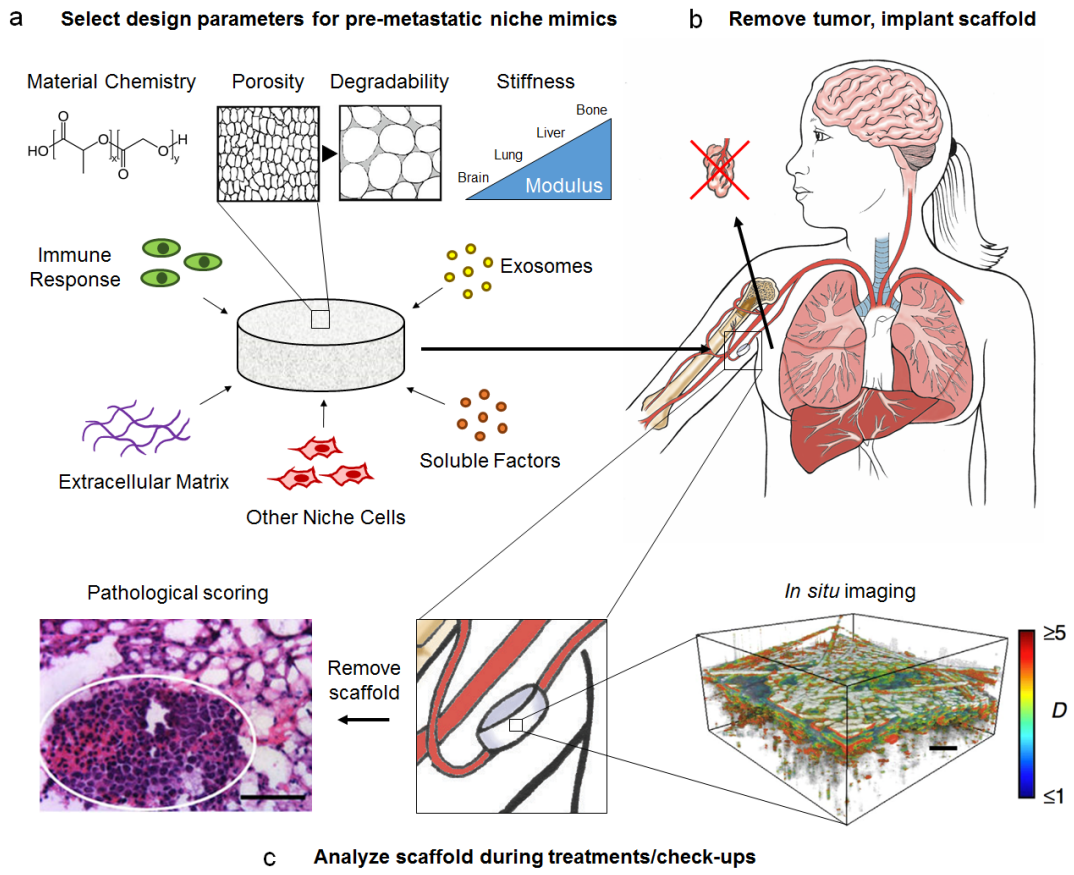

Figure 2.5: **Proposed detection strategy for metastatic breast cancer.** (A) Pre-metastatic niche oncomaterials may be designed from a variety of parameters, including the natural immune response to the implant, soluble factor delivery, extracellular matrix, and cell delivery. Parameters may be tuned depending on the cancer or the needs for a specific patient for designing the most effective oncomaterial. (B) After removal of the primary tumor, a biomaterial scaffold may be implanted subcutaneously, ideally before metastasis occurs. (C) Regular imaging at check-ups may be performed during the patients course of treatment. When using ISOCT, the shape factor (D) may be used to quantify microstructural alterations at the scaffold due to the arrival of metastatic tumor cells (scale bar = 200 μm). Illustrations courtesy of Katie Aguado.

2.7 Opportunities and Conclusions

Pre-metastatic niche mimics offer the ability to identify and validate critical factors leading to metastatic cell colonization in an ectopic site. Roles of inflammatory immune cells, secreted factors, ECM proteins, and delivered cells have been evaluated using niche mimics to determine contributions to metastatic cell homing and colonization. Furthermore, the capture of early metastatic cells at a pre-defined site may enable early detection of metastatic cell dissemination. The development of novel imaging modalities, or the engineering of probes to label colonizing tumor cells may enable real-time tracking of tumor cells or vascular leakiness at the niche during the evolution of the disease. This capture can reduce the burden of disease in solid organs, and provides an extended window of time over which a therapeutic intervention may improve outcomes. The use of oncomaterials supplemented with current therapeutic strategies such as surgery and chemotherapy may serve as a disruptive technique for combating metastasis. Extending beyond the concept of capturing tumor cells, scaffolds may be bioengineered to capture and manipulate other types of circulating niche components, including exosomes and immune cells that reflect disease (e.g., MDSCs). Furthermore, future work in the genetic profiling of captured metastatic cells at implanted niches may lead to the identification of the types of cells arriving at the scaffold (e.g. tumor stem cells, EpCAM+ cells), which may guide the discovery of precision targets to treat metastasis based on the disease biology. In sum, the successful integration of pre-metastatic niche components in biomaterials can enable the discovery of novel cues leading to metastasis, as well as provide novel detection and therapeutic strategies to combat disease progression.

CHAPTER III

Therapeutic Benefit of Scaffold Implantation

3.1 Authors

Shreyas S Rao, Grace G Bushnell, Samira M Azarin, Graham Spicer, Brian A Aguado, Jenna R Stoehr, Eric J Jiang, Vadim Backman, Lonnie D Shea, Jacqueline S Jeruss

3.2 Contributions

I worked closely with Shreyas for the latter half of this study including validation of early detection and ISOCT, reduction of tumor burden in liver and brain with scaffold implantation, post-surgical survival model, and reduction of CD11b+Gr-1hiLy6C- cells in the spleen and primary tumor of mice with scaffolds. Additionally, I performed Gr-1 depletion and survival studies independently to confirm the role of CD11b+Gr-1hiLy6C- myeloid derived suppressor cells in the survival benefit associated with scaffold implantation.

3.3 Abstract

The onset of distant organ metastasis from primary breast cancer marks the transition to a stage IV diagnosis. Standard imaging modalities often detect distant

metastasis when the burden of disease is high, underscoring the need for improved methods of detection to allow for interventions that would impede disease progression. Here, micro-porous poly(ε-caprolactone) scaffolds were developed that capture early metastatic cells and thus serve as a sentinel for early detection. These scaffolds were used to characterize the dynamic immune response to the implant spanning the acute and chronic foreign body response. The immune cell composition had stabilized at the scaffold after approximately 1 month, and changed dramatically within days to weeks after tumor inoculation, with CD11b+Gr1hiLy6C- cells having the greatest increase in abundance. Implanted scaffolds recruited metastatic cancer cells that were inoculated into the mammary fat pad *in vivo*, which also significantly reduced tumor burden in the liver and brain. Additionally, cancer cells could be detected using a label-free imaging modality termed inverse spectroscopic optical coherence tomography, and we tested the hypothesis that subsequent removal of the primary tumor after early detection would enhance survival. Surgical removal of the primary tumor following cancer cell detection in the scaffold significantly improved disease-specific survival. The enhanced disease-specific survival was associated with a systemic reduction in the CD11b+Gr1hiLy6C- cells as a consequence of the implant, which was further supported by Gr-1 depletion studies. Implementation of the scaffold may provide diagnostic and therapeutic options for cancer patients in both the high-risk and adjuvant treatment settings.

3.4 Introduction

The oncogenic progression of breast cancer from the primary tumor to distant metastatic sites is the critical event that defines stage IV disease [5, 116, 117]. Currently, metastatic disease is detected through radiologic imaging modalities after the burden of distant disease has become destructive to the host organ [118–120]. A limitation to the development of life-preserving timely interventions is the striking lack

of robust technologies capable of early detection of metastatic events. Additionally, experimental model systems are needed that permit systematic screening and examination of factors contributing to breast cancer metastasis in a controlled setting. Detection of circulating tumor cells (CTCs) is being pursued in both the experimental and clinical settings. While promising [121, 122], the widespread use of CTC capture is not without challenges, given the high biomarker sensitivity and specificity required to capture a low number of circulating CTCs [123, 124]. Furthermore, CTCs may not represent the population of cells capable of metastasis or these cells could circulate for long periods before invading distant organs. The capacity to identify metastatic cells or foci at the earliest possible time-point may permit the delivery of targeted treatment interventions prior to the compromise of distant organs, potentially translating into prolonged distant metastasis free outcomes. Thus, there is an urgent need for development of novel technologies to aid in the detection of metastatic events in the nascent setting.

An emerging approach for early detection lies with the implantation of a biomaterial scaffold that can capture metastatic cells [31]. These scaffolds were modeled after the concept of the pre-metastatic niche [8, 125], echoing Pagets seed and soil hypothesis proposed over a century ago [4, 6, 51, 125, 126]. This paradigm proposes that, prior to colonization by metastatic cells, supportive cells (e.g., fibroblasts, immune cells, endothelial cells), soluble factors, and extracellular matrix (ECM) components establish a microenvironment conducive to tumor cell homing and colonization [4, 6, 51, 126, 127]. Importantly, these studies indicate that metastasis to specific organs is not random, but is influenced by the properties of the local environment [8, 125, 127]. The initial translation of these principals led to the development and implementation of micro-porous poly(lactide-co-glycolide) (PLG) biomaterial scaffolds, which recruited metastatic breast cancer cells through the local immune response *in vivo*, resulting in decreased tumor burden at metastatic sites [31]. However, PLG

scaffolds were degradable over time scales considered too short for clinical translation.

In this report, we developed micro-porous poly(ε-caprolactone) (PCL) scaffolds with greater stability than the PLG scaffolds, to investigate the dynamic immune response and cellular events associated with PCL-scaffold-mediated recruitment of metastatic breast cancer cells. Specifically, utilizing PCL scaffolds in metastatic breast cancer murine models we examined if (a) metastatic cells could be recruited to the scaffold (b) metastatic cells could be detected in the scaffold at a nascent stage, prior to cancer cell colonization of other major organs, using label-free imaging modalities and (c) scaffold implantation could influence survival following detection of cancer cells in the scaffold and then subsequent surgical removal of the primary tumor. The favorable translational endpoints from these studies could lead to the integration of scaffold implants, fabricated using FDA approved materials, into breast cancer disease management plans. Moreover, scaffolds could be recovered to examine the biology of metastatic tumor cells in conjunction with niche cells enabling the development of patient-specific treatments.

3.5 Results

3.5.1 Micro-porous PCL scaffolds for *in vivo* recruitment of metastatic cells

We developed micro-porous PCL scaffolds (**Figure 3.1A**, 5 mm diameter and 2 mm height) to create microenvironments *in vivo* and subsequently examine their ability to recruit metastatic tumor cells. The porous interconnected architecture of the scaffold was confirmed using SEM imaging (**Figure 3.1B**). Micro-structural features such as porosity, pore volume, and mechanical properties (i.e., elastic modulus) were similar for PCL and previously reported PLG scaffolds [31] (**Supplemental, Table 3.1**). The ability of PCL scaffolds to persist and create a defined space *in vivo* was

investigated by implantation into the subcutaneous dorsal space of BALB/c and NSG mice. The subcutaneous site was selected for its accessibility and amenability to non-invasive imaging. Furthermore, neither 4T1 nor MDA-MB-231BR breast cancer cells typically metastasize to the subcutaneous space, thus the presence of cancer cells in the metastatic site would likely be associated with the presence of the scaffold. PCL scaffolds retrieved after 3 months experienced minimal degradation when compared to day 0 as opposed to PLG scaffolds, which had previously been employed for *in vivo* recruitment of tumor cells [31]. PLG scaffolds showed significant degradation over this time period as quantified by scaffold area (i.e., 66% in NSG and 77% in BALB/c mouse; **Supplemental, Figure 3.8**).

The dynamic immune response to the biomaterial implant was investigated throughout the acute and chronic phases. Implantation of the PCL scaffold into healthy BALB/c mice resulted in infiltration of CD45+ leukocytes by day 3. The number of CD45+ leukocytes remained relatively unchanged after day 14 post scaffold implantation (**Figure 3.1C**). However, the relative distribution of leukocyte populations examined, including innate and adaptive immune cells, changed dynamically following scaffold implantation. The percentage of inflammatory monocytes, identified as Ly6C+F4/80- cells, decreased after day 3 and remained relatively stable at later time points, whereas the percentage of dendritic cells, identified as CD11c+F4/80-, increased after day 3 and remained stable at later time points (**Figure 3.1D**). These two cell populations constituted the majority of cells (i.e., approx 65%) observed at the PCL scaffold at later time points. The percentage of macrophages, identified as CD11b+F4/80+ cells, significantly increased through day 14 (e.g., 8.8% at day 14 vs. 1.7% at day 3, **Figure 3.1D**, $p < 0.05$) and then returned to levels observed at day 3 (e.g., 1.4% at day 60, **Figure 3.1D**, $p = 0.99$ compared to day 3). In contrast, the levels of CD11b+Gr-1hiLy6C- cells remained low at all time points examined at 0.15% (**Figure 3.1D**). In the adaptive immune cell population, the percentage of

CD4+ helper T cells and CD8+ cytotoxic T cells significantly increased over time (e.g., 1% at day 3 to 9% at day 60 for CD4+ and 1.2% at day 3 to 3% at day 60 for CD8+ respectively, **Figure 3.1D**, $p < 0.05$). The percentage of B cells, identified as CD19+, and natural killer (NK) cells, identified as CD49b+, increased post day 3 and returned to day 3 levels at later time points (i.e., day 30 and 60; **Figure 3.1D**). Importantly, the relative percentages of leukocyte subpopulations were similar between day 30 and day 60 post scaffold implantation in BALB/c mice (**Figure 3.1D**). This trend was also observed in NSG mice (**Supplemental, Figure 3.9**). Based on the stabilization of cell populations after day 30, we utilized day 30 as a time point representing the chronic response to a scaffold implant in all following experiments.

We subsequently examined the recruitment of metastatic cells to a chronically implanted microporous scaffold (i.e., a scaffold that had been implanted for 30 days prior to tumor inoculation, a time corresponding to the chronic phase of the immune response). Flow cytometry and fluorescence imaging (**Figure 3.2**) performed for scaffolds retrieved at day 15 post tumor inoculation demonstrated the presence of mouse 4T1 tumor cells in the scaffold, indicating that the local microenvironment enabled recruitment of tumor cells. Total cell infiltration was significantly greater within PCL scaffolds compared to PLG scaffolds (i.e., approximately 6e5 cells in the PCL scaffold vs. approximately 1e5 cells in the PLG scaffold, $p < 0.0001$, **Figure 3.2A**) and a similar trend was observed for tumor cell recruitment (**Figure 3.2B**, $p < 0.01$). Scaffolds were also able to recruit human MDA-MB-231BR cells in NSG mice (**Supplemental, Figure 3.11**), indicating that such a system enabled recruitment of mouse and human breast cancer cells in the context of both immune competent and immune compromised mouse models, respectively.

Following tumor inoculation, the dynamics of immune cell populations at the PCL scaffold was subsequently characterized, as tumor cells are known to influence the recruitment of immune cells from the bone marrow (25). Flow cytometric analysis indi-

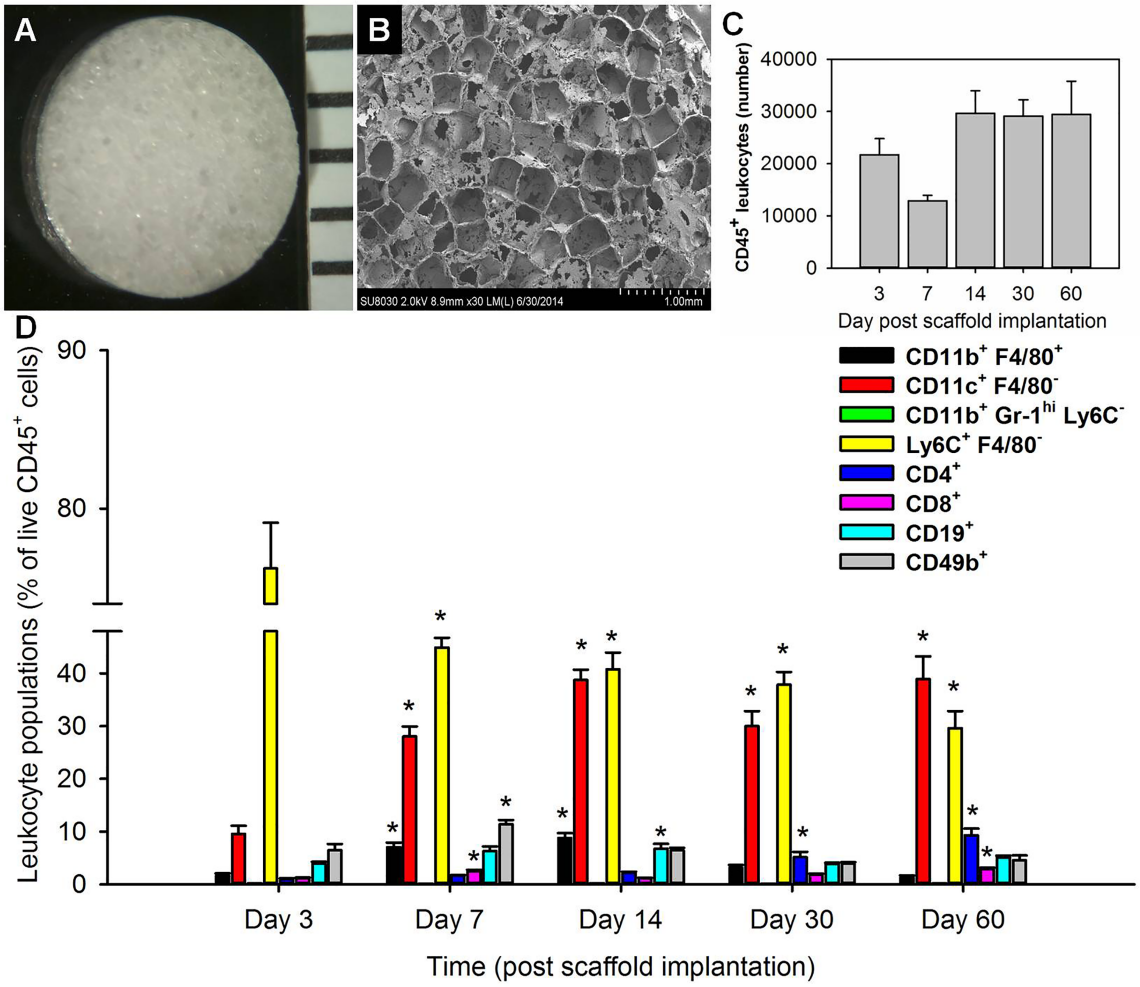

Figure 3.1: **Physical characteristics and dynamic immune cell response following implantation of micro-porous PCL scaffolds into the dorsal subcutaneous space of a BALB/c mouse.** Photomicrograph (A) and scanning electron micrograph (B) of a microporous PCL scaffold. SEM image shows the interconnected porous structure. (C) CD45+ leukocyte numbers and (D) Dynamics of CD11b+F4/80+, CD11c+F4/80-, CD11b+Gr-1hiLy6C-, Ly6C+F4/80-, CD4+, CD8+, CD19+, and CD49b+ immune cell populations expressed as a percentage of live CD45+ leukocytes at day 3, 7, 14, 30, and 60 post PCL scaffold implantation (N = 6 for each time point examined, *p <0.05 compared to day 3 as determined by the Tukey-HSD test post ANOVA). Error bars denote s.e.m.

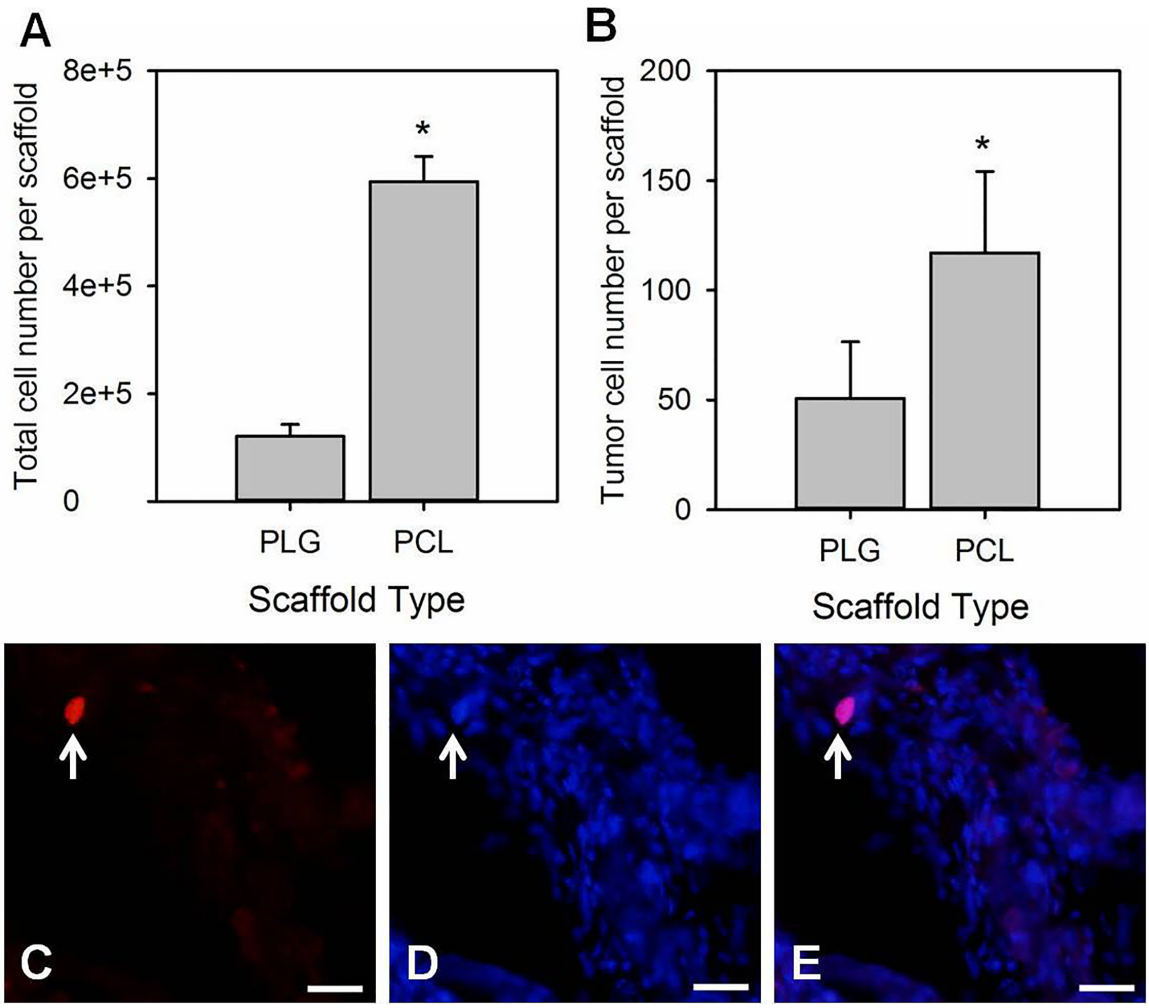

Figure 3.2: **Micro-porous scaffolds implanted for 30 days prior to tumor inoculation recruit metastatic cells.** Number of (A) total cells and (B) tumor cells (tdTomato+ cells) isolated from micro-porous PLG and PCL scaffolds at day 15 post tumor inoculation analyzed via flow cytometry (N = 10, *p <0.01 as determined by t-test for analysis of total cell numbers and Wilcoxon rank-sum test for tumor cell numbers). Fluorescence image of a PCL scaffold section shows the presence of a tumor cell (indicated by white arrow) as identified using tdTomato (C) and DAPI (D) fluorescence and their co-localization (E). Scale bar indicates 20 m. Error bars denote s.e.m.

cated an increase in Ly6C+F4/80- and CD11b+Gr-1hiLy6C- cells at the PCL scaffold site (**Figure 3.3C and 3.3D**, $p < 0.0005$). For example, the numbers of CD11b+Gr-1hiLy6C- cells increased from 0.1% at day 0 to 17% at day 21 post tumor inoculation ($p < 0.05$), an increase of two orders of magnitude relative to their numbers at the PCL scaffold site in tumor-free BALB/c mice (**Figure 3.1D, Figure 3.3C**). Both cell types have been implicated in the pre-metastatic niche [15, 16, 19, 51, 128]. In contrast, the percentages of CD11b+F4/80+ macrophages, CD11c+F4/80- dendritic cells, and CD8+ cytotoxic T cells decreased at the PCL scaffold site (**Figure 3.3A, 3.3C, 3.3F**, e.g., 30% at day 0 vs. 14% at day 21 for dendritic cells, $p < 0.05$). The percentage of CD19+ B cells, CD49b+ NK cells, and CD4+ helper T cells increased at day 3 and then decreased at later time points (**Figure 3.3G, 3.3H, 3.3E**). Specifically, NK cells increased from 4% at day 0 to 8% at day 3, followed by a decrease to 2.5% at day 21 post tumor inoculation (**Figure 3.3H**, $p < 0.05$). Interestingly, the immune cell dynamics at the PCL scaffold site reflected the dynamics observed in the spleen post tumor inoculation (**Figure 3.3** vs. **Supplemental, Figure 3.10**). In summary, the changing immune microenvironment at the PCL scaffold site post tumor inoculation correlated with recruitment of 4T1 tumor cells, and is consistent with prior literature reports on the role of the immune cells in the pre-metastatic niche [10, 15, 16, 19, 51, 128, 129].

3.5.2 Early detection of metastatic cells at the PCL scaffold

The ability to detect the presence of metastatic disease at an early stage was examined through evaluation of the percentage of tumor cells in the PCL scaffold relative to the cancer cells detected in typical metastatic sites such as the lung, liver, and brain, at day 5 post tumor inoculation. Flow cytometry analysis revealed that the PCL scaffolds had a detectable percentage of tumor cells (i.e., 0.005 +/- 0.002%) compared to the lung, liver, and the brain, none of which had detectable tumor cells

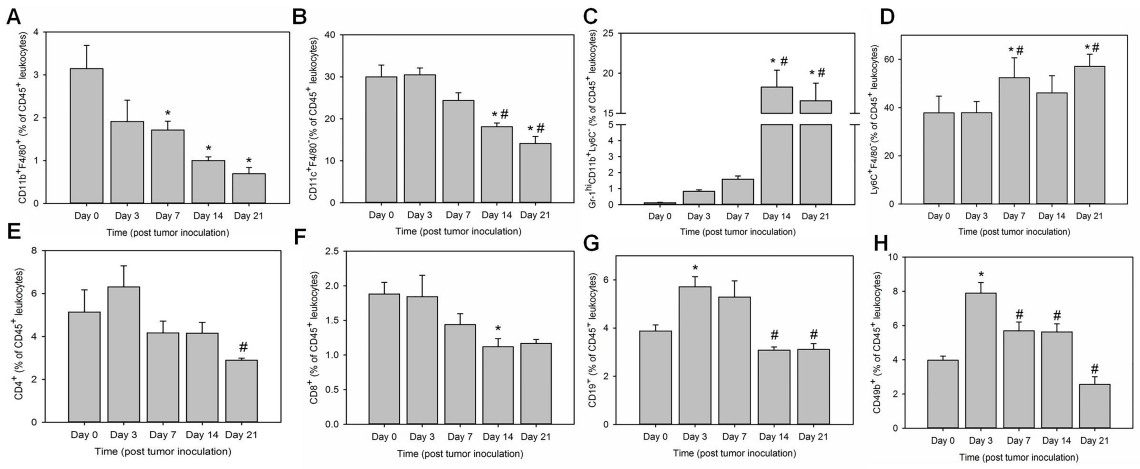

Figure 3.3: **Tumor progression influences dynamics of leukocyte populations at the PCL scaffold.** Percentage of (A) CD11b+F4/80+ (B) CD11c+F4/80- (C) Gr-1hiCD11b+Ly6C- (D) Ly6C+F4/80- innate immune cell populations and percentage of (E) CD4+ (F) CD8+ (G) CD19+ and (H) CD49b+ adaptive immune cell populations in the total population of live CD45+ leukocytes at day 0, 3, 7, 14, and 21 post tumor inoculation (N = 8 for each time point examined, $p < 0.05$ compared to day 0 and $p < 0.05$ compared to day 3 as determined by Tukey-HSD test post ANOVA). Error bars denote s.e.m.

(**Figure 3.4A and 3.4B**; N = 5 for lung, liver, and brain, N = 10 for PCL scaffolds, $p < 0.05$, Fishers exact test). The greater density of tumor cells observed at the PCL scaffold site compared to other organ sites supports the use of this tool for detecting metastatic disease at a nascent stage.

We subsequently investigated the feasibility of using a label-free imaging technique: inverse spectroscopic optical coherence tomography (ISOCT), for the early detection of metastatic disease in a chronic model of scaffold implantation. The tissue was modeled as a continuous random refractive index distribution, which enabled the refractive index correlation function shape factor D to be computed from the shape of the backscattering intensity spectrum obtained with ISOCT [130]. If D has a value between 0 and 3, it has a physical meaning of a mass fractal dimension, reflecting a more clumped structure associated with higher D. Prior studies of early carcinogenesis with ISOCT and a similar spectroscopic technique, low-coherence enhanced backscattering spectroscopy (LEBS), have revealed that D measured from tissue increases with cancer progression [130–132]. Thus, similar ultra-structural tissue modifications occurring in the pre-metastatic niche are likely to have an analogous effect on D. D has previously been reported to reflect mass-density distribution features at length scales of 35-350 nm [130]. In addition, D values from tissue have been demonstrated as a robust biomarker of early-stage carcinogenesis [130]. Consistent with these observations and data obtained via flow cytometric analysis (**Figure 3.4A and 3.4B**), a significant increase was observed in average D values obtained from ISOCT measurements at the PCL scaffold site in tumor bearing mice (N = 7) compared to tumor free mice (N = 8; $p < 0.05$, **Figure 3.4C**), confirming ultra-structural alterations to the scaffold and further indicative of the presence of tumor cells. The color map overlay of D values (**Figure 3.4D and 3.4E**) demonstrated the distribution throughout the scaffold. These results suggest that ISOCT could be employed for early detection of metastatic disease at the PCL scaffold.

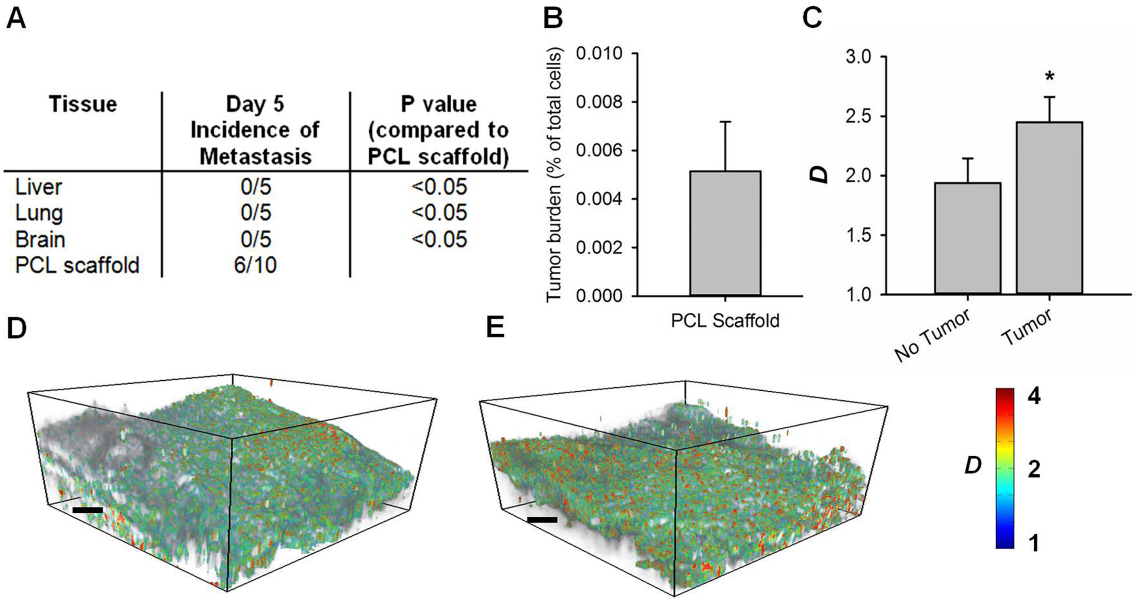

Figure 3.4: **Micro-porous PCL scaffolds enable early detection of metastatic cells in a chronic model of scaffold implantation.** (A) Number of mice with detectable tumor cells analyzed by flow cytometry in the lung, liver, and brain in a group of 5 mice at day 5 post tumor inoculation (N = 5 for lung, brain, and liver; N = 10 for PCL scaffolds, *p <0.05 as determined using the Fishers exact test). (B) Percentage of tdTomato+ tumor cells isolated from the PCL scaffold at day 5 post tumor inoculation analyzed via flow cytometry. (C) Average D value for PCL scaffolds isolated from tumor free and tumor bearing mice. Scaffolds from tumor bearing mice were isolated at day 5 post tumor inoculation. (N = 14 scaffolds for tumor free and N = 16 scaffolds for tumor bearing mice, *p <0.05 as determined using the Wilcoxon rank-sum test). Representative three dimensional maps of D generated via ISOCT analysis of PCL scaffolds in tumor free (D) and tumor bearing mice (E). Scale bars indicate 200 m. Error bars denote s.e.m.

3.5.3 PCL scaffold implantation reduces tumor burden and improves disease-specific survival

We subsequently investigated the hypothesis that the recruitment of metastatic cells to the chronically implanted PCL scaffolds may reduce the tumor burden at typical metastatic sites, such as the liver, brain, and the lung at day 15 post tumor inoculation. Flow cytometry analysis indicated that the percentage of tumor cells in the liver and the brain was reduced in mice receiving a PCL scaffold versus mice undergoing a mock surgery. As stated, the tumor burden was reduced by 64% for the liver (**Figure 3.5A**, N = 15, $p < 0.05$) and 75% for the brain (**Figure 3.5B**, N = 8 for mock surgery, N = 6 for scaffold implant, $p < 0.05$ as determined using the Wilcoxon rank-sum test in both cases). However, in this immunocompetent mouse model, a reduction in the tumor burden in the lung was not observed (**Figure 3.5C**, N = 11, $p = 0.7$) distinct from our previous observations in an immune compromised NSG mouse inoculated with human MDA-MB-231BR cells [31].

A post-surgical model of breast cancer metastasis was then applied to investigate the potential for PCL scaffold implants to influence survival. In this model, the primary tumor was resected at day 6 (**Supplemental, Figure 3.12**) or 10 (**Figure 3.6A**) post tumor inoculation, which corresponded to a time after which cancer cells were detectable in the scaffold by label-free imaging (i.e., day 5, **Figure 3.4**). The resected tumor weights were comparable for both groups, with tumors from the mock surgery group weighing 0.423 +/- 0.035 g versus tumors from scaffold implanted mice weighing 0.419 +/- 0.029 g at day 10 post inoculation ($p = 0.93$, t-test, **Figure 3.6B**). Kaplan-Meier survival analysis demonstrated a significant improvement in survival in mice receiving a PCL scaffold implant compared to mice receiving a mock surgery with resection at day 10 (**Figure 3.6C**, N = 7 per group, $p < 0.05$, Log-rank test). The sacrifice end-points utilized for mice in both groups for data corresponding to **Figure 3.6** are described in **Supplemental, Table 3.2**. With resection at day 6

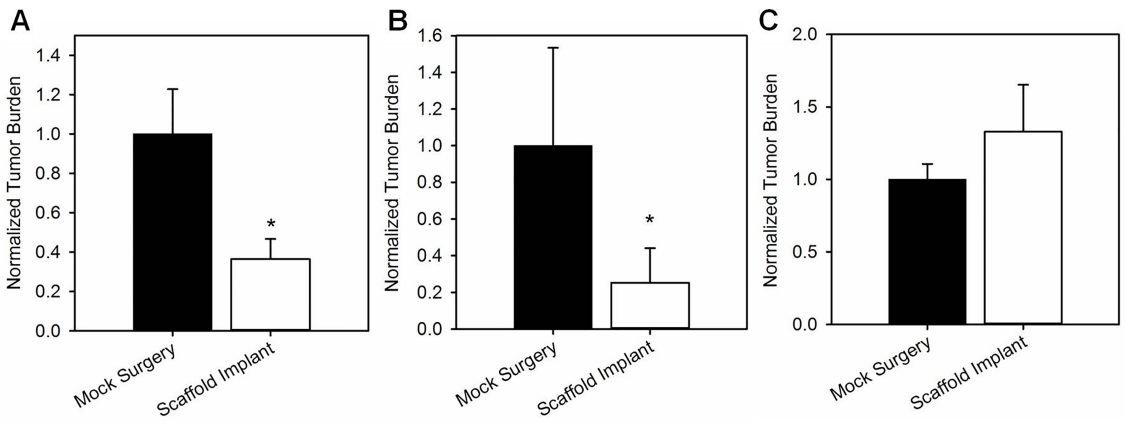

Figure 3.5: **Recruitment of 4T1 tumor cells to the PCL scaffold site reduces tumor burden in metastatic sites such as the liver and brain in a chronic model of scaffold implantation in BALB/c mice.** Normalized average tumor burden in the (A) liver, (B) brain, and the (C) lung for the scaffold and mock surgery groups. The average burden in the mock group was set to 1 (N = 6 for each group, * $p < 0.05$ compared to mock surgery as determined by the Wilcoxon rank-sum test). Tumor burden in the lung was identical in both groups. Error bars denote s.e.m.

post tumor inoculation, 40% of both mock and scaffold groups survived indefinitely (**Supplemental, Figure 3.13**) mirroring the 40% survival in the scaffold group with day 10 resection (**Figure 3.6C**), indicating that the scaffold increased the time over which a therapeutic intervention such as surgery can be performed and provide a survival benefit.

Given the greatest increase in the abundance of CD11b+Gr-1hiLy6C- cells (2 orders of magnitude change) at the PCL scaffold site post tumor inoculation, we hypothesized that the increased survival with scaffold implantation may reflect a differential distribution of CD11b+Gr-1hiLy6C- cells at the primary tumor (local) and the spleen (systemic). Flow cytometric analysis indicated that the abundance of CD11b+Gr-1hiLy6C- cells was reduced in mice receiving a scaffold implant versus mice receiving a mock surgery examined at day 10 post tumor inoculation. The burden of CD11b+Gr-1hiLy6C- cells was reduced by 39% in the primary tumor (**Figure 3.7A**) and 30% in the spleen (**Figure 3.7B**, N >7, $p < 0.05$ as determined by t-test

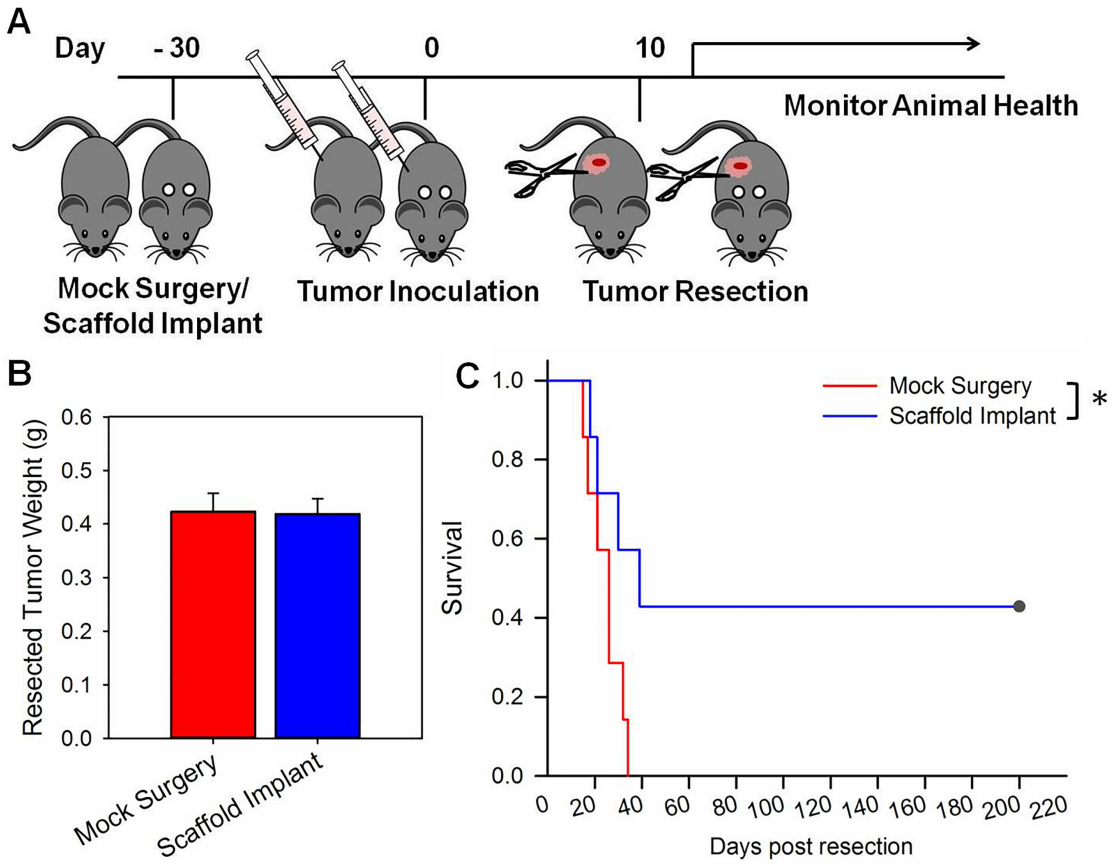

Figure 3.6: **Micro-porous PCL scaffolds improve survival in a post-surgical model of breast cancer metastasis.** (A) Schematic of experimental design to examine the influence of scaffold implant on survival (B) Average resected tumor weights for mock and scaffold group were identical, p = 0.93, t-test) (C) Kaplan-Meier survival curve for mice undergoing mock surgery versus mice receiving a scaffold implant (N = 7 for each group, *p <0.05 as determined using the Log rank test). Error bars denote s.e.m.

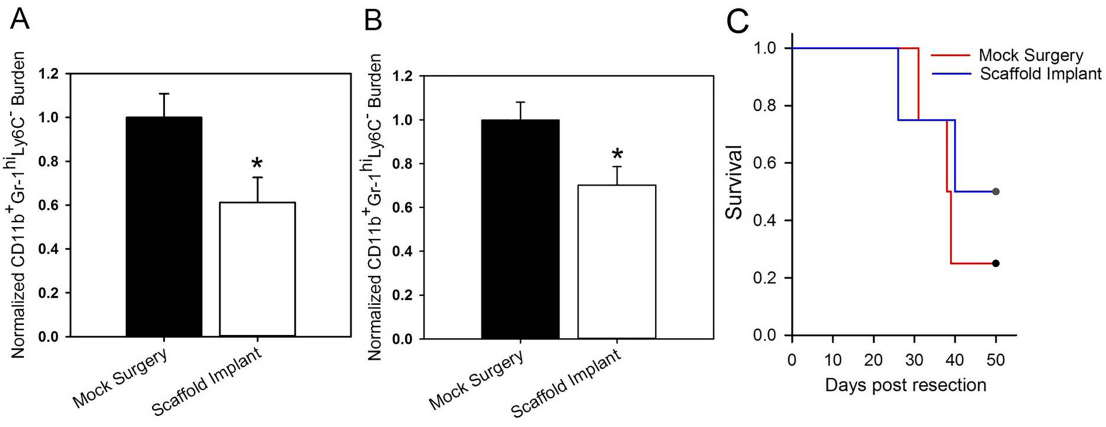

Figure 3.7: **Micro-porous PCL scaffolds reduce burden of CD11b+Gr-1hiLy6C- cells** in the (A) primary tumor and the (B) spleen in BALB/c mice. The percentage of CD11b+ Gr-1hi Ly6C- cells in the CD45+ leukocyte population was examined at day 10 post tumor inoculation via flow cytometry and is reported as normalized burden. (N = 7 for mock surgery; N = 8 for scaffold implant, *p <0.05 as determined using t-test). (C) Anti-Gr-1 depletion of CD11b+Gr-1hiLy6C- cells enhances survival in both mock and scaffold groups and diminishes the survival advantage observed for PCL implanted mice (N = 4 per group). Error bars denote s.e.m.

in both cases). This result suggests that, in part, presence of the scaffold contributes to a reduction in the abundance of key niche cells locally (i.e., primary tumor site) and systemically (i.e., spleen) that support metastasis. This observation was further investigated via Gr-1 antibody depletion of CD11b+Gr-1hiLy6C- cells *in vivo*, which was performed in the context of surgical resection (**Supplemental, Figure 3.13**). Mice receiving a mock surgery with Gr-1 depletion demonstrated survival greater than 20% by day 40 (**Figure 3.7C**), with no survival observed at this time without Gr-1 depletion (**Figure 3.6C**). Furthermore, with Gr-1 depletion, the observed difference in survival between mock and scaffold groups was not statistically significant (**Figure 3.7C**), further supporting the involvement of CD11b+Gr-1hiLy6C- cells in improving disease-specific survival in our model. Taken together, these results highlight the potential for PCL scaffold in improving disease-specific survival outcomes.

3.6 Discussion

In this study, micro-porous PCL scaffolds, implanted prior to tumor initiation, recruited metastatic cells at an early time-point in disease progression. The novel approach to this work was based on recapitulating some of the immunological aspects of the pre-metastatic niche, while prior reports have focused on materials to mimic properties of target organs (e.g., bone [33, 133], bone marrow [41]). Previous elegant studies of the pre-metastatic niche have identified some of the biological cues involved in cancer cell recruitment, such as the cellular components (e.g., hematopoietic and endothelial progenitor cells, immune cells), soluble factors (e.g., cytokines, chemokines), and ECM proteins [4, 6, 51, 125, 126]. Importantly, as indicated by Lyden [125, 127], the existence of the pre-metastatic niche implies that metastasis to a particular site is not random, but is predetermined, which supports the idea that a site could be engineered to attract metastatic cells. A synthetic scaffold provides an opportunity to create a defined environment to investigate the role of specific components involved in the colonization of metastatic cells. Scaffolds can be modified with specific niche components, such as stromal cells, ECM molecules, and cytokines to identify the key signals in the metastatic environment [27, 134], thereby providing a tool with which to advance fundamental studies of the pre-metastatic niche and tumor metastasis. Herein, the scaffold defines a site for immune cell infiltration, and we characterize the dynamic immune response associated with cancer cell recruitment.

The immune cell populations at the PCL scaffold, which had stabilized prior to tumor inoculation, were substantially altered post-tumor inoculation, suggesting that the changing foreign body response to the implant may contribute to metastatic cell recruitment. Immune cells are recognized as significant to the pre-metastatic niche [10, 15, 16, 19, 51, 128, 129]. As such, chemokine CCL-2 recruits inflammatory monocytes (Ly6C+F4/80- cells) to the pre-metastatic niche enabling metastasis of breast cancer cells [15]. Similarly, CD11b+Gr-1hiLy6C- cells are recruited via inflammatory

chemoattractants (e.g., S100A8 and S100A9) to pre-metastatic niches [135]. In addition, CD11b+Gr-1hiLy6C- cells are known to downregulate infiltration and suppress the function of T cells (CD4+ and CD8+ T cells) and NK cells [135–138]. Consistent with these observations, we found an increase in the levels of monocytes and CD11b+Gr-1hiLy6C- cells at the scaffold site post tumor inoculation and an associated decrease in the abundance of CD4+ T cells, CD8+ T cells, and CD49b+ NK cells, with the greatest change observed for CD11b+Gr-1hiLy6C- cells (i.e., more than two orders of magnitude). Importantly, the changing immune composition as a consequence of disease progression observed in the spleen largely reflected the dynamics at the scaffold site. Taken together, these results suggest that engineering a local microenvironment may be used to identify and modulate key components of cancer-associated immunogenicity in the pre-metastatic niche.

The implantation of PCL scaffolds enhanced disease-specific survival, which we hypothesized to be related to the decreased tumor burden in major organ sites and a reduction in systemic availability of key immune cells that support metastasis. The implantation of PCL scaffolds in the subcutaneous space reduced tumor burden in major organ sites (i.e., liver and brain) in an immunocompetent mouse model. We previously reported a reduction in burden in the lung in an immunocompromised mouse model using PLG scaffolds implanted in the intraperitoneal fat pad after tumor inoculation [31]. The results of the current study extend our previous observation and importantly suggest that a scaffold-based approach can contribute to the reduction in disease burden in solid organs in both immunocompetent and compromised mouse models and when implanted at different sites. Metastatic cells could be detected within chronically implanted PCL scaffolds by day 5 following tumor inoculation using ISOCT imaging, which allowed for label free detection of metastasis through changes in the tissue ultrastructure (e.g., matrix organization) and the presence of cancer cells that have a distinct nano-scale signature relative to normal cells [130]. In order to

employ ISOCT analysis for diagnostic screening of early metastasis, ultrastructural parameters measured with ISOCT (D, correlation length Ln, and refractive index fluctuation Bn), which independently change in the presence of carcinogenic tissue modification, would need to be investigated to establish a multivariate diagnostic for patients with metastatic disease.

The resection of the primary tumor at day 10 post tumor inoculation resulted in increased survival in mice that received a scaffold. The increased survival may result from a decreased burden of CD11b+Gr-1hiLy6C- cells observed locally at the primary tumor and systemically in the spleen of a scaffold-bearing mouse when compared to a mouse that received a mock surgery. Gr-1 depletion studies further supported this observation, as mice receiving a mock surgery survive longer in the context of Gr-1 depletion, and the difference between mock and scaffold groups was abrogated with Gr-1 depletion. As stated, CD11b+Gr-1hiLy6C- cells or myeloid derived suppressor cells (MDSCs) have been implicated in the pre-metastatic niche and the reduced abundance of these cells systemically may contribute to the reduced burden in solid organs and ultimately, to enhanced survival [134, 139, 140]. Finally, MDSCs have been identified in high numbers in patients with metastatic disease, correlating with clinical stage and metastatic disease burden and their levels are predictive of overall survival [141–143]. Thus, a scaffold-based approach that reduces the abundance of MDSCs could, in part, explain the survival benefit observed in our studies. Taken together, the ability to detect metastatic disease at an early stage, in combination with the survival benefit provided by the scaffold highlight the potential for this technology in transforming the current detection and management of metastatic disease.

The recruitment of metastatic cells to the scaffold, combined with label-free imaging for detection of nascent stage metastatic cells, and reduced burden of disease in solid organs (i.e., liver and brain), may ultimately allow for interventions when the disease burden is low that could translate to improved disease-specific outcomes. In

the clinical setting, the scaffold may be integrated into disease management plans by potentially serving as a sentinel site for detection of disease metastasis or recurrence. For example, the scaffold could be implanted in patients with a diagnosis of invasive cancer at the completion of adjuvant therapy, and monitored during scheduled follow-up visits using the optical imaging technique. If metastatic or recurrent disease was then detected, the scaffold could be explanted for cell retrieval and analysis to help guide targeted treatment decisions. Furthermore, in the setting of metastatic disease, given the potential survival benefit of the presence of the scaffold, patients may have extended disease-specific survival with excision of the primary tumor and scaffold implantation long-term. Finally, the scaffold may be implanted prophylactically to help detect early onset metastatic disease in high-risk patients.

Our results provide the first evidence that a scaffold for capture and detection of early metastatic cells, combined with an intervention shortly after detection of early metastasis (i.e., primary tumor excision) can enhance survival. This biomaterial approach is based on the host response to an implanted scaffold, thereby avoiding the presence of potentially deleterious cellular or biological components. PCL material is currently FDA approved for applications such as drug delivery, suture material, and wound dressings, which may facilitate translation to the clinic for the capture of metastatic cells [144]. Also, this material is biodegradable and would not need to be retrieved unless cancer cells are detected; and the degradation rate is relatively slow allowing the implant to be monitored for up to two years within a patient [145, 146]. Clinical studies would be necessary to appropriately integrate metastatic cell-capturing scaffolds into existing breast cancer management plans. Taken together, the results of this work showing prolonged survival with scaffold implantation, hold promise for reducing breast cancer morbidity and mortality.

3.7 Materials and Methods

3.7.1 Fabrication, characterization, and implantation of micro-porous scaffolds

Scaffold Fabrication and Characterization

For preparation of microporous PCL scaffolds, PCL microspheres were first prepared by emulsifying a 6% (w/w) solution of PCL (Lactel Absorbable Polymers, Birmingham, AL; Inherent viscosity = 0.65-0.85 dL/g) in dichloromethane in a 10% poly(vinyl alcohol) solution followed by homogenization at 10,000 rpm for 1 min. The solution was then stirred for 3 h. Microspheres were collected by centrifugation and washed at least 5 times in deionized water, followed by lyophilization for 48 h. To prepare micro-porous PCL scaffolds, PCL microspheres and salt particles (size range 250 425 m) were mixed in a 1:30 (w/w) ratio and pressed at 1500 psi in a steel die for 45 s. Polymer-salt discs were heated at 60 C for 5 min on each side, followed by foaming in high pressure CO2 at 800 psi for 24 h. Salt particles were removed by immersing discs in water. For experimental studies, scaffolds were sterilized using 70% ethanol, rinsed with sterile water, and dried on a sterile gauze pad. Microporous PLG scaffolds were prepared as described previously [147]. Scaffolds were characterized using mechanical testing, scanning electron microscopy, and calculation of porosity.

Scaffold Implantation

Microporous scaffolds were implanted in the subcutaneous space of either female BALB/c or NOD/SCID-IL2R-/- (NSG) mice (8-10 week old). All animal studies were performed in accordance with institutional guidelines and protocols approved by Northwestern University and the University of Michigan Institutional Animal Care and Use Committee. NSG mice were bred in house or purchased from the Jackson laboratory. BALB/c mice were purchased from the Jackson laboratory. For the implantation procedure, mice were anesthetized with an intraperitoneal injection of

Ketamine (10 mg/kg) and Xylazine (5 mg/kg). The upper back was shaved and prepped using a betadine swab followed by an ethanol swab (3X). An incision was made in the upper back and a subcutaneous pocket was created on each side, into which the scaffolds were inserted (2 scaffolds per mouse). The skin was closed using wound clips (Reflex 7mm, Roboz Surgical Instrument Co.) and surgical glue (3M Vetbond Tissue Adhesive).

3.7.2 Tumor inoculation

Orthotopic tumor inoculation was performed one month after scaffold implantation. MDA-MB-231BR-tdTomato-luc2 cells were obtained from the Northwestern University Developmental Therapeutics Core and authenticated by short tandem repeat DNA analysis and comparison to the ATCC STR profile database in 2013 (DDC Medical). 4T1-luc2-tdTomato cells were obtained from Perkin Elmer in 2014 and were used directly without additional authentication. 2 106 4T1-luc2-tdTomato (Perkin Elmer) or MDA-MB-231BR-tdTomato-luc2 cells in 50 L sterile phosphate buffer saline (PBS) (Life Technologies) were injected into the fourth right mammary fat pad of 12-14 week old female BALB/c or NSG mice.

3.7.3 Flow cytometry

Mice were euthanized at indicated times and retrieved scaffolds and organs were processed according to previously established procedures [31]. Flow cytometry staining and analysis were performed according to established procedures [31].

3.7.4 Scaffold sectioning and fluorescence imaging

Scaffolds retrieved from mice were rinsed in PBS and then immediately flash frozen in pre-chilled isopentane. Frozen scaffolds were then embedded in optimal cutting temperature (OCT; Cardinal Health) compound with 30% sucrose and sectioned using

a cryostat (Microm HM 525; Microm International) at 14 m. Scaffold sections were stored at -20 C until imaging. Cryosections were air-dried at room temperature for 30 min, fixed with 10% neutral buffered formalin, washed with tap water for 5 min, DI water for 10 min (2X) and cover slipped with ProLong Gold antifade aqueous mounting medium containing DAPI (Molecular Probes, Grand Island, NY). DAPI fluorescence was visualized using an excitation wavelength of 358 nm, and tdTomato fluorescence in cancer cells was visualized using an excitation wavelength of 532 nm. Images were viewed using an Olympus BX43 microscope and an Olympus DP72 digital camera with CellSens Entry software (Olympus) used for image capture and co-localization.

3.7.5 ISOCT imaging and analysis

ISOCT imaging and analysis was performed as described elsewhere [31, 112, 130, 148].

3.7.6 Post-surgical model of breast cancer metastasis and Gr-1 depletion

The influence of scaffold implant on survival was investigated using a post-surgical model of breast cancer metastasis. In this model, the 4T1 primary tumor was resected 6 or 10 days post tumor inoculation. Briefly, the primary tumor area was prepped using a betadine swab followed by an ethanol swab (3X). An incision was made along the right side of the lower half of the dorsal skin exposing the primary tumor. The tumor was picked up using needle nose-forceps and cut around the base using curved tip scissors. The skin was closed using MONOCRYL (poliglecaprone 25) suture (Ethicon, Inc.) and surgical glue (3M Vetbond Tissue Adhesive). Animal health was monitored daily after the procedure for activity and responsiveness including posture, mobility, body weight, grooming behavior, and respiratory conditions. Animals were euthanized if found in a moribund condition as an experimental endpoint. Mice

Scaffold Type	Elastic Modulus (KPa)	Porosity (%)	Pore Volume (mm3)
PLG	1004 +/- 112	96.7 +/- 0.001	38.1 +/- 0.04
PCL	664 +/- 97	94.7 +/- 0.005	37.2 +/- 0.18

Table 3.1: **Characterization of micro-porous PLG and PCL scaffolds (N = 10)**

that evidenced primary tumor re-growth were excluded from the analysis to avoid confounding effects arising from the primary tumor. For Gr-1 depletion studies, resection was performed at day 10 as described above and mice received 300 g anti-Gr-1 (clone RB6-8C5, Bio X Cell) via intraperitoneal injection at day 13 and 17 post tumor inoculation.

3.7.7 Data analysis

Data are presented as mean +/- standard error (s.e.m.). Animal studies were performed with at least two independent replicates of 48 female 812-week-old mice per group with random assignment. Multiple comparisons were performed using one-way ANOVA. Comparisons post ANOVA was performed using the Tukey-HSD test. For data that did not follow a normal distribution, comparison was performed using the non-parametric Wilcoxon rank-sum test. For comparing the relative number of mice containing detectable tumor cells in organs with scaffolds, a Fishers exact test was used to determine the p-value. Statistical analysis was performed using JMP Software (JMP Pro 11). For survival analysis, Kaplan-Meier curve was generated and statistical analysis was performed using a Log-rank test using Sigma Plot (Version 13).

3.8 Supplementary Figures

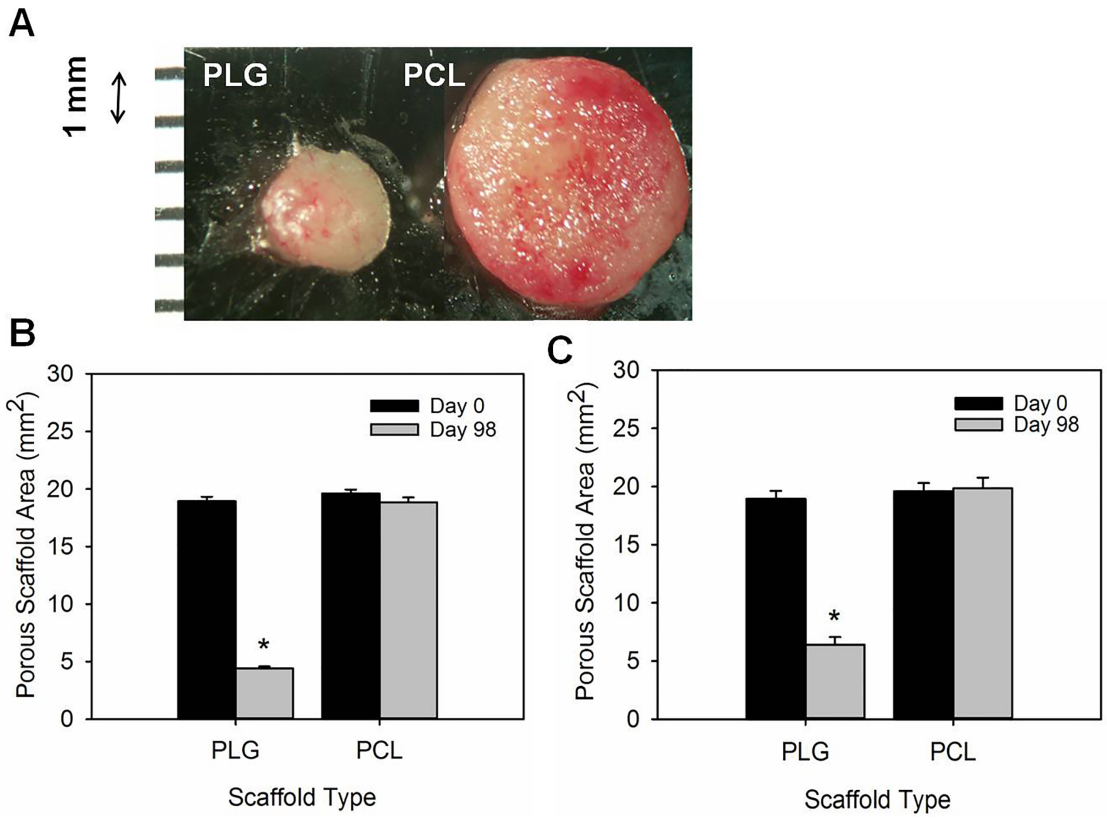

Figure 3.8: **Micro-porous PCL scaffolds persist and maintain a space for extended times *in vivo*.** (A) Representative photomicrographs of micro-porous PLG and PCL scaffolds retrieved from tumor free BALB/c mice at day 98 post scaffold implantation. Average scaffold area at day 0 versus day 98 for PLG and PCL scaffolds when tested in a BALB/c (B) and NSG (C) mouse model. N = 4; *p <0.0001 compared to day 0 for PLG scaffolds in BALB/c and NSG mouse; p = 0.22 compared to day 0 for PCL scaffolds in BALB/c mouse and p = 0.7 compared to day 0 for PCL scaffolds in NSG mouse as determined by t-test. Scaffold area was calculated using dimensions obtained from images of scaffolds taken at day 0 and day 98 post implantation using Image J software. Error bars denote s.e.m.

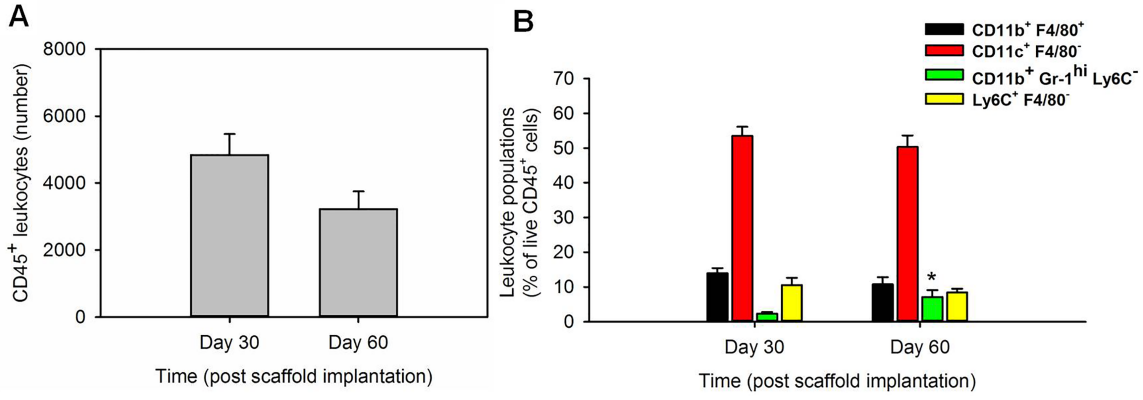

Figure 3.9: **Host response following implantation of micro-porous PCL scaffolds in the dorsal subcutaneous space of an NSG mouse *in vivo*.** (A) CD45+ leukocyte numbers and (B) Dynamics of CD11b+F4/80+, CD11c+F4/80-, CD11b+Gr-1hiLy6C-, and Ly6C+F4/80- populations expressed as a percentage of live CD45+ leukocytes at day 30 and day 60 post PCL scaffold implantation (N = 8 for each time point examined, *p <0.05 compared to day 30 as determined by t-test). The relative distribution of immune cell populations was nearly identical between day 30 and day 60 post scaffold implantation. Error bars denote s.e.m.

Reason for sacrifice	**Mock**	**Scaffold**
Hunched posture, bad grooming, and lethargy	2/7	1/7
Labored breathing	3/7	-
Hind limb paralysis	1/7	1/7
Forelimb paralysis	-	1/7
Cause unknown - mouse found dead	1/7	1/7
Experiment terminated – mice were healthy, no signs of disease observed	-	3/7

Table 3.2: **Sacrifice and endpoints observed in the post-surgical model in mock and scaffold groups**

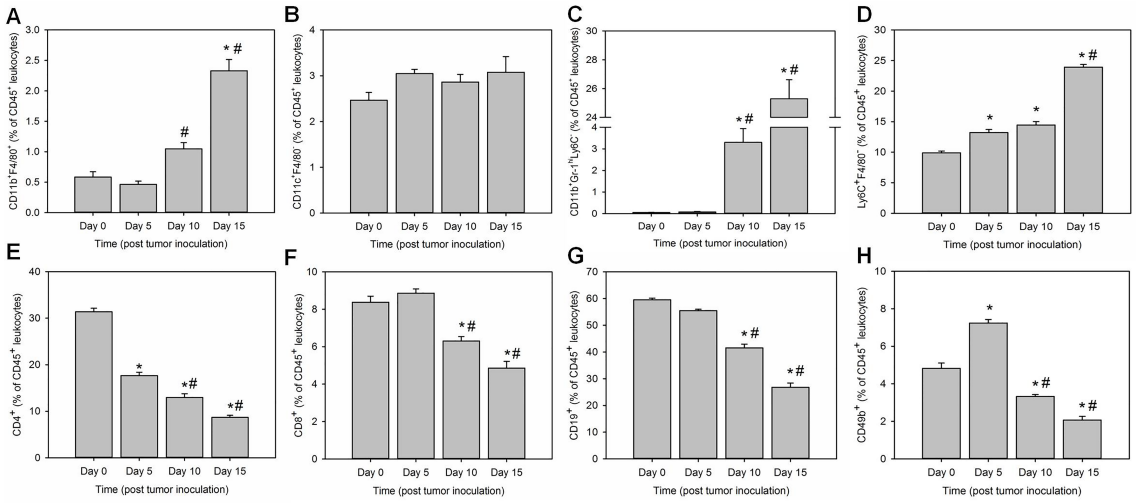

Figure 3.10: **Dynamics of immune cell populations in the spleen of BALB/c mice with a PCL scaffold implant at day 0, 5, 10, and 15 post tumor inoculation.** Percentage of (A) CD11b+F4/80+ (B) CD11c+F4/80- (C) CD11b+Gr-1hiLy6C- (D) Ly6C+F4/80- innate immune cell populations and percentage of (E) CD4+ (F) CD8+ (G) CD19+ and (H) CD49b+ adaptive immune cell populations in the total population of live CD45+ leukocytes. (N >5 for each time point examined, *p <0.05 compared to day 0 and #p <0.05 compared to day 5 as determined by Tukey-HSD test post ANOVA). Error bars denote s.e.m.

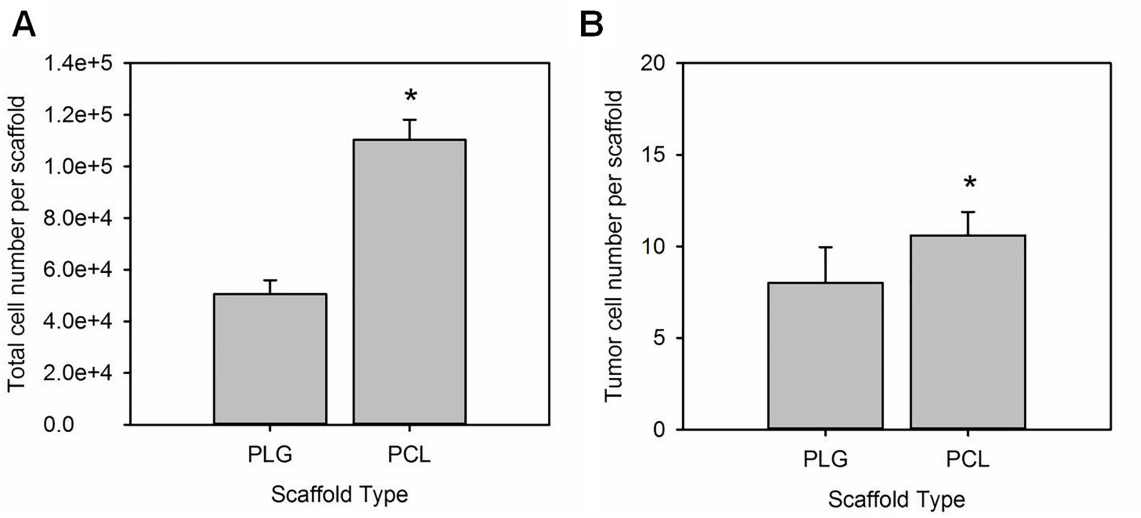

Figure 3.11: **Micro-porous PCL scaffolds enable recruitment of human MDA-MD-231BR cells in a chronic model of scaffold implantation.** (A) Total cell infiltration and (B) Tumor cell infiltration in PLG and PCL micro-porous scaffolds. Scaffolds were retrieved at day 15 post tumor inoculation, which was performed 1 month post scaffold implantation (N = 10 for each group, *p <0.05 as determined by t-test for analysis of total cell numbers and Wilcoxon rank-sum test for tumor cell numbers). Error bars denote s.e.m.

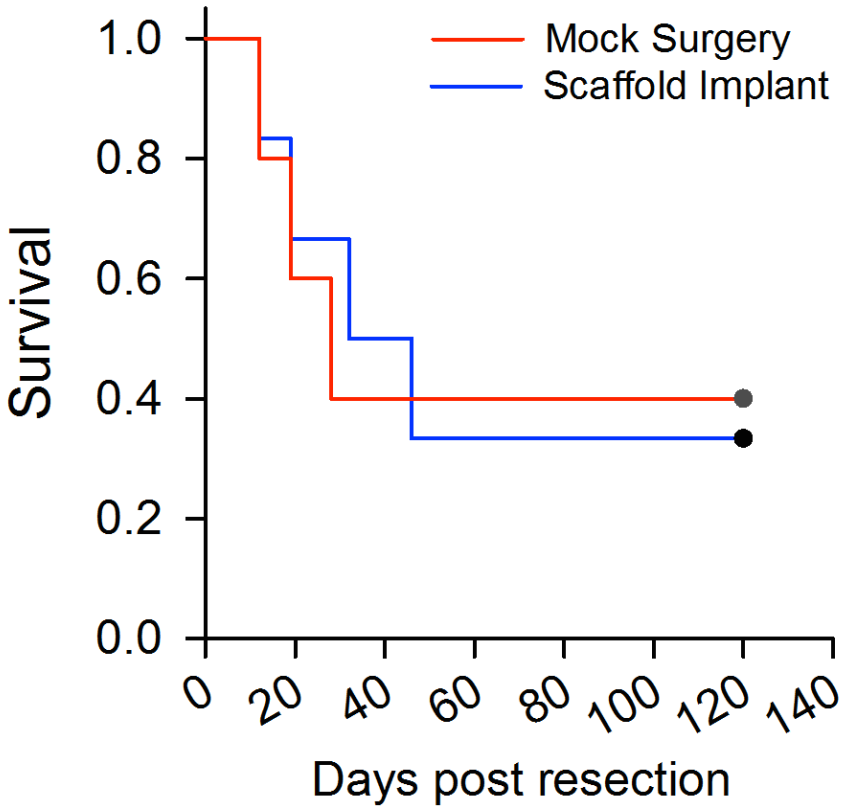

Figure 3.12: **Micro-porous PCL scaffolds do not significantly improve survival in a post-surgical model of breast cancer metastasis with day 6 post tumor inoculation resection.** (N >5 for each group).

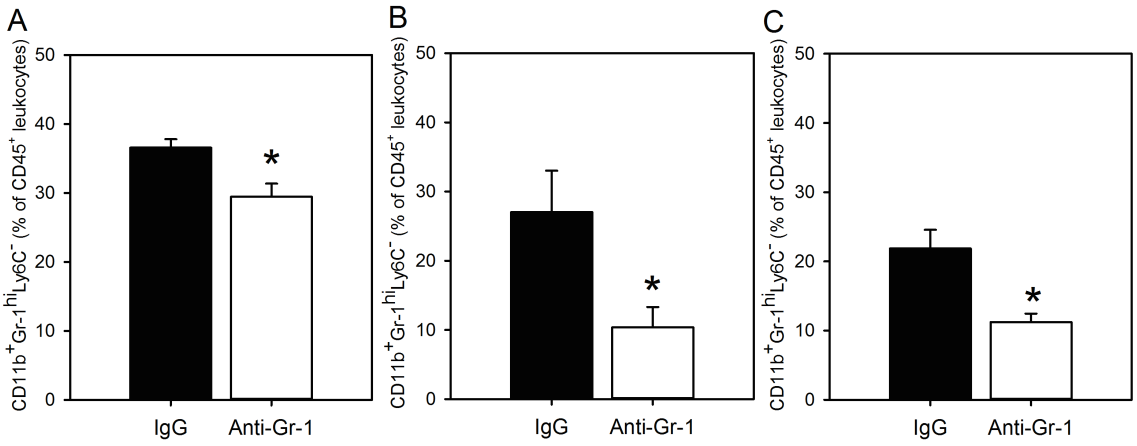

Figure 3.13: **Anti-Gr-1 depletion significantly reduces the presence of CD11b+Gr-1hiLy6C- MDSCs in the spleen** (A) primary tumor (B) and scaffold (C). The percentage of CD11b+Gr-1hiLy6C- cells in the CD45+ leukocyte population was examined via flow cytometry at day 15 post tumor inoculation after three 300 g antibody injections (day 5, 9, 13) (N=5 for spleen and primary tumor, N = 10 for scaffolds, performed in one experiment *$p<0.05$ as determined using t-test.) Error bars denote s.e.m.

CHAPTER IV

Scaffold Immunomodulation as a Platform to Probe the Pre-Metastatic Niche

4.1 Authors

Grace G Bushnell, Shreyas S Rao, Rachel M Hartfield, Yining Zhang, Robert S Oakes, Jacqueline S Jeruss, Lonnie D Shea

4.2 Abstract

Metastasis is responsible for the vast majority of cancer associated deaths. The formation of metastasis is directly preceded by the formation of a hospitable microenvironment supportive of metastasis known as the pre-metastatic niche. The study of the pre-metastatic niche has been significantly hampered by the stochasticity of its formation in natural organs. Implantable biomaterials have emerged as a model for the pre-metastatic niche and are capable of recruiting tumor cells *in vivo*. Biomaterial scaffolds can serve as a site for modulation of the microenvironment in order to probe the pre-metastatic niche and observe the impact on metastasis. Lentivirus can be delivered from PCL scaffolds *in vivo* and achieve long-term transgene expression (>30 days). Immune cells were the primary targets of lentiviral transgene expression *in vivo*. Macrophages, neutrophils and B cells were preferentially trans-

duced by lentivirus, while monocytes, CD4/CD8 T cells, and Natural Killer cells were less likely to express the transgene. IL10 delivery resulted in a significant decrease in tumor cell recruitment to scaffolds *in vivo*. Delivery of immunomodulatory CXCL12 lentivirus enhanced CD45+ immune cell recruitment to scaffolds while delivery of IL10 reduced immune cell recruitment. Multiple linear regression was employed across all immunomodulated microenvironments to identify key populations of immune cells responsible for tumor cell recruitment and found overall CD45+ immune and CD8+ T cell percentages to be significantly associated with reduced tumor cell recruitment, while CD11b+Gr1+ neutrophils and CD4+ T cell percentages were significantly associated with enhanced tumor cell recruitment. Conditioned media from immunomodulated scaffolds identified effects on tumor cell phenotype *in vitro* such as reduced proliferation from CXCL12 delivered microenvironments, enhanced proliferation from IL10 microenvironments, enhanced scratch closure in CCL2 microenvironments, and reduced closure in IL10 microenvironments. Altogether these findings support the idea that biomaterial scaffolds that recruit metastatic tumor cells *in vivo* are a robust platform to probe events in pre-metastatic niche formation, tumor cell recruitment and metastasis.

4.3 Introduction

Metastasis is the single greatest contributor to cancer associated deaths [149]. One of the many challenges in treating metastasis is a lack of biological understanding regarding the formation of metastasis permissive microenvironments known as the pre-metastatic niche. The seed and soil hypothesis postulated by Stephen Paget in 1889 hypothesized that something about the soil of organs that are targets for metastasis is primed to support the seed of the metastatic tumor cell [6]. This phenomenon was confirmed in a landmark study by Rosandra Kaplan and colleagues in 2005 and termed the pre-metastatic niche [8]. Since 2005, many more review articles

have been published on the pre-metastatic niche than primary literature which highlights the intense interest in this area but difficulty in its study. The steps directly preceding metastasis formation are particularly difficult to probe for a number of reasons. First, the pre-metastatic niche occurs in stochastic locations within a target organ and the altered locations make up a very small percentage of the organ itself [7, 51, 150]. Second, genetic alterations to probe the pre-metastatic niche often have to be done on an organism wide scale through genetically engineered mouse models and often have off-target effects on primary tumor development. Biomaterials that recruit metastatic cancer cells *in vivo* are an emerging technology to address both of these problems [30, 31, 34, 42, 151, 152]. First, they provide a defined site *in vivo* to which tumor cells are recruited, allowing for a concentrating effect of the factors and cell types associated with the pre-metastatic niche and metastasis. Second, they are readily modifiable on a local scale, such that the properties of the site may be altered without any off-target effects on the host at large. As a result, biomaterial scaffolds that model the pre-metastatic niche *in vivo* represent a transformative approach to understand the development of the pre-metastatic niche, the recruitment of tumor cells, and the contribution of individual factors to each of these processes [151].

Many factors associated with the pre-metastatic niche and metastasis have multifaceted effects on immune and tumor cells that make discerning their role in the local microenvironment of the pre-metastatic niche difficult. For example, CXCL12 or SDF-1 is known to be a chemoattractant for breast cancer cells [153] however, it also has broad effects on the immune system [154], fibroblasts [155] , and endothelial cells [156]. While many studies have investigated the role of such immunomodulatory factors on metastasis through knock-out genetically engineered mouse models [157], these factors have not been investigated on a purely local scale. Similarly, IL10 [158, 159] and CCL2 [15, 128] have both been implicated in metastasis, but their role on a local scale has not been elucidated.

In this study, we hypothesized that recruitment of tumor cells to the scaffold was driven by immune cells, and investigated modulation of the immune microenvironment as a means to influence tumor cell recruitment and to dissect the contribution of specific immune cell populations.

4.4 Results

4.4.1 Lentiviral delivery from scaffolds achieves sustained transgene expression in immune cells in the *in vivo* biomaterial microenvironment

The ability of poly(ε-caprolactone) (PCL) scaffolds to deliver lentivirus from the epididymal fat pad was assessed via delivery of firefly luciferase (FLUC) lentivirus and measured by bioluminescence imaging over 42 days following implantation (**Figure 4.1A**). Expression peaked at day 7 following implantation (6.36E6 +/- 1.98E6 photons/sec for FLUC loaded scaffolds and 1.81E4 +/-3.68E3 photons/sec for blank scaffolds) and was significantly higher than blank scaffolds at all time points investigated ($p<0.05$ via two-tailed Students T test). Next, we investigated what proportion of cells recruited to the scaffold was transduced by lentivirus. To this end, we delivered GFP lentivirus from PCL scaffolds and assessed the percentage of GFP+ cells by flow cytometry at day 7 following implantation. The percentage of GFP+ cells in scaffolds with GFP encoding lentivirus delivered was significantly higher than in blank scaffolds (2.54+/-0.81% for GFP and 1.7+/-0.08% for blank scaffolds, $p<0.05$ via two-sided t-test, **Figure 4.1B**). In this same experiment we also evaluated the relative distribution of immune cells within transduced and non-transduced cells by comparing the percentage of all cells for each immune population to the percentage of GFP+ cells for a given population for both innate (**Figure 4.1C**) and adaptive immune cell populations (**Figure 4.1D**). GFP+ cells that were transduced with lentivirus were more

likely to be CD45+ (35.52+/-15.48% CD45+ for all cells and 58.6+/-6.75% CD45+ for GFP+ cells), CD11b+F4/80+ (macrophages, 5.26+/-1.79% CD11b+F4/80+ of CD45+ for all cells and 16.46+/-3.84% CD11b+F4/80+ of CD45+ for GFP+ cells), CD11b+Gr1+ (neutrophils, 4.51+/-0.57% CD11b+Gr1+ of CD45+ for all cells and 16.5+/-2.64% CD11b+Gr1+ of CD45+ for GFP+ cells), CD19+ (B cells, 2.44+/-0.39% CD19+ of CD45+ for all cells and 10.8+/-1.26% CD19+ of CD45+ for GFP+ cells) and less likely to be Ly6C+F4/80- (monocytes, 36+/-6.73% Ly6C+F4/80- for all cells and 27.8+/-3.38% Ly6C+F4/80- for GFP+ cells), CD4+ (helper T cells, 1.34+/-0.23% CD4+ of CD45+ for all cells and 0.17+/-0.11 %CD4+ of CD45+ for GFP+ cells), CD8+ (cytotoxic T cells, 7.02+/-1.54 % CD8+ of CD45+ for all cells and 2.17+/-0.47% CD8+ of CD45+ for GFP+ cells), and CD49b+ (Natural Killer cells, 0.96+/-0.24% CD49b+ of CD45+ for all cells and 0.046+/-0.04 for GFP+ cells).

4.4.2 Lentiviral delivery of immunomodulatory factors successfully modulates the scaffold immune microenvironment *in vivo* and alters tumor cell recruitment

Following sustained transgene expression and identification of cells types transduced, we next investigated the effect of lentiviral delivery of immunomodulatory cytokines including CCL2 (MCP-1), CXCL12 (SDF-1), and IL-10 from PCL scaffolds in tumor-bearing mice. We first investigated the alterations in immune cell recruitment to the scaffold in each condition (**Figure 4.2A**) and found CXCL12 delivery significantly enhanced the percentage of CD45+ cells of total cells compared to FLUC control (35.9+/-5.9% CD45+ cells of total for CXCL12 and 31.4+/-3.2% of CD45+ cells of total for FLUC), while the delivery of IL10 significantly reduced the percentage of CD45+ cells of total compared to FLUC control (27.4+/-4.1% of CD45+ cells of total for IL10 and 31.4+/-3.2% of CD45+ cells of total for FLUC). We next investigated the effect of immunomodulatory cytokine delivery on tumor

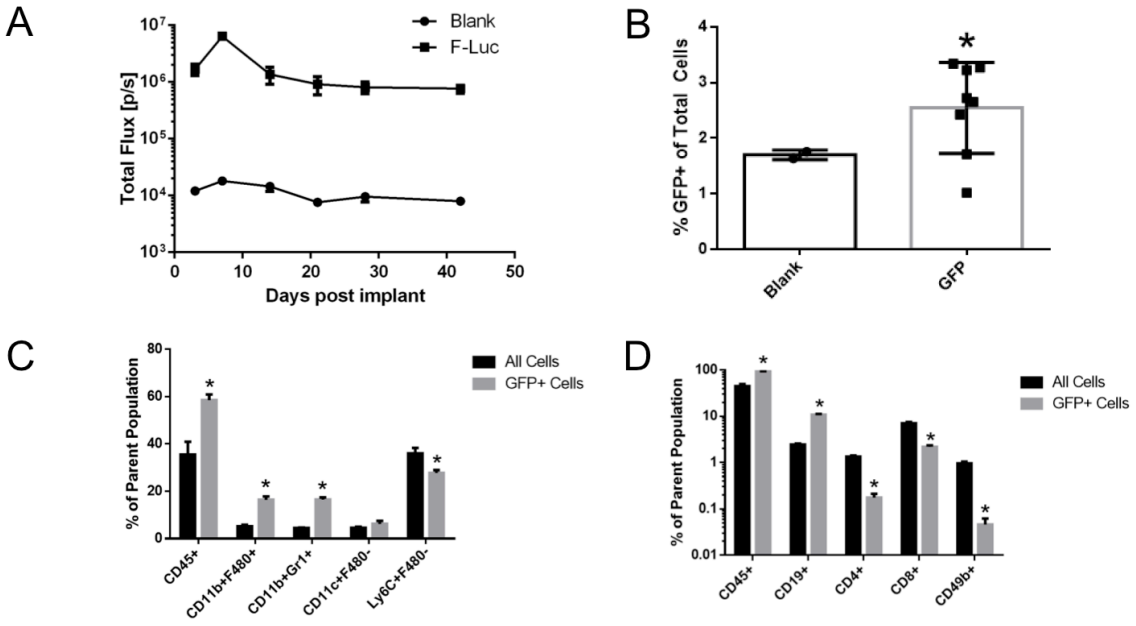

Figure 4.1: **Lentiviral delivery from scaffolds implanted in epididymal fat pad achieves sustained transgene expression in immune cells.** (A) Scaffolds implanted into epididymal fat pad and loaded with FLuc lentivirus demonstrate sustained transgene expression over 42 days, with expression peaking at day 7 and significantly higher ($p<0.05$) than Blank scaffolds at all time points investigated. (B) Scaffolds implanted into epididymal fat pad and loaded with eGFP lentivirus demonstrate a significantly higher percentage of GFP+ cells (*$p<0.05$) at day 7 following implantation. Flow cytometry evaluation of cells transduced by lentivirus for surface markers demonstrate populations more or less likely to be transduced by lentivirus including (C) innate immune cell populations CD45+, CD11b+F480+, CD11b+Gr1+, Ly6C+F480- cells and (D) adaptive immune cell populations including CD45+, CD19+, CD4+, CD8+, CD49b+ cells. (*$p<0.05$ via two-sided t-test)

cell recruitment to implanted scaffolds (**Figure 4.2B**) and found IL10 significantly reduced the percentage of tdTomato+ 4T1 metastatic tumor cells spontaneously arriving at the scaffold relative to all other conditions (0.06+/-.03% tdTomato+ of total cells for IL10, 0.13+/-04% tdTomato+ for FLUC, 0.09+/-0.02% tdTomato+ for CCL2, and 0.11+/-04% tdTomato+ for CXCL12). Following evaluation of a change in both overall immune cell recruitment and tumor cell recruitment, we next sought to understand if the relative distribution of immune cells changes with delivery of immunomodulatory factors (**Figure 4.2C**). To this end we evaluated the presence of innate immune cell populations: CD11b+F480+ macrophages, CD11b+Gr1+ neutrophils, CD11b+Gr1+Ly6C- myeloid derived suppressor cells, CD11c+F480- dendritic cells, Ly6C+F480- monocytes, and adaptive immune cell populations: CD4+ T cells, CD8+ T cells, CD19+ B cells, and CD49b+ NK cells by flow cytometry. We found a few small, but statistically significant differences between immunomodulatory conditions including a significant increase in CD11b+F480+ macrophages in CXCL12 (5.22+/-1.6%) relative to CCL2 (2.7+/-0.86%) and IL10 (3.26+/-0.65%), a significant decrease in CD11b+Gr1+Ly6C- myeloid derived suppressor cells in CCL2 (6.86+/-2.9%) relative to CXCL12 (15.7+/-9.4%) and IL10 (11.9+/-4.8%) conditions, a significant increase in CD11c+F480- dendritic cells in FLUC (22.0+/-2.6%) relative to CCL2 (17.1+/-2.2%) and IL10 (14.9+/-2.7%) and in CXCL12 (20.6+/-5.5%) relative to IL10 (14.9+/-2.7%), a significant increase in Ly6C+F480- monocytes in CCL2 (16.0+/-3.6%) relative to IL10 (12.1+/-3.4%), a significant increase in CD8+ T cells in CCL2 (9.8+/-2.3%) and IL10 (10.3+/-3.4%) relative to FLUC (6.97+/-1.7%) and CXCL12 (6.91+/-2.4%), and a significant increase in CD19+ B cells in CCL2 (2.70+/-1.3%) relative to FLUC (1.60+/-0.3%) , CXCL12 (1.43+/-0.7%), and IL10 (1.50+/-0.4%).

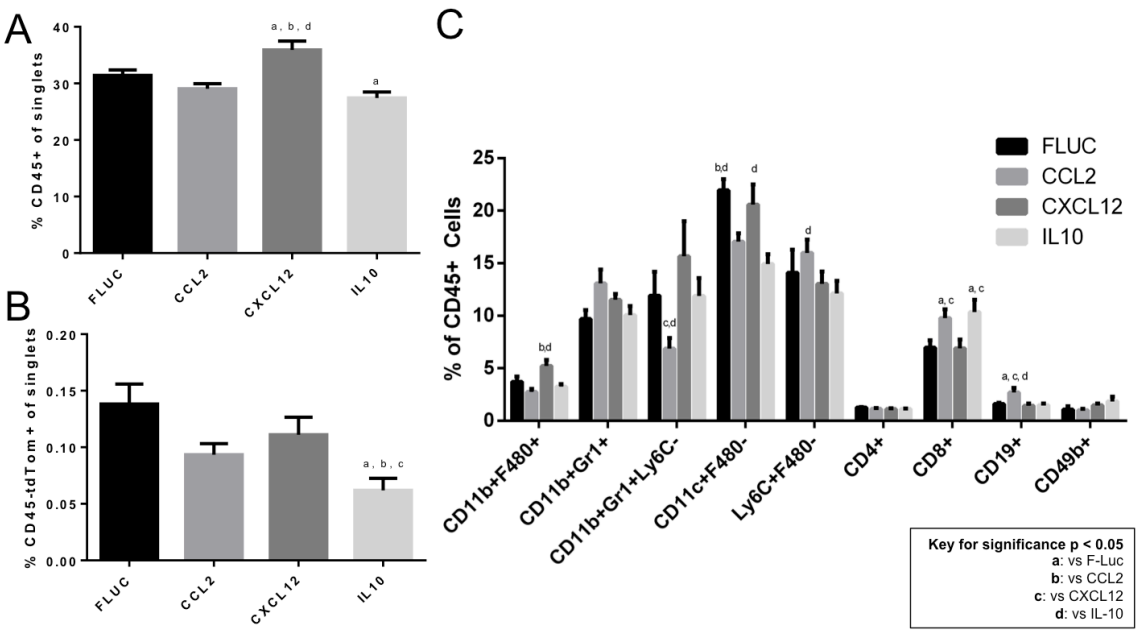

Figure 4.2: **Lentiviral delivery of immunomodulatory factors from scaffolds results in modulation of the scaffold immune microenvironment.** Delivery of immunomodulatory lentivirus alters (A) the percentage of CD45+ cells of singlets (B) the percentage of CD45-tdTomato+ 4T1 tumor cells, and (C) innate immune cell populations CD11b+F480+ macrophages, CD11b+Gr1+ neutrophils, CD11b+Gr1+Ly6C- myeloid derived suppressor cells, CD11c+F480- dendritic cells, Ly6C+F480- monocytes and adaptive CD4+ T cells, CD8+ T cells, CD19+ B cells, and CD49b+ NK cells as evaluated by flow cytometry. Letter indicates significance $p<0.05$ where a is significantly altered from FLuc, b from CCL2, c from CXCL12, and d from IL10.

4.4.3 Modulation of the scaffold immune microenvironment provides insights into immune cell populations critical to tumor cell recruitment *in vivo*

Following the finding that delivery of immunomodulatory lentivirus from biomaterial scaffolds alters immune cell recruitment subsequent tumor cell recruitment in vivo we next sought to use the immune marker and tumor cell marker flow cytometry data to investigate the role of individual immune cell populations in tumor cell recruitment. First, unsupervised hierarchical clustering was performed on the flow cytometry data to identify how different the immune microenvironments are when the all of the immune populations are taken into account (**Figure 4.3A**). We found that in general, samples of the same condition clustered together somewhat but there was significant variability in the data that could not be explained simply by the delivery of one cytokine. For example, two major clusters were identified with the first encompassing all FLUC and IL10 samples, all but one CXCL12 sample, and 3/6 IL10 samples. The second cluster contained one CXCL12 sample and one CCL2 sample and upon visual inspection it appears that the strongest indicators of this first level of clustering were due to higher than average content of CD19+ B cells and CD11b+Gr1+ neutrophils. Upon further subdividing the first cluster containing all FLUC, IL10, and most CXCL12 samples this cluster can be further subdivided into 3 clusters. The first of these three clusters contains 2/6 FLUC samples and 3/6 CXCL12 samples which appear to be clustering primarily on higher than average CD45+ and CD11b+Gr1+Ly6C- myeloid derived suppressor cell content. The second of these clusters contains 2/6 CXCL12 samples, 4/6 FLUC samples, 2/6 CCL2 samples, and 1/6 IL10 sample and appear to be similar primarily due to relatively high CD45-tdTomato+ tumor cell content and CD45+ cell content. The final cluster contains 5/6 IL10 samples, 2/6 CCL2, and 2/6 CXCL12 and the primary characteristic of this cluster appears to be relatively high CD8+ T cell content accompanied

by relatively high Ly6C+F480- monocyte content.

Since correlations between cell types were not obvious by unsupervised hierarchical clustering, we next performed correlation analysis to look at the correlation between each cell population in the scaffold microenvironments (**Figure 4.3B, Supplemental Figure 4.7**). Interestingly, we found CD11b+Gr1+ neutrophils, CD11c+F480- dendritic cells, Ly6C+F480- monocytes, CD4+ T cells, and CD19+ B cells to positively associated with tumor cell recruitment ($r>0$) while overall CD45+, CD11b+F480+ macrophages, CD11b+Gr1+Ly6C- putative myeloid derived suppressor cells, CD8+ T cells, and CD49b+ Natural Killer cells were all negatively correlated with tumor cell recruitment ($r<0$). Additionally, some immune cell populations were strongly positively correlated with each other including CD11b+Gr1+ neutrophils and CD19+ B cells ($r=0.75$), CD11b+F480+ macrophages and CD11b+Gr1+Ly6C- myeloid derived suppressor cells ($r=0.672$), and CD11b+Gr1+ neutrophils and Ly6C+F480- monocytes ($r=0.67$); while others had strong negative correlations including CD11b+Gr1+Ly6C- myeloid derived suppressor cells and Ly6C+F480- monocytes ($r=-0.72$). To investigate the key players in tumor cell recruitment further, we performed stepwise multiple linear regression analysis to create a model that explains the variability in the recruitment of tumor cells to the immunomodulated scaffold microenvironments (**Table 4.1**) with the percentage of tumor cells of total cells as the output and the percentage of each population (CD45+ total immune cells, CD11b+F480+ macrophages, CD11b+Gr1+ neutrophils, CD11b+Gr1+Ly6C- myeloid derived suppressor cells, CD11c+F480- dendritic cells, Ly6C+F480- monocytes, CD4+ T cells, CD8+ T cells, CD19+ B cells, and CD49b+ NK cells) as continuous predictors. This analysis method created a model with the equation Tumor-Cells = 0.0794 - 0.004651 CD45 + 0.00438 Neutrophil + 0.0756 CD4 - 0.00298 CD8 and a model $R2 = 69.69\%$, adjusted $R2 = 64.42\%$, and p-value <0.001 for the model. The positive coefficients for CD11b+Gr1+ neutrophils and CD4+ T cells indicate that these positively contribute

Predictor Term	P-value	Coefficient	Coefficient S.E.
Constant	0.118	0.0794	0.0489
%CD45+Live of singlets	<0.001	-0.004651	0.000973
%CD11b+Gr1+ of CD45+Live Cells	0.001	0.00438	0.00120
%CD4+ of CD45+Live Cells	0.001	0.0756	0.0206
%CD8+ of CD45+Live Cells	0.039	-0.00298	0.00137

Table 4.1: **Multiple Linear Regression for immunomodulated scaffolds identifies key immune cell populations role in tumor cell recruitment.** Regression Equation: Tumor-Cells = 0.0794 - 0.004651 CD45 + 0.00438 + 0.0756 CD4 - 0.00298 CD8. Model R2 = 69.69%, Adjusted R2 = 64.42%, p<0.001 for model.

to tumor cell recruitment, while total CD45+ cells and CD8+ T cells negatively contribute to tumor cell recruitment; similar to what we saw by simple linear correlations (**Figure 4.3B**).

4.4.4 Modulation of the scaffold immune microenvironment exhibits differential effects on tumor cell phenotype *in vitro*

Finally, we evaluated the effect of immunomodulated microenvironments on tumor cells *in vitro*. We did this by implanting FLUC control scaffolds in the right epididymal fat pad and a virus of interest (CCL2, CXCL12, IL10) in the left epididymal fat pad of the same mouse. Using this method, the FLUC scaffold in each mouse serves as an internal control. Seven days following implantation, we explanted scaffolds, placed them in sterile RPMI-1640, minced the scaffold, and allowed the cells to condition the media for 48 hours. This conditioned media was then used for various assays with tumor cells including proliferation (**Figure 4.4A**), scratch assay (**Figure 4.4B**), and mammosphere formation assay (**Figure 4.4C**). In proliferation assays CXCL12 suppressed tumor cell proliferation relative to FLUC controls (84,440+/-41,000 cells/well for FLUC and 54,400+/-15,000 cells/well for CXCL12) from the same set of mice while IL10 enhanced proliferation relative to FLUC controls (17,700+/-9,000 cells/well for FLUC and 35,900+/-24,000 cells/well for IL10)

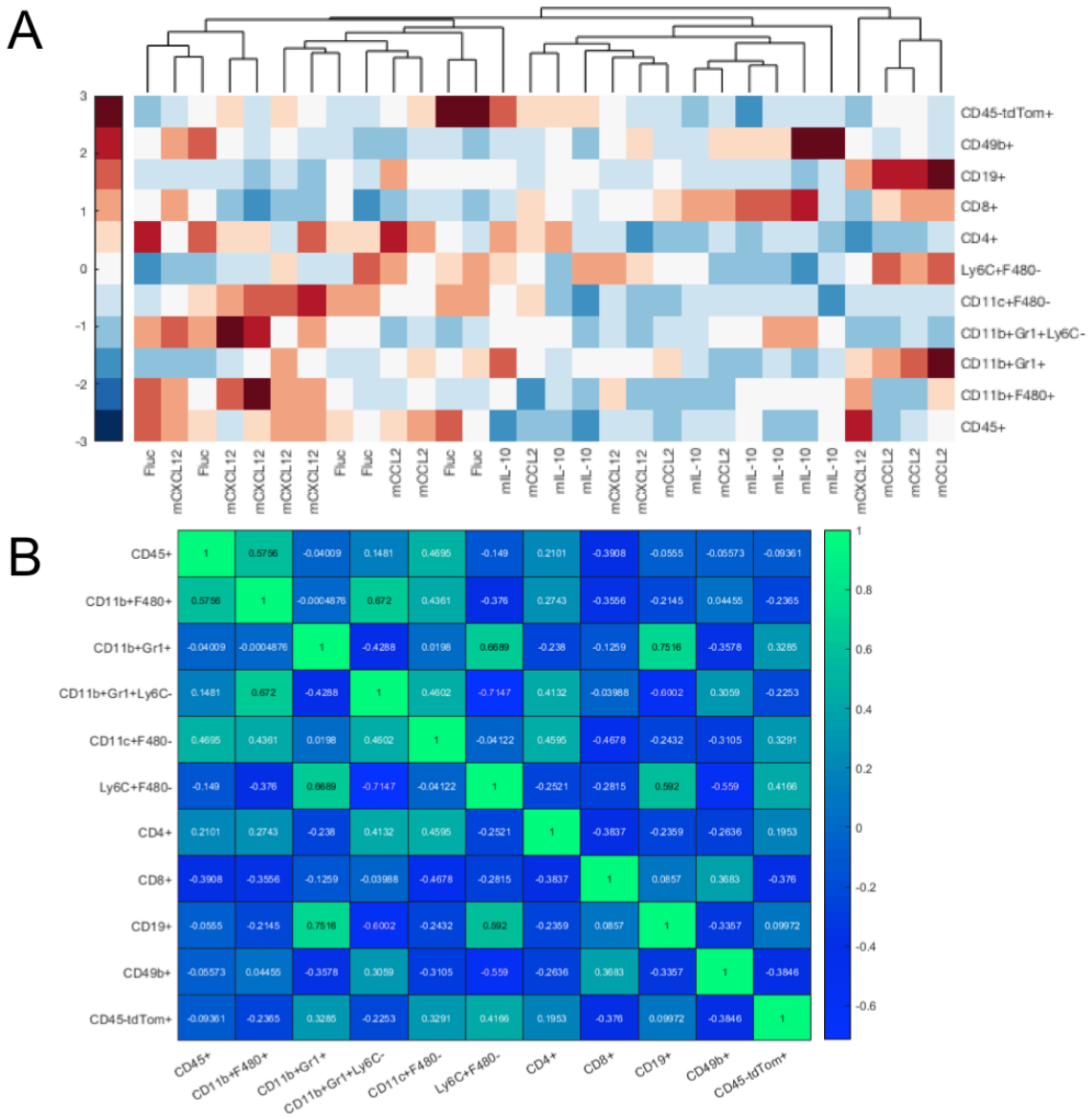

Figure 4.3: **Lentiviral delivery of immunomodulatory factors from scaffolds results in modulation of the scaffold immune microenvironment.** (A) Unsupervised hierarchical clustering of immune populations in scaffolds with Fluc, mCCL2, mCXCL12, or mIL-10 delivered. (B) Correlation analysis of immune cell populations and tumor cell recruitment showing heatmap of Pearson correlation coefficient values for each immune cell population and tumor cells identified as CD45-tdTom+

from the same mice (**Figure 4.4A**). In scratch assays CCL2 significantly enhanced the number of wells with partial closure relative to FLUC (11% partial in FLUC and 89% partial closure in CCL2), while IL10 significantly enhanced no closure (0% of scratches with no closure in FLUC and 42% of scratches in IL10 with no closure, **Figure 4.4B**). In mammosphere assays no significant differences in mammosphere formation ability were observed as a result of different immunomodulated conditioned medias, however a reduction in mammosphere formation ability was observed across all scaffold conditioned media samples relative to the RPMI-1640 unconditioned media (CTRL, **Figure 4.4C**).

4.5 Discussion

Metastasis is responsible for 90% of cancer related deaths [149]. Enhancing understanding of the key events for tumor cell recruitment and development of the pre-metastatic niche has the potential to significantly impact treatment of metastasis. The pre-metastatic niche has been particularly difficult to study given the stochastic, focal nature of development in pre-metastatic organs. In this study we validate the use of biomaterial scaffolds as a platform to engineer the pre-metastatic niche and observe the impact on immune cell recruitment and subsequent tumor cell recruitment. The standard platform for altering the properties of a pre-metastatic site and observing the impact on metastasis has been genetically engineered mouse models. However, these have a significant disadvantage as there are usually off-target effects other than the tissue of interest as well as the cost to develop these models is very high. Biomaterial scaffolds have been used to recruit tumor cells in models of breast [30, 31, 34, 42, 152], prostate [27], ovarian [29], melanoma [26] and leukemic [36] cancers. The recruitment of tumor cells to a site that is readily modifiable makes an ideal platform for probing the pre-metastatic and metastatic niche, however to this point only single factors have been identified for their ability to enhance tumor

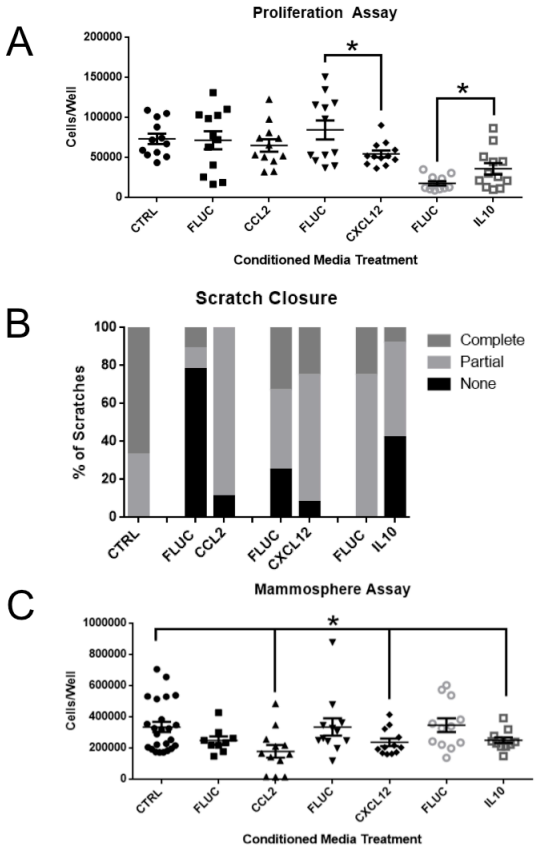

Student's t-Test P-Values

	CTRL	FLUC	CCL2	CXCL12	IL10
CTRL	1	0.12196	0.42120	0.02533	0.00077
FLUC		1	0.41640	0.01909	0.03685
CCL2			1	0.24552	0.01073
CXCL12				1	0.03700
IL10					1

Fisher's Exact Test P-Values

	CTRL	FLUC	CCL2	CXCL12	IL10
CTRL	1	0.00695	0.00126	0.32861	0.00011
FLUC		1	0.00337	0.55579	0.04231
CCL2			1	0.35489	0.15882
CXCL12				1	0.17568
IL10					1

Figure 4.4: **Scaffold immunomodulatory effect on tumor cell phenotype.** 4T1 tumor cells were grown *in vitro* and treated with conditioned media generated from scaffolds loaded with FLUC, CCL2, CXCL12, or IL10 in (A) proliferation assays where the number of cells per well was assessed by measuring tdTomato fluorescence via plate reader, (B) scratch assay where the number of scratches achieving complete, partial, or no closure was evaluated using light microscopy, and (C) mammosphere assay where tumor cells were plated in a mammosphere assay in ultra low attachment plates and allowed to grow as spheres in the presence of conditioned medias and proliferation of spheres assessed by measuring tdTomato fluorescence via plate reader.

cell recruitment[31, 34, 42] but no alterations have been found that reduce tumor cell recruitment relative to control, nor has the interplay between the immune microenvironment present in a scaffold and the subsequent recruitment of tumor cells been fully investigated.

To date, this study is the first to look at a range of inflammatory and anti-inflammatory factors to probe their effect on the immune microenvironment of the foreign body response, as well as their effect on tumor cell recruitment. While, we did see modulation of total immune cell content by flow cytometry, the changes of relative immune cell populations were smaller than expected. This may be a result of transducing only 2% of resident cells, even though detectable increases in the delivered factor were observed **Supplemental, Figure 4.6**. Even with relatively small changes in individual immune cell populations we found a decrease in tumor cell recruitment to IL10 loaded scaffolds. This finding is the first in which tumor cell recruitment has been negatively impacted simply by modulating the immune microenvironment of the scaffold.

While we did not observe large changes in individual immune cell populations present in the scaffold, we were able to use the sum total of the immune microenvironment as evaluated by surface marker flow cytometry to observe how delivery of various factors biased the whole immune environment. This multifaceted approach allowed us to investigate immune cell populations that are positively and negatively correlated with tumor cell recruitment. Interestingly, we found CD11b+Gr1+ neutrophils, CD11c+F480- dendritic cells, Ly6C+F480- monocytes, CD4+ T cells, and CD19+ B cells to positively associated with tumor cell recruitment, while overall CD45+, CD11b+F480+ macrophages, CD11b+Gr1+Ly6C- putative myeloid derived suppressor cells, CD8+ T cells, and CD49b+ Natural Killer cells were all negatively correlated with tumor cell recruitment. Neutrophils, monocytes, and CD4+ T cells were not surprising for their positive association with tumor cell recruitment as these

have been previously reported [150]. Similarly, the negative association of CD8+ T cells and CD49b+ Natural Killer cells is to be expected as these are well known negative-regulators of tumor cells at metastatic or pre-metastatic sites [150, 151]. However, the positive association of dendritic cells and B cells with metastasis has not been previously reported. Additionally, we were surprised to find CD11b+Gr1+Ly6C- putative myeloid derived suppressor cells were negatively associated with tumor cell recruitment in this context. It is possible that this cell population may be heterogeneous [160] and contain neutrophils as well as granulocytic MDSCs that may explain their negative impact on tumor cell recruitment [46]. These findings were then further investigated by creation of a multiple linear regression model with stepwise validation of terms to find the populations that were significantly associated with tumor cell recruitment. Similar to simple correlation analysis and as would be expected based on the literature, we found CD45+ and CD8+ T cells [161] to be negatively associated with recruitment and neutrophils [162] and CD4+ T cells [163] to be positively associated with tumor recruitment. This analysis indicates that tumor cell recruitment to a biomaterial scaffold *in vivo* can be described reasonably well by knowing the relative proportions of CD45+ immune cells, CD8+ T cells, CD4+ T cells, and CD11b+Gr1+ neutrophils. This finding is significant as it indicates that for a given patient, the relative distribution of immune cells could be tracked as a surrogate for tumor cell recruitment to the implant.

Finally, we investigated the role of the immunomodulated microenvironments on tumor cell phenotype *in vitro*. These experiments were performed with whole scaffold conditioned media and 4T1 mouse breast adenocarcinoma cells *in vitro* due to the relative difficulty of ascertaining the effect of a microenvironment on recruited tumor cells *in vivo* [151]. This approach also allowed for more controlled understanding of the effect of modulated microenvironments on tumor cell phenotype relative to direct analysis of recruited tumor cells which could be biased by recruitment of

different subpopulations of tumor cells to different microenvironments. Interestingly, we found CXCL12 modulated microenvironments significantly reduced proliferation relative to the FLUC control in the same mouse. This is consistent with other reports demonstrating that enhanced CXCL12 expression by the primary tumor inhibits tumor growth and metastasis through regulation of anti-tumor immunity [164]. This finding in the context of the various literatures surrounding CXCL12 role in breast cancer metastasis highlights ability of this platform to understand metastasis on a local scale instead of a primary tumor driven [164] or GEMM model [153]. Additionally, we found IL10 modulated microenvironments significantly enhanced proliferation relative to FLUC controls in the same set of mice. As a potent anti-inflammatory factor, IL10 is known to enhance metastasis through suppression of various immune surveillance mechanisms [159, 165] but in other cases has been found to reduce metastasis [158]. By using conditioned media from the modulated microenvironment, we remove all cell-contact dependent mechanisms and rely only on secreted factors. These results indicate that biasing the scaffold microenvironment toward a more immune suppressive role has dual effects on tumor cells: it reduces tumor cell recruitment to the scaffold but enhances proliferation. Additionally, we find by scratch assay that IL10 modulated microenvironments reduce migration of tumor cells in a scratch assay. This is consistent with the finding of reduced tumor cell recruitment to the scaffold. These findings highlight the ability of this platform to begin to tease out the role of various cytokines in metastasis on a local scale, rather than through global modulation of tumor cells or immune cells.

Lentiviral gene delivery from biomaterial scaffolds has been performed in the past with poly(lactide-co-glycolide) (PLG) scaffolds [31, 66, 166]. In this work we chose to use PCL scaffolds, as we have achieved higher levels of tumor cell recruitment in PCL relative to PLG [30] and thus hypothesized that we would have better resolution for identifying effects of immunomodulation on tumor cell recruitment. We achieved

long-term sustained transgene expression from scaffolds loaded with lentivirus and implanted into the epididymal fat pad, similar to previous work [66]. We found slightly different cell populations stably expressing the lentivirus transgene relative to previously reported work [66]. This may be a result of mouse strain differences (balb/c versus CD1) or biomaterial differences (PCL versus PLG). As the cells transduced with the lentivirus were more likely to be immune cells than non-immune cells, this represents an ideal platform for modulating the immune microenvironment.

In this study, we demonstrate the utility of lentiviral delivery from biomaterial scaffolds to alter immune cell populations and tumor cell recruitment *in vivo*. Application of this technology toward dissecting the role of various immune cell populations and secreted factors in metastasis provides an engineering platform to molecularly dissect metastatic processes, identify key pathways for intervention, ultimately providing new targets for the prevention and treatment of metastasis.

4.6 Materials and Methods

4.6.1 Lentivirus production

Lentiviral production was performed as previously described 24. Briefly, DNA encoding for eGFP, firefly luciferase, murine IL10, CCL2, or CXCL12 in a self-inactivating lentiviral vector cassette was purchased from Vector Builder. Lentivirus was produced in HEK-293FT cells grown in DMEM with 10% FBS. Lentiviral packaging vectors were co-transfected with the lentiviral vector into HEK293FT cells using Lipofectamine 2000 (Life Technologies). After 48 h, the supernatant was collected and cell debris removed via centrifugation. Lentiviral particles were then concentrated using PEG-it (System Biosciences) and re-suspended in sterile dPBS with 1M sucrose to aid in viral stability. Lentiviral titer was determined using qPCR Lentivirus Titer Kit (Applied Biological Materials). Typical titers ranged from 1e9 to 5e9 particles/mL.

4.6.2 Scaffold fabrication and implantation

Microsphere preparation. PCL microspheres were prepared as previously described11. Briefly, microspheres were prepared by emulsification of a 6% (w/w) solution of PCL (Lactel Absorbable Polymers; Inherent viscosity 0.65-0.85 dL/g) in dichloromethane in a 10% (w/v) poly(vinyl alcohol) solution followed by homogenization at 10,000 rpm for 1 minute. The solution was then stirred for 3 hours to evaporate dichloromethane solvent. Microspheres were then collected by centrifugation at 2000 x g for 10 minutes and washed at least five times in deionized water. Finally, microspheres were lyophilized for 48 hours.

Scaffold fabrication. Microporous PCL scaffolds were prepared by mixing PCL microspheres and sodium chloride crystals (250-425 μm in diameter) at a 1:30 (w/w) ratio. This salt and polymer microsphere mixture was then pressed in a steel die for 45 seconds at 1500 PSI. Polymer/salt disks were then heated at 60C for 5 minutes per side to melt polymer microparticles around salt crystals to form a continuous structure. Salt crystals were subsequently removed by immersion in water for 1.5 hours. Scaffolds were then sanitized for animal studies using 70% ethanol, rinsed with sterile water, and dried on a sterile surface.

Scaffold lentivirus loading. 2e7 viral particles (in 20 μL dPBS with 1M sucrose) were added to the scaffold using a micropipette, allowed to dry for 2 minutes and then immediately implanted into the mouse.

Scaffold implantation. Scaffolds were implanted into the epididymal fat pads of 8-week-old female balb/c mice (Jackson Laboratory) as previously described 10. For the implantation procedure, animals were anesthetized via isoflurane (2%, inhaled), prepared with Carprofen analgesia (5 mg/kg, subcutaneous injection), the belly was shaved and prepped using a Betadine swab followed by an ethanol swab and this procedure was repeated 3 times. A fenestrated sterile field was draped over the surgical area and a 1 cm incision was made in the skin parallel to the top of the hip.

Next, a 1 cm incision was made in the peritoneal wall and the epididymal fat pads were gently pulled out of the peritoneal cavity and placed on sterile gauze. Scaffolds were placed on the fat pad and the fat pad was manipulated to enclose the scaffold in fat. Each fat pad was gently re-inserted into the peritoneal cavity taking care to keep the scaffold enclosed in the fat tissue. The peritoneal wall was closed with 5-0 vicryl resorbable sutures (Ethicon). The skin was then closed using sterile wound clips (Reflex 9 mm, Roboz Surgical Instrument Co).

4.6.3 Tumor Inoculation

Animal studies were performed in accordance with institutional guidelines and protocols approved by the University of Michigan Institutional Animal Care and Use Committee (IACUC). Tumor inoculations were performed by injection of 2e6 4T1-tdTomato-luc2 (Perkin Elmer) cells in 50 μL PBS (Life Technologies) into the fourth right mammary fat pads of 10-week-old female Balb/c mice (Jackson Laboratory). Cell lines were confirmed to be pathogen free and authenticated by short tandem repeat DNA analysis and compared to the ATCC STR profile database (DDC Medical).

4.6.4 In vivo bioluminescence imaging

Luciferase expression was monitored longitudinally using an IVIS imaging system (Caliper). Mice were anesthetized with isoflurane and administered an intraperitoneal injection of d-luciferin (Caliper) at a dose of 150 mg/kg. Animals were then placed in the imaging chamber and images were acquired every 5 min for a total of 30 min or until the peak signal was found for each mouse. Signal intensity is reported as integrated light flux (photons/sec) as calculated by Living Image Software (Caliper).

4.6.5 Statistical Analysis

All results are presented as mean +/- standard error of mean (SEM). Statistical comparisons of parameters between groups were made using Students t-test for unpaired samples. A p value of <0.05 was considered statistically significant. Unsupervised hierarchical clustering was performed in MATLAB release 2018a.

4.6.6 Flow Cytometry

Scaffolds were minced, digested using Liberase TL (Roche) and strained through a 70 μm filter to produce a single cell suspension. Cells were pelleted via centrifugation at 500 x g for 5 min. Following isolation of a single cell suspension, cells were blocked using anti-CD16/32 (Biolegend) and stained with anti-mouse CD45 AF700 (Biolegend), CD11b V500, F4/80 PECy7, Gr1 PacBlue, Ly6C FITC, and CD11c APC for innate panel. For adaptive panel samples were stained with anti-mouse CD45 AF700, CD4 V500, CD8 FITC, CD19 PacBlue, and CD49b PECy7. Samples were run on MoFlo Astrios Flow Cytometer (Beckman Coulter) and data processed using FlowJo (TreeStar Inc.).

4.6.7 Conditioned Media Assays

Generation of conditioned media. Scaffolds were isolated, separated from epididymal fat pad and placed in 600 μL sterile RPMI 1640 media with non-essential amino acids, HEPES buffer, and without phenol red. Scaffolds were then minced using a microfeather scalpel and incubated at 37C and 5% CO2 for 48 hours. Following conditioning of media, supernatant was collected into microcentrifuge tubes (MCT) and centrifuged at 2000xg for 5 min at 4C. Supernatant was then transferred to a new MCT and stored at -80C until use.

Conditioned Media Assays. 4T1-tdTomato-luc2 cells were thawed and allowed to grow to confluency before passaging for proliferation, scratch and mammosphere

assays. All assays were performed in 96 well plates with 50 μL of conditioned media and 50 μL of serum-free or serum-containing RPMI 1640 as appropriate for the assay. For all conditioned media assays each condition was compared to a F-Luc control in the same mouse (F-Luc loaded and implanted into right fat pad and virus of interest loaded and implanted into left fat pad). RPMI 1640 with non-essential amino acids, HEPES buffer and without phenol red, was used as a control for all assays.

Proliferation Assays. Cells were plated at 50,000 cells/well and the number of cells was monitored once a day for four days using a plate reader with excitation at 554 and emission at 581 reading from the bottom of the plate. Scratch Assays. Cells were plated at 100,000 cells/well and allowed to attach for 12 hours. After 12 hours, a p200 pipette tip was used to create a scratch in the center of each well spanning the length of the well. The plate was gently shaken to remove any loosely attached cells. Next the media was replaced the 50 μL of the appropriate conditioned media and 50 μL of RPMI-1640 with 10% fetal bovine serum. Wells were imaged using a light microscope immediately after scratch formation and imaged every 3 hours following scratch formation to monitor scratch closure. At 12 hours following scratch formation each well was imaged and evaluated for full, partial or no closure of the scratch.

Mammosphere Assays. Cells were plated at 10,000 cells/well in an ultra-low attachment 96 well plate with 50 μL of mammosphere media and 50 μL of the appropriate conditioned media. Mammosphere formation was monitored with imaging via light microscope for 5 days and evaluation of whole well tdTomato fluorescence using a plate reader as with the proliferation assay above.

4.7 Supplemental Figures

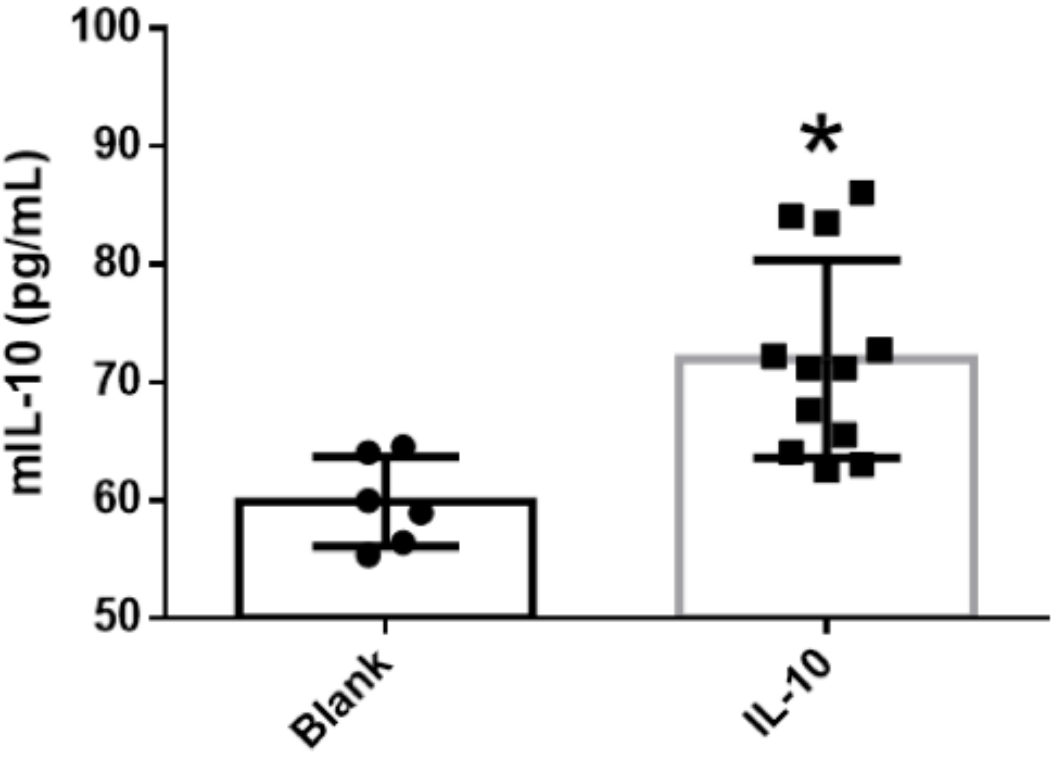

Figure 4.5: **Delivery of UBC-mIL10 lentivirus demonstrates significantly higher protein levels of mIL-10 as evaluated by ELISA** relative to scaffolds that receive no lentivirus.

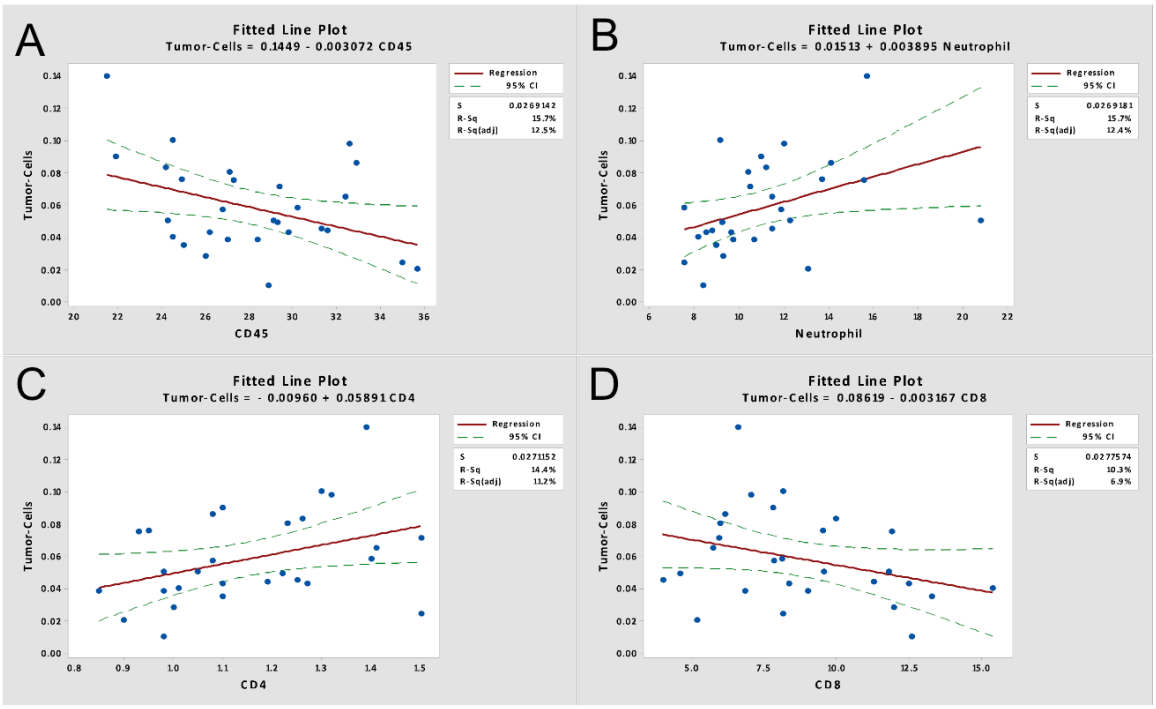

Figure 4.6: **Single linear regression of cell populations identified as significantly explaining variability in tumor cell recruitment** including (A) %CD45+Live cells of singlets (B) %CD11b+Gr1+ (Neutrophils) of CD45+Live cells (C) %CD4+ T cells of CD45+Live cells and (D) %CD8+ T cells of CD45+Live cells. Single regression line and 95% confidence interval are reported for each single linear regression.

CHAPTER V

Biomaterial Scaffolds Recruit an Aggressive Population of Metastatic Tumor Cells *in Vivo*

5.1 Authors

Grace G Bushnell, Tejaswini P Hardas, Scott Ronquist, Rachel M Hartfield, Yining Zhang, Robert S Oakes, Haiming Chen, Indika Rajapakse, Max S Wicha, Jacqueline S Jeruss, Lonnie D Shea

5.2 Abstract

For most cancers, metastasis is the point at which clinical treatment shifts from curative intent to extending survival. Biomaterial implants act as a synthetic pre-metastatic niche recruit metastatic cancer cells and provide a survival advantage, and their use as a diagnostic platform requires assessing their relevance to disease progression. Here, we show that scaffold captured tumor cells (SCAF) are 30 times more metastatic to the lung than primary tumor cells (PT), similar to cells derived from lung micrometastases (LUNG). SCAF cells were more aggressive *in vitro*, demonstrated higher levels of migration, invasion, and mammosphere formation, and had a greater proportion of cancer stem cells than PT. SCAF were highly enriched for gene sets associated with metastasis and had associated genome structural changes includ-

ing globally enhanced entropy. Collectively, our findings demonstrate that SCAF cells are distinct from PT, more closely resembling LUNG, indicating tumor cells retrieved from scaffolds are reflective of cells at metastatic sites.

5.3 Significance

The use of biomaterial scaffolds as a diagnostic requires assessing relevance of recruited cells to disease progression. Scaffold-recruited tumor cells are highly metastatic; resembling those found in the lung and were investigated for metastasis-associated genome structure changes. Scaffold-captured cells may serve as diagnostic towards developing a molecular staging of metastasis.

5.4 Introduction

In most types of cancer, the formation of distant metastases is the point at which the disease is no longer considered curable. Tumor cell colonization of distal sites occurs through a sequence of events, initiated by generation of pre-metastatic niches by cells originating in the bone marrow [8, 150, 167]. A small subset of tumor cells that have successfully invaded the tumor vasculature then home to these pre-conditioned locations [168] and are often more aggressive [5], resistant to therapy [169], and cancer stem cell like [170]. This suggests that neither the primary tumor nor CTCs are representative of cells with metastatic potential. At present, methods to detect metastasis involve radiologic imaging, which are capable of detecting metastatic foci 7-10 mm in size [171]. Imaging is typically performed for evaluation of clinical symptoms indicating compromised tissue function, and thus foci of this size are usually associated with late stage disease.

Most early detection strategies currently developed focus on the use of blood as a liquid biopsy. The umbrella term liquid biopsies includes circulating tumor cell

(CTC), circulating tumor DNA (ctDNA), and exosome detection in the blood: all of which are emerging as platforms to stage patients beyond the presence, size, and molecular characteristics of the primary tumor [172]. However, while each of these is associated with metastatic risk the interplay between the presence and relative number of each of these markers and presence of metastatic disease is tenuous. Biomaterial scaffolds that capture metastatic tumor cells [151] extend beyond the power of the liquid biopsy to capture immune cells associated with the metastatic niche and metastatic tumor cells themselves [30, 31, 34, 42, 152]. These technologies have been successful in mouse models of breast [30, 31, 34, 42, 152], ovarian [29], prostate [27], melanoma [26], and hematologic cancers [36] and have captured tumor cells, reduced metastatic burden [30, 31], and improved survival [30].

A crucial piece of scaffolds as a detection platform and alternative to liquid biopsy is understanding the phenotype of tumor cells recruited to biomaterial scaffolds *in vivo* testing the hypothesis that these cells are truly metastatic and similar to tumor cells that have colonized an organ. As poly(ε-caprolactone) (PCL) scaffold implantation in combination with surgical resection results in a survival advantage relative to mock surgery [30], we expect that the scaffold may be capturing an aggressive population of metastatic tumor cells. Identifying the phenotype of scaffold-captured tumor cells within the continuum of tumor cell phenotypes will inform the use of scaffolds as surrogates for metastatic sites, facilitating the development of therapeutic strategies targeting metastatic disease.

In this report, we derived cell lines from the primary tumor MDA-MB-231BR breast cancer xenografts, as well as matched lung micro-metastasis, and biomaterial scaffold captured-tumor cells. *In vitro* and *in vivo* assays were utilized to characterize phenotypic differences between these cell lines. Finally, we performed RNAseq and Hi-C to elucidate transcriptional and chromatin configuration differences that generate these phenotypic characteristics. These studies support the utility of scaffold-captured

cells as a metastasis surrogate to reveal molecular mechanisms and identify potential therapeutic targets for metastatic cancer.

5.5 Results

5.5.1 Tumor cell lines were derived from scaffold, primary tumor, and metastatic sites *in vitro*

We generated cell lines from various tumor cell locations *in vivo* including cells derived from subcutaneously implanted scaffolds and compared them to cell lines derived from primary tumors or lung metastases derived from the same set of mice. Based on previous reports, the earliest metastatic cells should be captured in the scaffold [30, 31], with metastases arriving in the lung at subsequent times. This difference in time of arrival may underlie some variations in these metastatic cell populations. Using a mouse cell depletion kit and magnetic activated cell sorting, we isolated human MDA-MB-231BR human breast cancer cells from each location. Approximately 10,000 cells were plated for PT-derived cells, whereas approximately 100 and 500 cells were isolated for scaffold and lung derived cells respectively. Representative images of each are shown (**Figure 5.1**). While PT cells attached and spread day 1 (**Figure 5.1A**), scaffold and lung-derived cells took much longer to attach and begin growing, likely due to plating density (**Figure 5.1B**). By day 12 of culture, scaffold-captured cells had attached and formed approximately 15 individual colonies and lung-derived cells had formed hundreds of colonies, whereas primary tumor formed confluent cultures without visible colonies (**Figure 5.1C**). Cells were passaged and cultured to develop stable cell lines, hereafter referred to as SCAF (scaffold-captured), LUNG (lung micro-metastasis derived) and PT (primary tumor-derived) cell lines.

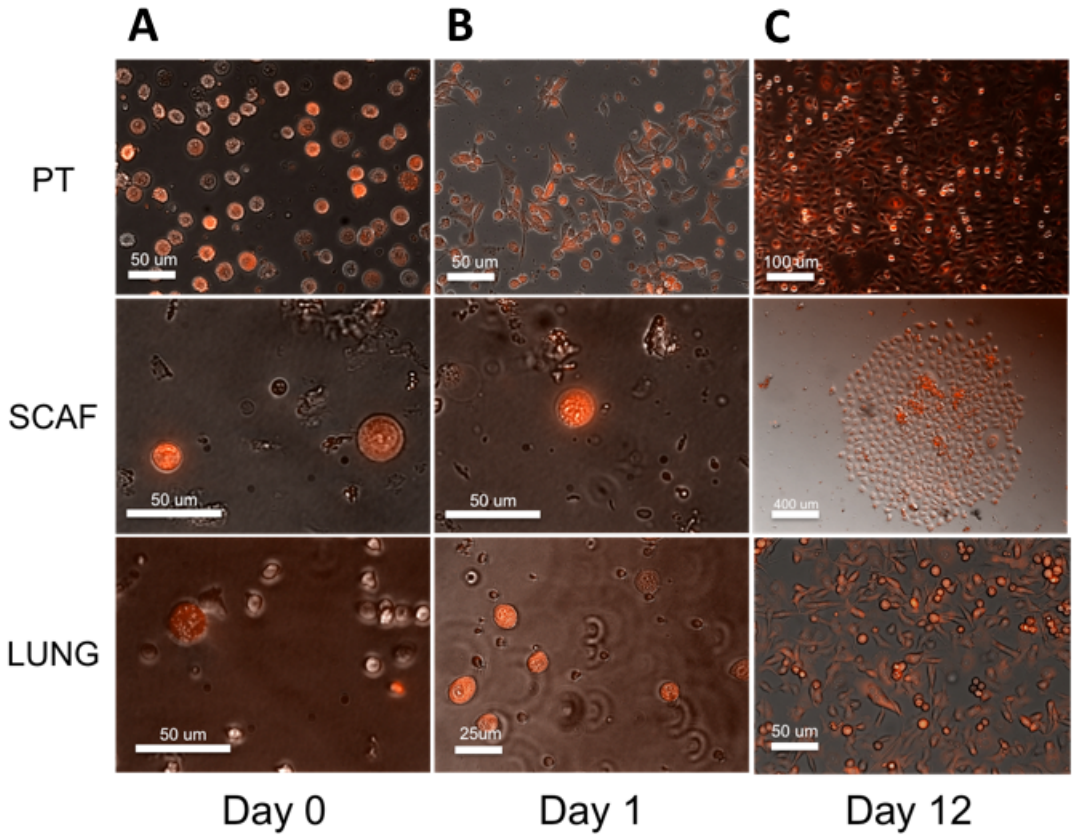

Figure 5.1: **Micro-porous scaffolds implanted in NSG mice recruit 231BR cells *in vivo*.** Tumor cells can be isolated by MACS mouse cell depletion and tdTomato+ primary tumor (PT), scaffold (SCAF), and lung (LUNG) derived tumor cells are evident initially at day 0 (A), PT cells begin to attach at day 1 but SCAF and LUNG cells remain in suspension (B), and by day 12 SCAF cells attached and grew out to form approximately 15 colonies of cells, LUNG cells grew out from approximately 500 cells and PT from approximately 1e5 cells (C). Scale bars represent 25, 50, 100 or 400 um as labeled.

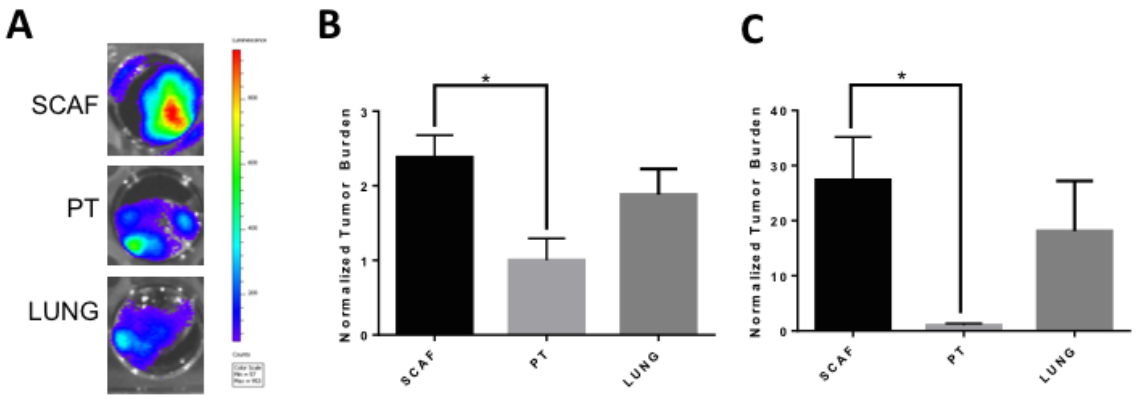

Figure 5.2: **SCAF cell line is highly metastatic *in vivo* compared to the PT cell line and similar to LUNG cell line.** (A) Representative bioluminescence images for lungs of mice inoculated with SCAF (n=11 mice), PT (n=5 mice), or LUNG (n=6 mice) cells. Tumor burden as measured by flow cytometry for tdTomato+ cells normalized to average tumor burden for PT cell line for scaffolds (B) and lungs (C). Error bars, SEM. *p<0.05 by two tailed t-test.

5.5.2 Scaffold-captured cells are highly metastatic *in vivo*

We investigated the metastatic capacity of these cell lines *in vivo*. Cell lines were orthotopically inoculated into NSG mice and allowed to grow for 21 days. Tumor and spleen mass were similar for all lines (data not shown). Representative bioluminescent images of the lungs indicate metastasis, with differential metastatic capacity for each (**Figure 5.2A**). Metastasis was quantified by the presence of tdTomato+ cells in tissue homogenates by flow cytometry. Metastatic tumor burden was significantly higher in implanted scaffolds (**Figure 5.2B**) (2.4 +/- 1.4 times higher) and lungs (**Figure 5.2C**) (27.3 +/- 22.5 times higher) for SCAF tumor-bearing mice relative to PT tumor-bearing mice ($p<0.05$ via t-test). Metastatic tumor burden was not significantly different between LUNG and PT or LUNG and SCAF in implanted scaffolds (**Figure 5.2B**) (1.9 +/- 1.2 times higher than PT) or lungs (**Figure 5.2C**) (18.1 +/- 22.3 times higher than PT). Collectively, these studies demonstrate that SCAF are more metastatic than PT and more comparable to LUNG.

5.5.3 Scaffold-captured cells display distinct phenotypic behavior *in vitro*

As scaffold-captured cells were highly metastatic *in vivo*, we next investigated the lines *in vitro* to identify mechanisms of enhanced metastasis. Assays were performed to analyze migration and invasion as well as cancer stem cell characteristics. Using a standard scratch assay, migration into a defect was quantified. Representative images demonstrate migrating tumor cells at 0 and 12 hours following the scratch (**Figure 5.3A**). PT and LUNG samples demonstrate failure to generate closure (7/12) or partial closure (5/12), and show no samples with full closure (**Figure 5.3B**). For the SCAF cell line, a statistically significant increase was observed in both partial (9/12) and total (2/12) closure and a significant decrease in no closure (1/12) was observed relative to PT and LUNG ($p<0.05$ via Fishers Exact Test).

The invasion characteristics were measured using a transwell invasion assay. Representative images are provided (**Figure 5.3C**). PT and LUNG invaded at a rate of 44 +/- 17 and 51.3 +/- 18.1 cells/image respectively (**Figure 5.3D**). Consistent with the scratch assay, a significant increase in the number of SCAF cells were observed, with 109 +/- 44 cells/image respectively. The results demonstrate that SCAF cells have a higher capacity for invasion and migration than either PT or LUNG.

We next investigated expression of cancer stem cell markers in each cell population. Using flow cytometry, we evaluated the expression of EpCAM, CD44 and CD24. Representative plots are provided, showing relative levels of EpCAM+ and CD44+CD24- cells in cell lines (**Figure 5.4A**). PT cells had 6.2 +/- 0.2% EpCAM+CD44+CD24- (CSC+) cells. A significantly increased proportion of CSC+ cells (7.3 +/- 0.2%) was observed for SCAF (**Figure 5.4B**). LUNG had a significantly decreased percentage of CSC+ cells relative to both PT and SCAF (5.3 +/- 0.4%) (**Figure 5.4B**).

The stem cell characteristics were also investigated via mammosphere assay, which measures self-renewal in suspension. Representative images are provided (**Figure 5.4C**), demonstrating mammosphere formation for SCAF, PT, and LUNG cell lines.

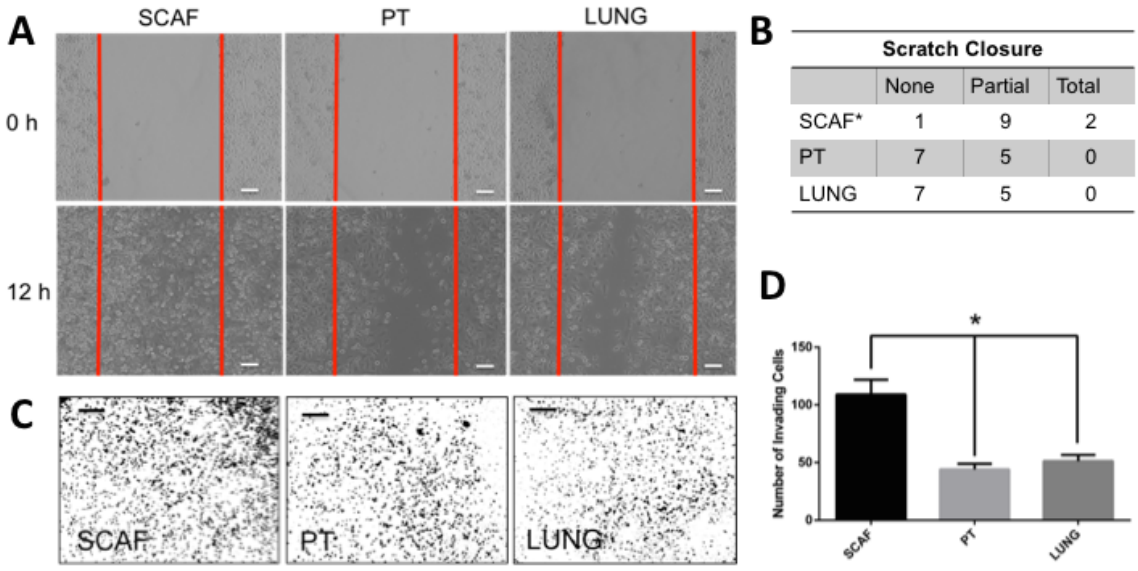

Figure 5.3: **SCAF cell line is more migratory and invasive than PT cell line and similar to metastatic cell lines.** SCAF and PT cells were analyzed in parallel for migration and invasion ability to close a scratch in 12h. SCAF cells close a scratch faster than PT and LUNG cells with representative images (scale bar 100 m) (A) and as quantified by the number of scratched with no closure, partial closure, or complete closure (B) (*$p<0.05$ relative to PT and LUNG via two tailed t-test, n=12 distinct samples per condition). SCAF cells were found to be more invasive as determined by transwell invasion assay than PT and LUNG cells with representative images (scale bar 400 μm) (C) and quantified as the number of invading cells in each 5x field of view (n=6 distinct samples per condition) (D).

PT generated 4.3 +/- 1.5 spheres/well of a 24 well culture dish, which was comparable to the LUNG, which was 3.9 +/- 1.9 spheres/well (**Figure 5.4D**). SCAF had significantly increased mammosphere formation capability with 9.4 +/- 3.1 spheres/well ($p<0.05$ relative to PT, and LUNG). Additionally, mammospheres in the SCAF line were much larger than PT or LUNG, however we cannot rule out that this was a result of aggregation of individual spheres thus only sphere number was quantified. Collectively, these results demonstrate that the scaffold sequesters a population of cells that have increased capacity for migration and invasion, and increased proportion of cancer stem cells, both of which could contribute to the survival advantage provided by the scaffold.

5.5.4 Scaffold-captured cell transcriptome is more similar to Lung derived than PT derived cells

We next utilized RNAseq to characterize transcriptomic differences between the cell lines that might account for their phenotypic properties. We identified 14,232 genes with measured expression, 2901 of which were differentially expressed (Benjamini-Hochberg corrected $p<0.05$ and log fold change >0.6) between SCAF and PT cells and 14,572 genes with measured expression, 2,398 genes of which were differentially expressed between SCAF and LUNG cells. A small subset of the most differentially expressed genes (**Supplemental, Figure 5.9A**) was confirmed using qRT-PCR (**Supplemental, Figure 5.9B**). Of this set of genes, the vast majority (19/20) were found to be more similarly expressed between SCAF and LUNG compared to SCAF and PT. The PAM50 gene set [173] was interrogated, and the majority of genes (35/50) were more similarly expressed in SCAF and LUNG when compared to SCAF and PT. These genes included Myc, MDM2, ESR1, ERBB2, EGFR, CCNB1, CXCR1, IL8, IL6R, IL6ST. Using unsupervised hierarchical clustering with all samples and genes, SCAF cells clustered separately from all PT samples and all but one

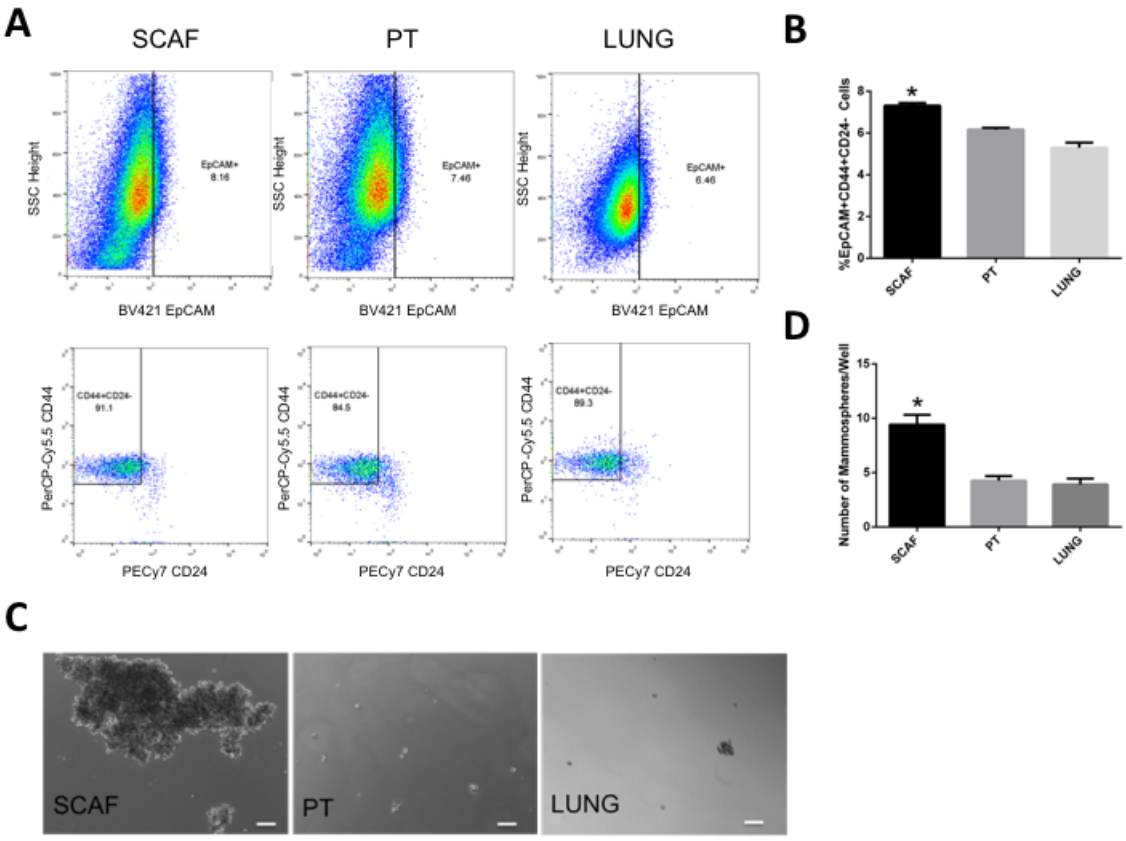

Figure 5.4: **Scaffold-captured tumor cell line shows higher proportion of cancer stem cell like cells.** (A) Representative flow plots for SCAF, PT, and LUNG cell lines. (B) Percentage of EpCAM+CD44+CD24- cancer stem cells (n=3 distinct samples per condition). (C) Representative images of mammospheres from SCAF, PT, and LUNG cell lines. (D) Number of mammospheres per well for each cell line. (n=12 distinct samples per condition). Error bars represent s.e.m. *$p<0.01$ relative to PT, and LUNG lines via two tailed t-test.

LUNG sample (**Figure 5.5A**). Using gene set enrichment analysis (GSEA), TNFα via NFκB signaling and epithelial-to-mesenchymal transition (EMT) were positively enriched and glycolysis was depleted in SCAF (false discovery rate q-value <0.25 and p<0.05) relative to PT (**Figure 5.5B**). EMT was also enriched in SCAF relative to LUNG (**Figure 5.5C**) along with E2F Targets, Myc Targets, and G2M Checkpoint. Similarly, Estrogen Response and Myogenesis were depleted in SCAF relative to both PT and LUNG and Peroxisome and IL-6, JAK/STAT3 signaling were depleted in SCAF relative to LUNG (**Figure 5.5C**). No pathways were enriched in PT relative to LUNG by GSEA, however TNFα via NFκB signaling was enriched in LUNG relative to PT (NES 1.969 with FDR q-value <0.001). Collectively, this analysis of gene expression indicates that the SCAF phenotype aligns more closely to LUNG than to PT.

5.5.5 Scaffold-captured cells have a distinct chromatin structure resulting in functional changes consistent with enhanced aggressiveness and metastatic ability

We subsequently compared SCAF and PT cell lines by Hi-C [174] to investigate chromatin structure and genome organization differences that may give rise to differential gene expression and resultant functional behavior including metastatic phenotype. Hi-C data was collected from SCAF and PT lines and analyzed in conjunction with RNAseq results at three scales: 1 Mb, 100 kb, and gene/pathway level binning (**Supplemental, Figure 5.10**). Overall, the Hi-C matrices appear similar with the same translocations and copy number changes visible within the Toeplitz normalized matrices at 1 Mb binning (**Figure 5.6A**). With filtering to the 95th percentile of each matrix, translocations are visible as blocks of strong trans interchromosomal interactions and unbalanced and balanced translocations have an L or X appearance respectively and were found to be matched between SCAF and PT (**Supplemental,**

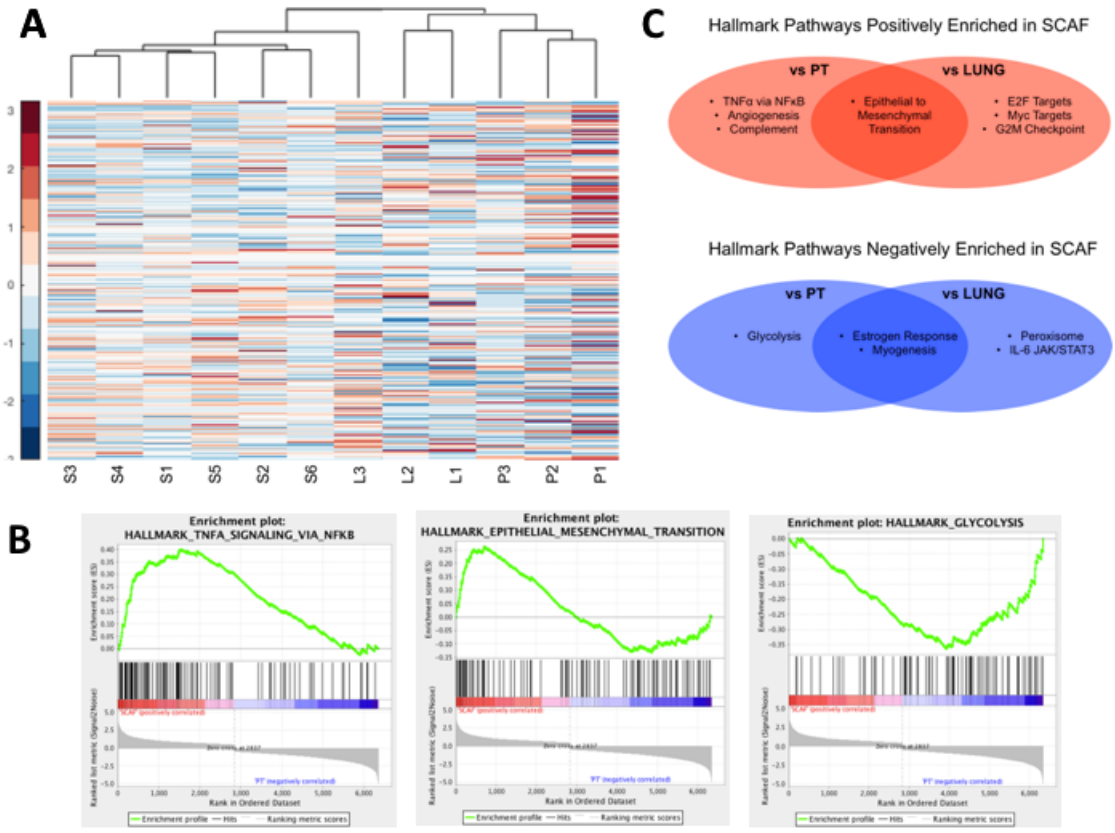

Figure 5.5: **Scaffold-captured tumor cell line shows distinct transcriptome from PT and similar to LUNG by RNAseq** demonstrating 2901 differentially expressed (DE) genes relative to PT (of 14232 with measured expression) and 2398 DE genes relative to LUNG (of 14572 with measured expression). (A) Heat map with unsupervised hierarchical clustering of all genes with measured expression for SCAF (S1-S6, n=6), PT (P1-P3, n=3), and LUNG (L1-L3, n=3) demonstrating SCAF cells have a distinct transcriptome relative to LUNG and PT but cluster more closely with LUNG than PT. (B) Gene set enrichment analysis (GSEA) enrichment plots for pathways altered in SCAF transcriptome relative to PT (C) Gene set enrichment analysis for Hallmark pathways positively enriched in SCAF vs PT and SCAF vs LUNG (red) and negatively enriched in SCAF vs PT and SCAF vs LUNG (blue) (false discovery rate q-value <0.25 and p-value <0.05)

Figure 5.11A). Copy number changes can also be visualized by looking at the sum of Hi-C contacts at 100 Mb binning for each chromosome and these were also found to be concordant between SCAF and PT (**Supplemental, Figure 5.11B**). Additionally, the copy number normalization method published by Seaman et al.[175] was utilized to investigate differential breakpoints. No differential breakpoints were found between SCAF and PT samples. Normalized 1 Mb Hi-C contact matrices were first investigated for large-scale structural differences by summing the counts for each 1 Mb bin in one dimension. Bins with a value more than 4 standard deviations above the mean were identified as altered in structure and starred in red (**Figure 5.6B**) with all having higher contact density in SCAF compared to PT. These altered bins were then investigated for changes in gene expression (**Figure 5.6C**), which showed that the increased genomic interaction measured by Hi-C was accompanied by an increase in expression in SCAF relative to PT for the majority of bins. For bins with altered gene expression the average number of genes per bin that were differentially expressed with a log2 fold change >0.6 was significantly increased relative to randomly selected bins of the same number of genes ($p<0.05$). Next, eigenvalue decomposition (**Figure 5.6D**) and calculation of entropy difference between samples was performed on 100 kb binned matrices for each chromosome (**Figure 5.6E**) demonstrating enhanced entropy in SCAF relative to PT for the majority of chromosomes. Additionally, the Fiedler vector (the eigenvector associated with the second smallest eigenvalue of the Laplacian matrix [176]) was calculated for each 100 kb binned matrix for each chromosome and plotted with the Hi-C contact matrix and RNAseq at the same binning. Structural differences from PT to SCAF were found in the Fiedler vector for chromosomes 11 (**Figure 5.7A**), 18 and 21 (not shown).

Next, Hi-C contact matrices were generated at the gene level for the whole genome (**Figure 5.7B**, top) and individual chromosomes 18 and 21 identified as altered in structure at 1 Mb and 100 kb (**Figure 5.7B**). Finally, changes in centrality were

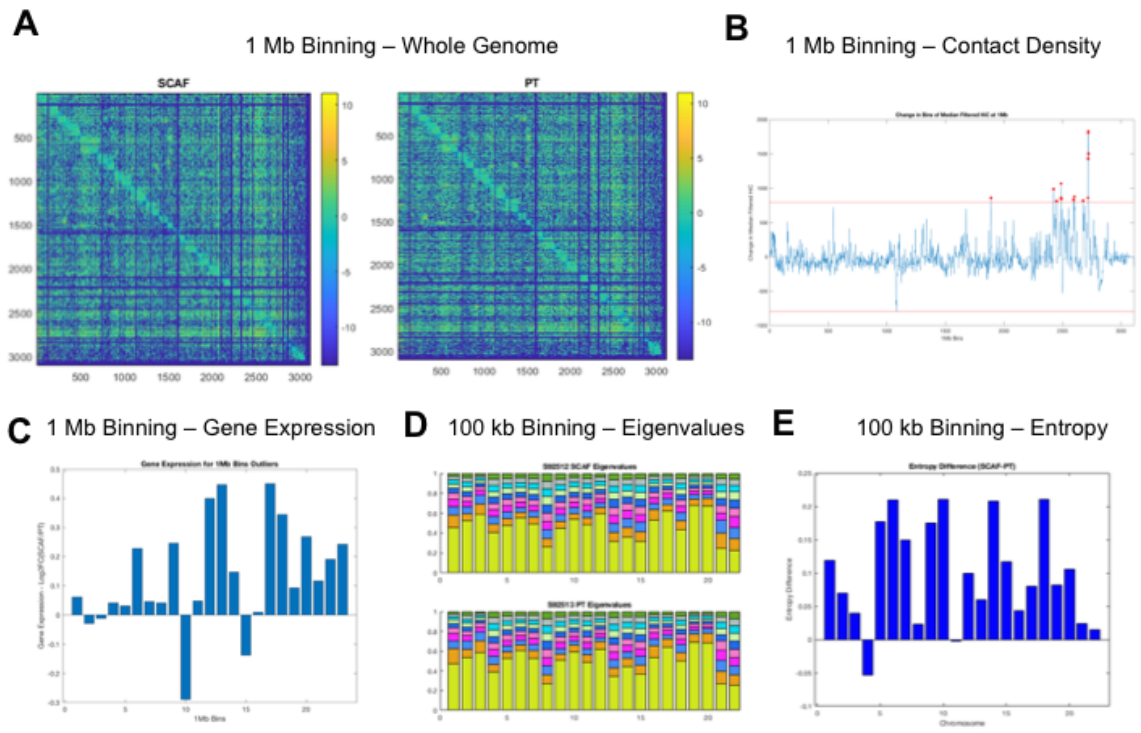

Figure 5.6: **SCAF tumor cells show distinct genome structure identified by Hi-C.** (A) Hi-C contact matrices for SCAF and PT cells at 1 Mb binning. (B) Contact density difference (SCAF-PT) for each 1 Mb bin calculated by summing the counts for each bin in one dimension. Bins with a value more than 4 standard deviations above the mean were identified as altered in structure and starred in red. (C) Log2 fold change in gene expression for SCAF/PT plotted for each of the altered bins identified in B. For identified bins with higher counts for SCAF, most have a corresponding higher gene expression. (D) Eigenvalue decomposition of 100 kb Hi-C matrices for each chromosome showing subtle differences in the eigenvalues for both samples. (E) Entropy difference for SCAF - PT calculated for each chromosome at 100 kb resolution.

calculated for each gene (Hi-C) and combined with gene expression (RNAseq) in principal component analysis (PCA) to reduce the dimension of the data while maintaining meaningful variability. Projections of each bin onto the first two PCs are shown (**Figure 5.7C**). To quantify which genes have the greatest change, the distance in the PC space from PT to SCAF samples was calculated. Genes whose distance from PT to SCAF changed more than 4 standard deviations from the mean whole genome distance were identified as altered in structure/function. KEGG pathways were then selected based on RNAseq (**Figure 5.5C**) to investigate enrichment of structure/function changes within subsets of genes (**Table S3**). By centrality analysis the KEGG MAPK, ErbB, HIF-1α, FoxO, mTOR, PI3-Akt, AMPK, VEGF, Focal Adhesion, TNFα, Leukocyte Transendothelial Migration, Cancer, and Breast Cancer pathways were significantly altered from PT to SCAF ($p<0.05$) (**Figure 5.7C**). Similarly, distances greater than 4 standard deviations above the mean could be observed for specific genes within pathways including COL6A1, FN1, and CTNNB1 for the Focal Adhesion pathway (**Figure 5.7C**). Finally, based on GSEA implicating NFϰB as a key regulatory pathway, genes with NFϰB binding sites were investigated for changes in structure/function. By centrality analysis, genes with NFϰB binding sites were significantly altered in structure and function. Altered genes more than 4 standard deviations above the mean were identified including HSP90AB1, COL7A1, EIF5A, and BRD2 among others (**Figure 5.7C**). Taken together, these results indicate we can identify genome structure organizational differences that are associated with development of a metastatic phenotype.

5.6 Discussion

In this study metastatic tumor cells derived from those captured by microporous PCL scaffolds *in vivo* were investigated for their phenotype relative to tumor cells from the primary tumor, and metastatic lung lesions. This work was motivated by

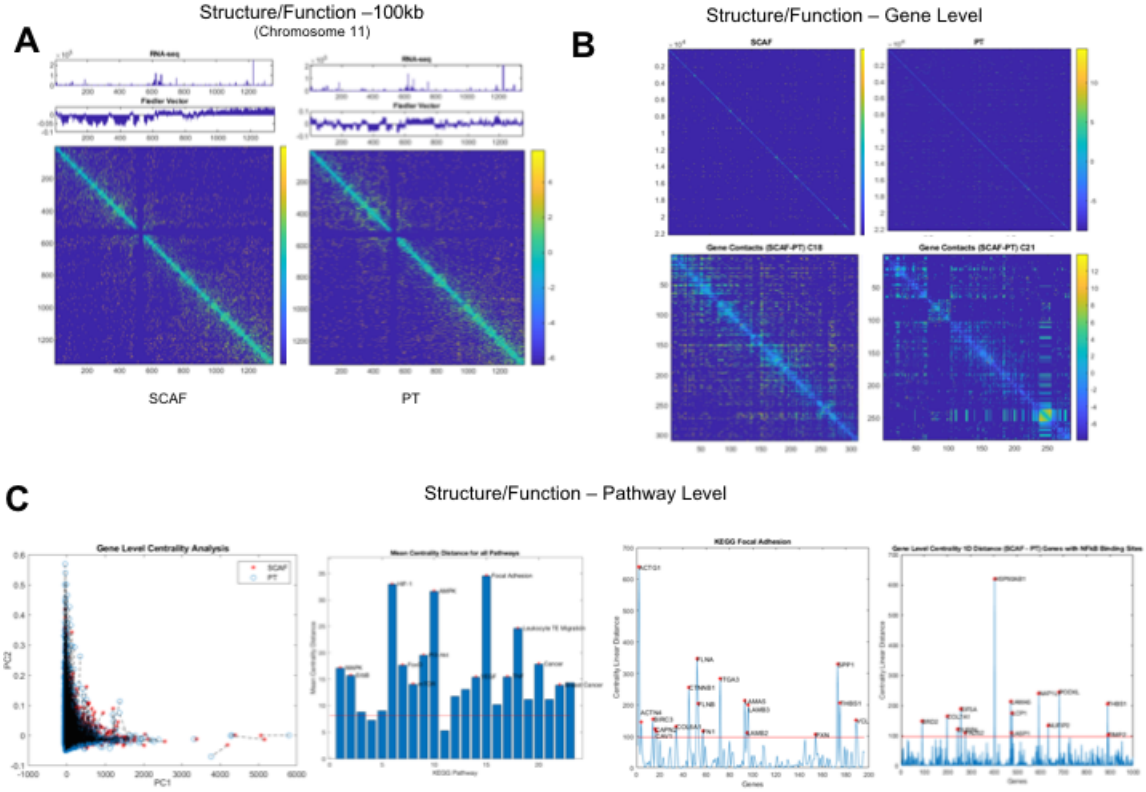

Figure 5.7: **SCAF cells demonstrate differential structure and function relationships from PT cells.** Structure (Hi-C matrix and corresponding Fielder Vector) and function (RNAseq) investigated at the 100kB level for Chromosome 11 (A). Structure relationships for the whole genome (top) for SCAF and PT and differences in gene level contacts for chromosome 18 and 21 visualized as the SCAF matrix PT matrix (bottom) (B). Gene level centrality analysis for the whole genome comparing structure/function for SCAF and PT pairs for each gene connected by dashed black line (C). KEGG pathways investigated for difference in centrality distance from SCAF to PT for genes in a given pathway, red stars indicate pathways that are significantly different from the mean genome-wide centrality distance by two tailed t-test. Centrality distance for SCAF PT calculated for KEGG Focal Adhesion Pathway and for genes with NFκB binding sites. Red stars indicate genes that are more than four standard deviations above the genome-wide mean centrality distance.

the idea that scaffold-captured cells may be more easily sampled, while accessing organ-derived metastatic cells would necessitate an invasive biopsy with potential for high morbidity and false negative results dependent upon the extent of disease progression. Our work and that of others have demonstrated that scaffolds recapitulate multiple elements of the pre-metastatic niche *in vivo* along with the capacity to capture metastatic cells within a biomaterial implant [151]. Analyzing these cells along the continuum of cancer cell phenotypes provides a foundation for using a scaffold biopsy to impact patient care, such as for the development of personalized therapies [177]. We developed stable cell lines from metastatic locations in order to have sufficient numbers of cells for in depth *in vitro* behavioral, functional, and molecular assays and *in vivo* metastasis assays. Notably, the scaffold-derived tumor cells were highly metastatic *in vivo*, demonstrated substantial invasiveness *in vitro*, and molecular analysis indicated these cells were similar to cells derived from metastatic lung lesions.

SCAF and LUNG were more highly metastatic than PT *in vivo*, supporting the notion that cells captured by the scaffold represent a population with the ability to successfully metastasize and colonize a tissue. Interestingly, the SCAF line showed comparable ability to metastasize to both scaffold and lung tissues, which differs from literature that has reported cell proclivity to metastasize to the location of origin [64, 178, 179]. The concordant metastatic tropism to lung for both SCAF and LUNG suggests that the metastatic traits of SCAF are not site specific yet are indicative of overarching traits required for metastasis. Consistent with increased aggressiveness *in vivo*, scaffold-captured cells were more migratory, invasive, and stem-like *in vitro* than cells from the primary tumor. These results provide the first evidence that tumor cells derived from biomaterial scaffolds are a functionally aggressive and metastatic population of cells, with the capacity to spread to distal sites and compromise organ function.

Unsupervised hierarchical clustering of RNAseq data identified that SCAF clustered more closely with LUNG than with PT. Additionally, upon investigation of the top differentially expressed genes between SCAF and PT, 19/20 of these genes showed greater homology between SCAF and LUNG when compared with SCAF and PT. Similarly, for the PAM50 gene set 35/50 genes had more similar expression between SCAF and LUNG than for SCAF and PT. Collectively, these results indicate that scaffold and lung-derived cells, both originating from metastatic sites, show greater homology compared to scaffold-captured cells and those derived from the primary tumor.

Further investigation of the tumor cell phenotypes by GSEA identified pathways significantly enriched/depleted in SCAF cells relative to PT and LUNG. Hallmark pathways [180] enriched in SCAF relative to PT included TNFα signaling via NFκB, Epithelial to Mesenchymal Transition (EMT), Angiogenesis, and Complement. TNFα signaling through NFκB has been shown to enhance stemness of breast cancer cells [134], angiogenesis and complement are indicators of metastasis and survival in patients [181, 182], and EMT is closely linked to metastasis and stemness [183, 184]. Interestingly, EMT is enriched in SCAF relative to both PT and LUNG. This observation, in combination with the ideas that (i) the earliest metastatic tumor cells colonized the scaffold prior to the lung [31], (ii) SCAF are more homogeneous than LUNG, as demonstrated by hierarchical clustering, (iii) IL-6 JAK/Stat3 signaling was enriched in LUNG relative to SCAF which may enhance metastasis *in vivo* through paracrine communication with myeloid derived suppressor cells but may not influence phenotype *in vitro* [185] and (iv) SCAF cells are more stem-like and demonstrate higher entropy/plasticity may explain why the SCAF line was more migratory and invasive than the LUNG line *in vitro*. Hallmark pathways enriched in SCAF relative to LUNG also included E2F targets [186], Myc targets [187], and G2M checkpoint [187]: all important axes in breast cancer. Peroxisome and IL-6 JAK/Stat3 signaling

were enriched in LUNG relative to SCAF and have been implicated in therapeutic resistance [188] and stemness [185]. Importantly, TNFα signaling through NFκB was enriched in both SCAF and LUNG relative to PT, indicating this may be the crucial pathway for gaining enhanced metastatic ability for these cells. These results suggest that LUNG and SCAF may evolve toward similar phenotypes through the same dominant transcriptional program (TNFα via NFκB) but with different accessory programs facilitating site-specific adaptations (i.e. SCAF with EMT and LUNG with IL-6 JAK/Stat3 signaling) [185], which is consistent with other observations of metastatic lines [85]. This supports the use of scaffold as a sampling location and also suggests that both metastatic locations are derived from a similar pool of cells yet may experience differential evolutionary pressure and adaptation at different distal sites. The scaffold has the capacity to provide a sampling site that would be clinically easy to access relative to an organ biopsy and contains a source of cells with clear phenotypic and molecular similarities to the pathologic metastatic site.

The underlying genome/chromatin organization role in the development of metastatic phenotype from PT to SCAF was identified with Hi-C. Using a multi-scale approach, we found structural changes linked to functional outcomes at all points. Critically, for all except chromosome 4, entropy for SCAF was higher than PT, indicating a more dysregulated network consistent with the concept of increased aggressiveness and phenotypic flexibility that are hallmarks of stemness and metastasis [189–191]. We chose to analyze SCAF as a surrogate for other metastatic sites due to the *in vivo* and transcriptomic similarity of these cells to the LUNG. Importantly, no copy number changes or additional translocations were observed, indicating the karyotype from PT to SCAF was conserved. Even at 1 Mb binning analysis of whole genome contact density we found structural differences between SCAF and PT indicating areas of chromosomes 11, 18, and 21 with a higher density of intrachromosomal contacts for SCAF. Interestingly, there were no locations identified where PT had

higher contact density. Investigating these altered bins further, we found the vast majority had higher expression in SCAF indicating increased connectivity resulted in enhanced gene expression. Similarly, we observed subtle changes in both eigenvalue decomposition and Von Neumann entropy for each chromosome. At 100 kb we found chromosomes 11, 18 and 21 identified by contact density at 1 Mb to have differences in Fiedler vector consistent with a change in structure from SCAF to PT. We also investigated the centrality of each chromosome at the gene level (structure) and gene expression (function) for the whole genome and identified significantly altered pathways in structure/function. Implicated genes in these pathways include many genes associated with metastasis and stemness including COL6A1, FN1, ITGA3, IL11, IL6ST, IL8, and TGFβR2. In particular, IL8 has been implicated in enhanced stemness, aggressiveness [192, 193], and resistance to therapy [194]. Finally, based on GSEA of RNAseq data implicating TNFα via NFϰB signaling as the common transcriptional program associated with metastatic phenotype in both SCAF and LUNG cells, we investigated structure/ function relationships for genes with NFϰB binding sites. We found this gene set to be significantly altered from PT to SCAF in structure/function. This further supports NFϰB as one of the major drivers of phenotypic change from non-metastatic to metastatic phenotype [195–197]. Our data are among the first to connect genome/chromatin structure alterations to changes in functional gene expression driving metastatic phenotype.

5.7 Outlook

Our results provide primary evidence that biomaterial scaffold-captured tumor cells are a functionally aggressive and metastatic population capable of distal organ colonization. Taken together, this work demonstrates scaffold recruited tumor cells are similar to other metastatic sites, but also represent a population of highly aggressive, stem-like cells whose capture may hold promise for reducing breast cancer

mortality. Additionally, these results support the possibility that metastatic phenotype can be gained through changes in genome structure impacting functional gene expression rather than mutational alterations. Heritable alterations in tumor cell phenotype and plasticity thus may be equally as important as mutational changes for development of metastatic ability. The scaffold platform technology provides a unique opportunity to analyze the earliest metastatic cells, enabling the analysis of tumor cells that have left the primary tumor and colonized a distal site. This platform provides an unprecedented opportunity for analysis and development of tools for personalized medicine.

5.8 Methods

5.8.1 Scaffold fabrication and implantation

Microsphere preparation. PCL microspheres were prepared by emulsification of a 6% (w/w) solution of PCL (Lactel Absorbable Polymers; Inherent viscosity 0.65-0.85 dL/g) in dichloromethane in a 10% (w/v) poly(vinyl alcohol) solution followed by homogenization at 10,000 rpm for 1 minute. The solution was then stirred for 3 hours to evaporate dichloromethane solvent. Microspheres were then collected by centrifugation at 2000 x g for 10 minutes and washed at least five times in deionized water. Finally, microspheres were lyophilized for 48 hours.

Scaffold fabrication. Microporous PCL scaffolds were prepared by mixing PCL microspheres and sodium chloride crystals (250-425 μm in diameter) at a 1:30 (w/w) ratio. This salt and polymer microsphere mixture was then pressed in a steel die for 45 seconds at 1500 PSI. Polymer/salt disks were then heated at 60C for 5 minutes per side to melt polymer microparticles around salt crystals to form a continuous structure. Salt crystals were subsequently removed by immersion in water for 1.5 hours. Scaffolds were then disinfected for animal studies using 70% ethanol, rinsed

with sterile water, and dried on a sterile surface.

Scaffold Implantation. All animal studies were performed in accordance with institutional guidelines and protocols (PRO00007801) approved by the University of Michigan Institutional Animal Care and Use Committee. Scaffolds were implanted into the dorsal subcutaneous space of 8-week-old female NOD/SCID-IL2Rγ-/- (NSG) mice (Jackson Laboratory) immediately above the shoulder blades and as physically distant from the fourth-right mammary fat pad as possible. For the implantation procedure, animals were anesthetized via isoflurane (2%, inhaled), prepared with Carprofen analgesia (5 mg/kg, subcutaneous injection), the upper back was shaved and prepped using a Betadine swab followed by an ethanol swab and this procedure was repeated 3 times. A fenestrated sterile field was draped over the surgical area and a 1 cm incision was made in the upper back. Following incision, subcutaneous pockets were created perpendicular to the incision, into which sanitized scaffolds were inserted (2 scaffolds/mouse). The skin was then closed using sterile wound clips (Reflex 7 mm, Roboz Surgical Instrument Co).

5.8.2 Tumor inoculation

Tumor inoculations were performed by injection of 2e6 MDA-MB-231BR-tdTomato-luc2 (parental line, Northwestern University Developmental Therapeutics Core) or 231BR-SCAF,-PT, or -LUNG derived cell lines in 50 μL PBS (Life Technologies) into the fourth right mammary fat pads of 10-week-old female NSG mice (Jackson Laboratory). Cell lines were confirmed to be pathogen- and mycoplasma-free and authenticated by short tandem repeat DNA analysis and compared to the ATCC STR profile database (DDC Medical).

5.8.3 Magnetic Mouse Cell Depletion and Culture

Mice were euthanized four weeks following tumor inoculation and scaffolds and organs were retrieved and washed in Hanks Balanced Salt Solution (HBSS, Life Technologies). Samples were minced using microscissors in Liberase TL or TM (0.38 mg/mL, Roche) and incubated at 37C for 20 minutes. Following incubation with liberase, the enzyme was neutralized via addition of 0.5M EDTA (Life Technologies) and digested tissues were strained through a 70 μm filter in FACS buffer [PBS (Life Technologies) with 0.5% Bovine Serum Albumin (Sigma Aldrich) and 2 mM EDTA (Life Technologies)]. Cells were counted using a Countess Automated Cell Counter (Invitrogen) and magnetically sorted using a Mouse Cell Depletion Kit (Miltenyi) according to manufacturer instructions. Human cell fractions were cultured in DMEM D6429 (Sigma Aldrich) with 10% FBS and 1% penicillin/streptomycin until growth of tumor cell colonies was evident. Following the first passage of cells, culture was continued without antibiotics. Care was taken to minimize passage number of tumor cells, for all experiments the passage number was less than ten.

5.8.4 Flow cytometry to identify tdTomato+ tumor cells

For quantification of *in vivo* metastatic ability of 231BR-SCAF, -PT, and LUNG derived cell lines, mice were euthanized three weeks after tumor inoculation and retrieved scaffolds and lungs were washed in HBSS (Life Technologies) and processed with liberase as described for Magnetic Mouse Cell Depletion above. Following isolation of a single cell suspension, tdTomato+ tumor cells were quantified using a MoFlo Astrios Flow Cytometer (Beckman Coulter). The detection sensitivity for cancer cells via flow cytometry was 0.002% (i.e. 5 cancer cells in 250,000 total cells) [31]. Gating strategy is provided in **Supplemental, Figure 5.12A**. Metastasis assays were repeated twice.

5.8.5 Scratch assays

Scratch assays were performed as described by Justus et al [198]. Briefly, cells were seeded in 24 well plates and allowed to grow to form a confluent monolayer. A sterile 200 μL pipette tip was used to create a wound in the monolayer. The surface was washed with PBS (Life Technologies) to remove any detached cells and replaced with media. Images were taken immediately after wounding, 5h and 10-12h after wounding. Results were quantified by identification of the proportion of scratches that had no closure at endpoint (no cells touching from either side of wound), partial closure (at least 2 cells from either side of wound in direct contact), or complete closure (no evidence of wound remains). Assays were repeated 3 times.

5.8.6 Transwell invasion assays

Transwell assays were performed as described by Justus et al. [198]. Briefly, Matrigel invasion chambers (BD Biosciences) were rehydrated for 30 min at 37C using 500 μL serum-free media. 750 μL of chemoattractant media (serum-containing) was placed in the receiver well plate. Cells were harvested using TryplE (Life Technologies), counted and suspended at 50,000 cells/mL in serum-free media. Rehydrated invasion chambers were transferred to receiver well plate containing chemoattractant and 500 μL of cell suspension was added to each insert. Care was taken to prevent trapped air between the insert and chemoattractant media. Assays were incubated for 24h at 37C and subsequently stained and fixed using crystal violet in ethanol. Invaded cells were imaged directly on the membrane using a Nikon Eclipse inverted microscope and imaged at 10X. Four images per well were captured and cell numbers were quantified in ImageJ using automatic particle counting with constant image thresholds. Assays were repeated three times.

5.8.7 Cancer stem cell marker flow cytometry and mammosphere assay

Proportion of cancer stem cell like tumor cells in each cell line was determined by quantification of EpCAM+CD44+CD24- cell population by flow cytometry. Tumor cells were harvested using TryplE (Life Technologies), counted and suspended at 1e7 cells/mL. Cells were evenly split between control and test conditions and stained with anti-human BV421 EpCAM (clone EBA-1, BD Biosciences), PerCP-Cy5.5 CD44 (clone G44-26, BD Biosciences), and PE/Cy7 CD24 (clone ML5, Biolegend). Samples were run on MoFlo Astrios Flow Cytometer (Beckman Coulter) and data processed using FlowJo (TreeStar Inc.). Gating strategy is provided in **Supplemental, Figure 5.12B**. Cancer stem cell marker flow cytometry was repeated three times. Mammosphere assays were performed as described by Tarasewicz et al. [199]

5.8.8 RNAseq sample preparation, library construction, and sequencing

Cells were harvested using TryplE (Life Technologies), counted and suspended at 5e6 cells/mL. RNA was isolated using High Pure RNA Isolation Kit (Roche) according to manufacturer instructions. Isolated RNA concentrations were quantified using NanoDrop 2000 (Thermo Fisher) and resuspended at 80 ng/μL. RNA samples were kept at -80C until further use. RNA quality was assessed using an Agilent 2100 Bioanalyzer. The DNA Sequencing Core at University of Michigan performed library construction and sequencing using the Hiseq-4000 platform using single-end 50-base sequence reads with a multiplex of 6 per sequencing lane.

5.8.9 Transcriptome analysis

Transcriptome analysis was performed as previously described [175]. For RNAseq data processing the raw reads were checked with FastQC to identify potential quality issues in the raw data. Next, Tophat and Bowtie were used to align the reads to a human reference transcriptome (HG19). Alignment settings were kept on de-

fault except for -b2-very-sensitive, -no-coverage-search and -no-novel-juncs in order to limit the search to known transcripts only. FastQC was then performed again on the mapped reads. Cufflinks/Cuffdiff were then utilized to quantify expression and perform differential expression analysis using parameter settings multi-read-correct and upper-quartile-norm. CummeRbund was then used to format the cufflinks output. Benjamini-Hochberg procedure was used in CummeRbund for multiple testing method correction. Gene level analysis was performed using fragments per kilobase per million reads (FPKM) values outputted by Cufflinks and log2 fold change with pseudocounts. Bin level gene expression vectors were calculated using raw counts outputted by cufflinks and adding up the counts for all the genes in each bin then normalizing by million reads to convert them to FPM. Gene Set Enrichment analysis [200, 201]was performed with GSEA v3.0 software.

5.8.10 Hi-C sample preparation, library construction, and sequencing

Hi-C library construction was performed as described by Chen et al [202]. Briefly 2e6 cells for each condition were crosslinked with 1% formaldehyde (Fisher Scientific) in serum-free media for 10 min at room temperature and subsequently quenched with glycine (Sigma Aldrich) to a final concentration of 0.125 M. Crosslinked cells were flash frozen in liquid nitrogen and stored at -80C until the construction of libararies. Crosslinked cells were thawed on ice and resuspended in 1 mL lysis buffer (10 mM Tris-HCl, 10 mM NaCL, 0.2% Igpel (Signma Aldrich) and incubated for 15 min. Cells were next homogenized on ice and the lysate was transferred to a 1.7 mL tube. Cells were collected by centrifugation (5 min at 2000xg) and washed twice in NEB buffer. HindIII digestion was then performed in NEB buffer at 37C overnight. Following digestion, restriction overhang ends were filled and labeled with biotin. Samples were then ligated at 16C for 4 h in a reaction containing 1x ligation buffer, 1% Triton X-100 (Sigma Aldrich), 1 mg/mL bovine serum albumin (Fisher Scientific), 10 mM

ATP (Sigma Aldrich) and 50 u T4 DNA ligase (Life Technologies). Proteinase K (0.5 mg, Life Technologies) was then added and incubated for 4 h at 65C. After this incubation an additional 0.5 mg proteinase K was added to each tube and the incubation was continued overnight at 65C. DNA was then extracted using phenol:chloroform (1:1) and desalted using AMICON ultra centrifugal filter unit (Millipore) with 1x TE buffer. Biotin was then removed from un-ligated ends, DNA purified with signle phenol extraction and precipitated by addition of ethanol. DNA was resuspended in water and fragmentation was performed using a sonicator (Covaris). Fragments of 200-400 bp were recovered with Agencourt AMPure XP (Beckman Coulter) utilizing manufacturer protocols. DNA fragment ends were repaired and purified with a MinElute column, and A-tailing was performed. Streptavidin pull-down of biotinylated Hi-C DNA was performed. Illumina adapter ligation was then performed and then DNA was amplified by 15 PCR cycles for Illumina HiSeq Sequencing. A standard quality control protocol was performed prior to sequencing and all libraries passed. Samples were pooled and sequence in a single lane of a flow cell on HiSeq 4000 to generate paired-end sequence reads at 100 bases per end read.

5.8.11 Nucleome analysis

Generation of Hi-C Matrices: A standard pipeline was used to process Hi-C sequence data using the University of Michigan Bioinformatics Core facilities. Raw sequence reads were processed with FastQC for data quality control and paired-end reads were mapped to the HG19 reference human genome using Bowtie2. HOMER was used to develop the contact matrix at 100 kb and 1 Mb resolution. Analysis of Hi-C Matrices: Hi-C matrices were normalized, plotted, and analyzed in conjunction with RNAseq data for cell lines using the 4D Nucleome Analysis Toolbox (4D-NAT) described by Seaman et al [175].

5.8.12 Whole Exome Sequencing

Sequencing: SCAF, PT, and LUNG cell lines were cultured and passaged as described above. Roughly 2e6 cells were isolated and genomic DNA was isolated with Qiagen DNEasy kit according to manufacturer instructions. Samples were submitted to the UMich DNA sequencing core and the core performed quality control, exome capture using the Nimblegen Human Exome Capture kit, and paired-end sequencing at 150 bases per end read using the Illumina HiSeq-4000 platform with 100x coverage for each cell line.

Analysis: Genestack platform was used for analysis of whole exome sequencing data. Quality control was performed using FastQC algorithm Adaptors and contaminants were trimmed according to methods published by Aronesty et al [203] and then sequences were mapped onto the human reference genome HG19. Quality control of the mapped reads was again performed using the FastQC algorithm. Variant calling and effect prediction was then performed using SAMtools and SnpEff algorithms respectively and variants were selected to only include those resulting in missense or nonsense mutations with a quality >60. Gene ontology analysis of mutant genes was then performed using the Gene Ontology Consortium software (Consortium 2004).

5.9 Supplementary Figures

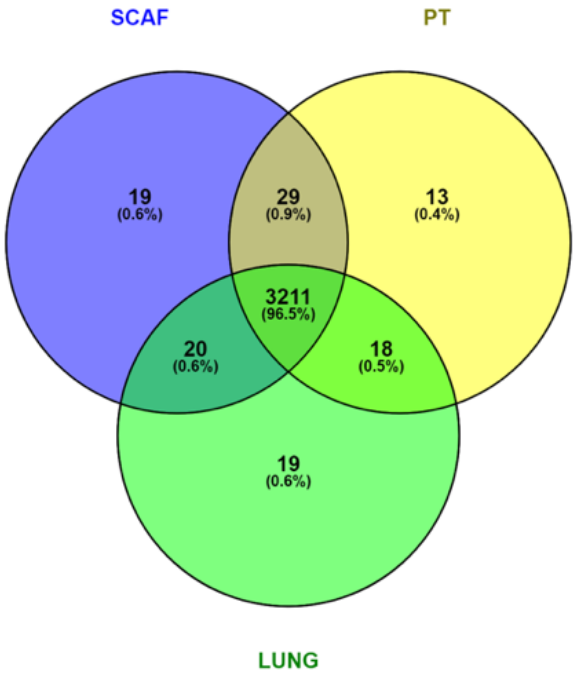

Figure 5.8: **Whole exome sequencing demonstrates similar numbers of mutations for all samples.** Venn diagram showing intragenic missense or nonsense mutations relative to human hg19 (GRCh37) reference genome with quality greater than 60 for each line and those that are shared among cell lines.

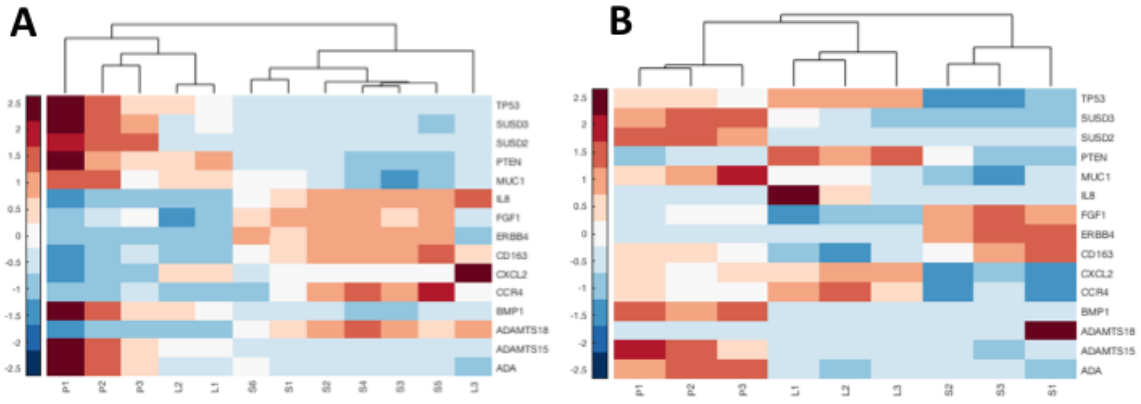

Figure 5.9: **RNAseq supplemental information.** (A) Heat map of top differentially expressed genes between SCAF, PT, and LUNG cells, TPM normalized to SCAF across two RNAseq experiments. (B) Gene expression of selected genes by qRT-PCR, delta-delta-cT relative to PT. Heatmaps normalized across row for each gene for each data set.

SCAF	PT	LUNG	SCAF/LUNG	SCAF/PT	PT/LUNG
ACC112205.1, CCNG1	AC008267.1, GS1-124k5.2	AK4	AC093495.4, RP11-434D12.1, XPC	AC091435.1	AC010907.5, DCDC2C
AP000487.5, PPF1A1	AC015989.2	BHLHE22	AIDA	ANKRD20A2	AL161645.1, SYCE1
C4orf32	AC105052.1	CANX	BAGE4	ANO2	ARFGAP1
CPEB4	CDH13	CD8A	CABP2	C1ORF220, C1orf220	C12ord76
CTD-2571L23.8, GLTSCR1	CEL, RP11-326L24.4	FAM21A	CTB-186G2.1, MAP4K1	C20orf111	CGB7
DNM2, TMED1	CREG2	FBXO34	CTD-2611O12.2	CASS4	CNOT6L
DPAGT1	DNAJC25	FLJ22184	CTNNA3, LRRTM3	CBX2	ENG
FAM27D1	HBG1	IER5L	FAM111A	CCBP2, RRP7A	F2RL3
FBXO17, SARS2	HCAR1, RP11-324E6.6	LEFTY1	GOLGA8L	CCDC92, DNAH10	HERC3, NAP1L5
IGHV4-59	IP6K2	LYZL2, RP11-14C22.5	HSD3B1	CCNO	KLRG2
KRT6C	OR6C76	MGAT2	KHNYN	CKAP4	NLRX1
NKX1-1	RP3-402G11.5	OR4K1	MEDAG	ELF3, RP11-510N19.5	PRKRA
NRXN2	ZNF787	PLBD2, SLC4A6	MEGF9	FAM21B	RNF224
PCYOX1L		PLEKHA7	NIN	HHIPL1	RP11-757C15.3, RP11-849H4.2
POTEI		PSPC1	PRR4, TAS2R30	INSL3	SCAP
RASIP1		RECQL	PR13-578N3.3	KCNK17	TRBV11-1
SCAF11		RRP7A	SFRP4	MAP4K1	UCHL1
STK35		TBX1	SLC4A2	MYB	ZNF302
TM4SF1		VQA5A	SOD3	OR4K1, ZMYM5	
			TCF15	PARVG, RP11-944L7.4	
				PBX1P1	
				PTPN7	
				RANBP2	
				RP1-93H18.6	
				SLC35E2B	
				SNX29P2	
				TAOK3	
				ZNF683	

Table 5.1: **Intragenic missense or nonsense mutations with quality greater than 60 for each cell line** (SCAF, PT, LUNG) and those shared between each pair (SCAF and LUNG, SCAF and PT, PT and LUNG.)

Pathway	Altered Genes	Expected Genes	Fold Enrich-ment	+/-	Raw p-value	FDR
Diseases of glycosy-lation	42	18.96	2.22	+	2.54E-05	1.26E-02
Diseases associated with O-glycosylation of proteins	29	9.41	3.08	+	2.49E-06	4.96E-03
O-linked glycosyla-tion	35	15.14	2.31	+	5.33E-05	2.12E-02
Extracellular matrix organization	69	39.83	1.73	+	8.14E-05	2.70E02
Olfactory Signaling pathway	96	57.15	1.68	+	1.02E-0.5	1.02E-05
Signaling by Wnt	14	39.42	0.36	-	1.58E-06	1.05E-02

Table 5.2: **Gene Ontology Terms Significantly Altered in Genes with Mutations in SCAF, PT and LUNG cell lines**

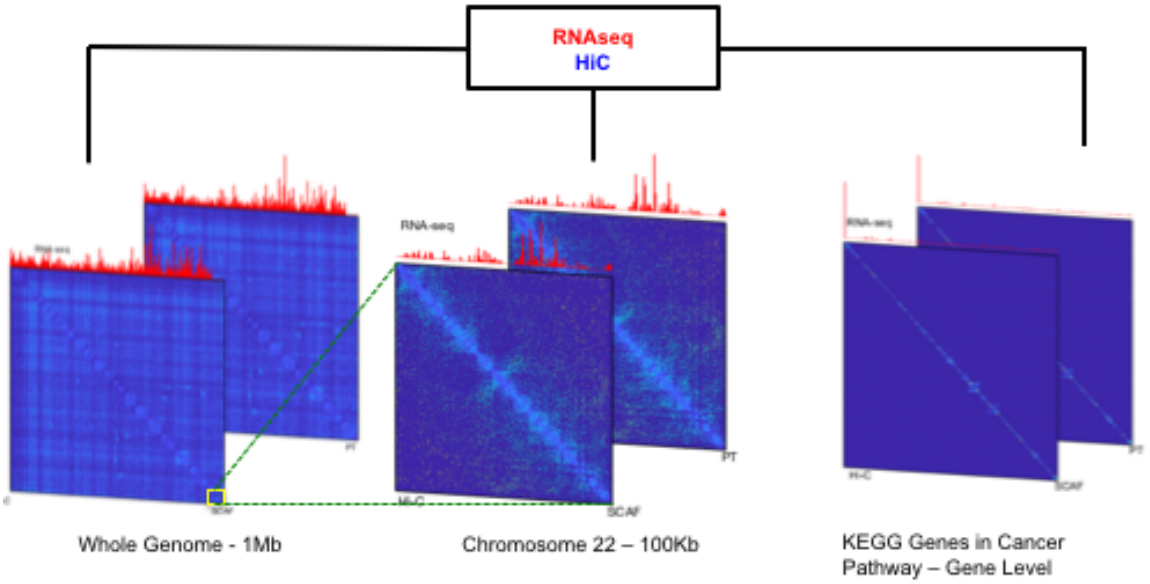

Figure 5.10: **Schematic of Hi-C and RNAseq data analysis scales**

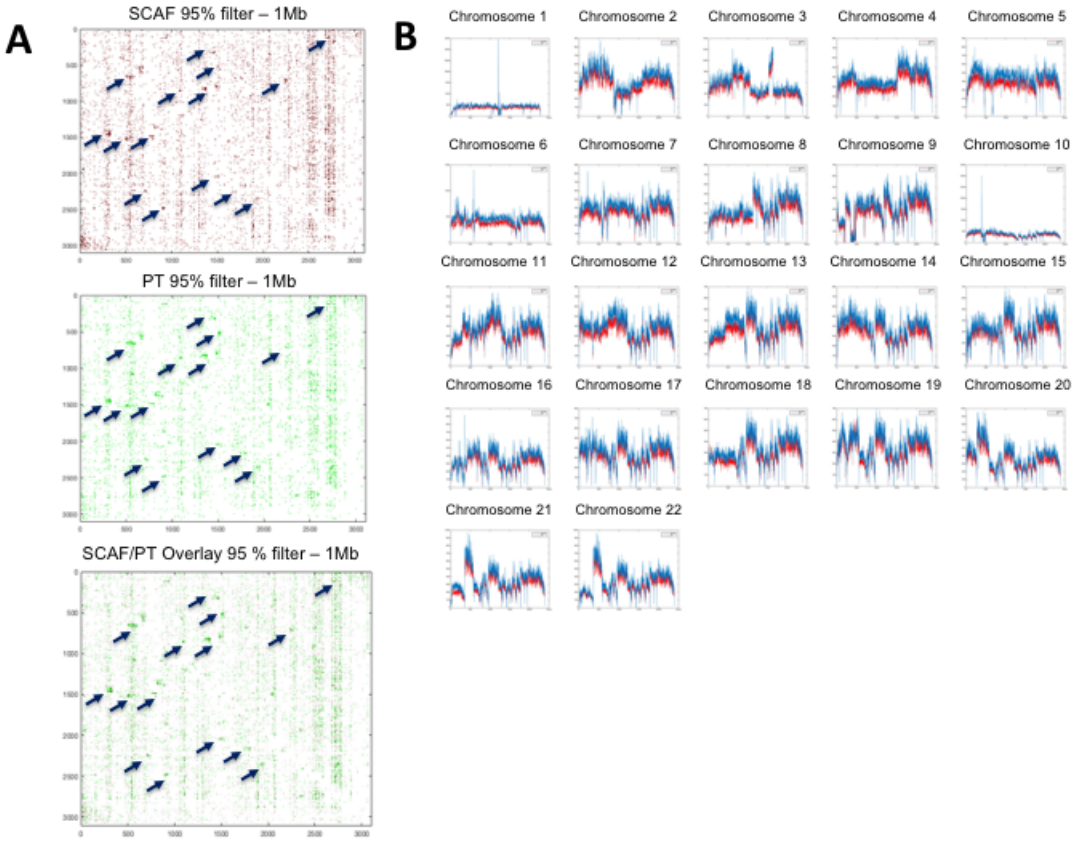

Figure 5.11: **Hi-C does not reveal additional copy number variations, translocations, or breakpoint mutations between SCAF and PT cell line.** (A) Hi-C contact matrix at 1 Mb binning with filtering to 95th percentile to show translocations with a butterfly appearance marked with arrows in both SCAF and PT and the overlay. (B) Sum of Hi-C counts for each cell line (SCAF in red, PT in blue) for each chromosome 1-22 demonstrating concordance of translocations and copy number changes between cell lines.

ID	Name
hsa04010	MAPK
hsa04012	ErbB
hsa04020	Calcium
hsa04060	Cytokine-Cytokine
hsa04062	Chemokine
hsa04066	HIF-1
hsa04068	FoxO
hsa04150	PI3-Akt
hsa04152	AMPK
hsa04154	Cell adhesion
hsa04310	Wnt
hsa04350	TGF-β
hsa04370	VEGF
hsa04510	Focal Adhesion
hsa04550	Stem Cell Pluripotentcy
hsa04668	TNF-α
hsa04710	Circadian Rhythm
hsa05200	Cancer
hsa05206	miRNAs in Cancer
hsa05224	Breast Cancer

Table 5.3: **KEGG Pathways Investigated for Structure/Function Relationships**

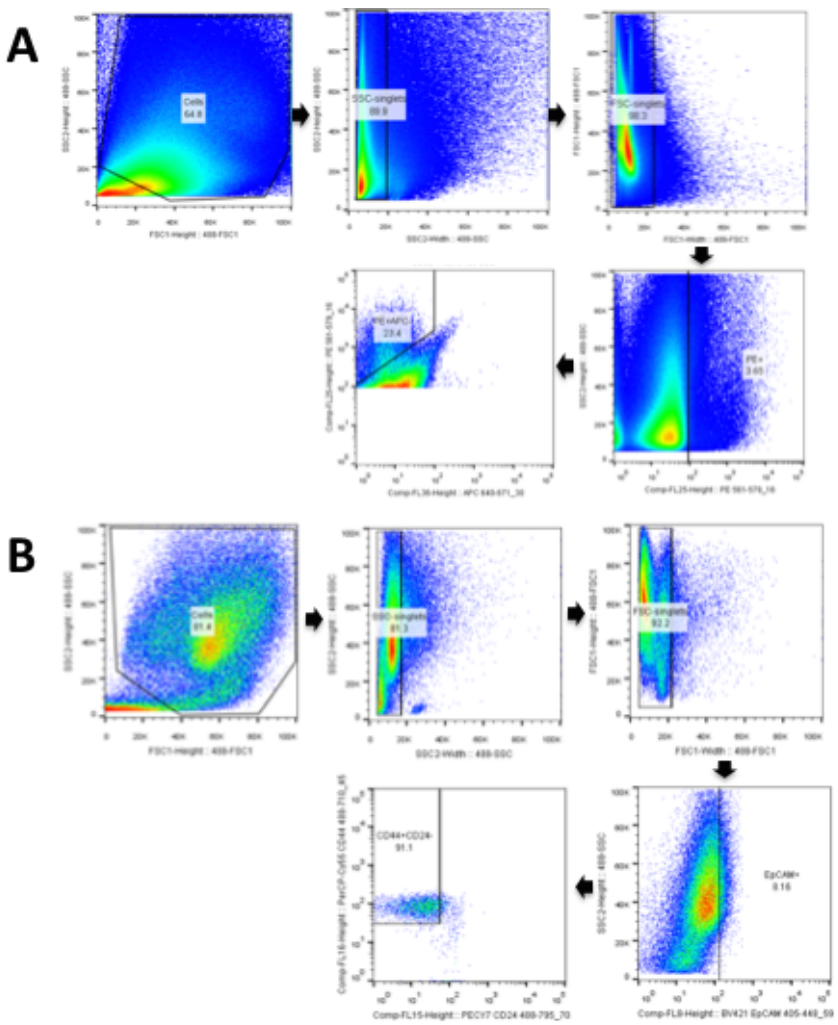

Figure 5.12: **Gating strategies for flow cytometric experiments.** (A) Gating strategy for analysis of tumor cells in tissues for *in vivo* metastasis assay showing identification of cells, singlets gated by side scatter, singlets gated by forward scatter, PE+ (tdTomato+) single positive cells, and finally PE+APC- (tdTomato+ events that are not autofluorescent in the dump channel APC). (B) Gating strategy for analysis of cancer stem cell surface markers showing identification of cells, singlets gated by side scatter, singlets gated by forward scatter, EpCAM+ cells gated as BV421+, and CD44+CD24- cells gated as PerCP-Cy5.5+PECy7-. All gates were set according to appropriate positive and negative controls and antibodies were tittered to develop assays. Each arrow indicates a nested gate where the positive population from the previous plot is represented on the subsequent plot.

CHAPTER VI

Scaffolds for early detection and therapeutic benefit in spontaneous models of tumorigenesis and metastasis

6.1 Authors

Grace G Bushnell, Ramdane Harouaka, Lidong Wang, Shreyas S Rao, Rachel M Hartfield, Yining Zhang, Robert S Oakes, Diane Simeone, Howard Crawford, Max S Wicha, Jacqueline S Jeruss, Lonnie D Shea

6.2 Abstract

The formation of distant metastasis represents the shift from a curable disease to non-curable for most patients. Currently, no clinical method is available to identify metastasis before it has affected the function of a vital organ. We have developed a biomaterial implant that recruits immune cells associated with the pre-metastatic niche and metastasis and thus recruits tumor cells *in vivo*. This platform has demonstrated promise in orthotopic mouse models of breast cancer, yet to this point has not been tested in spontaneous models of tumorigenesis and metastasis which are more representative of the progression of human disease. Here we show scaffolds recruit

tumor cells in the PyMT model of spontaneous breast cancer and the KPCY model of spontaneous pancreatic cancer. In addition to the recruitment of tumor cells, scaffold implantation also facilitated a two order of magnitude improvement in sensitivity of detection relative to blood in the KPCY model and also reduced metastatic tumor burden in the liver. Scaffolds also demonstrated tumor-progression dependent immunomodulation in both models, with the changes in immune cell populations diverging from breast cancer to pancreatic cancer. Finally, the scaffold platform also identified differential changes in immune cell crucial to recruitment of metastatic tumor cells in both models including total immune cells in PyMT and dendritic cells and macrophages in KPCY models. Collectively, our findings demonstrate the utility of scaffolds for the recruitment of tumor cells and reflection of tumor-dependent immunomodulation in spontaneous models of tumorigenesis and metastasis.

6.3 Introduction

Metastasis is responsible for 90% of cancer-related deaths [149]. The spread of tumor cells from the location of origin to secondary sites is deadly for two reasons. First, metastasis is often not detected until the function of an organ has been compromised. Second, when chemotherapeutic agents are deployed at this high state of tumor burden, resistance to these therapies often develops. Methods for the early detection of metastasis are a crucial need in order to intervene earlier at a time when tumor burden is low and provide a better opportunity for eradication of the disease.

An emerging technology for early detection of metastasis is biomaterial scaffolds that recruit metastatic tumor cells *in vivo*. Degradable microporous materials including poly(lactide-co-glycolide) and poly(ε-caprolactone) have been employed to recruit immune cells associated with the pre-metastatic niche and metastasis which in turn recruit tumor cells in orthotopic syngeneic mouse [30] and xenogeneic human [31] models of breast cancer. Similar materials have also been employed for the

recruitment of leukemic [36], prostate [27], ovarian [29], and melanoma [26] models of cancer. The utility of simple biomaterials to recruit tumor cells in a diverse array of orthotopic and subcutaneous models of metastasis indicates there are common features of the foreign body response to an implanted material and various material modifications that may be performed to enhance metastasis to an ectopic implanted site. However, to date the ability of biomaterial scaffolds to recruit tumor cells has not been investigated in any spontaneous models of tumorigenesis and metastasis.

Spontaneous models of tumorigenesis recapitulate key features of cancer disease progression as it occurs in humans far better than orthotopic or subcutaneous models [204, 205]. For example, in subcutaneous models of metastasis, tumor cells do not reside in the normal microenvironment of the organ of origin, but instead form a tumor with the help of Matrigel under the skin. This model does not represent the selective pressures that exist in the normal tumor microenvironment for a given type of cancer [206], with the exception of melanoma. In orthotopic models of metastasis, tumor cells are injected into the organ or tissue or origin but already have the ability to metastasize and thus do not replicate the processes in humans where not all tumor cells present in the primary tumor are capable of invasion, dissemination, and metastatic colonization [149, 207]. In spontaneous model of tumorigenesis the minimum number of genetic insults is provided in a tissue specific manner in order to cause tumorigenesis in this tissue. This serves in stark contrast to models where a tumor cell line that has been passaged many times *in vitro* is injected into a tissue. Tumor cell lines have many more mutations and genetic aberrations relative to human tumors, are adapted to *in vitro* culture conditions, and often represent very late stages of disease [208, 209]. While there are relatively few models of spontaneous tumorigenesis that also spontaneously metastasize, these provide a better platform for a more translational model of human tumor development and metastasis.

Though biomaterial scaffolds recruit tumor cells in mouse models of breast cancer

[30, 31, 34, 42, 152], to date no studies have investigated tumor cell recruitment to an engineered site in pancreatic cancer. Pancreatic ductal adenocarcinoma has the worst prognosis of any cancer with a 5-year survival rate of 3% [210]. Low survival is not only due to the aggressive nature of the primary tumor and impact on a vital organ, unlike breast or prostate cancer, but due to the very high likelihood of metastasis in these patients. Pancreatic cancer is often not diagnosed until metastasis has already occurred [210]. While there is a critical need to develop technologies to identify metastasis at its earliest stages for all cancers, it is clear that these technologies could have substantial impact on the diagnosis and progression of pancreatic cancer. This platform also allows investigation of the ability of biomaterial scaffolds to recruit tumor cells in cancers that metastasize to different organs (i.e. breast most commonly to the lung and pancreatic most commonly to the liver).

In this report we use the spontaneous MMTV-PyMT model of breast cancer and the spontaneous KPCY model of pancreatic cancer to investigate the ability of biomaterial scaffolds to recruit tumor cells and identify tumor dependent immunomodulation.

6.4 Results

6.4.1 Scaffolds recruit tumor cells in a spontaneous model of breast cancer

The ability of scaffolds to recruit tumor cells in a spontaneous model of breast cancer was initially assessed by implanting scaffolds subcutaneously into RFP+PyMT+ or RFP+ mice at 6 weeks of age prior to palpable tumor formation. Once tumors reached endpoint size (approximately 13-14 weeks of age) mice were euthanized and scaffolds, lungs, and primary tumors were explanted for flow cytometric analysis of RFP+ tumor cells. In order to account for varied RFP background in different tissues

present even in the RFP+ tumor-free control mice, each tissue was normalized to the tumor-free RFP+ control tissue. The highest fold change in RFP+ cells from tumor free was observed for the primary tumor tissue as expected (6.907 +/- 6.886 fold change from tumor free). Interestingly, the scaffolds had a higher fold change than lungs (1.712+/-0.8835 for scaffolds and 1.445+/-0.5179 for lungs), though not statistically significant, indicating similar metastatic tumor burden in scaffolds and lungs (**Figure 6.1A**). We next investigated the impact of scaffold implantation on disease progression relative to a mock surgery. We found scaffold implantation trended toward reduced primary tumor burden (2.304 +/- 1.36 g for scaffold implanted mice and 4.320 +/- 1.501 g for mock surgery mice) though this was not statistically significant (**Figure 6.1B**). We also found the same trend in spleen weight with PyMT- tumor free mice having the lowest spleen weight (145.3 +/- 36.50 mg), PyMT+ tumor bearing mice implanted with scaffolds had a slightly higher spleen weight (188.3 +/- 68.30 mg), and PyMT+ tumor bearing mice receiving a mock surgery having the highest spleen weight (246.3 +/- 73.55 mg) though these differences were not statistically significant (**Figure 6.1C**). Finally, we investigated the impact of scaffold implantation on metastasis and found similar levels of liver and lung tumor burden for both scaffold implanted and mock surgery mice (Liver burden 1.138 +/- 0.2269 for scaffold implanted and 1.433 +/- 0.5163 fold change from tumor free for mock surgery and Lung burden 1.104 +/- 0.2275 for scaffold implanted and 1.215 +/- 0.08842 for mock surgery, **Figure 6.1D**). Thus we conclude in this model scaffolds recruit spontaneously metastasizing tumor cells but do not significantly impact primary or metastatic tumor burden and disease progression.

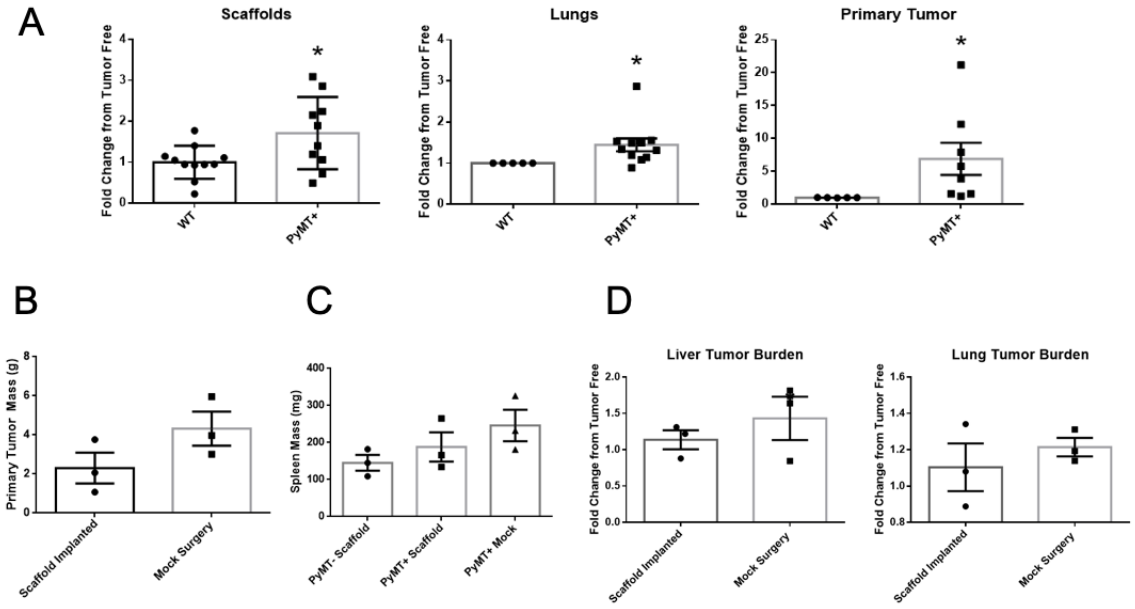

Figure 6.1: **Microporous scaffolds recruit tumor cells in the MMTV-PyMT model of transgenic, spontaneous breast cancer tumorigenesis and metastasis and do not significantly influence disease progression or metastasis.** (A) Flow cytometry evaluation of fold change of RFP+ tumor cells in scaffolds, lungs, and primary tumor in PyMT+ mice relative to WT mice. (B) Primary tumor mass for scaffold implanted mice relative to mice receiving mock surgery. (C) Spleen mass for wild-type mice implanted with scaffolds, PyMT+ mice implanted with scaffolds, and PyMT+ mice receiving mock surgery. (D) Metastatic tumor burden in the liver and lungs of mice receiving either scaffold implantation or mock surgery.

6.4.2 Scaffolds can be used to monitor the dynamic immune system changes in spontaneous breast cancer development

The dynamic immune response to the scaffold was next evaluated in the context of disease progression by evaluating the changes in immune cell populations in the lung, primary tumor, scaffold, and spleen via multicolor flow cytometry for surface markers associated with immune cells including CD45+ total immune cells, CD11b+Gr1+ neutrophils, CD11c+F4/80- dendritic cells, CD11b+F4/80+ macrophages, Ly6C+ F4/80- monocytes, CD4+ T cells, CD8+ T cells, CD19+ B cells, and CD49b+ natural killer cells (**Figure 6.2**). Each tissue is normalized to the RFP+ tumor free control in order to better view the change associated with tumor development in each tissue. We found a significant reduction in CD45+ immune cells in the primary tumor (0.138 +/- 0.08269 fold change from tumor free) and a significant increase in the lungs (2.121 +/- 1.587 fold change from tumor free, **Figure 6.2A**).We found a significant increase in CD11b+Gr1+ neutrophils in all tissues evaluated with a fold change of 4.314 +/- 2.915 for lung, 74.71 +/- 68.58 for primary tumor, 1.838 +/- 1.079 for scaffolds, and 6.463 +/- 5.139 for spleens (**Figure 6.2B**). CD11c+F4/80- dendritic cells were found to be significantly elevated in tumor bearing mice primary tumor (14.49 +/- 12.46 fold change) and scaffolds (1.372 +/- 0.8327 fold change, **Figure 6.2C**). CD11b+F4/80+ macrophages were found to be significantly increased in the primary tumor (57.76 +/- 44.74) and significantly decreased in the scaffold relative to tumor bearing mice (0.7255 +/- 0.2384 fold change, **Figure 6.2D**). Ly6C+F4/80- monocytes were found to be significantly altered in all tumor bearing tissues with a fold change of 1.346 +/- 0.2655 for lung, 0.5971 +/- 0.4341 for primary tumor, 2.032 +/- 0.8675 for scaffold, 1.712 +/- 0.7720 for spleen (**Figure 6.2E**). CD4+ T cells were found to be significantly reduced in tumor bearing lung (0.7182 +/- 0.0960 fold change) and primary tumor (0.4509 +/- 0.4446 fold change, **Figure 6.2F**). CD8+ T cells were also found to be significantly reduced in the tumor bearing lung (0.9567

+/- 0.5193 fold change) and primary tumor (0.3129 +/- 0.2804 fold change, **Figure 6.2G**). CD19+ B cells were significantly reduced in the lung with a fold change of 0.610 +/- 0.2940 relative to tumor free (**Figure 6.2H**). CD49b+ natural killer cells were not significantly altered from tumor free due to high variability in this population of immune cells (**Figure 6.2I**).

Following the identification of many immune cell populations in the scaffold being significantly altered with tumor progression (CD11b+Gr1+, CD11c+F480-, CD11b+ F480+, Ly6C+F480-) we next investigated the dynamics of immunomodulation with tumor progression by implanting multiple scaffolds in tumor free and tumor bearing mice at 5 weeks of age. Each week until the mice reached endpoint tumor size (11 weeks of age) scaffolds were explanted from the mice and a new set implanted as a survival surgery. Analysis of scaffolds explanted at each time point allowed us to track the changes of each cell population over time with disease progression (**Figure 6.3**). The majority of populations investigated varied over time but did not appear to follow a trend with disease progression including CD45+ total immune cells (**Figure 6.3A**), CD11b+Ly6C+ monocytes (**Figure 6.3C**), CD11b+F4/80+ macrophages (**Figure 6.3D**), CD11c+F4/80- dendritic cells (**Figure 6.3E**), CD4+ T cells (**Figure 6.3F**), CD8+ T cells (**Figure 6.3G**), and CD49b+ natural killer cells (**Figure 6.3I**). However, some populations clearly tracked with tumor progression including CD11b+Gr1+ neutrophils steadily increasing with tumor progression (**Figure 6.3B**) and CD19+ B cells decreasing with tumor progression (**Figure 6.3H**). We also evaluated the presence of tumor cells at each of these time points and found this population to be relatively stable over time (**Figure 6.3J**).

Following the determination of immune dynamics at the scaffold longitudinally in the same cohort of mice, we next sought to understand how these dynamics compare to the changes in immune cell populations occurring in the spleen, lung, and primary tumor with disease progression. To this end we isolated tissues at various ages close

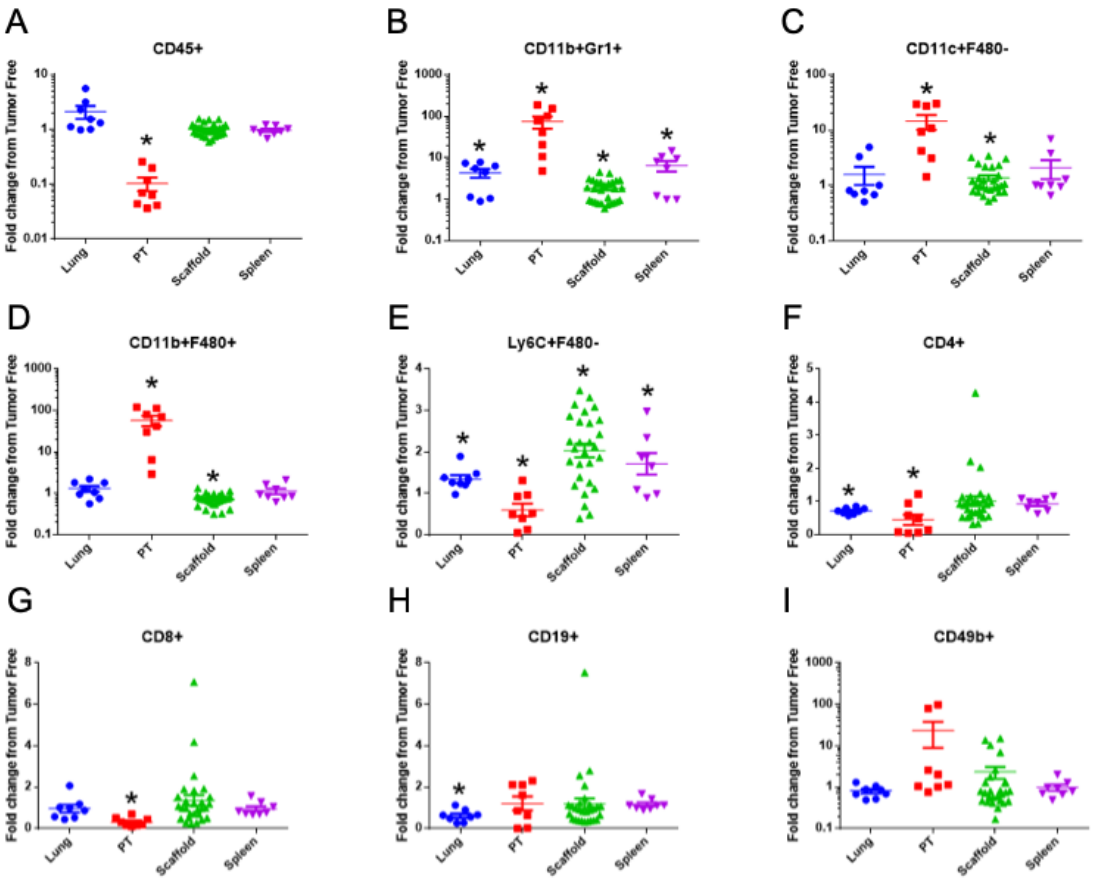

Figure 6.2: **Breast tumor-dependent immunomodulation occurs at the scaffold site and is similar to modulation observed in the spleens of PyMT+ mice.** Flow cytometric evaluation of surface markers for immune cells and reported as fold change in % of each population from tumor free (WT, PyMT- mice) relative to tumor bearing (PyMT+ mice) for lung, primary tumor (PT), scaffold, and spleen for (A) CD45+ (B) CD11b+Gr1+ (C) CD11c+F480- (D) CD11b+F480+ (E) Ly6C+F480- (F) CD4+ (G) CD8+ (H) CD19+ and (I) CD49b+ immune cells.

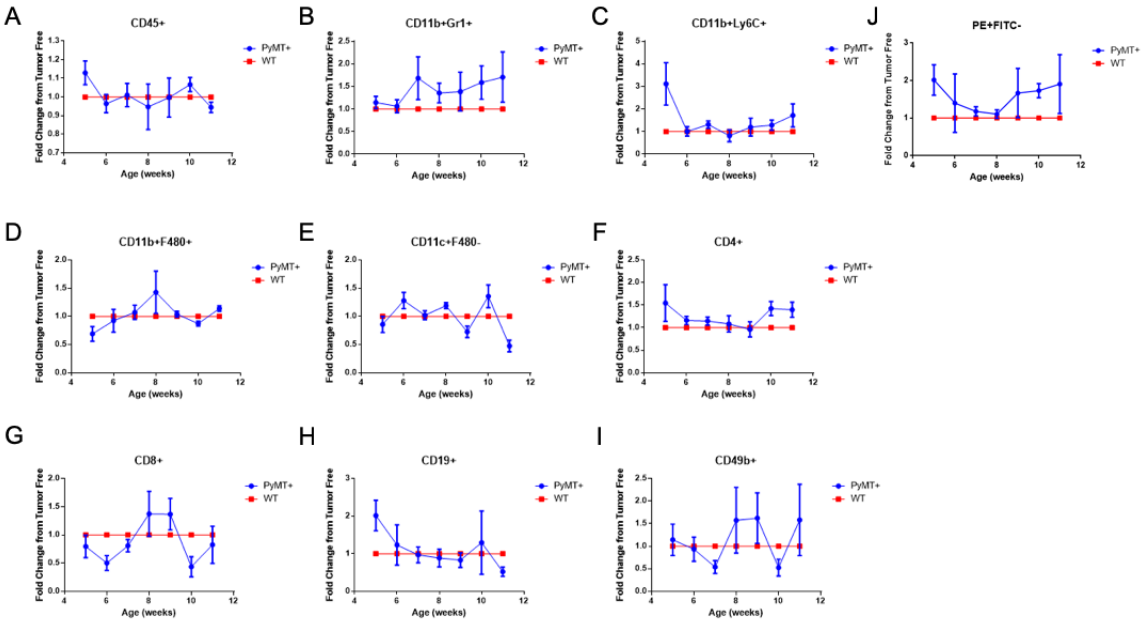

Figure 6.3: **Breast tumor-dependent immunomodulation and tumor cell recruitment to the scaffold can be monitored longitudinally in a single cohort of mice.** Flow cytometric evaluation of surface markers for immune cells and reported as fold change in % of each population from tumor free (WT, PyMT- mice) relative to tumor bearing (PyMT+ mice) for scaffolds for (A) CD45+ (B) CD11b+Gr1+ (C) CD11c+F480- (D) CD11b+F480+ (E) Ly6C+F480- (F) CD4+ (G) CD8+ (H) CD19+ and (I) CD49b+ immune cells and (J) PE+FITC- Tumor cells to observe dynamics of immune cell populations over time with tumor progression.

to tumor-size endpoint (12-14 weeks of age) and investigated changes in immune cell populations in each tissue with time (**Figure 6.4**). Linear regression analysis was performed on each tissue over time and those with significant linear relationships were assessed. We found the scaffold demonstrates a significant positive linear relationship with time for CD45+ (**Figure 6.4A**) and CD11b+Gr1+ cells (**Figure 6.4B**) with a trend similar to that of the lung. Significant negative linear relationships were found in the scaffold for CD11c+F4/80- dendritic cells (**Figure 6.4C**) and CD4+ T cells (**Figure 6.4F**). The trends observed over time in general agree between the scaffold, spleen, and lung with the only exception being CD8+ T cells (**Figure 6.4G**).

6.4.3 Scaffolds enrich tumor cells relative to blood and reduce metastatic tumor burden in spontaneous pancreatic cancer

The ability of scaffolds to recruit tumor cells in a spontaneous model of pancreatic cancer was next assessed by implanting scaffolds subcutaneously into KPCY or CY mice at 8 weeks of age prior to tumor formation. We first assessed a very early timepoint in tumor progression and isolated scaffolds, blood, liver, and pancreas at 12 weeks of age (**Figure 6.5**). We first evaluated metastasis to the scaffold implant by quantifying the number of YFP+ cells in each scaffold. We found 309 +/- 304 YFP+ pancreatic cells per scaffold and found that the number of tumor cells per scaffold appeared to be associated with the stage of the tumor (**Figure 6.5A**) with scaffolds from a mouse with PanIN1 and PanIN2 lesions having an average of 699 YFP+ cells/scaffold relative to mice with ADM and PanIN1 lesions demonstrating an average of 114 YFP+ cells/scaffold. We next investigated whether the number of YFP+ cells found in the scaffold could be explained by the concentration of these cells in the blood and found a two order of magnitude enrichment of YFP+ cells in scaffolds relative to blood (**Figure 6.5B**). We next investigated if scaffold implantation relative to mock surgery altered the progression of disease by quantifying YFP+ cells in the

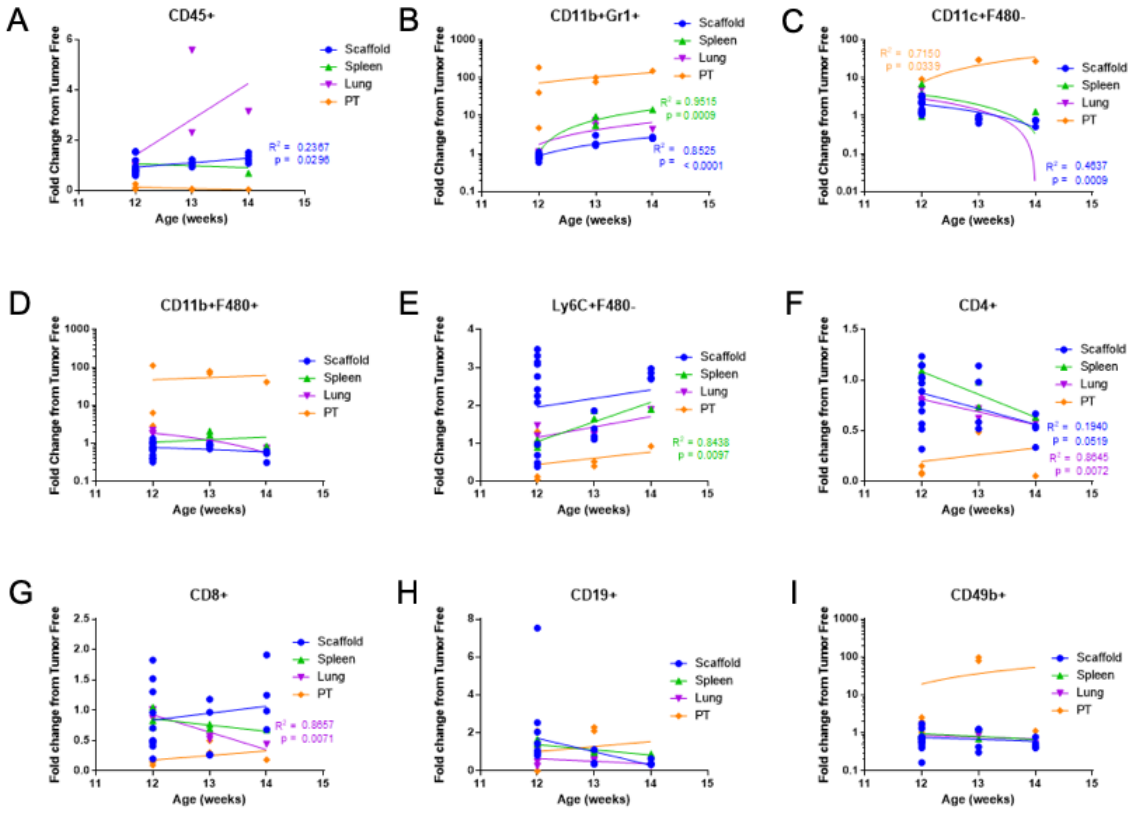

Figure 6.4: **Breast tumor-dependent immunomodulation demonstrates similar dynamics in spleen, scaffold, and lung with tumor progression.** Changes in immune cell populations were evaluated at various stages in tumor progression within scaffolds spleen, lung, and primary tumor via flow cytometry for (A) CD45+ (B) CD11b+Gr1+ (C) CD11c+F480- (D) CD11b+F480+ (E) Ly6C+F480- (F) CD4+ (G) CD8+ (H) CD19+ and (I) CD49b+ immune cells. Linear regression analysis was performed for each tissue with cell populations having a significant ($p<0.05$ for linear regression) linear relationship with age and thus tumor progression reported in the matching color for the tissue.

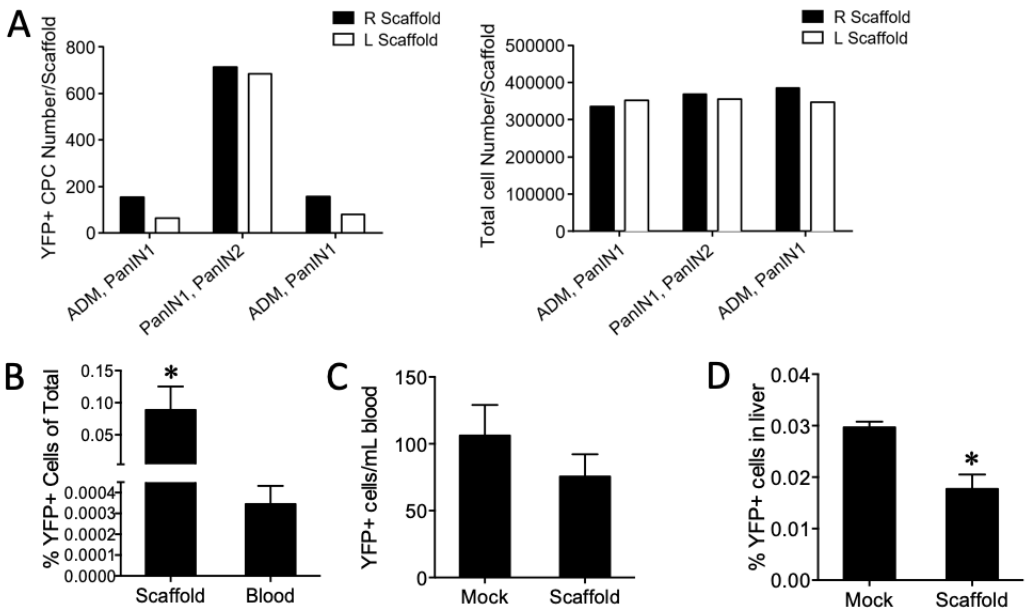

Figure 6.5: **Scaffolds recruit tumor cells in KPCY model of pancreatic cancer, enrich tumor cell concentration relative to blood, and reduce metastatic tumor burden in the liver relative to mock surgery.** (A) Scaffolds capture tumor cells corresponding to tumor histopathological grade as evaluated by quantification of YFP+ cells via flow cytometry relative to the total number of cells per scaffold. (B) Scaffolds significantly enrich tumor cells relative to blood as evaluated via flow cytometry for percentage of YFP+ cells in scaffolds relative to blood. (C) Scaffolds trend toward reduced metastatic tumor burden in blood and (D) significantly reduce ($p<0.05$) tumor burden in the liver relative to a mock surgery.

blood (**Figure 6.5C**) and liver (**Figure 6.5D**). We found no statistical difference between the number of YFP+ cells in the blood of mock mice relative to scaffold implanted mice, however we did find a statistically significant reduction in YFP+ cells present in the liver of mice that receive scaffolds relative to a mock surgery (0.030 +/- 0.005 % YFP+ for mock surgery mice and 0.017 +/- .004 % YFP+ for scaffold implanted mice).

6.4.4 Scaffolds can be used to monitor the dynamic immune system changes as a result of spontaneous pancreatic cancer

As in the PyMT model, we next evaluated the dynamic immune response to the scaffold in the context of disease progression by evaluating the changes in immune cell populations in the liver, pancreas, scaffold, and spleen (**Figure 6.6**). We found significant increase in the proportion of CD45+ cells present in pancreas (7.861 +/- 2.668 fold change from tumor-free CY) and a significant decrease in CD45+ cells in the spleen (0.7513 +/- .1227 fold change from tumor free, **Figure 6.6A**). We also found a significant increase in CD11b+Gr1+ neutrophils in scaffolds (1.370 +/- 0.5013) and spleens (4.355 +/- 3.429) of tumor bearing mice relative to tumor free (**Figure 6.6B**). We observed a significant increase in CD11c+F4/80- dendritic cells in the pancreas (**Figure 6.6C**, 4.605 +/- 3.609), a significant decrease in CD11b+F4/80+ macrophages in the liver (**Figure 6.6D**, 0.6274 +/- 0.2325), a significant increase in Ly6C+F4/80- monocytes in the spleen (**Figure 6.6E**, 1.185 +/- 0.8896), and finally a significant decrease in CD4+ T cells in the liver (**Figure 6.6F**, 0.4941 +/- 0.3145). For all cell types, scaffolds and spleens tended to demonstrate the same trend from tumor-free CY mice.

We next sought to investigate the ability of scaffolds to dynamically indicate disease progression. To this end, we used CD45+ cells present in the pancreas as a surrogate for age, as this was significantly linearly associated with age (p=0.0031) and gave better discrimination between mice that we the same age but at different stages of tumor progression (**Figure 6.7A**). We then used the burden of CD45+ cells in the pancreas as a surrogate for disease progression and performed linear regressions of each cell type present in each tissue against this independent variable. We found YFP+CD45- cells also increased linearly with age in scaffolds, though this was not significant (**Figure 6.7B**). We found CD11b+Gr1+ did not vary with disease progression in this model (**Figure 6.7C**), though they were elevated relative

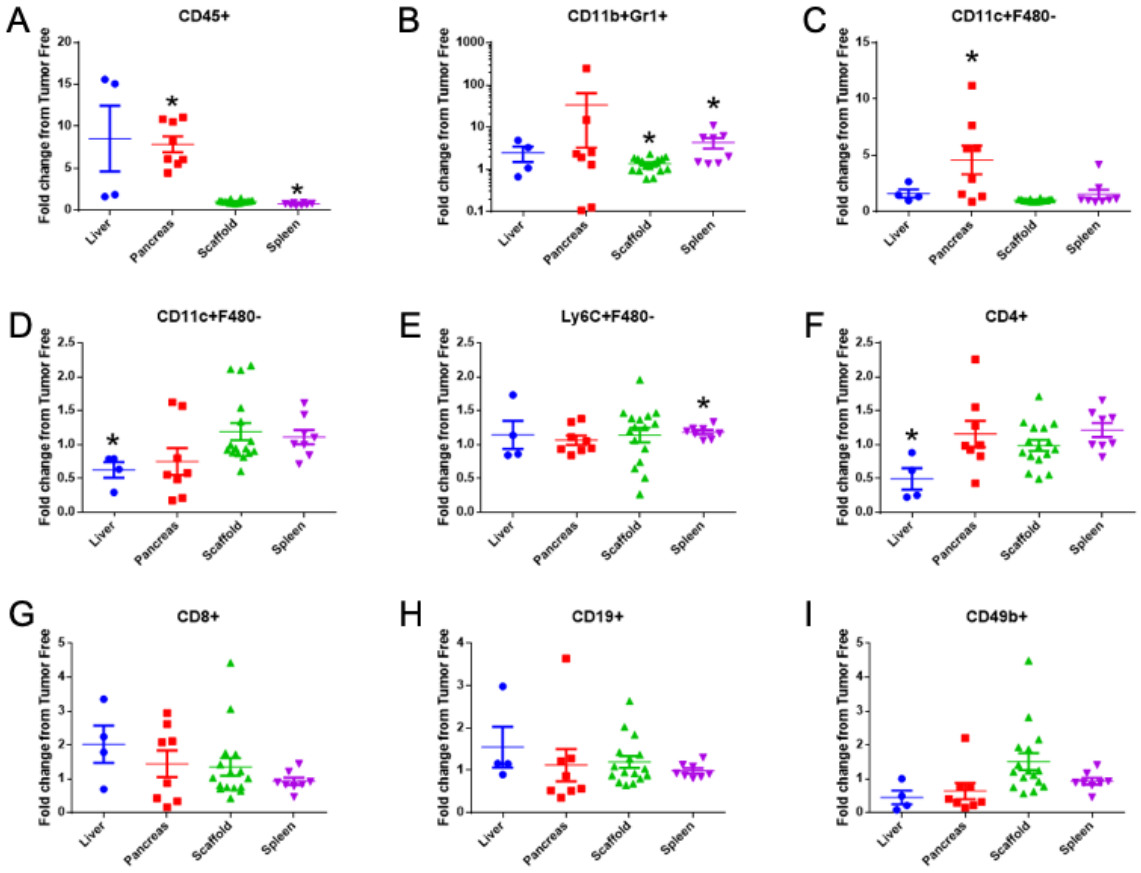

Figure 6.6: **Pancreatic tumor-dependent immunomodulation occurs at the scaffold site and is similar to modulation observed in the spleens of KPCY mice.** Flow cytometric evaluation of surface markers for immune cells and reported as fold change in % of each population from tumor free (CY mice) relative to tumor bearing (KPCY mice) for lung, pancreas, scaffold, and spleen for (A) CD45+ (B) CD11b+Gr1+ (C) CD11c+F480- (D) CD11b+F480+ (E) Ly6C+F480- (F) CD4+ (G) CD8+ (H) CD19+ and (I) CD49b+ immune cells.

to tumor free at all timepoints investigated. However, F4/80+ macrophages (**Figure 6.7D**), Ly6C+ monocytes (**Figure 6.7E**), CD4+ T cells (**Figure 6.7F**), CD8+ T cells (**Figure 6.7G**), CD19+ B cells (**Figure 6.7H**), and CD49b+ natural killer cells (**Figure 6.7I**) all had a significant linear relationship with disease progression. Interestingly innate immune cell populations including macrophages and monocytes decreased with disease progression while adaptive cell populations including CD4+ and CD8+ T cells, B cells, and natural killer cells all increased at the scaffold with disease progression. Additionally, the scaffold and the spleen demonstrated similar slopes with linear regression with the exception of CD19+ B cells (**Figure 6.7H**).

6.4.5 Scaffold immune signatures can distinguish between breast and pancreatic cancer conditioning and identify key immune players associated with tumor cell recruitment

Finally, we investigated whether immune signatures from scaffolds could distinguish between breast and pancreatic cancer dependent immunomodulation. To this end we first performed unsupervised hierarchical clustering for each scaffold sample immune populations (CD45+ total immune cells, CD11b+Gr1+ neutrophils, CD11b+F480+ macrophages, CD11c+F480- dendritic cells, CD11b+Ly6C+ monocytes, CD4+ T cells, CD8+ T cells, CD19+ B cells, and CD49b+ natural killer cells, **Figure 6.8A**). Using this approach most RFP+PyMT+ samples cluster on the left and most KPCY cluster on the right. However, 5 KPCY samples cluster on the left with the PyMT samples. Interestingly, these all appear to have high levels of Ly6C+F4/80- monocytes relative to other samples. KPCY samples on the right cluster appear to be differentiated primarily by their high levels of adaptive cell populations relative to other samples, including CD49b+ natural killer cells, CD19+ B cells, and CD4+ and CD8+ T cells. As hierarchical clustering was unable to separate PyMT from KPCY clearly, we next performed principal component analysis (PCA)

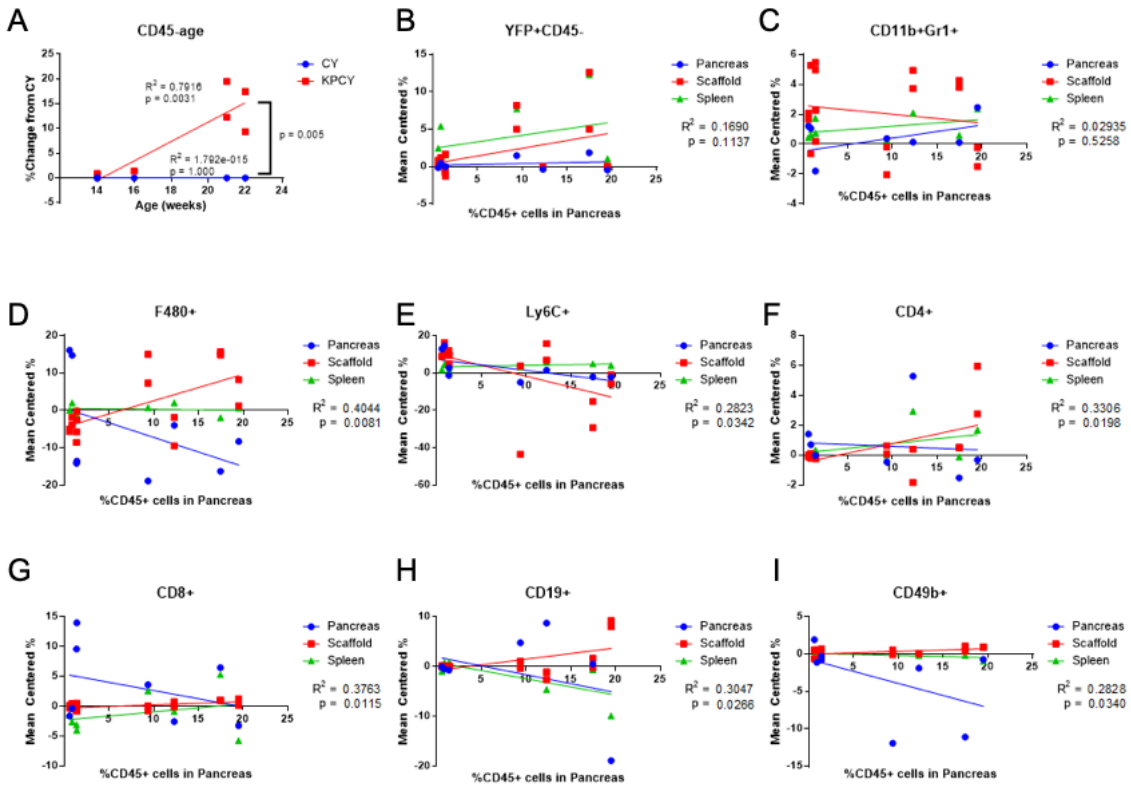

Figure 6.7: **Pancreatic tumor-dependent immunomodulation demonstrates dynamic response with tumor progression.** Changes in immune cell populations were evaluated at various stages in tumor progression within scaffolds spleen and pancreas via flow cytometry. First, the progression of CD45+ cell burden in the pancreas was confirmed by its significant linear relationship with age in (A). Then the % change in CD45+ cell burden was used as a surrogate for tumor progression and dependent variable against (B) YFP+CD45- tumor cells, (C) CD11b+Gr1+, (D) F480+, (E) Ly6C+, (F) CD4+, (G) CD8+, (H) CD19+, and (I) CD49b+ cells. Linear regression analysis was performed for each tissue, only scaffolds were found to have significant linear relationships with tumor progression and R2 and p-value of the linear regression for scaffolds are reported on each plot.

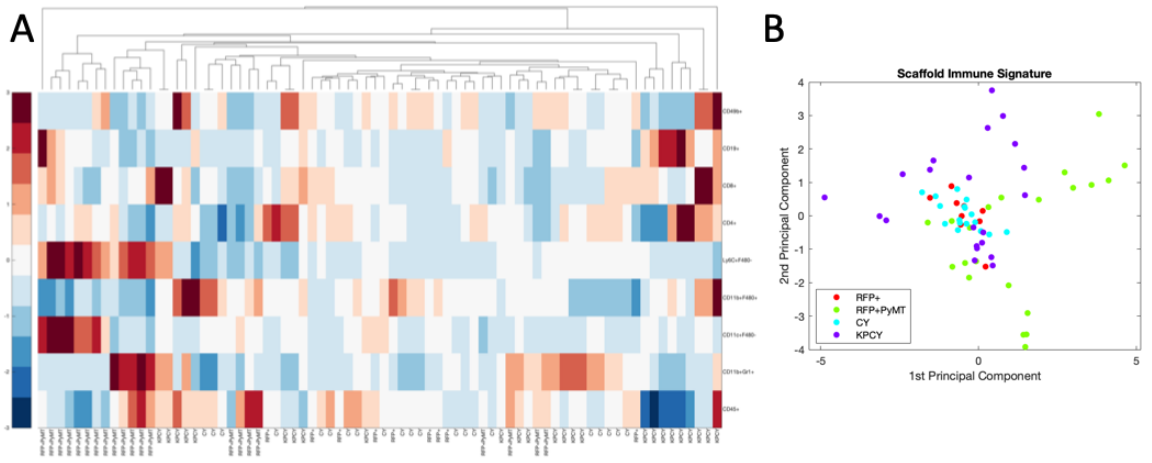

Figure 6.8: **Scaffold immune signature can distinguish breast tumor bearing mice (RFP+PyMT+) from pancreatic tumor bearing mice (KPCY).** (A) Unsupervised hierarchical clustering of scaffold immune signatures from flow cytometry from CY, KPCY, RFP+, and RFP+PyMT+ mice. (B) These scaffold immune signatures from flow cytometry data were fed into principal component analysis and demonstrate separation of RFP+PyMT+ scaffolds from KPCY scaffolds.

and plotted the scores in the first two principal components for each sample (**Figure 6.8B**). PCA more successfully discriminated samples based on the multivariate nature of the immune signature as demonstrated by most KPCY samples diverging to the upper left quadrant while PyMT samples diverge to the bottom right quadrant.

Next, we investigated the role of immune cell populations and their association with tumor cell recruitment in both the PyMT breast cancer model (**Figure 6.9A**) and the KPCY pancreatic cancer model (**Figure 6.9B**). To this end we first performed correlation analysis of immune cell populations and tumor cell recruitment showing a heatmap of the Pearson correlation coefficient for each immune cell population and tumor cells. A number of positive correlations were found between immune cell populations for PyMT including CD4+ and Ly6C+ cells (0.6667), CD8+ and CD49b+ cells (0.712), and total CD45+ and CD4+ (0.6066) and CD45+. Negative correlations were also found between populations including F480+ and Ly6C+ (-0.5535), F480+ and CD19+ cells (-0.5426), and CD4+ and CD8+ T cells (-0.5039).

Next, stepwise multiple linear regression analysis was performed to build a model that explains the contribution of immune cells to tumor cell recruitment. For PyMT scaffolds, this approach found that the total number of CD45+ cells was positively associated with recruitment (coefficient 3.089 +/- 0.937 and p = 0.004), CD8+ cells are negatively associated with recruitment (coefficient -0.563 +/- 0.280 and p = 0.058), and CD49b+ cells are positively associated with recruitment (coefficient 0.596 +/- 0.208 and p = 0.010). The model R2 however, was relatively low 46.72%, indicating that there is variability in tumor cell recruitment that cannot be explained by the immune cell composition of the scaffold. Applying the same approach to KPCY we found a number of positive associations between immune cell populations including CD45+ and F480+ cells (0.6351), CD45+ and CD49b+ cells (0.6338), CD11b+Gr1+ and Ly6C+ cells (0.5378), F480+ and CD19+ cells (0.5095), F480+ and CD49b+ cells (0.6127), and CD4+ and CD49b+ cells (0.5691). Additionally, some negative associations between immune cell types were identified including F480+ and Ly6C+ cells (-0.8029), Ly6C+ and CD4+ cells (-0.6081), and Ly6C+ and CD19+ cells (-0.5895). Next, stepwise multiple linear regression analysis identified populations significantly contributing to a model of tumor cell recruitment. This approach identified CD11c+ dendritic cells to be positively associated with recruitment (coefficient 2.674 +/- 0.885 and p = 0.012), F480+ macrophages to be positively associated with recruitment (coefficient 1.336 +/- 0.176 and p <0.001), CD8+ T cells to be negatively associated with recruitment (coefficient - 0.1264 +/- 0.0776 and p = 0.132), and CD49b+ natural killer cells to be positively associated with recruitment (coefficient 0.6260 +/- 0.0917 and p <0.001).

6.5 Discussion

In this study poly(ε-caprolactone) biomaterial scaffolds were investigated for their ability to recruit tumor cells in two spontaneous models of tumorigenesis and metas-

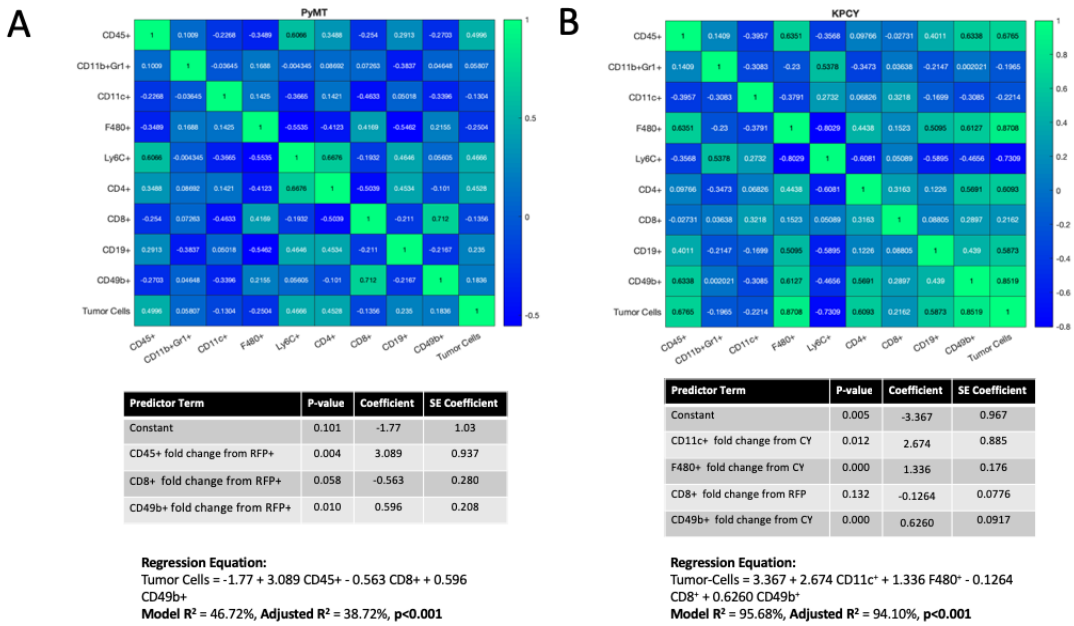

Figure 6.9: **Scaffold immune signatures can identify key immune players in tumor cell recruitment to biomaterial scaffolds in models of breast and pancreatic cancer.** Correlation analysis of immune cell populations and tumor cell recruitment showing heatmap of Pearson correlation coefficient values for each immune cell population and tumor cells and stepwise multiple linear regression of these immune signatures with tumor cells as a response and changes in immune cell populations as predictors identifying terms significantly contributing to tumor cell recruitment in (A) PyMT breast cancer model and (B) KPCY pancreatic cancer model.

tasis for breast and pancreatic cancer. This work was motivated by the idea that implanted biomaterials have been found to recruit tumor cells in many diverse orthotopic models of metastasis, however their function in spontaneous models of metastasis has never been reported. The ability of scaffolds to recruit tumor cells in these models is crucial for an indication that this technology may be applicable in human patients, as orthotopic models of metastasis do not represent the timeline or cascade of events that must occur in a human patient for a tumor to develop and metastasis to occur.

Indeed, we found biomaterial scaffolds recruit tumor cells in spontaneous breast cancer and pancreatic cancer. In the PyMT model of breast cancer we found that at endpoint tumor size (12-14 weeks of age) scaffolds on average had more tumor cells than the lungs, the primary site of metastasis in this model. Additionally, by longitudinal analysis of the same cohort of mice, we found tumor cells were detectable as early as 5 weeks of age in these mice, indicating we recruit early metastatic tumor cells similar to the finding of disseminated tumor cells in the bone marrow in these models [211]. Interestingly, we observed dynamics of RFP+PyMT+ tumor cells within the scaffold in the same cohort of mice, with tumor cells being significantly elevated at 5 weeks of age, demonstrating a reduction in number from 6-8 weeks of age, and returning to significantly elevated levels from 10-11 weeks of age. These dynamics somewhat mirror the elevation of CD8+ T cells and CD49b+ natural killer cells at these timepoints and thus may be a result of enhanced adaptive immunity clearing early metastatic cells at these timepoints [212]. We also observed early dissemination of tumor cells in the KPCY model of pancreatic cancer. At stages prior to full pancreatic ductal adenocarcinoma, we observed YFP+ pancreatic cells in the scaffold, blood, and liver of KPCY mice, similar to findings reported in the literature [213]. Importantly, we found the scaffold enriched these YFP+ cells two order of magnitude relative to the blood. This indicates that tumor cells are not simply

non-specifically collected within the scaffold as a result of their presence in the blood, but also demonstrates that the scaffold platform provides a significant advantage over the detection of circulating tumor cells [214, 215].

Interestingly, we found in a trend toward reduced primary tumor burden in the PyMT model, however this was not statistically significant. Additionally, this did not seem to translate into a reduction in metastatic tumor burden in scaffold implanted mice relative to mock surgery mice. However, in the KPCY model we found a scaffold implantation provided a significant reduction in YFP+ cells in the liver of scaffold implanted mice relative to those receiving a mock surgery. This was accompanied by a trend towards reduced numbers of circulating YFP+ cells in the blood of scaffold implanted mice relative to mock mice, however this was not statistically significant. These differences between models in ability to impact metastatic burden may be attributed to the high level of variability between individual mice obscuring some effects in the PyMT model relative to the KPCY model.

Importantly, we found the scaffold demonstrated tumor-progression dependent immunomodulation in both models of breast and pancreatic cancer. In both cases, the alterations in the scaffold immune microenvironment most closely followed the immune changes observed in the spleen. This finding is similar to our findings in orthotopic models of breast cancer [30, 31] and likely represents changes in the systemic availability of immune cells in the blood, and thus a change in the immune cells responding to the biomaterial as part of the foreign body response. In the PyMT model we found an increase in CD11b+Gr1+ neutrophils, CD11c+F480+ dendritic cells, Ly6C+F480- monocytes, and a decrease in CD11b+F480+ macrophages in tumor bearing mice relative to tumor free. In the KPCY model we found a similar increase in CD11b+Gr1+ neutrophils in tumor bearing mice relative to tumor free. Interestingly, the dynamics of immune cell populations with tumor progression were quite different between the two models. In the PyMT model we found an increase

in CD45+ cells and neutrophils and a decrease in dendritic cells and CD4+ T cells. In the KPCY model we found a decrease in macrophages and monocytes and an increase in CD4+ and CD8+ T cells, CD19+ B cells and CD49b+ natural killer cells with tumor progression. These trends observed in the scaffold track with the changes observed in the spleen with tumor progression for all cell types with the exception of CD8+ T cells in the PyMT model and CD19+ B cells in the KPCY model. This highlights the ability of the scaffold to largely reflect systemic immune changes, but also reflect changes occurring in the primary tumor and metastatic sites as the increase in CD8+ T cells in PyMT is concordant with the trend in the primary tumor. After observing different trends with primary tumor progression in both models we next asked if the immune signature within the scaffold alone was enough to distinguish between mice bearing breast and pancreatic cancer. Unsupervised hierarchical clustering identified some separation between PyMT and KPCY samples. However, principal component analysis was better able to identify divergence of immune cell populations between PyMT and KPCY. This finding highlights the ability of a biomaterial scaffold to not only recruit tumor cells but serve as a sentinel for different mechanisms of immunomodulation.

We also sought to understand if the scaffold could provide insights into positive and negative regulators of tumor cell recruitment in two very different models of metastasis. To this end we performed multiple linear regression of immune cell populations as predictors and tumor cell recruitment as the independent variable. In the PyMT model we found CD45+, CD8+, and CD49b+ cells to be significantly associated with recruitment of tumor cells with CD45+ cells and CD49b+ cells as positive regulators of recruitment and CD8+ cells as negative regulators of tumor cell recruitment. Similarly, in the KPCY model we found CD8+ cells to be negatively associated with recruitment and CD49b+ cells to be positively associated with recruitment. However, in contrast with the PyMT model, CD45+ cells were not associated

with recruitment while CD11c+ and F480+ cells were both positively associated with tumor cell recruitment. Interestingly, the model of tumor cell recruitment for KPCY had a much higher adjusted-R2 (94.10% relative to 38.72% for PyMT) indicating there may be other cell populations or microenvironmental factors contributing to tumor cell recruitment in the PyMT model that cannot be explained simply by the changes in immune cell populations within the scaffold. The finding that CD49b+ cells are positively associated with tumor cell recruitment to the scaffold is surprising as natural killer cells are capable of controlling metastasis by eliminating metastatic tumor cells [216–218]. However, it is possible that a greater population of natural killer cells is associated with a larger pool of metastatic tumor cells in response to an attempt to eliminate these cells. It is also possible that an increase in natural killer cells may be associated with NK cell exhaustion and thus reduced tumor cell killing [219].

For the first time, these results report the recruitment of tumor cells in spontaneous models of tumorigenesis and metastasis and the first evidence that this platform recruits metastatic pancreatic tumor cells. Additionally, this work supports the use of biomaterial scaffolds for monitoring the dynamic immune response as a result of primary tumor development and metastasis. Importantly, we also show the first evidence that the immune response to biomaterial scaffolds differs in the context of different cancer models. The scaffold platform technology represents a unique opportunity to recruit tumor cells and reflect tumor dependent immunomodulation in diverse models of metastasis. Thus this platform provides unprecedented opportunity for the early detection of metastasis.

6.6 Materials and Methods

6.6.1 Transgenic animal models

Animal studies were performed in accordance with institutional guidelines and protocols approved by the University of Michigan Institutional Animal Care and Use Committee (IACUC). MMTV-PyMT-RFP (PyMT+RFP+) mice and their respective tumor free control MMTV-RFP (RFP+) as well as KPCY mice (Pdx1-Cre KrasG12D p53fl/+ RosaYFP) and CY (Pdx1-Cre RosaYFP) mice were bred in house. Scaffold implantation was performed between 5-8 weeks of age in these mice, prior to tumor formation. For both models, mice were monitored a minimum of three times a week for the duration of experiments for evidence of tumor-related morbidity. Mice were sacrificed when tumors reached endpoint size as defined by the animal use protocol (PRO00007801) or exhibited limited physical activity.

6.6.2 Scaffold fabrication and implantation

Microsphere preparation. PCL microspheres were prepared as previously described (ref). Briefly, microspheres were prepared by emulsification of a 6% (w/w) solution of PCL (Lactel Absorbable Polymers; Inherent viscosity 0.65-0.85 dL/g) in dichloromethane in a 10% (w/v) poly(vinyl alcohol) solution followed by homogenization at 10,000 rpm for 1 minute. The solution was then stirred for 3 hours to evaporate dichloromethane solvent. Microspheres were then collected by centrifugation at 2000 x g for 10 minutes and washed at least five times in deionized water. Finally, microspheres were lyophilized for 48 hours.

Scaffold fabrication. Microporous PCL scaffolds were prepared by mixing PCL microspheres and sodium chloride crystals (250-425 m in diameter) at a 1:30 (w/w) ratio. This salt and polymer microsphere mixture was then pressed in a steel die for 45 seconds at 1500 PSI. Polymer/salt disks were then heated at 60C for 5 minutes

per side to melt polymer microparticles around salt crystals to form a continuous structure. Salt crystals were subsequently removed by immersion in water for 1.5 hours. Scaffolds were then sanitized for animal studies using 70% ethanol, rinsed with sterile water, and dried on a sterile surface.

Scaffold implantation. Scaffolds were implanted into the subcutaneous space of 8-week-old female NOD/SCID-IL2Rγ-/- (NSG) or balb/c mice as previously described (ref). For the implantation procedure, animals were anesthetized via isoflurane (2%, inhaled), prepared with Carprofen analgesia (5 mg/kg, subcutaneous injection), the upper back was shaved and prepped using a Betadine swab followed by an ethanol swab and this procedure was repeated 3 times. A fenestrated sterile field was draped over the surgical area and a 1 cm incision was made in the upper back. Following incision, subcutaneous pockets were created perpendicular to the incision, into which sanitized scaffolds were inserted (2 scaffolds/mouse). The skin was then closed using sterile wound clips (Reflex 7 mm, Roboz Surgical Instrument Co).

Longitudinal scaffold explant and reimplantation. For longitudinal tracking of one cohort of mice over time, 2 scaffolds were explanted from each mouse once a week. Mice were anesthetized as described above and shaved directly over the scaffold implant site. The surgical site was prepared as described and a 5-10 mm incision was made between the two implanted scaffolds. Both scaffolds were explanted and a fresh pair of scaffolds was implanted into the same location. The incision was closed with 4-0 vicryl resorbable sutures (Ethicon).

6.6.3 Statistical and Computational Analysis

Statistical Analysis. All statistical tests were performed in Prism version 6.0.1. All graphs are reported as mean with standard error of the mean unless otherwise stated. Linear regressions were performed in Prism. All statistical tests were performed as a two sided T test with unequal variances unless otherwise stated after checking for

normality of data distribution.

Hierarchical clustering and principal component analysis. Unsupervised hierarchical clustering was performed in MATLAB 2018a with normalization across rows and clustering across columns. Principal component analysis was performed in MATLAB 2018a.

Multiple Linear Regression Analysis. Stepwise multiple linear regression analysis was performed in Minitab version 18 with alpha = 0.15 to add or remove terms.

6.6.4 Flow Cytometry

Scaffolds were minced, digested using Liberase TL (Roche) and strained through a 70 m filter to produce a single cell suspension. Cells were pelleted via centrifugation at 500 x g for 5 min. Following isolation of a single cell suspension, cells were blocked using anti-CD16/32 (Biolegend) and stained with anti-mouse CD45 AF700 (Biolegend), CD11b V500, F4/80 PECy7, Gr1 PacBlue, Ly6C FITC for PyMT and Ly6C PE for KPCY, and CD11c APC for innate panel. For adaptive panel samples were stained with anti-mouse CD45 AF700, CD4 V500, CD8 FITC for PyMT and CD8 PE for KPCY, CD19 PacBlue, and CD49b PECy7. Samples were run on MoFlo Astrios Flow Cytometer (Beckman Coulter) and data processed using FlowJo (TreeStar Inc.).

CHAPTER VII

Non-invasive ultrasound imaging for early detection

7.1 Authors

Grace G Bushnell*, Xiaowei Hong*, Shreyas S Rao, Rachel M Hartfield, Yining Zhang, Robert S Oakes, Jacqueline S Jeruss, Cheri X Deng, Lonnie D Shea *these authors contributed equally to this work

7.2 Abstract

For most cancers, the formation of distant metastasis is the point at which clinical treatment shifts from curative intent to palliative care. We have developed a biomaterial implant that acts as a synthetic pre-metastatic niche and recruits metastatic cancer cells in xenogeneic human and syngeneic mouse models of breast cancer. Here, we investigate ultrasound as a non-invasive strategy for detecting metastasis to the synthetic scaffold.. Spectral ultrasound imaging (SUSI), which detects parameters related to the composition and structure of tissues, identified changes at the earliest time point that tumor cells were recruited to scaffolds. SUSI demonstrated changes in spectral parameters with tumor status in orthotopic models of both human and mouse breast cancer cells in mice. The associated changes were reflected in the cellu-

lar composition of the scaffold microenvironment, and not the acellular composition. This included an increase in the number of CD31+CD45- endothelial cells in tumor bearing mice (1237 +/- 252 cells for control and 1909 +/- 385 cells for tumor bearing scaffolds). Finally, the changes in SUSI parameters was used to develop a classification model to stratify tumor free and tumor bearing status from scaffold parameters. Combination of a linear discriminant analysis model and a bagged decision trees model resulted in an area under the curve of 0.92 for prediction. Ultrasound is widely used in the clinic and the potential for early non-invasive detection of metastasis could facilitate clinical translation of the scaffolds for monitoring metastatic disease.

7.3 Introduction

Metastasis is responsible for 90% of cancer related deaths [116]. This transition to stage IV disease has a devastating prognosis for many reasons. First, metastasis is not often detected until whole organ systems have been compromised. Currently, a definitive diagnosis of metastasis relies on the use of PET, CT, or MRI to locate and visualize a metastatic lesion, typically >7-8mm in diameter [171]. Second, widespread metastatic disease is often more resistant to therapy, more aggressive, and overall much harder to treat. Early detection of metastatic disease or a risk of metastasis has significant potential to reduce cancer mortality associated with metastasis by allowing interventions when the burden of disease is low.

Early detection strategies have primarily focused on the use of blood as a liquid biopsy. Liquid biopsies including circulating tumor cell (CTC), circulating tumor DNA (ctDNA), and exosome detection in the blood are emerging as a technology to stage patients beyond the presence, size, and molecular characteristics of the primary tumor [172]. However, the connection between the presence and relative number of each of these markers and metastasis is still unclear. For example, while a high number of circulating tumor cells (5 CTCs in 7.5 mL blood) correlates with poor

prognosis [220], studies in animal models have shown that 99.99% of CTCs do not have the ability to metastasize [168] and thus understanding when to intervene in a patient that has a high number of CTCs is still elusive. Biomaterial scaffolds that capture metastatic tumor cells [151] extend beyond liquid biopsy to capture immune cells associated with the metastatic niche and metastatic tumor cells themselves [30, 31, 34, 42, 152]. These technologies have been successful in mouse models of breast [30, 31, 34, 42, 152], ovarian [29], prostate [27, 81], melanoma [26] and hematologic cancers [36] and have captured tumor cells, reduced metastatic burden [30, 31], and improved survival [30].

A crucial piece of this detection platform is non-invasive monitoring of the implant for metastasis. Inverse spectroscopic optical coherence tomography (ISOCT) has been implemented in this system in order to detect the presence of tumor cells at the earliest stages of metastatic cell dissemination, prior to detection of tumor cells in vital organs [30, 31]. However, optical imaging techniques are highly specialized and not currently available in the clinic. Additionally, while the resolution of optical techniques is high, the penetration depth is low [112, 148] such that this technology is unlikely to be successful in non-invasive imaging through human skin.

Ultrasound imaging is the most commonly used imaging modality in radiology due to its noninvasive and nondestructive nature and optimal balance of resolution and penetration depth for many clinical applications. Spectral ultrasound imaging (SUSI), an imaging modality extended from the conventional grayscale B-mode ultrasound imaging, utilizes the raw radiofrequency data (RF) of ultrasound backscattered signals to extract quantitative measures of tissue properties. Power spectra of the RF signals can be computed and calibrated such that all system effects are removed and linear regression of the calibrated spectra over the bandwidth of imaging provides quantitative parameters for a given tissue including slope, midband fit (MBF), average acoustic scatter diameter, and acoustic concentration. Spectral characteristics

have been previously used to characterize atherosclerotic plaque composition [221], changes in tissue properties for the prostate [222], pancreas, and lymph node [223], and non-invasively monitor the development of tissue-engineered constructs *in vitro* [224–227].

In this study, we demonstrate the use of SUSI for determination of tissue characteristics that correspond with spontaneous metastatic tumor cell arrival to a biomaterial scaffold *in vivo*. We investigated the parameter alterations that occur from healthy to tumor bearing mice within biomaterial scaffolds for models of orthotopic human and mouse breast cancer metastasis. We also developed a classification algorithm to classify healthy and tumor bearing mice according to SUSI parameter measurement in scaffolds. Finally, we evaluated the biological components of the scaffold that changed with tumor inoculation in order to identify those components that changing SUSI parameters used to stratify tumor bearing from healthy samples. The use of SUSI in combination with scaffolds that capture metastatic tumor cells has the potential to create a non-invasive platform for identifying metastatic disease at its earliest stages, allowing for intervention while disease burden is low and profoundly impacting cancer mortality as a result of metastasis.

7.4 Results

7.4.1 SUSI detects changes in mouse-tumor bearing mice relative to tumor free at late stages of metastatic disease

The ability of SUSI to distinguish between late stage tumor bearing mice and healthy controls was initially assessed by explanting scaffolds from healthy and 4T1 breast tumor bearing mice at day 14 following inoculation and imaging ex vivo. Day 14 post tumor inoculation represents a timepoint at which tumor cells are present both in the scaffold and in the lung and liver as micrometastases [30]. Grayscale images

(**Figure 7.1A**) with 3D reconstruction (left panel) and section (right panel) for tumor free and tumor bearing conditions show no obvious changes in implant structure at the macroscopic scale. Assessment of SUSI parameters demonstrated clear distinctions between tumor free and tumor bearing mice at this relatively late stage (**Figure 7.1B**) including significantly lower slope for tumor bearing scaffolds (control: 0.103 +/- 0.076 and tumor bearing: 0.0583 +/- 0.078 dB/MHz). Additionally, acoustic scatter diameter (ASD: 20.82 +/- 1.88 μm for control and 21.90 +/- 1.83 μm for tumor bearing) and average acoustic concentration (AAC: 42.77 +/- 3.02 dB[mm-3] for control and 44.41 +/- 3.17 dB[mm-3] for tumor bearing) were both higher for tumor bearing relative to tumor free. For each parameter the number of pixels outside of the sample 95% confidence interval were also assessed for their alteration between control and tumor bearing scaffolds (**Figure 7.1C**). This approach gave more consistent differences between tumor bearing and control scaffolds with all parameters assessed having statistically significant alterations from control to tumor bearing scaffolds. Interestingly, for all parameters the number of pixels outside of the 95% confidence interval was lower in tumor bearing mice, including grayscale (23017 +/- 8772 pixels for control and 20210 +/- 6859 pixels for tumor bearing scaffolds) and mid-band fit (426 +/- 197 pixels for control and 369 +/- 142 pixels for tumor bearing scaffolds) which were not significantly different by measurement of the raw parameter value itself (**Figure 7.1B**).

7.4.2 SUSI detects changes in mouse and human-tumor bearing mice relative to tumor free at early stages of metastatic disease

Following the finding that SUSI was capable of detecting tissue changes in scaffolds from tumor bearing mice at late time points relative to control, we next investigated the ability of SUSI to identify changes at early stages of metastasis. We chose day 5 following inoculation of breast adenocarcinoma cells as this time point is associated

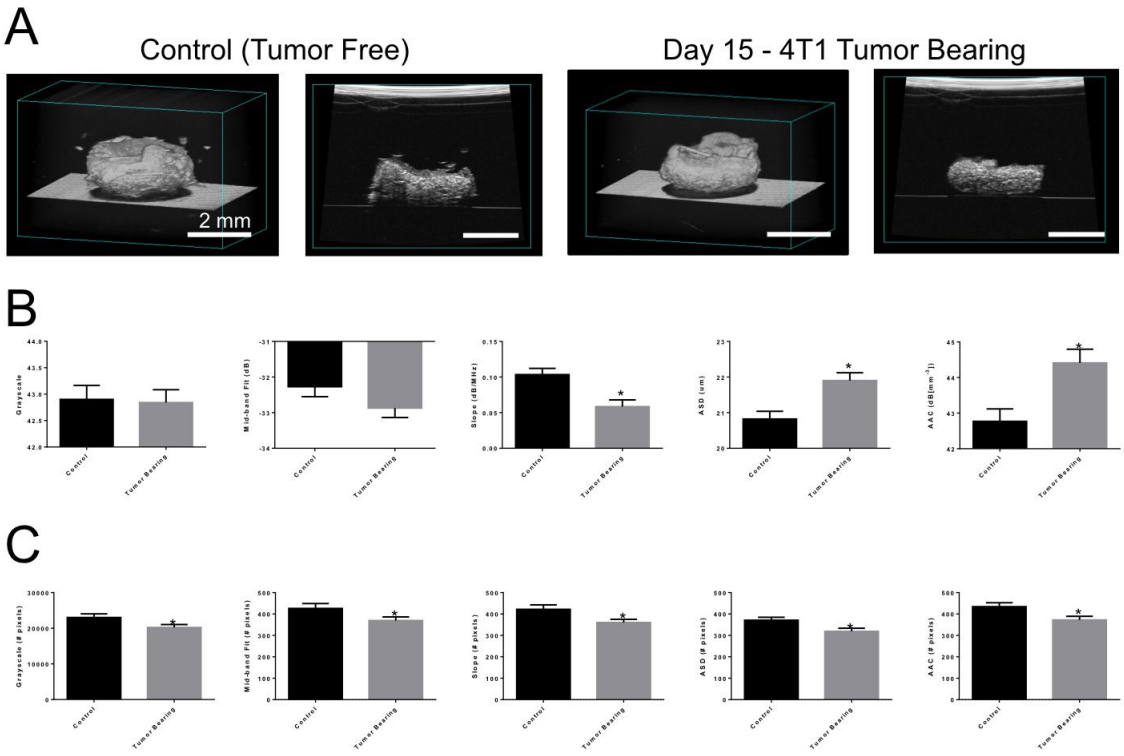

Figure 7.1: **SUSI detects changes in mouse-tumor bearing mice relative to tumor-free at late stages of metastatic disease.** (A) Grayscale images of scaffolds from tumor free and tumor bearing mice. (B) Raw parameter values generated by SUSI analysis of control and tumor bearing scaffolds including grayscale, mid-band fit, slope, ASD, and AAC. (C) Confidence interval analysis of parameters showing the number of pixels lower than the lower bound of the 95% confidence interval of the sample for that given parameter per frame. Error bars s.e.m. *$p<0.05$ via two-sided t-test

with occasional tumor cells in the scaffold yet not metastasis to vital organs [30, 31]. Again, instead of looking at the raw parameters from SUSI we assessed the number of pixels outside of each samples 95% confidence interval. Like late-stage tumors we found that there were not any visible macroscopic alterations in implant architecture in three dimensional reconstructions or gray scale slices for scaffolds in mice bearing either human (231-BR) or mouse (4T1) tumors at day 5 compared to their tumor free controls (**Figure 7.2A, C**). Also similar to late stage disease, we found the number of pixels outside of the sample 95% confidence interval to be significantly lower in scaffolds from tumor bearing mice relative to control for both human and mouse breast tumors (**Figure 7.2B, D**). The number of pixels was significantly altered for all parameters for the comparison of scaffolds from mice bearing day 5 human 231-BR tumors relative to control. For mice bearing mouse 4T1 tumors, all parameters except for AAC (624 +/- 234 pixels for control and 561 +/- 207 pixels for tumor bearing) were significantly altered between control and tumor bearing scaffolds.

7.4.3 SUSI detects changes in cellular composition and extracellular matrix with tumor progression and metastasis

Following identification of the ability for SUSI to detect changes in tumor bearing relative to control scaffolds in both human and mouse breast cancer at early and late stages of disease, we next sought to identify the biological changes being detected by SUSI in the scaffolds. We first investigated changes in extracellular matrix (ECM) associated genes as these are both likely to be observed by SUSI [224–227] and are also altered in the pre-metastatic niche [8, 42, 150] We investigated expression of Col1a1, Col4a1, Fn1, Lox, and Mmp2 and found no significant differences in gene expression between control and 4T1 tumor bearing scaffolds at day 7 post inoculation (**Figure 7.3A**). As no differences were observed in gene expression of ECM associated genes we next investigated changes in cell populations within the scaffolds. Previous work

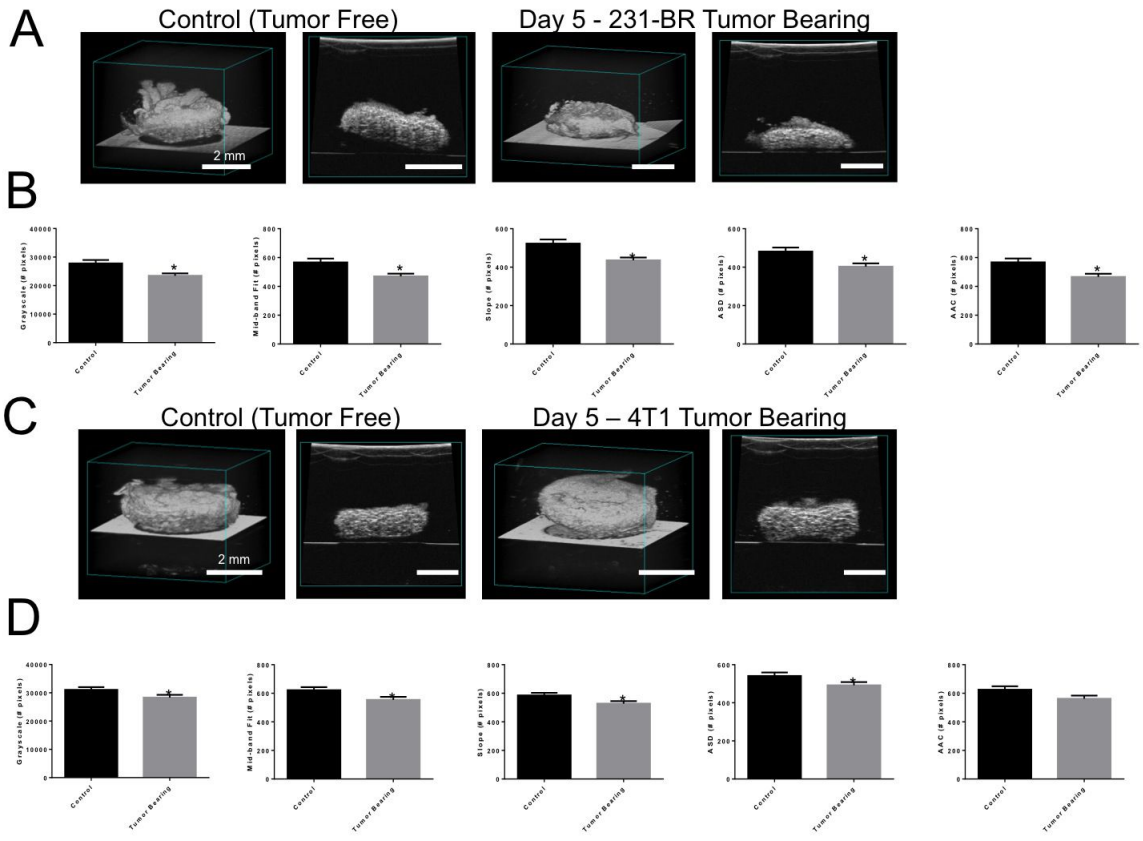

Figure 7.2: **SUSI detects changes in mouse and human-tumor bearing mice relative to tumor-free at early stages of metastatic disease.** (A) Grayscale images of scaffolds taken from control and 231-BR tumor bearing mice at day 5 post-inoculation. (B) Number of pixels lower than the 95% confidence interval for each sample and each parameter showing grayscale, mid-band fit, slope, ASD, and AAC for control and day 5 231-BR tumor bearing scaffolds. (C) Grayscale images of scaffolds taken from control and 4T1 tumor bearing mice at day 5 post-inoculation. (D) Number of pixels lower than the 95% confidence interval for each sample and each parameter showing grayscale, mid-band fit, slope, ASD, and AAC for control and day 5 4T1 tumor bearing scaffolds. Error bars s.e.m. *$p<0.05$ via two-sided t-test

with scaffolds in tumor bearing mice has identified major changes in immune cell populations as a result of tumor development and metastatic progression [30, 31, 34, 42, 152], however other stromal populations had not been investigated. As a result, we performed flow cytometry to identify numbers of CD31+ endothelial cells present in each scaffold (**Figure 7.3B**). A significantly increased number of CD31+CD45- endothelial cells were present in the scaffolds of day 5 4T1 tumor bearing mice relative to control scaffolds (1237 +/- 252 cells for control and 1909 +/- 385 cells for tumor bearing scaffolds). We next sought to determine if our findings of alterations in SUSI properties would be recapitulated in both decellularized scaffolds (**Figure 7.3C**) and by isolating the cells from scaffolds and imaging these in a collagen gel (**Figure 7.3D**). While no statistically significant differences between control and day 5 4T1 tumor bearing scaffolds were observed with either decellularized scaffolds or investigating scaffold-derived cells in collagen gel, scaffold-derived cells better mirror the changes we saw in whole scaffolds. In decellularized scaffolds the number of pixels outside of the 95% confidence interval decreased for grayscale, ASD, and AAC for tumor bearing relative to control. However, the number of pixels for MBF and slope increased for tumor bearing relative to control. For scaffold-derived cells, the number of pixels outside of the 95% confidence interval decreased for all parameters in tumor bearing relative to control, consistent with the whole scaffold. Scaffold-derived cells in a collagen gel also reflect the trends observed with spleen-derived cells in a collagen gel where we found a statistically lower number of pixels outside of the 95% confidence interval for all parameters (**Figure 7.3E**). Previous work has identified immune cell populations are altered similarly with tumor inoculation in both implanted scaffolds and spleens [30, 31] and these results are concordant with that finding. Representative grayscale images of scaffold-derived and spleen-derived cells in collagen gels as well as decellularized scaffolds can be found in **Supplemental, Figure 7.5** and SUSI parameters for the blank scaffold can be found in **Supplemental, Figure 7.6**.

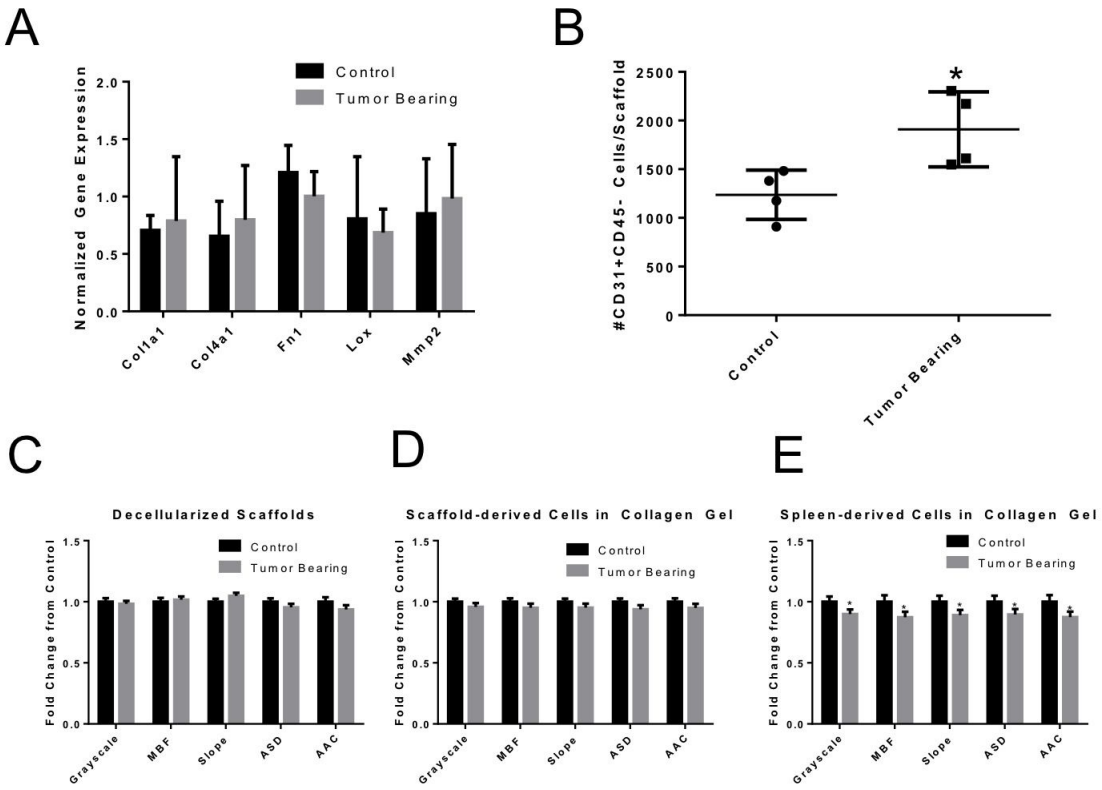

Figure 7.3: **SUSI detects changes in cellular composition and extracellular matrix with tumor progression and metastasis.** (A) qRT-PCR data showing normalized gene expression for ECM associated genes including Col1a1, Col4a1, Fn1, Lox, and Mmp2 for scaffolds from control and day 15 4T1 tumor bearing mice. (B) Flow cytometric analysis of CD31+CD45- endothelial cells in scaffolds from control and day 15 4T1 tumor bearing mice. (C) SUSI analysis of decellularized scaffolds taken from control and day 5 4T1 tumor bearing mice showing fold change from control of number of pixels under 95% confidence interval for each sample for each parameter including grayscale, mid-band fit (MBF), ASD, and AAC. (D) SUSI analysis of scaffold-derived cells in a collagen gel taken from control and day 5 4T1 tumor bearing mice showing fold change from control of number of pixels under 95% confidence interval for each sample and each parameter including grayscale, MBF, ASD, and AAC. (E) SUSI analysis of spleen-derived cells in a collagen gel taken from control and day 5 4T1 tumor bearing mice showing fold change from control of number of pixels under 95% confidence interval for each sample and each parameter including grayscale, MBF, ASD, and AAC. Error bars s.e.m. *$p<0.05$ via two-sided t-test

7.4.4 SUSI parameters are able to classify tumor free and tumor bearing mice with good sensitivity and specificity

We next built classification models to discriminate between tumor bearing and control mice based on a consistent decrease in the number of pixels outside of the 95% confidence interval observed in tumor bearing scaffolds. A schematic of the method used to develop classification models is provided (**Figure 7.4A**) and a schematic of experimental timeline is provided (**Supplemental, Figure 7.7**). A heatmap with unsupervised hierarchical clustering across samples is shown for the number of pixels outside of the 95% confidence interval for each parameter and each sample in the test cohort (**Figure 7.4B**). Using unsupervised hierarchical clustering most tumor free control samples (TF) cluster on the left and most tumor bearing samples (TB) cluster on the right of the heatmap. However, the number of trees generated in the clustering indicates the samples are heterogeneous in each classification and that a simple cutoff value for each parameter cannot suffice to predict tumor status. Thus, linear discriminant and bagged decision trees models were created to classify the test cohort based on the training cohort. Each model gave each sample a score from 0 to 1 based on the likelihood of being tumor free (0) or tumor bearing (1) and these scores are plotted in **Figure 7.4C**, demonstrating good separation in scores of tumor free and tumor bearing scaffolds. A receiver operating characteristics (ROC) curve was created for the classification of both models individually and the linear addition of both models, with any score greater than 1 classified as tumor bearing (**Figure 7.4D**). The area under the curve was calculated for each and the combined score was found to outperform the individual models (Combined AUC: 0.92, Linear Discriminant Analysis AUC: 0.88, and Bagged Decision Trees AUC: 0.87)

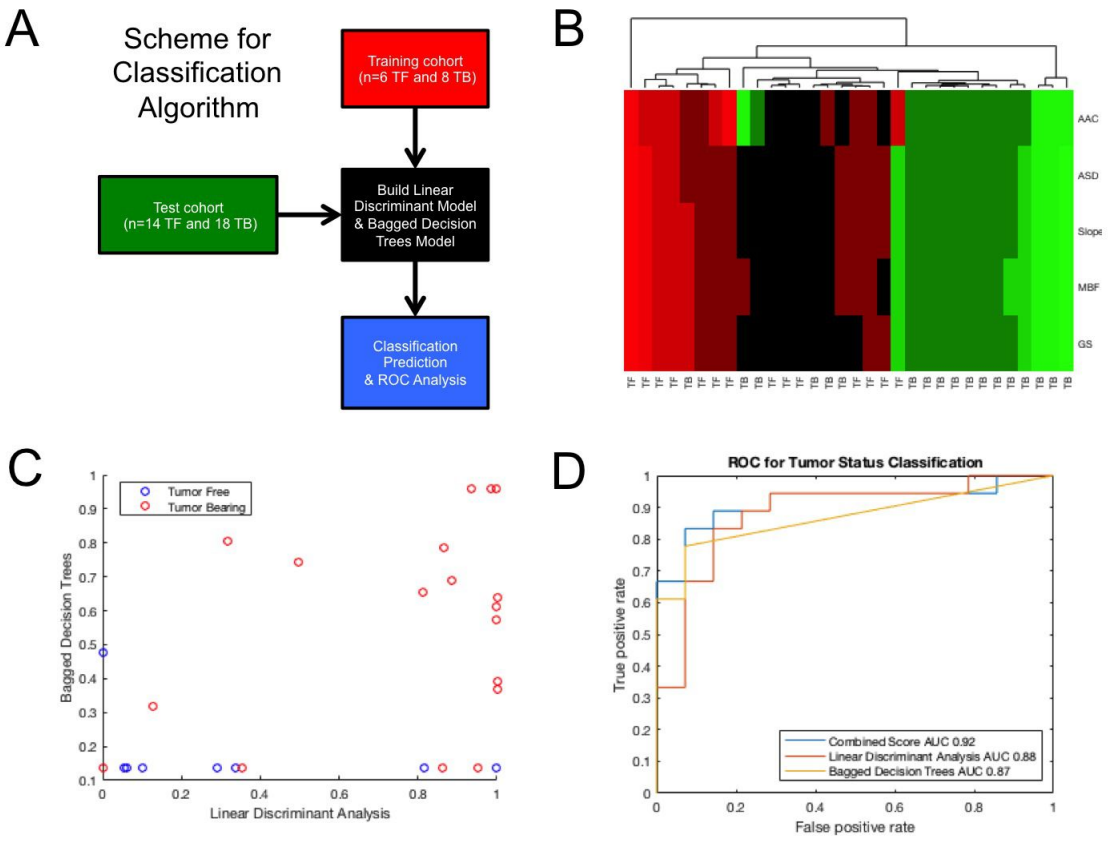

Figure 7.4: **SUSI parameters are able to classify tumor free and tumor bearing mice with good sensitivity and specificity.** (A) Schematic of method used to classify samples as tumor free or tumor bearing. A training cohort of n=6 tumor free and n=8 tumor bearing mice was used to build both a linear discriminant model and a bagged decision trees model. The test cohort was then fed into the model and the classification predicted. (B) Heatmap with unsupervised hierarchical clustering of test cohort data normalized across each parameter. (C) Classification of test cohort data and score given by each algorithm indicating prediction of either tumor free status (score of 0) or tumor bearing status (score of 1). (D) Receiver Operating Characteristic curve for tumor status classification showing the classification accuracy for the combined score including both bagged decision tree and linear discriminant analysis models and each model alone

7.5 Discussion

Metastasis is responsible for 90% of cancer-related deaths in part, because no clinical strategies currently detect metastasis prior to the compromise of organ function. In this work, we validate the use of SUSI on implanted scaffolds for the early detection of metastasis at time points where no tumor cells are found in vital organs [30, 31] but are found in implanted scaffolds in two animal models of breast cancer metastasis.

Inverse spectroscopic imaging (ISOCT) has also been used to detect ultrastructural tissue changes associated with metastasis in these models [30, 31], however ISOCT is greatly limited by a low penetration depth and expense of imaging platforms. Traditional ultrasound imaging alone is often used in the clinic for evaluation of primary breast cancer [228] indicating bedside ultrasound is a safe, non-invasive, and highly cost-effective technology that fits well with current practice. Importantly, SUSI represents a significant improvement beyond traditional grayscale techniques, as these are unable to detect changes associated with metastasis, and is able to monitor objective and quantitative parameters that are intrinsic to the properties of tissues. In this study, while we recorded the absolute value of the SUSI including grayscale, mid-band fit, slope, ASD, and AAC, we found that for all parameters the number of pixels outside of the 95% confidence interval for each sample better separated tumor bearing and tumor free scaffolds. For all parameters the number of pixels outside of the sample 95% confidence interval was found to be lower in tumor bearing scaffolds indicating not only small but significant differences in SUSI parameters and tissue properties, but also a fundamental change in tissue heterogeneity. The ability to use these parameters and change in implant infiltrate homogeneity (by the number of pixels outside the 95% confidence interval for each sample) provides promising translation for human samples as longitudinal monitoring is operator and system independent and is dependent upon the heterogeneity of a tissue rather than

the absolute value of a tissue parameter. This finding was similar in both syngeneic (mouse 4T1) and xenogeneic (human 231-BR) mouse models of spontaneous metastasis. This result was expected as we observe similar changes in tumor cell arrival and immune/stroma alteration with the development of the pre-metastatic niche and transition to metastasis in implanted scaffolds [30, 31]. We have also successfully detected changes associated with metastasis in both models using ISOCT [30, 31]. Additionally, the observed changes in SUSI do appear to have some progression associated with early compared to relatively late stage metastasis. For 4T1-inoculated mice all parameters are significantly altered between tumor free and tumor bearing at day 15 whereas at day 5 only 4/5 parameters were significantly altered.

The observed alterations in SUSI parameters were hypothesized to be associated with changes in ECM as this has been robustly measured using SUSI [229] and is associated with the pre-metastatic niche [10, 51, 150] and metastasis to implanted biomaterial scaffolds [42], however we did not find significant alterations in ECM associated genes by qRT-PCR and decellularized scaffolds did not recapitulate the change from tumor free to tumor bearing scaffolds (2/5 parameters were significantly different between decellularized and whole scaffolds, while no parameters (0/5) were significantly altered from the imaged scaffold cells to whole scaffolds). Thus, we looked at cellular alterations and found a significant increase in endothelial cells, which are also associated with metastasis and the pre-metastatic niche [8, 60]. We have also already discovered a number of other significant changes in immune cells at this time point [30, 31], which may also be part of the cellular changes SUSI detects between tumor free and tumor bearing scaffolds.

Classification models built on the input of SUSI data were able to classify tumor bearing and tumor free mice with good sensitivity and specificity. As a result, we believe that SUSI of implanted biomaterial scaffolds represents a promising tool to enable the non-invasive early detection of metastasis. The scaffold may be non-

invasively monitored using SUSI, which is both operator and system independent, to identify changes indicative of metastasis risk and then the scaffold explanted and analyzed via histology, RT-qPCR, or other techniques to validate the arrival and presence of immune cells (myeloid derived suppressor cells etc. [30, 31]) and gene signatures (unpublished data, Oakes et al.) associated with metastasis as well as directly quantifying the arrival of tumor cells. Early detection may enable the initiation of early chemotherapeutic treatment among high-risk patients while the burden of disease is low before whole organ systems are compromised. Specifically, we foresee this scaffold platform and imaging technologies being used in patients who have received a diagnosis of invasive breast cancer, completed chemotherapy and surgery, and are deemed cancer-free but may experience metastatic recurrence. Non-invasive monitoring of a scaffold implant is complementary and potentially advantageous over liquid biopsy approaches as the scaffold identifies risk of metastasis based on presence of metastatic niche forming cells and tumor cells that have successfully metastasized to a tissue and are similar to the metastatic lung (unpublished data, Bushnell et al.).

7.6 Outlook

In this study, we demonstrate the utility of SUSI to detect changes associated with metastasis to biomaterial scaffolds in both syngeneic mouse and xenogeneic human models of spontaneous metastasis before tumor cells are detectable in vital organs. SUSI imaging of biomaterial scaffolds represents an important technological advancement in the early and non-invasive detection of metastasis, providing a platform for detection leading to early intervention and reducing mortality from cancer metastasis.

7.7 Materials and Methods

7.7.1 Scaffold fabrication and implantation

Microsphere preparation. PCL microspheres were prepared as previously described [30]. Briefly, microspheres were prepared by emulsification of a 6% (w/w) solution of PCL (Lactel Absorbable Polymers; Inherent viscosity 0.65-0.85 dL/g) in dichloromethane in a 10% (w/v) poly(vinyl alcohol) solution followed by homogenization at 10,000 rpm for 1 minute. The solution was then stirred for 3 hours to evaporate dichloromethane solvent. Microspheres were then collected by centrifugation at 2000 x g for 10 minutes and washed at least five times in deionized water. Finally, microspheres were lyophilized for 48 hours.

Scaffold fabrication. Microporous PCL scaffolds were prepared by mixing PCL microspheres and sodium chloride crystals (250-425 μm in diameter) at a 1:30 (w/w) ratio. This salt and polymer microsphere mixture was then pressed in a steel die for 45 seconds at 1500 PSI. Polymer/salt disks were then heated at 60C for 5 minutes per side to melt polymer microparticles around salt crystals to form a continuous structure. Salt crystals were subsequently removed by immersion in water for 1.5 hours. Scaffolds were then sanitized for animal studies using 70% ethanol, rinsed with sterile water, and dried on a sterile surface.

Scaffold implantation. Scaffolds were implanted into the subcutaneous space of 8-week-old female NOD/SCID-IL2R-/- (NSG) or balb/c mice as previously described [30]. For the implantation procedure, animals were anesthetized via isoflurane (2%, inhaled), prepared with Carprofen analgesia (5 mg/kg, subcutaneous injection), the upper back was shaved and prepped using a Betadine swab followed by an ethanol swab and this procedure was repeated 3 times. A fenestrated sterile field was draped over the surgical area and a 1 cm incision was made in the upper back. Following incision, subcutaneous pockets were created perpendicular to the incision, into which

sanitized scaffolds were inserted (2 scaffolds/mouse). The skin was then closed using sterile wound clips (Reflex 7 mm, Roboz Surgical Instrument Co).

7.7.2 Tumor Inoculation

Animal studies were performed in accordance with institutional guidelines and protocols approved by the University of Michigan Institutional Animal Care and Use Committee (IACUC). Tumor inoculations were performed by injection of 2e6 MDA-MB-231BR-tdTomato-luc2 (Northwestern University Developmental Therapeutics Core) or 4T1-tdTomato-luc2 (Perkin Elmer) cells in 50 μL PBS (Life Technologies) into the fourth right mammary fat pads of 10-week-old female NSG mice or Balb/c mice respectively (Jackson Laboratory). Cell lines were confirmed to be pathogen free and authenticated by short tandem repeat DNA analysis and compared to the ATCC STR profile database (DDC Medical).

7.7.3 Ultrasound Imaging

The Vevo 770 system (Visualsonics, Toronto, Canada) with a 55 MHz center frequency single element transducer (Vevo 708 scan head) were used to image scaffolds ex vivo or in situ. Scaffolds were imaged with B-mode, 3D scan mode, and radiofrequency mode to acquire data for SUSI analysis.

7.7.4 Spectral Ultrasound Imaging (SUSI) Analysis

Grayscale. Raw backscattered RF data was Hilbert transformed to obtain the complex analytical signal p(y,z). Grayscale values were determined as the mean absolute value of the signal over the selected region as:

$$GS(y,z) = \log_{10}[p(y,z)]$$

Spectral parameters. The power spectra of each RF scan line was calculated by

taking the Fast Fourier Transform of the segment of signals gated by a hamming window with 0.2 μs sliding with a 0.1 μs offset. For calibration and removal of system-dependent factors the power spectrum was divided by the spectrum of a perfect reflector (oil-water interface). Slope (m) and mid-band fit (MBF) were determined using linear regression to the calibrated power spectrum within a -9 dB bandwidth. Acoustic scatter diameter (a), the effective size of acoustic scatters in a tissue, was assessed using slope (m), the geometry index (n), the center frequency of the imaging transducer (fc), and bandwidth of the transducer (b):

$$a = 2 * \sqrt{0.25n * \frac{[b - (1 - \frac{b^2}{4})]}{b^3 f_c^2} - \frac{m}{105.5 f_c}}$$

Acoustic concentration (CQ2) was calculated by using MBF, scatter diameter (a), and a shape dependent factor (E):

$$CQ^2 = \frac{(e^{0.23(MBF - g_1 n - g_2(\frac{a}{2})^2)})}{Ea^{2(n-1)}}$$

$$g_1(f_c, b) = 4.34[\ln(f_c(1 - \frac{b^2}{4})^{0.5}(\frac{2+b}{2-b})^{\frac{1}{b}}) - 1]$$

$$g_2(f_c, b) = -76.9{f_c}^2(3 + \frac{b^2}{4})$$

Average scatter diameter (ASD) and average acoustic concentration were calculated as the average value of the scatter size (a) and acoustic concentration (CQ2) respectively in the chosen region. AAC values are given in decibel scale. For each parameter 95% confidence intervals were calculated for each sample and the number and percentage of pixels above or below the 95% confidence interval quantified for each sample.

7.7.5 Statistical Analysis

Regions in at least 10 frames from each scaffold were identified and quantified by GS value and spectral parameters. All results are presented as mean +/- standard error of mean (SEM). Statistical comparisons of parameters between groups were made using Students t-test for unpaired samples. A p value of ¡0.05 was considered statistically significant.

7.7.6 RT-qPCR Analysis

Scaffolds were explanted from tumor-free and tumor bearing mice, flash frozen in isopentane, and stored until use. Total RNA was isolated from explanted scaffolds via homogenization in TRIzol (Thermo Fisher, Waltham, MA). Samples were centrifuged at 10,000 x g to remove non-soluble particles. Total RNA was isolated using Direct-zolTM RNA Miniprep Plus kit (Zymo Research Corp, Irvine, CA). RNA concentration and purity were assessed by light absorbance via NanoDrop 2000c (Thermo Fisher). cDNA was generated from RNA via reverse transcription using SuperScriptTM VILOTM cDNA synthesis kit (Thermo Fisher). Taqman probes were purchased from Thermo Fisher including Mm00495386m1 (Lox), Mm00439498m1(Mmp2), Mm00801666g1 (Col1a1), Mm01210125m1 (Col4a1), Mm01256744m1 (Fn1) and reference genes Gapdh, Tbp, Ywhaz, Hmbs, Ubc. RT-qPCR was performed on CFX ConnectTM Real-Time PCR Detection System (Bio-Rad Inc, Hercules, CA) with CFX Manager Software.

7.7.7 Decellularization of scaffolds

Scaffolds were decellularized using the method described by Aguado et al. [42]. In brief, scaffolds were explanted from tumor-free and tumor bearing mice and washed in dPBS, then treated with sequential 30 min washes in 1%, 2% and 3% Triton X-100 (Sigma Aldrich), followed by an overnight incubation in 0.1% sodium dodecyl

sulfate (SDS) with shaking at 4'C. This treatment was repeated the following day until scaffolds were completely decellularized.

7.7.8 Preparation of cell suspensions for SUSI

Single cell suspensions were prepared as described above for flow cytometry. Following preparation of a single cell suspension cells were added to 4 mg/mL collagen I, 5x DMEM solution, Fetal Bovine Serum, and 0.1N NaOH at a ratio of 1:5:2:1:1 resulting in a collagen gel with a final concentration of approx 500,000 cells/mL, 1x DMEM, 2 mg/mL collagen I, 10% FBS, and 0.01N NaOH. Gels were plated in a 24 well plate and allowed to crosslink for 30 min at 37'C prior to imaging.

7.8 Supplemental Figures

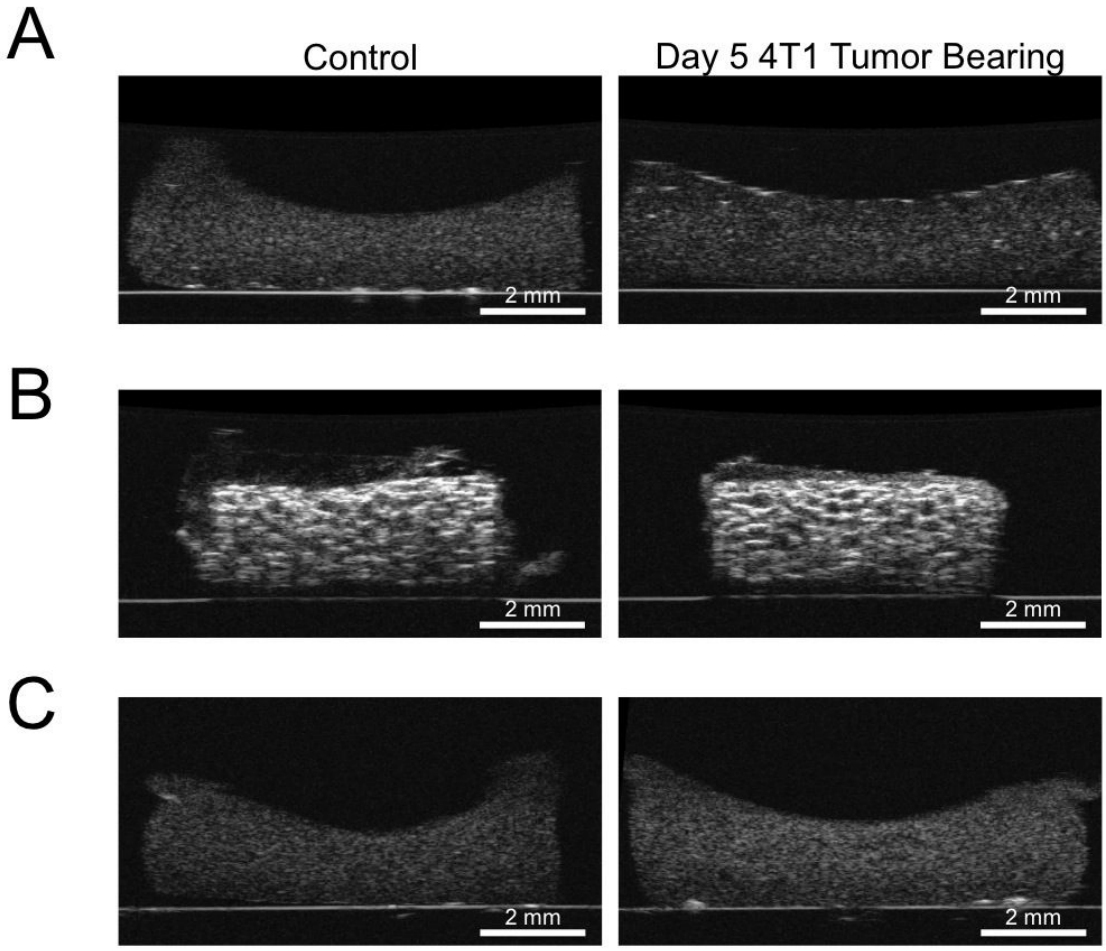

Figure 7.5: **SUSI detects changes in tumor bearing spleens relative to control.** (A) Representative grayscale images of cells from control or day 5 4T1 tumor bearing scaffolds embedded in a collagen gel. (B) Representative grayscale images of decellularized scaffolds from control or day 5 4T1 tumor bearing mice. (C) Representative grayscale images of cells from control or day 5 4T1 tumor bearing spleens embedded in a collagen gel.

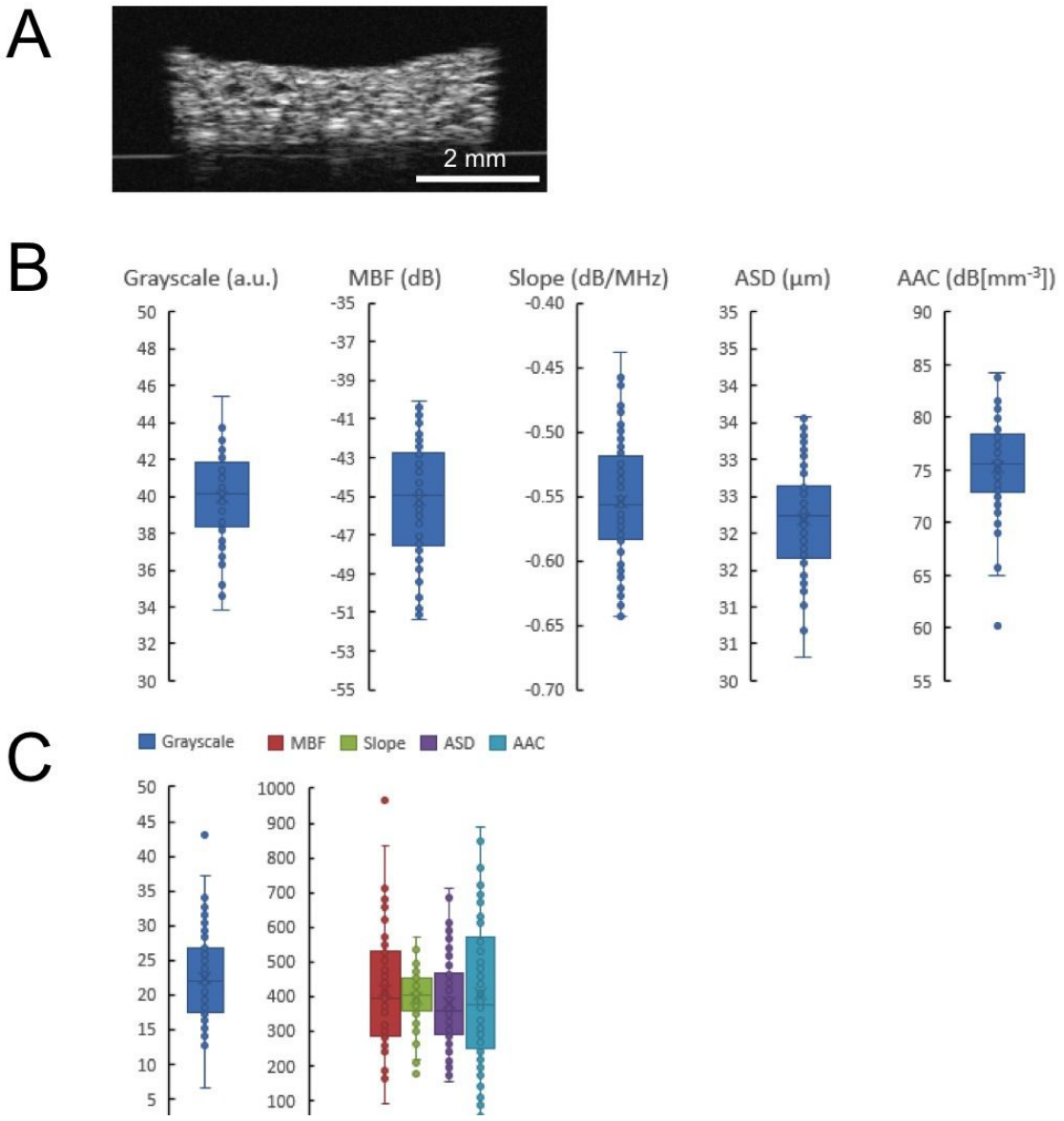

Figure 7.6: **SUSI parameters for blank scaffold. (A) representative B-mode image of a blank scaffold.** (B) SUSI analysis results including grayscale, mid-band fit (MBF), ASD, and AAC of blank scaffolds. (C) SUSI analysis results of pixels under 95% confidence interval for each sample and each parameter including grayscale, MBF, ASD, and AAC of blank scaffolds

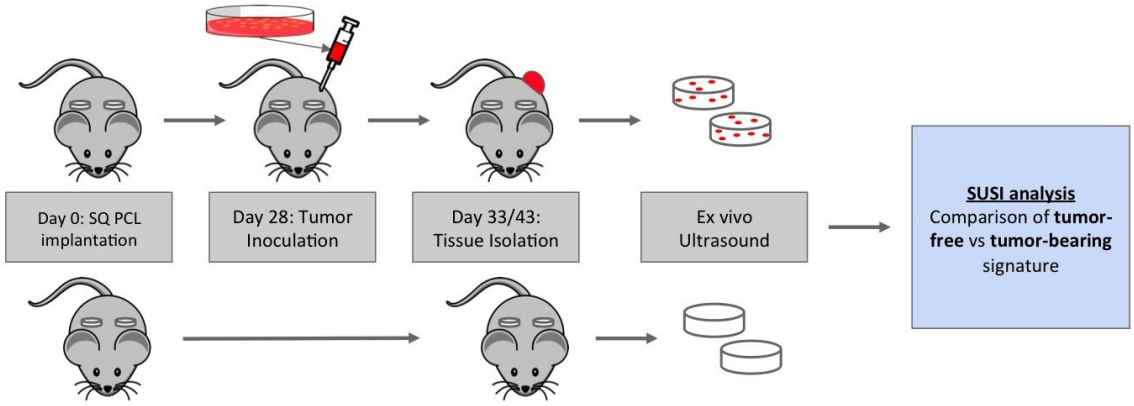

Figure 7.7: **Schematic of experimental timeline for SUSI experiments.**

CHAPTER VIII

Conclusions and Future Directions

8.1 Summary of Findings

Taken together, the work presented in this dissertation describes developing a biomaterial implant for the early detection of metastasis, therapeutic benefit, and as a tool to study metastasis. By recruiting tumor cells to a defined site *in vivo* metastasis can be detected non-invasively using both optical and ultrasound techniques. Furthermore, the diversion of immune cells associated with metastasis as well as tumor cells themselves to the implant significantly enhanced survival in a mouse model of therapeutic tumor resection. The phenotype of tumor cells recruited to the implant was elucidated and compared to tumor cells derived from the primary tumor and lung metastasis. Scaffold-recruited tumor cells were found to be a highly aggressive population of metastatic tumor cells with many phenotypic and functional similarities to tumor cells found in the lung. Additionally, immunomodulation at the scaffold site was used to study the effect of cytokine delivery on immune and tumor cell recruitment *in vivo* and identified key immune populations associated with tumor cell recruitment across a range of different immune microenvironments. The scaffold platform was also evaluated in two transgenic models of tumorigenesis and metastasis including one breast cancer model and one pancreatic cancer model. Implants were found to recruit tumor cells and demonstrate tumor-progression dependent immune

dynamics, providing further evidence for their translatability to human patients. The research described in this dissertation continues the previous work done in this area and advances the promise for the utility of this platform in a clinical setting.

8.2 Significance and Impact

The work presented in this dissertation addresses a crucial gap in the current treatment of cancer. Metastasis is not detected until late stages of the disease, when many billions of tumor cells have colonized a vital organ. This research furthers the development of a platform to enable the detection of metastasis at its earliest stages, when intervention and treatment may have a greater impact on patient survival. The strategy of using a biomaterial platform to detect metastatic tumor cells is in contrast to liquid biopsy detection of CTCs by capturing tumor cells that are capable of metastasis, unlike an estimated 99.99% of circulating tumor cells. In **Chapter 3** we develop an implant that is stable for months *in vivo* and yet is able to recruit tumor cells long after implantation. We also demonstrate in a mouse model of tumor resection, scaffold implantation enhances survival relative to mock surgery. These findings both increase translatability of the scaffold platform to patients as the scaffold would be stable for months as well as indicate the scaffold may have use as a therapy as well as detection platform. In **Chapter 4** we investigated immunomodulation at the scaffold implant as a way to elucidate novel contributors to metastatic progression and recruitment to the implant that had not previously been identified. This approach may be further applied to many other factors associated with metastasis and the pre-metastatic niche as a more controlled system for identifying the local contributions of individual factors to metastasis. Additionally, this approach may also be used to enhance tumor cell recruitment to the implant, potentially enhancing the signal to noise ratio in the clinical setting. In **Chapter 5** we discuss the phenotype of tumor cells recruited to biomaterial implants and investigate whether these tumor cells are a

population capable of metastasis. Indeed, we find tumor cells recruited to the implant represent an aggressive population of metastatic tumor cells whose diversion may be partially responsible for the therapeutic and survival benefits found in **Chapter 3**. In **Chapter 6**, we test the function of biomaterial implants in transgenic models of tumorigenesis and metastasis that are more clinically translatable than orthotopic models. Scaffolds recruited spontaneously metastasizing breast and pancreatic tumor cells in these models and demonstrated tumor-progression-dependent immunomodulation. The finding of tumor cell recruitment in pancreatic cancer is particularly significant as it is the cancer with the lowest survival rate as a result of its rapid progression to metastasis. Finally, in **Chapter 7** we describe the use of non-invasive ultrasound imaging for the detection of metastasis at the scaffold implant. Ultrasound is a more translatable platform for non-invasive imaging in humans relative to optical techniques previously used and thus represents and important finding for translation of the scaffold as a detection platform for metastasis. Collectively this work highlights the opportunities for translation of this device as a tool to detect metastasis early and potentially reduce metastatic tumor burden as well as a platform to study metastasis.

8.3 Future Directions

The following section proposes future studies that will enhance the significance and impact of the work presented in this dissertation.

8.3.1 Single cell analysis of tumor and immune cells recruited to biomaterial scaffolds

Single cell analysis is a burgeoning technique in biomedical research [230] and has the ability to gain information about individual cell types in a tissue, their transcriptome, and the heterogeneity of these populations. Single cell transcriptome analysis of tumor cells recruited to biomaterial scaffolds was an original aim of this disser-

tation, however collection of a sufficient number of metastatic tumor cells using a variety of techniques including fluorescence-activated cell sorting (FACS), magnetic-activated cell sorting (MACS), and circulating tumor cell capture devices including EpCAM+ dendrimer coated surfaces [231], Labyrinth microfluidic cell sorting device [232], flexible microspring array device [233], and Hydro-seq (unpublished data, Yu-Chih Chen). Ultimately, as these approaches were not successful, the cell lines from various metastatic locations were created in order to have sufficient number of tumor cells for analysis including phenotypic and functional analyses that could not have been performed with directly isolated tumor cells. While techniques for single cell analysis were relatively exhaustive there were a few areas that were not investigated due to their ease of availability including laser-capture microdissection [234] and Seq-Well [235]. It is likely that a combinatorial approach used to purify tumor cells from the scaffold and remove polymer debris with a microfluidic method will achieve greater success.

Single cell analysis of the immune and stromal infiltrate in biomaterial scaffolds is another key area for future work. While this dissertation and the work before it have performed exhaustive flow cytometric characterization of immune cell surface markers and the dynamics of these populations with scaffold implantation and tumor development, surface marker analysis does not provide any clues into the various phenotypes possible for each of these cell types and their role within the paracrine signaling to develop, maintain, and progress the pre-metastatic and metastatic niche. This is an area of immediate interest and exploration for the future.

8.3.2 Understanding the alterations within the scaffold microenvironment that are required for tumor cell recruitment in different cancer types

One original aim of this dissertation was to develop a model for tumor cell recruitment as a function of the various immune cell populations present. As we see variability in both tumor cell recruitment and immune cell populations present at the scaffold this provides a natural avenue to investigate the interplay between these populations. Indeed, this analysis was performed in both **Chapter 4** and **Chapter 6** in order to elucidate the role of various immune cell populations in tumor cell recruitment in three different models of metastasis including orthotopic and spontaneous breast cancer and spontaneous pancreatic cancer. While models were developed for each, simply associating the presence of various immune cell populations does not provide information or insight into the phenotype of these cells, what they are secreting and how they are interacting with tumor cells either directly or indirectly. This dissertation provides key cell populations for further investigation including CD4 and CD8+ T cells, whose role at the pre-metastatic niche has yet to be fully elucidated and have not been implicated in tumor cell recruitment to biomaterial scaffolds to date (**Chapter 2**), neutrophils which have dual roles in metastasis promotion and suppression [236], dendritic cells whose direct role in metastasis is not yet well established [47, 142, 237], and natural killer cells which are primarily shown to eliminate metastatic tumor cells [238] but in these studies demonstrated an increase with increased tumor cell presence. These populations may be further elucidated for their roles via single cell sequencing as described above, adoptive transfer of labeled cells [239] and observation of trafficking to the scaffold, and/or validation in a broader range of immunomodulated microenvironments. Further investigation into this area not only facilitates a greater understanding of the mechanisms of biomaterial scaffold function in various models, but also provides crucial insights into common mecha-

nisms of metastasis across various tumor types and crucial correlates for translation to patients.

8.3.3 Improved understanding of immune cell trafficking and education within the scaffold microenvironment

The work presented in this dissertation provides evidence that the foreign body response is dynamic and sensitive to systemic immunomodulation that occurs during cancer progression. However, it is still unknown at what time scales this turnover and trafficking of immune cells as part of the foreign body response occur on. Furthermore it is unknown whether immune cells are educated by the foreign body response to the implant and alter their phenotype relative to the blood in the context of tumor-dependent immunomodulation. It is also unclear if these immune cells may be educated within the scaffold microenvironment and then leave the scaffold and traffic to other areas of the host, including potential metastatic sites or the primary tumor itself. These questions can be investigated via labeling of immune cells and adoptive transfer as a preliminary step [239]. Furthermore they could also be explored by cell painting approaches [240], optogenetic-like approaches [241], or transplant of a scaffold containing cells from a labeled host into a non-labeled host. Each of these approaches has significant experimental considerations and potential pitfalls but beginning with simple adoptive transfer experiments may begin to answer some of these questions. While of secondary interest to scaffold function as a pre-metastatic niche, these questions are important toward further the understanding of the foreign body response in the context of cancer or other immunomodulating conditions.

8.3.4 Improved understanding of tumor cell dormancy within the scaffold microenvironment

Although we consistently observe tumor cells arriving to the scaffold implant in many varied models of cancer metastasis we have never seen secondary tumor formation at the implant, even over time scales greater than one year for survival studies after tumor resection. Furthermore we performed preliminary experiments transplanting scaffolds containing tumor cells from 4T1-bearing balb/c mice into NSG immunocompromised mice. In this experiment (data not shown) we did not observe secondary tumor formation at the transplanted scaffolds and the mice eventually died of old age. In contrast, in a control experiment to understand if this phenomenon was simply a result of the low number of cells present within the scaffold, we seeded 20 4T1-tdTomato-luc2 cells on scaffolds and implanted them into NSG mice. We found all scaffolds implanted demonstrated tumor formation by 4 weeks after implantation. This result led us to hypothesize that there may be something about the established foreign body response that prevents these tumor cells from forming a secondary tumor at the implant when they arrive. However, it seems if the tumor cells arrive first before the foreign body response is established it seems they have an advantage and are able to subvert the microenvironment to allow their expansion. This is particularly interesting due to the fact that 20 tumor cells is well below the reported number of tumor cells that is required to form a tumor in limiting dilution assays to identify cancer stem cell frequency in the 4T1 tumor cell line [242]. The long term fate of tumor cells recruited to scaffolds is a crucial area for further study as the ability of the scaffold site to serve as an active site that promotes secondary tumor growth would be detrimental to clinical translation. Furthermore, enhanced understanding of the mechanisms of quiescence or dormancy at the implant may help provide basic answers within the field of tumor dormancy that have been very difficult to study in animal models.

8.3.5 Translation of biomaterial scaffolds for detection of metastasis

The first crucial consideration for clinical translation of the platform technology discussed herein is device design and fabrication including material, fabrication method, and size. Scaffold design and size are crucial to scaffold function in humans. We anticipate that the appropriate size for humans will be a scaffold 13 mm in diameter (instead of the 5 mm used in mouse studies) and 2 mm in height. This size allows for a large enough implant that it could be biopsied multiple times if needed but also small enough that it should not be noticeable or cause any discomfort for the patient. Additionally, fabrication must be conducted in a GMP facility and thus strides have been made to fabricate PCL scaffolds using a melt-dispersion process (Youngblood et al., unpublished) which is easily adaptable to GMP practices compared to the synthesis of polymer microparticles. The melt-dispersion process also allows for a greater level of quality control on the end product as there will no longer be any batch-to-batch variability in microparticle size.

The method of non-invasive imaging and other analysis techniques are the next critical components of translation of this platform into humans. This dissertation reports the use of high frequency ultrasound for monitoring of scaffold tissue parameters associated with metastasis in mice. Studies to determine the feasibility of longitudinal monitoring must be performed in patients as well. However, the first studies in humans with the scaffold will likely be a simple readout of whether tumor cells were recruited to the scaffold or not via histology and staining for carcinoma associated markers like pan-cytokeratin. If tumor cells and immune cells associated with metastasis are recruited to the scaffold implant, the next step will be validating a protocol for non-invasive imaging and longitudinal monitoring of patient implants.

This dissertation reports on the ability of biomaterial scaffolds to recruit tumor cells in a variety of different models including orthotopic human 231BR and mouse 4T1 triple negative breast cancer models as well as transgenic models of breast cancer

and pancreatic cancer. These results indicate a common mechanism of metastasis in these models and recruitment of tumor cells and metastasis-associated immune cells to the scaffold in varied disease models. Transgenic models are the most translatable implemented in the Shea Lab to date, however more work should be done with other models of cancer metastasis to determine scaffold function in these models. Current evidence points to the idea that the scaffold may be suitable for use in a wide array of metastasizing cancers, but further investigation is warranted.

An emerging method for the detection of metastasis or tumor progression is the analysis of the scaffold microenvironment and gene signature (Oakes et al., unpublished). These results indicate that the scaffold gene signature is capable of predicting sensitivity or resistance to an applied therapy, in this case resection of the primary tumor. These results are an exciting complement to the detection of tumor cells and provide a platform for detection of tumor-dependent immunomodulation that may be more sensitive than the detection of tumor cells themselves. However, it remains to be seen if this information could be gathered from a simple blood test rather than using the foreign body response to an implanted scaffold. Further work to elucidate the differential gene expression that may be indicative of tumor progression and/or metastasis between the immune cells as part of the foreign body response to the scaffold and those in the blood must be performed.

With the development of new responsive biomaterials, there is an opportunity for the next generation of scaffolds that recruit metastatic cancer cells and respond to tumor-dependent immunomodulation to be dynamic and responsive (or smart) [152] and provide a simple readout as the result of tumor cell recruitment, the presence of a soluble factor associated with metastasis, or the binding of a specific immune cell type to a ligand in the material. These next generation smart materials have the unique opportunity to provide a very simple readout and integrated biochemical or biomolecular assay within the material, at the cost of increased complexity of the

material itself and potentially greater barriers to regulation. Clinical implementation of materials for metastasis detection will require either development of smart materials or use of simple materials like those described in this dissertation with development and validation of more complex assays for the analysis of tumor cell arrival and alteration of immune cell populations and/or gene expression.

Given the significant preclinical findings previously published and presented in this dissertation, there is sufficient evidence to move forward in a Phase I trial for safety and efficacy of a poly(ε-caprolactone) scaffold to recruit metastatic tumor cells in stage IV breast cancer patients. This trial has been designed, approved by the Institutional Review Board and Tumor Board at University of Michigan and is currently waiting for approval from the Food and Drug Administration for the scaffold device. This trial will be the first step toward implementing this technology in patients for the detection of metastasis and will provide crucial evidence for moving forward to implementing the scaffold for the early detection of metastasis in patients who have been through treatment and declared cancer-free but are still at risk for future metastatic recurrence.

BIBLIOGRAPHY

BIBLIOGRAPHY

[1] E B Ranklin and A J Giaccia. Hypoxic control of metastasis. *Science*, 352 (6282):175–180, 2016.

[2] S Turajlic and C Swanton. Metastasis as an evolutionary process. *Science*, 352 (6282):169–174, 2016.

[3] D X Nguyen, P D Bos, and J Massague. Metastasis: from dissemination to organ-specific colonization. *Nat Rev Cancer*, 9(4):274–284, 2009. doi: 10.1038/nrc2622. URL `http://www.ncbi.nlm.nih.gov/pubmed/19308067`.

[4] I J Fidler. The pathogenesis of cancer metastasis: the 'seed and soil' hypothesis revisited. *Nat Rev Cancer*, 3(6):453–458, 2003. doi: 10.1038/nrc1098. URL `http://www.ncbi.nlm.nih.gov/pubmed/12778135`.

[5] G P Gupta and J Massague. Cancer metastasis: building a framework. *Cell*, 127(4):679–695, 2006. doi: 10.1016/j.cell.2006.11.001. URL `http://www.ncbi.nlm.nih.gov/pubmed/17110329`.

[6] S Paget. The distribution of secondary growths in cancer of the breast. *Lancet*, 133(3421):98–101, 1889. URL `http://www.ncbi.nlm.nih.gov/pubmed/2673568`.

[7] Héctor Peinado, Maša Alečković, Simon Lavotshkin, Irina Matei, Bruno Costa-Silva, Gema Moreno-Bueno, Marta Hergueta-Redondo, Caitlin Williams, Guillermo García-Santos, Cyrus Ghajar, Ayuko Nitadori-Hoshino, Caitlin Hoffman, Karen Badal, Benjamin A Garcia, Margaret K Callahan, Jianda Yuan, Vilma R Martins, Johan Skog, Rosandra N Kaplan, Mary S Brady, Jedd D Wolchok, Paul B Chapman, Yibin Kang, Jacqueline Bromberg, David Lyden, M Aleckovic, Simon Lavotshkin, Irina Matei, Bruno Costa-Silva, Gema Moreno-Bueno, Marta Hergueta-Redondo, Caitlin Williams, G Garcia-Santos, Cyrus Ghajar, Ayuko Nitadori-Hoshino, Caitlin Hoffman, Karen Badal, Benjamin A Garcia, Margaret K Callahan, Jianda Yuan, Vilma R Martins, Johan Skog, Rosandra N Kaplan, Mary S Brady, Jedd D Wolchok, Paul B Chapman, Yibin Kang, Jacqueline Bromberg, and David Lyden. Melanoma exosomes educate bone marrow progenitor cells toward a pro-metastatic phenotype through MET. *Nature medicine*, 18(6):883–91, 2012. ISSN 1546-170X. doi: 10.1038/nm.2753.

[8] R N Kaplan, R D Riba, S Zacharoulis, A H Bramley, L Vincent, C Costa, D D MacDonald, D K Jin, K Shido, S A Kerns, Z Zhu, D Hicklin, Y Wu, J L Port,

N Altorki, E R Port, D Ruggero, S V Shmelkov, K K Jensen, S Rafii, and D Lyden. VEGFR1-positive haematopoietic bone marrow progenitors initiate the pre-metastatic niche. *Nature*, 438(7069):820–827, 2005. doi: 10.1038/nature04186. URL http://www.ncbi.nlm.nih.gov/pubmed/16341007.

[9] S C Chafe, Y Lou, J Sceneay, M Vallejo, M J Hamilton, P C McDonald, K L Bennewith, A Moller, and S Dedhar. Carbonic anhydrase IX promotes myeloid-derived suppressor cell mobilization and establishment of a metastatic niche by stimulating G-CSF production. *Cancer Res*, 75(6):996–1008, 2015. doi: 10.1158/0008-5472.CAN-14-3000. URL https://www.ncbi.nlm.nih.gov/pubmed/25623234.

[10] J T Erler, K L Bennewith, T R Cox, G Lang, D Bird, A Koong, Q T Le, and A J Giaccia. Hypoxia-induced lysyl oxidase is a critical mediator of bone marrow cell recruitment to form the premetastatic niche. *Cancer Cell*, 15(1):35–44, 2009. doi: 10.1016/j.ccr.2008.11.012. URL http://www.ncbi.nlm.nih.gov/pubmed/19111879.

[11] A J Giles, C M Reid, J D Evans, M Murgai, Y Vicioso, S L Highfill, M Kasai, L Vahdat, C L Mackall, D Lyden, L Wexler, and R N Kaplan. Activation of Hematopoietic Stem/Progenitor Cells Promotes Immunosuppression Within the Pre-metastatic Niche. *Cancer Res*, 76(6):1335–1347, 2016. doi: 10.1158/0008-5472.CAN-15-0204. URL http://www.ncbi.nlm.nih.gov/pubmed/26719537.

[12] M Kowanetz, X Wu, J Lee, M Tan, T Hagenbeek, X Qu, L Yu, J Ross, N Korsisaari, T Cao, H Bou-Reslan, D Kallop, R Weimer, M J Ludlam, J S Kaminker, Z Modrusan, N van Bruggen, F V Peale, R Carano, Y G Meng, and N Ferrara. Granulocyte-colony stimulating factor promotes lung metastasis through mobilization of Ly6G+Ly6C+ granulocytes. *Proc Natl Acad Sci U S A*, 107(50):21248–21255, 2010. doi: 10.1073/pnas.1015855107. URL https://www.ncbi.nlm.nih.gov/pubmed/21081700.

[13] Y Liu, Y Gu, Y Han, Q Zhang, Z Jiang, X Zhang, B Huang, X Xu, J Zheng, and X Cao. Tumor Exosomal RNAs Promote Lung Pre-metastatic Niche Formation by Activating Alveolar Epithelial TLR3 to Recruit Neutrophils. *Cancer Cell*, 30(2):243–256, 2016. doi: 10.1016/j.ccell.2016.06.021. URL https://www.ncbi.nlm.nih.gov/pubmed/27505671.

[14] P B Olkhanud, D Baatar, M Bodogai, F Hakim, R Gress, R L Anderson, J Deng, M Xu, S Briest, and A Biragyn. Breast cancer lung metastasis requires expression of chemokine receptor CCR4 and regulatory T cells. *Cancer Res*, 69(14):5996–6004, 2009. doi: 10.1158/0008-5472.CAN-08-4619. URL http://www.ncbi.nlm.nih.gov/pubmed/19567680.

[15] B Z Qian, J Li, H Zhang, T Kitamura, J Zhang, L R Campion, E A Kaiser, L A Snyder, and J W Pollard. CCL2 recruits inflammatory monocytes to facilitate

breast-tumour metastasis. *Nature*, 475(7355):222–225, 2011. doi: 10.1038/nature10138. URL http://www.ncbi.nlm.nih.gov/pubmed/21654748.

[16] J. Sceneay, M. T. Chow, a. Chen, H. M. Halse, C. S. F. Wong, D. M. Andrews, E. K. Sloan, B. S. Parker, D. D. Bowtell, M. J. Smyth, and a. Moller. Primary Tumor Hypoxia Recruits CD11b+/Ly6Cmed/Ly6G+ Immune Suppressor Cells and Compromises NK Cell Cytotoxicity in the Premetastatic Niche. *Cancer Research*, 72(16):3906–3911, 2012. ISSN 0008-5472. doi: 10.1158/0008-5472.CAN-11-3873. URL https://www.ncbi.nlm.nih.gov/pubmed/22751463.

[17] Bruno Costa-Silva, Nicole M Aiello, Allyson J Ocean, Swarnima Singh, Haiying Zhang, Basant Kumar Thakur, Annette Becker, Ayuko Hoshino, Milica Tešić Mark, Henrik Molina, Jenny Xiang, Tuo Zhang, Till-Martin Theilen, Guillermo García-Santos, Caitlin Williams, Yonathan Ararso, Yujie Huang, Gonçalo Rodrigues, Tang-Long Shen, Knut Jørgen Labori, Inger Marie Bowitz Lothe, Elin H Kure, Jonathan Hernandez, Alexandre Doussot, Saya H Ebbesen, Paul M Grandgenett, Michael a Hollingsworth, Maneesh Jain, Kavita Mallya, Surinder K Batra, William R Jarnagin, Robert E Schwartz, Irina Matei, Héctor Peinado, Ben Z Stanger, Jacqueline Bromberg, and David Lyden. Pancreatic cancer exosomes initiate pre-metastatic niche formation in the liver. *Nature cell biology*, (6), 2015. ISSN 1476-4679. doi: 10.1038/ncb3169. URL https://www.nature.com/articles/ncb3169.pdf.

[18] Ayuko Hoshino, Bruno Costa-Silva, Tang-Long L Shen, Goncalo Rodrigues, Ayako Hashimoto, Milica Tesic Mark, Henrik Molina, Shinji Kohsaka, Angela Di Giannatale, Sophia Ceder, Swarnima Singh, Caitlin Williams, Nadine Soplop, Kunihiro Uryu, Lindsay Pharmer, Tari King, Linda Bojmar, Alexander E. Davies, Yonathan Ararso, Tuo Zhang, Haiying Zhang, Jonathan Hernandez, Joshua M. Weiss, Vanessa D. Dumont-Cole, Kimberly Kramer, Leonard H. Wexler, Aru Narendran, Gary K. Schwartz, John H. Healey, Per Sandstrom, K J Labori, Elin H. Kure, Paul M. Grandgenett, Michael A. Hollingsworth, Maria de Sousa, Sukhwinder Kaur, Maneesh Jain, Kavita Mallya, Surinder K. Batra, William R. Jarnagin, Mary S. Brady, Oystein Fodstad, Volkmar Muller, Klaus Pantel, Andy J. Minn, Mina J. Bissell, Benjamin A. Garcia, Yibin Kang, Vinagolu K. Rajasekhar, Cyrus M. Ghajar, Irina Matei, Hector Peinado, Jacqueline Bromberg, David Lyden, Knut Jørgen Labori, Elin H. Kure, Paul M. Grandgenett, Michael A. Hollingsworth, Maria de Sousa, Sukhwinder Kaur, Maneesh Jain, Kavita Mallya, Surinder K. Batra, William R. Jarnagin, Mary S. Brady, Oystein Fodstad, Volkmar Muller, Klaus Pantel, Andy J. Minn, Mina J. Bissell, Benjamin A. Garcia, Yibin Kang, Vinagolu K. Rajasekhar, Cyrus M. Ghajar, Irina Matei, Hector Peinado, Jacqueline Bromberg, and David Lyden. Tumour exosome integrins determine organotropic metastasis. *Nature*, 527(7578):329–335, 2015. ISSN 0028-0836. doi: 10.1038/nature15756. URL http://www.nature.com/doifinder/10.1038/nature15756 http://www.ncbi.nlm.nih.gov/pubmed/26524530.

[19] Sachie Hiratsuka, Akira Watanabe, Hiroyuki Aburatani, and Yoshiro Maru. Tumour-mediated upregulation of chemoattractants and recruitment of myeloid cells predetermines lung metastasis. *Nature Cell Biology*, 8(12):1369–1375, 2006. ISSN 1465-7392. doi: 10.1038/ncb1507. URL http://www.nature.com/doifinder/10.1038/ncb1507 http://www.ncbi.nlm.nih.gov/pubmed/17128264.

[20] B J Gill and J L West. Modeling the tumor extracellular matrix: Tissue engineering tools repurposed towards new frontiers in cancer biology. *J Biomech*, 47(9):1969–1978, 2014. doi: 10.1016/j.jbiomech.2013.09.029. URL http://www.ncbi.nlm.nih.gov/pubmed/24300038.

[21] David W. Infanger, Maureen E. Lynch, and Claudia Fischbach. Engineered Culture Models for Studies of Tumor-Microenvironment Interactions. *Annual Review of Biomedical Engineering*, 15(1):29–53, 2013. ISSN 1523-9829. doi: 10.1146/annurev-bioeng-071811-150028.

[22] L Gu and D J Mooney. Biomaterials and emerging anticancer therapeutics: engineering the microenvironment. *Nat Rev Cancer*, 16(1):56–66, 2016. doi: 10.1038/nrc.2015.3. URL https://www.ncbi.nlm.nih.gov/pubmed/26694936.

[23] S M Ehsan, K M Welch-Reardon, M L Waterman, C C Hughes, and S C George. A three-dimensional in vitro model of tumor cell intravasation. *Integr Biol (Camb)*, 6(6):603–610, 2014. doi: 10.1039/c3ib40170g. URL http://www.ncbi.nlm.nih.gov/pubmed/24763498.

[24] J S Jeon, S Bersini, M Gilardi, G Dubini, J L Charest, M Moretti, and R D Kamm. Human 3D vascularized organotypic microfluidic assays to study breast cancer cell extravasation. *Proc Natl Acad Sci U S A*, 112(1):214–219, 2015. doi: 10.1073/pnas.1417115112. URL http://www.ncbi.nlm.nih.gov/pubmed/25524628.

[25] J S Jeon, I K Zervantonakis, S Chung, R D Kamm, and J L Charest. In vitro model of tumor cell extravasation. *PLoS One*, 8(2):e56910, 2013. doi: 10.1371/journal.pone.0056910. URL http://www.ncbi.nlm.nih.gov/pubmed/23437268.

[26] C Y Ko, L Wu, A M Nair, Y T Tsai, V K Lin, and L Tang. The use of chemokine-releasing tissue engineering scaffolds in a model of inflammatory response-mediated melanoma cancer metastasis. *Biomaterials*, 33(3):876–885, 2012. doi: 10.1016/j.biomaterials.2011.10.002. URL http://www.ncbi.nlm.nih.gov/pubmed/22019117.

[27] Francesca Bersani, Jungwoo Lee, Min Yu, Robert Morris, Rushil Desai, Sridhar Ramaswamy, Mehmet Toner, Daniel a Haber, and Biju Parekkadan. Bioengineered implantable scaffolds as a tool to study stromal-derived factors in metastatic cancer models. *Cancer research*, 74(24):7229–7238,

2014. ISSN 1538-7445. doi: 10.1158/0008-5472.CAN-14-1809. URL http://www.ncbi.nlm.nih.gov/pubmed/25339351.

[28] D Barkan, H Kleinman, J L Simmons, H Asmussen, A K Kamaraju, M J Hoenorhoff, Z Y Liu, S V Costes, E H Cho, S Lockett, C Khanna, A F Chambers, and J E Green. Inhibition of metastatic outgrowth from single dormant tumor cells by targeting the cytoskeleton. *Cancer Res*, 68(15):6241–6250, 2008. doi: 10.1158/0008-5472.CAN-07-6849. URL http://www.ncbi.nlm.nih.gov/pubmed/18676848.

[29] A de la Fuente, L Alonso-Alconada, C Costa, J Cueva, T Garcia-Caballero, R Lopez-Lopez, and M Abal. M-Trap: Exosome-Based Capture of Tumor Cells as a New Technology in Peritoneal Metastasis. *J Natl Cancer Inst*, 107(9), 2015. doi: 10.1093/jnci/djv184. URL http://www.ncbi.nlm.nih.gov/pubmed/26150590.

[30] Shreyas S. Rao, Grace G. Bushnell, Samira M. Azarin, Graham Spicer, Brian A. Aguado, Jenna R. Stoehr, Eric J. Jiang, Vadim Backman, Lonnie D. Shea, and Jacqueline S. Jeruss. Enhanced survival with implantable scaffolds that capture metastatic breast cancer cells in vivo. *Cancer Research*, 76(18):5209–5218, sep 2016. ISSN 15387445. doi: 10.1158/0008-5472.CAN-15-2106. URL http://europepmc.org/abstract/med/27635043.

[31] Samira M Azarin, Ji Yi, Robert M Gower, Brian A Aguado, Megan E Sullivan, Ashley G Goodman, Eric J Jiang, Shreyas S Rao, Yinying Ren, Susan L Tucker, Vadim Backman, Jacqueline S Jeruss, and Lonnie D Shea. ARTICLE In vivo capture and label-free detection of early metastatic cells. *Nature Communications*, 6:8094, 2015. doi: 10.1038/ncomms9094.

[32] L Thibaudeau, A V Taubenberger, B M Holzapfel, V M Quent, T Fuehrmann, P Hesami, T D Brown, P D Dalton, C A Power, B G Hollier, and D W Hutmacher. A tissue-engineered humanized xenograft model of human breast cancer metastasis to bone. *Dis Model Mech*, 7(2):299–309, 2014. doi: 10.1242/dmm.014076. URL http://www.ncbi.nlm.nih.gov/pubmed/24713276.

[33] Jodie E Moreau, Kristen Anderson, Joshua R Mauney, Trang Nguyen, David L Kaplan, and Michael Rosenblatt. Tissue-engineered bone serves as a target for metastasis of human breast cancer in a mouse model. *Cancer Research*, 67 (21):10304, 2007. ISSN 1538-7445. doi: 10.1158/0008-5472.CAN-07-2483. URL http://www.ncbi.nlm.nih.gov/pubmed/17974972.

[34] B A Aguado, J J Wu, S M Azarin, D Nanavati, S S Rao, G G Bushnell, C B Medicherla, and L D Shea. Secretome identification of immune cell factors mediating metastatic cell homing. *Sci Rep*, 5:17566, 2015. doi: 10.1038/srep17566.

[35] S P Pathi, D D Lin, J R Dorvee, L A Estroff, and C Fischbach. Hydroxyapatite nanoparticle-containing scaffolds for the study of breast cancer bone metastasis.

Biomaterials, 32(22):5112–5122, 2011. doi: 10.1016/j.biomaterials.2011.03.055. URL https://www.ncbi.nlm.nih.gov/pubmed/21507478.

[36] Jungwoo Lee, Matthew Li, Jack Milwid, Joshua Dunham, Claudio Vinegoni, Rostic Gorbatov, Yoshiko Iwamoto, Fangjing Wang, Keyue Shen, Kimberley Hatfield, et al. Implantable microenvironments to attract hematopoietic stem/cancer cells. *Proceedings of the National Academy of Sciences*, 109(48): 19638–19643, 2012.

[37] S R Vaiselbuh, M Edelman, J M Lipton, and J M Liu. Ectopic human mesenchymal stem cell-coated scaffolds in NOD/SCID mice: an in vivo model of the leukemia niche. *Tissue Eng Part C Methods*, 16(6):1523–1531, 2010. doi: 10.1089/ten.tec.2010.0179. URL http://www.ncbi.nlm.nih.gov/pubmed/20586611.

[38] E De Vlieghere, F Gremonprez, L Verset, L Marien, C J Jones, B De Craene, G Berx, B Descamps, C Vanhove, J P Remon, W Ceelen, P Demetter, M Bracke, B G De Geest, and O De Wever. Tumor-environment biomimetics delay peritoneal metastasis formation by deceiving and redirecting disseminated cancer cells. *Biomaterials*, 54:148–157, 2015. doi: 10.1016/j.biomaterials.2015.03.012. URL http://www.ncbi.nlm.nih.gov/pubmed/25907048.

[39] J A Nemeth, J F Harb, U Barroso Jr., Z He, D J Grignon, and M L Cher. Severe combined immunodeficient-hu model of human prostate cancer metastasis to human bone. *Cancer Res*, 59(8):1987–1993, 1999. URL http://www.ncbi.nlm.nih.gov/pubmed/10213511.

[40] T S Xia, G Z Wang, Q Ding, X A Liu, W B Zhou, Y F Zhang, X M Zha, Q Du, X J Ni, J Wang, S Y Miao, and S Wang. Bone metastasis in a novel breast cancer mouse model containing human breast and human bone. *Breast Cancer Res Treat*, 132(2):471–486, 2012. doi: 10.1007/s10549-011-1496-0. URL http://www.ncbi.nlm.nih.gov/pubmed/21638054.

[41] F. Philipp Seib, Janice E. Berry, Yusuke Shiozawa, Russell S. Taichman, and David L. Kaplan. Tissue engineering a surrogate niche for metastatic cancer cells. *Biomaterials*, 51:313–319, 2015. ISSN 18785905. doi: 10.1016/j.biomaterials.2015.01.076. URL http://www.ncbi.nlm.nih.gov/pubmed/25771021.

[42] B.A. Aguado, J.R. Caffe, D. Nanavati, S.S. Rao, G.G. Bushnell, S.M. Azarin, and L.D. Shea. Extracellular matrix mediators of metastatic cell colonization characterized using scaffold mimics of the pre-metastatic niche. *Acta Biomaterialia*, 33, 2016. ISSN 18787568 17427061. doi: 10.1016/j.actbio.2016.01.043.

[43] A V Taubenberger, V M Quent, L Thibaudeau, J A Clements, and D W Hutmacher. Delineating breast cancer cell interactions with engineered bone microenvironments. *J Bone Miner Res*, 28(6):1399–1411, 2013. doi: 10.1002/jbmr.1875. URL http://www.ncbi.nlm.nih.gov/pubmed/23362043.

[44] S Bersini, J S Jeon, G Dubini, C Arrigoni, S Chung, J L Charest, M Moretti, and R D Kamm. A microfluidic 3D in vitro model for specificity of breast cancer metastasis to bone. *Biomaterials*, 35 (8):2454–2461, 2014. doi: 10.1016/j.biomaterials.2013.11.050. URL https://www.ncbi.nlm.nih.gov/pubmed/24388382.

[45] L Yang, C M Edwards, and G R Mundy. Gr-1+CD11b+ myeloid-derived suppressor cells: formidable partners in tumor metastasis. *J Bone Miner Res*, 25(8):1701–1706, 2010. doi: 10.1002/jbmr.154. URL http://www.ncbi.nlm.nih.gov/pubmed/20572008.

[46] Dmitry I. Gabrilovich and Srinivas Nagaraj. Myeloid-derived suppressor cells as regulators of the immune system. *Nat Rev Immunol*, 9(3):162–174, 2009. ISSN 1474-1733. doi: 10.1038/nri2506. URL http://www.nature.com/doifinder/10.1038/nri2506 http://www.ncbi.nlm.nih.gov/pubmed/19197294.

[47] S K Sharma, N K Chintala, S K Vadrevu, J Patel, M Karbowniczek, and M M Markiewski. Pulmonary alveolar macrophages contribute to the premetastatic niche by suppressing antitumor T cell responses in the lungs. *J Immunol*, 194(11):5529–5538, 2015. doi: 10.4049/jimmunol.1403215. URL http://www.ncbi.nlm.nih.gov/pubmed/25911761.

[48] T R Cox, R M Rumney, E M Schoof, L Perryman, A M Hoye, A Agrawal, D Bird, N A Latif, H Forrest, H R Evans, I D Huggins, G Lang, R Linding, A Gartland, and J T Erler. The hypoxic cancer secretome induces pre-metastatic bone lesions through lysyl oxidase. *Nature*, 522(7554), 2015. ISSN 0028-0836. doi: 10.1038/nature14492.

[49] A C Monteiro, A C Leal, T Goncalves-Silva, A C Mercadante, F Kestelman, S B Chaves, R B Azevedo, J P Monteiro, and A Bonomo. T cells induce pre-metastatic osteolytic disease and help bone metastases establishment in a mouse model of metastatic breast cancer. *PLoS One*, 8(7):e68171, 2013. doi: 10.1371/journal.pone.0068171. URL http://www.ncbi.nlm.nih.gov/pubmed/23935856.

[50] W Tan, W Zhang, A Strasner, S Grivennikov, J Q Cheng, R M Hoffman, and M Karin. Tumour-infiltrating regulatory T cells stimulate mammary cancer metastasis through RANKL-RANK signalling. *Nature*, 470(7335):548–553, 2011. doi: 10.1038/nature09707. URL http://www.ncbi.nlm.nih.gov/pubmed/21326202.

[51] H Peinado, S Lavotshkin, and D Lyden. The secreted factors responsible for pre-metastatic niche formation: old sayings and new thoughts. *Semin Cancer Biol*, 21(2):139–146, 2011. doi: 10.1016/j.semcancer.2011.01.002. URL http://www.ncbi.nlm.nih.gov/pubmed/21251983.

[52] H A Smith and Y Kang. The metastasis-promoting roles of tumor-associated immune cells. *J Mol Med (Berl)*, 91(4):411–429, 2013. doi: 10.1007/s00109-013-1021-5. URL http://www.ncbi.nlm.nih.gov/pubmed/23515621.

[53] M B Headley, A Bins, A Nip, E W Roberts, M R Looney, A Gerard, and M F Krummel. Visualization of immediate immune responses to pioneer metastatic cells in the lung. *Nature*, 2016. doi: 10.1038/nature16985. URL http://www.ncbi.nlm.nih.gov/pubmed/26982733.

[54] J M Anderson, A Rodriguez, and D T Chang. Foreign body reaction to biomaterials. *Semin Immunol*, 20(2):86–100, 2008. doi: 10.1016/j.smim.2007.11.004. URL https://www.ncbi.nlm.nih.gov/pubmed/18162407.

[55] S Franz, S Rammelt, D Scharnweber, and J C Simon. Immune responses to implants - a review of the implications for the design of immunomodulatory biomaterials. *Biomaterials*, 32(28): 6692–6709, 2011. doi: 10.1016/j.biomaterials.2011.05.078. URL https://www.ncbi.nlm.nih.gov/pubmed/21715002.

[56] A G Mikos, L V McIntire, J M Anderson, and J E Babensee. Host response to tissue engineered devices. *Adv Drug Deliv Rev*, 33(1-2):111–139, 1998. URL https://www.ncbi.nlm.nih.gov/pubmed/10837656.

[57] R M Boehler, J G Graham, and L D Shea. Tissue engineering tools for modulation of the immune response. *Biotechniques*, 51 (4):239–40, 242, 244 passim, 2011. doi: 10.2144/000113754. URL https://www.ncbi.nlm.nih.gov/pubmed/21988690.

[58] Xiao Qing Liu, Rosemarie Kiefl, Claudia Roskopf, Fei Tian, and Rudolf M. Huber. Interactions among Lung Cancer Cells, Fibroblasts, and Macrophages in 3D Co-Cultures and the Impact on MMP-1 and VEGF Expression. *PLoS One*, 11(5):e0156268, 2016. ISSN 19326203. doi: 10.1371/journal.pone.0156268. URL https://www.ncbi.nlm.nih.gov/pubmed/27232698.

[59] Yang Liu and Xuetao Cao. Characteristics and Significance of the Pre-metastatic Niche. *Cancer Cell*, 30(5):668–681, 2016. ISSN 18783686. doi: 10.1016/j.ccell.2016.09.011. URL http://dx.doi.org/10.1016/j.ccell.2016.09.011 https://www.ncbi.nlm.nih.gov/pubmed/27846389.

[60] S Hiratsuka, A Watanabe, Y Sakurai, S Akashi-Takamura, S Ishibashi, K Miyake, M Shibuya, S Akira, H Aburatani, and Y Maru. The S100A8-serum amyloid A3-TLR4 paracrine cascade establishes a pre-metastatic phase. *Nat Cell Biol*, 10(11):1349–1355, 2008. doi: 10.1038/ncb1794. URL http://www.ncbi.nlm.nih.gov/pubmed/18820689.

[61] M R Rutkowski, T L Stephen, N Svoronos, M J Allegrezza, A J Tesone, A Perales-Puchalt, E Brencicova, X Escovar-Fadul, J M Nguyen, M G

Cadungog, R Zhang, M Salatino, J Tchou, G A Rabinovich, and J R Conejo-Garcia. Microbially driven TLR5-dependent signaling governs distal malignant progression through tumor-promoting inflammation. *Cancer Cell*, 27(1):27–40, 2015. doi: 10.1016/j.ccell.2014.11.009. URL https://www.ncbi.nlm.nih.gov/pubmed/25533336.

[62] Hannah H. Yan, Michael Pickup, Yanli Pang, Agnieszka E. Gorska, Zhaoyang Li, Anna Chytil, Yipeng Geng, Jerome W. Gray, Harold L. Moses, and Li Yang. Gr-1+CD11b+ myeloid cells tip the balance of immune protection to tumor promotion in the premetastatic lung. *Cancer Research*, 70(15):6139–6149, 2010. ISSN 00085472. doi: 10.1158/0008-5472.CAN-10-0706. URL http://www.ncbi.nlm.nih.gov/pubmed/20631080.

[63] V Krishnan, E A Vogler, D M Sosnoski, and A M Mastro. In vitro mimics of bone remodeling and the vicious cycle of cancer in bone. *J Cell Physiol*, 229(4):453–462, 2014. doi: 10.1002/jcp.24464. URL http://www.ncbi.nlm.nih.gov/pubmed/24022654.

[64] Y Kang, P M Siegel, W Shu, M Drobnjak, S M Kakonen, C Cordon-Cardo, T A Guise, and J Massague. A multigenic program mediating breast cancer metastasis to bone. *Cancer Cell*, 3(6):537–549, 2003. URL http://www.ncbi.nlm.nih.gov/pubmed/12842083.

[65] S Rafii and D Lyden. S100 chemokines mediate bookmarking of premetastatic niches. *Nat Cell Biol*, 8(12):1321–1323, 2006. doi: 10.1038/ncb1206-1321. URL https://www.ncbi.nlm.nih.gov/pubmed/17139281.

[66] R M Gower, R M Boehler, S M Azarin, C F Ricci, J N Leonard, and L D Shea. Modulation of leukocyte infiltration and phenotype in microporous tissue engineering scaffolds via vector induced IL-10 expression. *Biomaterials*, 35(6):2024–2031, 2014. doi: 10.1016/j.biomaterials.2013.11.036. URL https://www.ncbi.nlm.nih.gov/pubmed/24309498.

[67] H Kwon, H J Kim, W L Rice, B Subramanian, S H Park, I Georgakoudi, and D L Kaplan. Development of an in vitro model to study the impact of BMP-2 on metastasis to bone. *Journal of Tissue Engineering and Regenerative Medicine*, 4(8):590–599, 2010. doi: 10.1002/term.268.

[68] Y Katsuno, A Hanyu, H Kanda, Y Ishikawa, F Akiyama, T Iwase, E Ogata, S Ehata, K Miyazono, and T Imamura. Bone morphogenetic protein signaling enhances invasion and bone metastasis of breast cancer cells through Smad pathway. *Oncogene*, 27(49):6322–6333, 2008. doi: 10.1038/onc.2008.232. URL https://www.ncbi.nlm.nih.gov/pubmed/18663362.

[69] Brian T Feeley, Lucie Krenek, Nancy Liu, Wellington K Hsu, Seth C Gamradt, Edward M Schwarz, Johnny Huard, and Jay R Lieberman. Overexpression of noggin inhibits BMP-mediated growth of osteolytic prostate cancer lesions. *Bone*, 38(2):154–166, 2006.

[70] A S Azmi, B Bao, and F H Sarkar. Exosomes in cancer development, metastasis, and drug resistance: a comprehensive review. *Cancer Metastasis Rev*, 32(3-4):623–642, 2013. doi: 10.1007/s10555-013-9441-9. URL https://www.ncbi.nlm.nih.gov/pubmed/23709120.

[71] B K Thakur, H Zhang, A Becker, I Matei, Y Huang, B Costa-Silva, Y Zheng, A Hoshino, H Brazier, J Xiang, C Williams, R Rodriguez-Barrueco, J M Silva, W Zhang, S Hearn, O Elemento, N Paknejad, K Manova-Todorova, K Welte, J Bromberg, H Peinado, and D Lyden. Double-stranded DNA in exosomes: a novel biomarker in cancer detection. *Cell Res*, 24(6):766–769, 2014. doi: 10.1038/cr.2014.44. URL https://www.ncbi.nlm.nih.gov/pubmed/24710597.

[72] H Valadi, K Ekstrom, A Bossios, M Sjostrand, J J Lee, and J O Lotvall. Exosome-mediated transfer of mRNAs and microRNAs is a novel mechanism of genetic exchange between cells. *Nat Cell Biol*, 9(6):654–659, 2007. doi: 10.1038/ncb1596. URL https://www.ncbi.nlm.nih.gov/pubmed/17486113.

[73] L T Brinton, H S Sloane, M Kester, and K A Kelly. Formation and role of exosomes in cancer. *Cell Mol Life Sci*, 72(4):659–671, 2015. doi: 10.1007/s00018-014-1764-3. URL http://www.ncbi.nlm.nih.gov/pubmed/25336151.

[74] J S Desgrosellier and D A Cheresh. Integrins in cancer: biological implications and therapeutic opportunities. *Nat Rev Cancer*, 10(1):9–22, 2010. doi: 10.1038/nrc2748. URL http://www.ncbi.nlm.nih.gov/pubmed/20029421.

[75] L E Barney, E C Dandley, L E Jansen, N G Reich, A M Mercurio, and S R Peyton. A cell-ECM screening method to predict breast cancer metastasis. *Integr Biol (Camb)*, 7(2):198–212, 2015. doi: 10.1039/c4ib00218k. URL http://www.ncbi.nlm.nih.gov/pubmed/25537447.

[76] P M Crapo, T W Gilbert, and S F Badylak. An overview of tissue and whole organ decellularization processes. *Biomaterials*, 32(12):3233–3243, 2011. doi: 10.1016/j.biomaterials.2011.01.057.

[77] W D Lu, L Zhang, C L Wu, Z G Liu, G Y Lei, J Liu, W Gao, and Y R Hu. Development of an Acellular Tumor Extracellular Matrix as a Three-Dimensional Scaffold for Tumor Engineering. *PLoS One*, 9(7), 2014. doi: ARTN e103672 10.1371/journal.pone.0103672.

[78] D K Mishra, M J Thrall, B N Baird, H C Ott, S H Blackmon, J M Kurie, and M P Kim. Human lung cancer cells grown on acellular rat lung matrix create perfusable tumor nodules. *Ann Thorac Surg*, 93(4):1075–1081, 2012. doi: 10.1016/j.athoracsur.2012.01.011. URL https://www.ncbi.nlm.nih.gov/pubmed/22385822.

[79] Aranzazu Villasante, Alessandro Marturano-Kruik, and Gordana Vunjak-Novakovic. Bioengineered human tumor within a bone niche. *Biomaterials*, 35

(22):5785–5794, 2014. ISSN 18785905. doi: 10.1016/j.biomaterials.2014.03.081. URL http://dx.doi.org/10.1016/j.biomaterials.2014.03.081.

[80] B M Holzapfel, J C Reichert, J T Schantz, U Gbureck, L Rackwitz, U Noth, F Jakob, M Rudert, J Groll, and D W Hutmacher. How smart do biomaterials need to be? A translational science and clinical point of view. *Advanced Drug Delivery Reviews*, 65(4):581–603, 2013. doi: 10.1016/j.addr.2012.07.009.

[81] E Lee, E J Fertig, K Jin, S Sukumar, N B Pandey, and A S Popel. Breast cancer cells condition lymphatic endothelial cells within pre-metastatic niches to promote metastasis. *Nature Communications*, 5, 2014. doi: ARTN 4715 10.1038/ncomms5715.

[82] S K Wculek and I Malanchi. Neutrophils support lung colonization of metastasis-initiating breast cancer cells. *Nature*, advance on(7582): 1–21, 2015. ISSN 0028-0836. doi: 10.1038/nature16140. URL http://dx.doi.org/10.1038/nature16140.

[83] R Kalluri. The biology and function of exosomes in cancer. *J Clin Invest*, 126(4):1208–1215, 2016. doi: 10.1172/JCI81135. URL https://www.ncbi.nlm.nih.gov/pubmed/27035812.

[84] Astrid De Boeck, An Hendrix, Dawn Maynard, Mieke Van Bockstal, Annick Daniëls, Patrick Pauwels, Christian Gespach, Marc Bracke, and Olivier De Wever. Differential secretome analysis of cancerassociated fibroblasts and bone marrowderived precursors to identify microenvironmental regulators of colon cancer progression. *Proteomics*, 13(2):379–388, 2013.

[85] Toshiyuki Yoneda, Paul J Williams, Toru Hiraga, Maria Niewolna, and R Nishimura. A bone-seeking clone exhibits different biological properties from the MDA-MB-231 parental human breast cancer cells and a brain-seeking clone in vivo and in vitro. *J Bone Miner Res*, 16(8):1486–1495, 2001. doi: 10.1359/jbmr.2001.16.8.1486. URL https://www.ncbi.nlm.nih.gov/pubmed/11499871.

[86] H Hugo, M L Ackland, T Blick, M G Lawrence, J A Clements, E D Williams, and E W Thompson. Epithelial–mesenchymal and mesenchymal–epithelial transitions in carcinoma progression. *J Cell Physiol*, 213(2):374–383, 2007. doi: 10.1002/jcp.21223. URL http://www.ncbi.nlm.nih.gov/pubmed/17680632.

[87] B Ell and Y Kang. Transcriptional control of cancer metastasis. *Trends Cell Biol*, 23(12):603–611, 2013. doi: 10.1016/j.tcb.2013.06.001. URL http://www.ncbi.nlm.nih.gov/pubmed/23838335.

[88] O H Ocana, R Corcoles, A Fabra, G Moreno-Bueno, H Acloque, S Vega, A Barrallo-Gimeno, A Cano, and M A Nieto. Metastatic colonization requires the repression of the epithelial-mesenchymal transition inducer Prrx1.

Cancer Cell, 22(6):709–724, 2012. doi: 10.1016/j.ccr.2012.10.012. URL http://www.ncbi.nlm.nih.gov/pubmed/23201163.

[89] Cyrus M. Ghajar, Héctor Peinado, Hidetoshi Mori, Irina R. Matei, Kimberley J. Evason, Hélène Brazier, Dena Almeida, Antonius Koller, Katherine A. Hajjar, Didier Y R Stainier, Emily I. Chen, David Lyden, and Mina J. Bissell. No Title. 15(7), 2013. doi: 10.1038/ncb2767.

[90] Filippo G Giancotti. Mechanisms governing metastatic dormancy and reactivation. *Cell*, 155(4):750–764, 2013.

[91] Keith J Luzzi, Ian C MacDonald, Eric E Schmidt, Nancy Kerkvliet, Vincent L Morris, Ann F Chambers, and Alan C Groom. Multistep Nature of Metastatic Inefficiency. *The American Journal of Pathology*, 153(3):865–873, 1998. doi: 10.1016/s0002-9440(10)65628-3.

[92] L Weiss. Metastatic inefficiency. *Adv Cancer Res*, 54:159–211, 1990. URL https://www.ncbi.nlm.nih.gov/pubmed/1688681.

[93] L Weiss. Metastatic inefficiency: intravascular and intraperitoneal implantation of cancer cells. *Cancer Treat Res*, 82:1–11, 1996. URL https://www.ncbi.nlm.nih.gov/pubmed/8849940.

[94] L Holmgren, M S O'Reilly, and J Folkman. Dormancy of micrometastases: balanced proliferation and apoptosis in the presence of angiogenesis suppression. *Nat Med*, 1(2):149–153, 1995. URL https://www.ncbi.nlm.nih.gov/pubmed/7585012.

[95] S Meng, D Tripathy, E P Frenkel, S Shete, E Z Naftalis, J F Huth, P D Beitsch, M Leitch, S Hoover, D Euhus, B Haley, L Morrison, T P Fleming, D Herlyn, L W Terstappen, T Fehm, T F Tucker, N Lane, J Wang, and J W Uhr. Circulating tumor cells in patients with breast cancer dormancy. *Clin Cancer Res*, 10(24):8152–8162, 2004. doi: 10.1158/1078-0432.CCR-04-1110. URL https://www.ncbi.nlm.nih.gov/pubmed/15623589.

[96] G N Naumov, I C MacDonald, P M Weinmeister, N Kerkvliet, K V Nadkarni, S M Wilson, V L Morris, A C Groom, and A F Chambers. Persistence of solitary mammary carcinoma cells in a secondary site: a possible contributor to dormancy. *Cancer Res*, 62(7):2162–2168, 2002. URL https://www.ncbi.nlm.nih.gov/pubmed/11929839.

[97] Dalit Barkan, Jeffrey E. Green, and Ann F. Chambers. Extracellular matrix: A gatekeeper in the transition from dormancy to metastatic growth. *European Journal of Cancer*, 46(7):1181–1188, 2010. ISSN 09598049. doi: 10.1016/j.ejca.2010.02.027.

[98] C Arrigoni, S Bersini, M Gilardi, and M Moretti. In Vitro Co-Culture Models of Breast Cancer Metastatic Progression towards Bone.

Int J Mol Sci, 17(9), 2016. doi: 10.3390/ijms17091405. URL https://www.ncbi.nlm.nih.gov/pubmed/27571063.

[99] S Talukdar and S C Kundu. Engineered 3D Silk-Based Metastasis Models: Interactions Between Human Breast Adenocarcinoma, Mesenchymal Stem Cells and Osteoblast-Like Cells. *Advanced Functional Materials*, 23(42):5249–5260, 2013. doi: 10.1002/adfm.201300312.

[100] S Sieh, A V Taubenberger, M L Lehman, J A Clements, C C Nelson, and D W Hutmacher. Paracrine interactions between LNCaP prostate cancer cells and bioengineered bone in 3D in vitro culture reflect molecular changes during bone metastasis. *Bone*, 63:121–131, 2014. doi: 10.1016/j.bone.2014.02.001. URL http://www.ncbi.nlm.nih.gov/pubmed/24530694.

[101] B Weigelt, J L Peterse, and L J van 't Veer. Breast cancer metastasis: markers and models. *Nat Rev Cancer*, 5(8):591–602, 2005. doi: 10.1038/nrc1670. URL http://www.ncbi.nlm.nih.gov/pubmed/16056258.

[102] C A Klein. Parallel progression of primary tumours and metastases. *Nat Rev Cancer*, 9(4):302–312, 2009. doi: 10.1038/nrc2627. URL http://www.ncbi.nlm.nih.gov/pubmed/19308069.

[103] H Esmaeilsabzali, T V Beischlag, M E Cox, A M Parameswaran, and E J Park. Detection and isolation of circulating tumor cells: principles and methods. *Biotechnol Adv*, 31(7):1063–1084, 2013. doi: 10.1016/j.biotechadv.2013.08.016. URL http://www.ncbi.nlm.nih.gov/pubmed/23999357.

[104] H J Yoon, M Kozminsky, and S Nagrath. Emerging role of nanomaterials in circulating tumor cell isolation and analysis. *ACS Nano*, 8(3):1995–2017, 2014. doi: 10.1021/nn5004277. URL http://www.ncbi.nlm.nih.gov/pubmed/24601556.

[105] M G Krebs, R L Metcalf, L Carter, G Brady, F H Blackhall, and C Dive. Molecular analysis of circulating tumour cells-biology and biomarkers. *Nat Rev Clin Oncol*, 11(3):129–144, 2014. doi: 10.1038/nrclinonc.2013.253. URL http://www.ncbi.nlm.nih.gov/pubmed/24445517.

[106] K Pantel, R H Brakenhoff, and B Brandt. Detection, clinical relevance and specific biological properties of disseminating tumour cells. *Nature Reviews Cancer*, 8(5):329–340, 2008. doi: 10.1038/nrc2375.

[107] S Riethdorf, H Fritsche, V Muller, T Rau, C Schindlbeck, B Rack, W Janni, C Coith, K Beck, F Janicke, S Jackson, T Gornet, M Cristofanilli, and K Pantel. Detection of circulating tumor cells in peripheral blood of patients with metastatic breast cancer: a validation study of the CellSearch system. *Clin Cancer Res*, 13(3):920–928, 2007. doi: 10.1158/1078-0432.CCR-06-1695. URL http://www.ncbi.nlm.nih.gov/pubmed/17289886.

[108] Colette A. Bichsel, Samy Gobaa, Stefan Kobel, Chiara Secondini, George N. Thalmann, Marco G. Cecchini, and Matthias P. Lutolf. Diagnostic microchip to assay 3D colony-growth potential of captured circulating tumor cells. *Lab on a Chip*, 12(13):2313–2316, 2012. ISSN 1473-0197. doi: 10.1039/c2lc40130d. URL http://xlink.rsc.org/?DOI=c2lc40130d https://www.ncbi.nlm.nih.gov/pubmed/22565166.

[109] J Lee, N Kohl, S Shanbhang, and B Parekkadan. Scaffold-integrated microchips for end-to-end in vitro tumor cell attachment and xenograft formation. *Technology (Singap World Sci)*, 3(4):179–188, 2015. doi: 10.1142/S2339547815500065. URL https://www.ncbi.nlm.nih.gov/pubmed/26709385.

[110] M Yu, A Bardia, N Aceto, F Bersani, M W Madden, M C Donaldson, R Desai, H Zhu, V Comaills, Z Zheng, B S Wittner, P Stojanov, E Brachtel, D Sgroi, R Kapur, T Shioda, D T Ting, S Ramaswamy, G Getz, A J Iafrate, C Benes, M Toner, S Maheswaran, and D A Haber. Cancer therapy. Ex vivo culture of circulating breast tumor cells for individualized testing of drug susceptibility. *Science*, 345(6193):216–220, 2014. doi: 10.1126/science.1253533. URL https://www.ncbi.nlm.nih.gov/pubmed/25013076.

[111] Natalia Bednarz-Knoll, Catherine Alix-Panabières, and Klaus Pantel. Clinical relevance and biology of circulating tumor cells. *Breast Cancer Research*, 13(6): 1, 2011.

[112] J Yi and V Backman. Imaging a full set of optical scattering properties of biological tissue by inverse spectroscopic optical coherence tomography. *Opt Lett*, 37(21):4443–4445, 2012. doi: 10.1364/OL.37.004443. URL http://www.ncbi.nlm.nih.gov/pubmed/23114323.

[113] B J Tauro, D W Greening, R A Mathias, S Mathivanan, H Ji, and R J Simpson. Two distinct populations of exosomes are released from LIM1863 colon carcinoma cell-derived organoids. *Mol Cell Proteomics*, 12(3):587–598, 2013. doi: 10.1074/mcp.M112.021303. URL https://www.ncbi.nlm.nih.gov/pubmed/23230278.

[114] M S Sosa, P Bragado, and J A Aguirre-Ghiso. Mechanisms of disseminated cancer cell dormancy: an awakening field. *Nat Rev Cancer*, 14(9):611–622, 2014. doi: 10.1038/nrc3793. URL https://www.ncbi.nlm.nih.gov/pubmed/25118602.

[115] M Cristofanilli, G T Budd, M J Ellis, A Stopeck, J Matera, M C Miller, J M Reuben, G V Doyle, W J Allard, L W Terstappen, and D F Hayes. Circulating tumor cells, disease progression, and survival in metastatic breast cancer. *N Engl J Med*, 351(8):781–791, 2004. doi: 10.1056/NEJMoa040766. URL https://www.ncbi.nlm.nih.gov/pubmed/15317891.

[116] Christine L Chaffer and Robert A Weinberg. A Perspective on Cancer Cell Metastasis. *Science*, 331(6024):1559–1564,

2011. ISSN 0036-8075. doi: 10.1126/science.1203543. URL http://science.sciencemag.org/content/sci/331/6024/1559.full.pdf http://www.sciencemag.org/cgi/doi/10.1126/science.1203543.

[117] A F Chambers, A C Groom, and I C MacDonald. Dissemination and growth of cancer cells in metastatic sites. *Nat Rev Cancer*, 2(8):563–572, 2002. doi: 10.1038/nrc865. URL http://www.ncbi.nlm.nih.gov/pubmed/12154349.

[118] R Murakami, S Kumita, T Yoshida, K Ishihara, T Kiriyama, K Hakozaki, K Yanagihara, S Iida, and S Tsuchiya. FDG-PET/CT in the diagnosis of recurrent breast cancer. *Acta Radiol*, 53(1):12–16, 2012. doi: 10.1258/ar.2011.110245. URL http://www.ncbi.nlm.nih.gov/pubmed/22067206.

[119] K Engelhard, H P Hollenbach, K Wohlfart, E von Imhoff, and F A Fellner. Comparison of whole-body MRI with automatic moving table technique and bone scintigraphy for screening for bone metastases in patients with breast cancer. *Eur Radiol*, 14(1):99–105, 2004. doi: 10.1007/s00330-003-1968-7. URL http://www.ncbi.nlm.nih.gov/pubmed/12845463.

[120] T C Lauenstein, S C Goehde, C U Herborn, M Goyen, C Oberhoff, J F Debatin, S G Ruehm, and J Barkhausen. Whole-body MR imaging: evaluation of patients for metastases. *Radiology*, 233(1):139–148, 2004. doi: 10.1148/radiol.2331030777. URL http://www.ncbi.nlm.nih.gov/pubmed/15317952.

[121] S Maheswaran and D A Haber. Circulating tumor cells: a window into cancer biology and metastasis. *Curr Opin Genet Dev*, 20(1):96–99, 2010. doi: DOI 10.1016/j.gde.2009.12.002.

[122] M Yu, S Stott, M Toner, S Maheswaran, and D A Haber. Circulating tumor cells: approaches to isolation and characterization. *J Cell Biol*, 192(3):373–382, 2011. doi: 10.1083/jcb.201010021. URL http://www.ncbi.nlm.nih.gov/pubmed/21300848.

[123] S A Joosse and K Pantel. Biologic challenges in the detection of circulating tumor cells. *Cancer Res*, 73(1):8–11, 2013. doi: 10.1158/0008-5472.CAN-12-3422. URL http://www.ncbi.nlm.nih.gov/pubmed/23271724.

[124] P Paterlini-Brechot and N L Benali. Circulating tumor cells (CTC) detection: clinical impact and future directions. *Cancer Lett*, 253(2):180–204, 2007. doi: 10.1016/j.canlet.2006.12.014. URL http://www.ncbi.nlm.nih.gov/pubmed/17314005.

[125] R N Kaplan, S Rafii, and D Lyden. Preparing the "soil": the premetastatic niche. *Cancer Res*, 66(23):11089–11093, 2006. doi: 10.1158/0008-5472.CAN-06-2407. URL http://www.ncbi.nlm.nih.gov/pubmed/17145848.

[126] B Psaila and D Lyden. The metastatic niche: adapting the foreign soil. *Nat Rev Cancer*, 9(4):285–293, 2009. doi: 10.1038/nrc2621. URL http://www.ncbi.nlm.nih.gov/pubmed/19308068.

[127] Rosandra N Kaplan, Bethan Psaila, and David Lyden. Bone marrow cells in the 'pre-metastatic niche': within bone and beyond. *Cancer metastasis reviews*, 25(4):521–9, dec 2006. ISSN 0167-7659. doi: 10.1007/s10555-006-9036-9. URL http://www.ncbi.nlm.nih.gov/pubmed/17186383.

[128] Takanori Kitamura, Bin-Zhi Qian, and Jeffrey W. Pollard. Immune cell promotion of metastasis. *Nature Reviews Immunology*, 15(2), 2015. ISSN 1474-1733. doi: 10.1038/nri3789.

[129] Binzhi Qian, Yan Deng, Jae Hong Im, Ruth J Muschel, Yiyu Zou, Jiufeng Li, Richard a Lang, and Jeffrey W Pollard. A distinct macrophage population mediates metastatic breast cancer cell extravasation, establishment and growth. *PloS one*, 4(8):e6562, jan 2009. ISSN 1932-6203. doi: 10.1371/journal.pone.0006562.

[130] J Yi, A J Radosevich, Y Stypula-Cyrus, N N Mutyal, S M Azarin, E Horcher, M J Goldberg, L K Bianchi, S Bajaj, H K Roy, and V Backman. Spatially resolved optical and ultrastructural properties of colorectal and pancreatic field carcinogenesis observed by inverse spectroscopic optical coherence tomography. *J Biomed Opt*, 19(3):36013, 2014. doi: 10.1117/1.JBO.19.3.036013. URL http://www.ncbi.nlm.nih.gov/pubmed/24643530.

[131] A J Radosevich, N N Mutyal, J Yi, Y Stypula-Cyrus, J D Rogers, M J Goldberg, L K Bianchi, S Bajaj, H K Roy, and V Backman. Ultrastructural alterations in field carcinogenesis measured by enhanced backscattering spectroscopy. *J Biomed Opt*, 18(9):97002, 2013. doi: 10.1117/1.JBO.18.9.097002. URL http://www.ncbi.nlm.nih.gov/pubmed/24008865.

[132] A J Radosevich, N N Mutyal, J D Rogers, B Gould, T A Hensing, D Ray, V Backman, and H K Roy. Buccal spectral markers for lung cancer risk stratification. *PLoS One*, 9(10):e110157, 2014. doi: 10.1371/journal.pone.0110157. URL http://www.ncbi.nlm.nih.gov/pubmed/25299667.

[133] Boris M. Holzapfel, Ferdinand Wagner, Daniela Loessner, Nina P. Holzapfel, Laure Thibaudeau, Ross Crawford, Ming-Tat Ling, Judith A. Clements, Pamela J. Russell, and Dietmar W. Hutmacher. Species-specific homing mechanisms of human prostate cancer metastasis in tissue engineered bone. *Biomaterials*, 35(13):4108–4115, apr 2014. ISSN 01429612. doi: 10.1016/j.biomaterials.2014.01.062. URL http://linkinghub.elsevier.com/retrieve/pii/S0142961214000921.

[134] Zhaoyang Li, Yanli Pang, Sudheer Kumar Gara, B R Achyut, Christopher Heger, Paul K Goldsmith, Scott Lonning, and Li Yang. Gr1+ CD11b+ cells are responsible for tumor promoting effect of TGFβ in breast cancer progression. *International Journal of Cancer*, 131(11):2584–2595, 2012.

[135] J Markowitz, R Wesolowski, T Papenfuss, T R Brooks, and W E Carson 3rd. Myeloid-derived suppressor cells in breast cancer. *Breast Can-*

cer Res Treat, 140(1):13–21, 2013. doi: 10.1007/s10549-013-2618-7. URL http://www.ncbi.nlm.nih.gov/pubmed/23828498.

[136] E M Hanson, V K Clements, P Sinha, D Ilkovitch, and S Ostrand-Rosenberg. Myeloid-derived suppressor cells down-regulate L-selectin expression on CD4+ and CD8+ T cells. *J Immunol*, 183(2):937–944, 2009. doi: 10.4049/jimmunol.0804253. URL http://www.ncbi.nlm.nih.gov/pubmed/19553533.

[137] M Elkabets, V S Ribeiro, C A Dinarello, S Ostrand-Rosenberg, J P Di Santo, R N Apte, and C A Vosshenrich. IL-1beta regulates a novel myeloid-derived suppressor cell subset that impairs NK cell development and function. *Eur J Immunol*, 40(12):3347–3357, 2010. doi: 10.1002/eji.201041037. URL http://www.ncbi.nlm.nih.gov/pubmed/21110318.

[138] B Hoechst, T Voigtlaender, L Ormandy, J Gamrekelashvili, F Zhao, H Wedemeyer, F Lehner, M P Manns, T F Greten, and F Korangy. Myeloid derived suppressor cells inhibit natural killer cells in patients with hepatocellular carcinoma via the NKp30 receptor. *Hepatology*, 50(3):799–807, 2009. doi: 10.1002/hep.23054. URL http://www.ncbi.nlm.nih.gov/pubmed/19551844.

[139] Minu K Srivastava, Li Zhu, Marni Harris-White, Upendra Kar, Min Huang, Ming F Johnson, Jay M Lee, David Elashoff, Robert Strieter, and Steven Dubinett. Myeloid suppressor cell depletion augments antitumor activity in lung cancer. *PLoS One*, 7(7):e40677, 2012.

[140] Gary Kohanbash, Kayla McKaveney, Masashi Sakaki, Ryo Ueda, Arlan H Mintz, Nduka Amankulor, Mitsugu Fujita, John R Ohlfest, and Hideho Okada. GM-CSF promotes the immunosuppressive activity of glioma-infiltrating myeloid cells through interleukin-4 receptor-α. *Cancer Res*, 73(21):6413–6423, 2013. URL http://cancerres.aacrjournals.org/content/73/21/6413.full.pdf.

[141] C M Diaz-Montero, M L Salem, M I Nishimura, E Garrett-Mayer, D J Cole, and A J Montero. Increased circulating myeloid-derived suppressor cells correlate with clinical cancer stage, metastatic tumor burden, and doxorubicin-cyclophosphamide chemotherapy. *Cancer Immunol Immunother*, 58(1):49–59, 2009. doi: 10.1007/s00262-008-0523-4. URL http://www.ncbi.nlm.nih.gov/pubmed/18446337.

[142] B Almand, J R Resser, B Lindman, S Nadaf, J I Clark, E D Kwon, D P Carbone, and D I Gabrilovich. Clinical significance of defective dendritic cell differentiation in cancer. *Clin Cancer Res*, 6(5):1755–1766, 2000. URL http://www.ncbi.nlm.nih.gov/pubmed/10815894.

[143] S Cole, A Montero, E Garret-Mayer, G Onicescu, T Vandenberg, S Hutchens, and C Diaz-Montero. Elevated Circulating Myeloid Derived Suppressor Cells (MDSC) Are Associated with Inferior Overall Survival (OS) and Correlate with

Circulating Tumor Cells (CTC) in Patients with Metastatic Breast Cancer. *In: Thirty-Second Annual CTRCAACR San Antonio Breast Cancer Symposium: Cancer Research, San Antonio, TX*, 2009.

[144] F Couet, N Rajan, and D Mantovani. Macromolecular biomaterials for scaffold-based vascular tissue engineering. *Macromol Biosci*, 7(5):701–718, 2007. doi: 10.1002/mabi.200700002. URL `http://www.ncbi.nlm.nih.gov/pubmed/17477449`.

[145] H J Sung, C Meredith, C Johnson, and Z S Galis. The effect of scaffold degradation rate on three-dimensional cell growth and angiogenesis. *Biomaterials*, 25(26):5735–5742, 2004. doi: 10.1016/j.biomaterials.2004.01.066. URL `http://www.ncbi.nlm.nih.gov/pubmed/15147819`.

[146] J Kohn, S Abramson, and R Langer. Bioresorbable and Bioerodible Materials. In B D Ratner, A S Hoffman, F J Schoen, and J E Lemons, editors, *Biomaterials Science: An Introduction to Materials in Medicine*, pages 115–127. Elsevier Academic Press, San Diego, 2004.

[147] J H Jang, C B Rives, and L D Shea. Plasmid delivery in vivo from porous tissue-engineering scaffolds: transgene expression and cellular transfection. *Molecular Therapy*, 12(3):475–483, 2005. doi: 10.1016/j.ymthe.2005.03.036. URL `http://www.ncbi.nlm.nih.gov/pubmed/15950542`.

[148] J Yi, A J Radosevich, J D Rogers, S C P Norris, I R Capoglu, A Taflove, and V Backman. Can OCT be sensitive to nanoscale structural alterations in biological tissue? *Optics Express*, 21(7):9043–9059, 2013. doi: Doi 10.1364/Oe.21.009043.

[149] Douglas Hanahan and Robert A. Weinberg. Hallmarks of cancer: The next generation, 2011. ISSN 00928674.

[150] Hector Peinado, Haiying Zhang, Irina R Matei, Bruno Costa-Silva, Ayuko Hoshino, Goncalo Rodrigues, Bethan Psaila, Rosandra N Kaplan, Jacqueline F Bromberg, Yibin Kang, Mina J Bissell, Thomas R Cox, Amato J Giaccia, Janine T Erler, Sachie Hiratsuka, Cyrus M Ghajar, and David Lyden. Pre-metastatic niches: organ-specific homes for metastases. *Nat Rev Cancer*, 17(5):302–317, 2017. doi: 10.1038/nrc.2017.6. URL `http://dx.doi.org/10.1038/nrc.2017.6`.

[151] Brian A Aguado, Grace G Bushnell, Shreyas S Rao, Jacqueline S Jeruss, and Lonnie D Shea. Engineering the pre-metastatic niche. 1:77, June 2017.

[152] Brian A Aguado, Joseph C Grim, Adrianne M Rosales, Jana J Watson-Capps, and Kristi S Anseth. Engineering precision biomaterials for personalized medicine, 2018. ISSN 19466242.

[153] Beverly A Teicher and Simon P Fricker. Cxcl12 (sdf-1)/cxcr4 pathway in cancer. *Clinical cancer research*, pages 1078–0432, 2010.

[154] Albert Zlotnik and Osamu Yoshie. Chemokines: a new classification system and their role in immunity. *Immunity*, 12(2):121–127, 2000.

[155] Akira Orimo, Piyush B Gupta, Dennis C Sgroi, Fernando Arenzana-Seisdedos, Thierry Delaunay, Rizwan Naeem, Vincent J Carey, Andrea L Richardson, and Robert A Weinberg. Stromal fibroblasts present in invasive human breast carcinomas promote tumor growth and angiogenesis through elevated sdf-1/cxcl12 secretion. *Cell*, 121(3):335–348, 2005.

[156] Elena De Falco, Daniele Porcelli, Anna Rita Torella, Stefania Straino, Maria Grazia Iachininoto, Alessia Orlandi, Silvia Truffa, Paolo Biglioli, Monica Napolitano, Maurizio C Capogrossi, et al. Sdf-1 involvement in endothelial phenotype and ischemia-induced recruitment of bone marrow progenitor cells. *Blood*, 104(12):3472–3482, 2004.

[157] Magda Kucia, Ryan Reca, Katarzyna Miekus, Jens Wanzeck, Wojtek Wojakowski, Anna Janowska-Wieczorek, Janina Ratajczak, and Mariusz Z Ratajczak. Trafficking of normal stem cells and metastasis of cancer stem cells involve similar mechanisms: pivotal role of the sdf-1–cxcr4 axis. *Stem cells*, 23 (7):879–894, 2005.

[158] Namita Kundu, Theresa L Beaty, Marian J Jackson, and Amy M Fulton. Antimetastatic and antitumor activities of interleukin 10 in a murine model of breast cancer. *JNCI: Journal of the National Cancer Institute*, 88(8):536–541, 1996.

[159] Yunping Luo, He Zhou, Jörg Krueger, Charles Kaplan, Sung-Hyung Lee, Carrie Dolman, Dorothy Markowitz, Wenyuan Wu, Cheng Liu, Ralph A Reisfeld, et al. Targeting tumor-associated macrophages as a novel strategy against breast cancer. *The Journal of clinical investigation*, 116(8):2132–2141, 2006.

[160] Je-In Youn and Dmitry I Gabrilovich. The biology of myeloid-derived suppressor cells: the blessing and the curse of morphological and functional heterogeneity. *European journal of immunology*, 40(11):2969–2975, 2010.

[161] Youjin Lee, Sogyong L Auh, Yugang Wang, Byron Burnette, Yang Wang, Yuru Meng, Michael Beckett, Rohit Sharma, Robert Chin, Tony Tu, et al. Therapeutic effects of ablative radiation on local tumor require cd8+ t cells: changing strategies for cancer treatment. *Blood*, 114(3):589–595, 2009.

[162] Wei Liang and Napoleone Ferrara. The complex role of neutrophils in tumor angiogenesis and metastasis. *Cancer immunology research*, 4(2):83–91, 2016.

[163] David G DeNardo, Jairo B Barreto, Pauline Andreu, Lesley Vasquez, David Tawfik, Nikita Kolhatkar, and Lisa M Coussens. Cd4+ t cells regulate pulmonary metastasis of mammary carcinomas by enhancing protumor properties of macrophages. *Cancer cell*, 16(2):91–102, 2009.

[164] Sharon A Williams, Yuka Harata-Lee, Iain Comerford, Robin L Anderson, Mark J Smyth, and Shaun R McColl. Multiple functions of cxcl12 in a syngeneic model of breast cancer. *Molecular cancer*, 9(1):250, 2010.

[165] Purevdorj B Olkhanud, Bazarragchaa Damdinsuren, Monica Bodogai, Ronald E Gress, Ranjan Sen, Katarzyna Wejksza, Enkhzol Malchinkhuu, Robert P Wersto, and Arya Biragyn. Tumor-evoked regulatory b cells promote breast cancer metastasis by converting resting cd4+ t cells to t-regulatory cells. *Cancer research*, 2011.

[166] RM Boehler, R Kuo, S Shin, AG Goodman, MA Pilecki, JN Leonard, and LD Shea. Lentivirus delivery of il-10 to promote and sustain macrophage polarization towards an anti-inflammatory phenotype. *Biotechnology and bioengineering*, 111(6):1210–1221, 2014.

[167] B Psaila, R N Kaplan, E R Port, and D Lyden. Priming the 'soil' for breast cancer metastasis: the pre-metastatic niche. *Breast Dis*, 26:65–74, 2006. URL `http://www.ncbi.nlm.nih.gov/pubmed/17473366`.

[168] Isaiah J Fidler. Metastasis: quantitative analysis of distribution and fate of tumor emboli labeled with 125I-5-iodo-2-deoxyuridine. *Journal of the National Cancer Institute*, 45(4):773–782, 1970.

[169] Ana Maria Gonzalez-Angulo, Flavia Morales-Vasquez, and Gabriel N Hortobagyi. Overview of resistance to systemic therapy in patients with breast cancer. In *Breast Cancer Chemosensitivity*, pages 1–22. Springer, 2007.

[170] Tathiane M. Malta, Artem Sokolov, Andrew J. Gentles, Tomasz Burzykowski, Laila Poisson, John N. Weinstein, Bożena Kamińska, and Joerg Huelsken. Machine Learning Identifies Stemness Features Associated with Oncogenic Dedifferentiation. *Cell*, 173(2):338–354.e15, apr 2018. ISSN 0092-8674. doi: 10.1016/J.CELL.2018.03.034.

[171] Yusuf Emre Erdi. Limits of tumor detectability in nuclear medicine and PET. *Molecular imaging and radionuclide therapy*, 21(1):23, 2012. ISSN 21461414. doi: 10.4274/Mirt.138. URL `http://cms.galenos.com.tr/FileIssue/4/509/article/23-28.pdf`.

[172] Catherine Alix-Panabières and Klaus Pantel. Clinical applications of circulating tumor cells and circulating tumor DNA as liquid biopsy. 2016. ISSN 21598290. doi: 10.1158/2159-8290.CD-15-1483.

[173] Roy R L Bastien, Álvaro Rodríguez-Lescure, Mark T W Ebbert, Aleix Prat, Blanca Munárriz, Leslie Rowe, Patricia Miller, Manuel Ruiz-Borrego, Daniel Anderson, and Bradley Lyons. PAM50 breast cancer subtyping by RT-qPCR and concordance with standard clinical molecular markers. *BMC medical genomics*, 5(1):44, 2012.

[174] Thomas Ried and Indika Rajapakse. The 4D Nucleome, 2017.

[175] Laura Seaman, Haiming Chen, Markus Brown, Darawalee Wangsa, Geoff Patterson, Jordi Camps, Gilbert S Omenn, Thomas Ried, and Indika Rajapakse. Nucleome Analysis Reveals StructureFunction Relationships for Colon Cancer. *Molecular Cancer Research*, 15(7):821–830, 2017.

[176] Fan R K Chung. *Spectral graph theory*. Number 92. American Mathematical Soc., 1997. ISBN 0821803158.

[177] Adam A Friedman, Anthony Letai, David E Fisher, and Keith T Flaherty. Precision medicine for cancer with next-generation functional diagnostics. *Nature Reviews Cancer*, 15(12):747, 2015.

[178] A J Minn, G P Gupta, P M Siegel, P D Bos, W Shu, D D Giri, A Viale, A B Olshen, W L Gerald, and J Massague. Genes that mediate breast cancer metastasis to lung. *Nature*, 436(7050):518–524, 2005. doi: 10.1038/nature03799. URL `http://www.ncbi.nlm.nih.gov/pubmed/16049480`.

[179] P D Bos, X H Zhang, C Nadal, W Shu, R R Gomis, D X Nguyen, A J Minn, M J van de Vijver, W L Gerald, J A Foekens, and J Massague. Genes that mediate breast cancer metastasis to the brain. *Nature*, 459(7249):1005–1009, 2009. doi: 10.1038/nature08021. URL `http://www.ncbi.nlm.nih.gov/pubmed/19421193`.

[180] A Liberzon, C Birger, H Thorvaldsdottir, M Ghandi, J P Mesirov, and P Tamayo. The Molecular Signatures Database (MSigDB) hallmark gene set collection. Cell Syst. 2015; 1 (6): 41725.

[181] B K Linderholm, H Hellborg, U Johansson, G Elmberger, L Skoog, J Lehtiö, and R Lewensohn. Significantly higher levels of vascular endothelial growth factor (VEGF) and shorter survival times for patients with primary operable triple-negative breast cancer. *Annals of oncology*, 20(10):1639–1646, 2009.

[182] Brandon L Pierce, Rachel Ballard-Barbash, Leslie Bernstein, Richard N Baumgartner, Marian L Neuhouser, Mark H Wener, Kathy B Baumgartner, Frank D Gilliland, Bess E Sorensen, and Anne McTiernan. Elevated biomarkers of inflammation are associated with reduced survival among breast cancer patients. *Journal of Clinical Oncology*, 27(21):3437, 2009.

[183] Caitlin D May, Nathalie Sphyris, Kurt W Evans, Steven J Werden, Wenjun Guo, and Sendurai A Mani. Epithelial-mesenchymal transition and cancer stem

cells: a dangerously dynamic duo in breast cancer progression. *Breast Cancer Research*, 13(1):202, 2011.

[184] Ming Luo, Michael Brooks, and Max S Wicha. Epithelial-mesenchymal plasticity of breast cancer stem cells: implications for metastasis and therapeutic resistance. *Current pharmaceutical design*, 21(10):1301–1310, 2015.

[185] Dongjun Peng, Takashi Tanikawa, Wei Li, Lili Zhao, Linda Vatan, Wojciech Szeliga, Shanshan Wan, Shuang Wei, Yin Wang, and Yan Liu. Myeloid-derived suppressor cells endow stem-like qualities to breast cancer cells through IL6/STAT3 and NO/NOTCH cross-talk signaling. *Cancer research*, 76(11): 3156–3165, 2016.

[186] Jackie L Johnson, Smitha Pillai, Danielle Pernazza, Saïd M Sebti, Nicholas J Lawrence, and Srikumar P Chellappan. Regulation of matrix metalloproteinase genes by E2F transcription factors: RbRaf-1 interaction as a novel target for metastatic disease. *Cancer research*, 72(2):516–526, 2012.

[187] Li Ma, Jennifer Young, Harsha Prabhala, Elizabeth Pan, Pieter Mestdagh, Daniel Muth, Julie Teruya-Feldstein, Ferenc Reinhardt, Tamer T Onder, and Scott Valastyan. miR-9, a MYC/MYCN-activated microRNA, regulates E-cadherin and cancer metastasis. *Nature cell biology*, 12(3):247, 2010.

[188] Zhibo Yang, Rozita Bagheri-Yarmand, Seetharaman Balasenthil, Gabriel Hortobagyi, Aysegul A Sahin, Christopher J Barnes, and Rakesh Kumar. HER2 regulation of peroxisome proliferator-activated receptor gamma (PPAR-gamma) expression and sensitivity of breast cancer cells to PPAR-gamma ligand therapy. *Clinical Cancer Research*, 9(8):3198–3203, 2003.

[189] Regina Berretta and Pablo Moscato. Cancer biomarker discovery: the entropic hallmark. *PLoS One*, 5(8):e12262, 2010.

[190] Maxime Tarabichi, Aline Antoniou, Manuel Saiselet, Jaime Miguel Pita, Guy Andry, Jacques Emile Dumont, Vincent Detours, and Carine Maenhaut. Systems biology of cancer: entropy, disorder, and selection-driven evolution to independence, invasion and swarm intelligence. *Cancer and Metastasis Reviews*, 32(3-4):403–421, 2013.

[191] Christopher R S Banerji, Simone Severini, Carlos Caldas, and Andrew E Teschendorff. Intra-tumour signalling entropy determines clinical outcome in breast and lung cancer. *PLoS computational biology*, 11(3):e1004115, 2015.

[192] Jagdeep K Singh, Bruno M Simões, Sacha J Howell, Gillian Farnie, and Robert B Clarke. Recent advances reveal IL-8 signaling as a potential key to targeting breast cancer stem cells. *Breast Cancer Research*, 15(4):210, 2013.

[193] Andrew R Chin and Shizhen Emily Wang. Cytokines driving breast cancer stemness. *Molecular and cellular endocrinology*, 382(1):598–602, 2014.

[194] Ina H Benoy, Roberto Salgado, Peter Van Dam, Katrien Geboers, Eric Van Marck, Simon Scharpé, Peter B Vermeulen, and Luc Y Dirix. Increased serum interleukin-8 in patients with early and metastatic breast cancer correlates with early dissemination and survival. *Clinical Cancer Research*, 10(21):7157–7162, 2004.

[195] Margit A Huber, Ninel Azoitei, Bernd Baumann, Stefan Grünert, Andreas Sommer, Hubert Pehamberger, Norbert Kraut, Hartmut Beug, and Thomas Wirth. NFkB is essential for epithelial-mesenchymal transition and metastasis in a model of breast cancer progression. *The Journal of clinical investigation*, 114 (4):569–581, 2004.

[196] Simi Ali and Gwendal Lazennec. Chemokines: novel targets for breast cancer metastasis. *Cancer and Metastasis Reviews*, 26(3-4):401–420, 2007.

[197] Daniele Santini, Gaia Schiavon, Bruno Vincenzi, Laura Gaeta, Francesco Pantano, Antonio Russo, Cinzia Ortega, Camillo Porta, Sara Galluzzo, and Grazia Armento. Receptor activator of NF-kB (RANK) expression in primary tumors associates with bone metastasis occurrence in breast cancer patients. *PLoS One*, 6(4):e19234, 2011.

[198] Calvin R Justus, Nancy Leffler, Maria Ruiz-Echevarria, and Li V Yang. In vitro cell migration and invasion assays. *Journal of visualized experiments: JoVE*, (88), 2014.

[199] Elizabeth Tarasewicz, Robert S Oakes, Misael O Aviles, Joelle Straehla, Kathryn M Chilton, Joseph T Decker, Jia Wu, Lonnie D Shea, and Jacqueline S Jeruss. Embryonic stem cell secreted factors decrease invasiveness of triple-negative breast cancer cells through regulome modulation. *Cancer biology & therapy*, 19(4):271–281, 2018.

[200] Vamsi K Mootha, Cecilia M Lindgren, Karl-Fredrik Eriksson, Aravind Subramanian, Smita Sihag, Joseph Lehar, Pere Puigserver, Emma Carlsson, Martin Ridderstråle, and Esa Laurila. PGC-1alpha-responsive genes involved in oxidative phosphorylation are coordinately downregulated in human diabetes. *Nature genetics*, 34(3):267, 2003.

[201] Aravind Subramanian, Pablo Tamayo, Vamsi K Mootha, Sayan Mukherjee, Benjamin L Ebert, Michael A Gillette, Amanda Paulovich, Scott L Pomeroy, Todd R Golub, and Eric S Lander. Gene set enrichment analysis: a knowledge-based approach for interpreting genome-wide expression profiles. *Proceedings of the National Academy of Sciences*, 102(43):15545–15550, 2005.

[202] Haiming Chen, Jie Chen, Lindsey A Muir, Scott Ronquist, Walter Meixner, Mats Ljungman, Thomas Ried, Stephen Smale, and Indika Rajapakse. Functional organization of the human 4D Nucleome. *Proceedings of the National Academy of Sciences*, 112(26):8002–8007, 2015.

[203] Erik Aronesty. Comparison of sequencing utility programs. *The Open Bioinformatics Journal*, 7(1), 2013.

[204] Thomas J Rosol, Sarah H Tannehill-Gregg, Bruce E LeRoy, Stefanie Mandl, and Christopher H Contag. Animal models of bone metastasis. *Cancer*, 97(S3): 748–757, 2003.

[205] Julio A Aguirre-Ghiso. Models, mechanisms and clinical evidence for cancer dormancy. *Nature Reviews Cancer*, 7(11):834, 2007.

[206] Jerald J Killion, Robert Radinsky, and Isaiah J Fidler. Orthotopic models are necessary to predict therapy of transplantable tumors in mice. *Cancer and Metastasis Reviews*, 17(3):279–284, 1998.

[207] James E Talmadge, Rakesh K Singh, Isaiah J Fidler, and Avraham Raz. Murine models to evaluate novel and conventional therapeutic strategies for cancer. *The American journal of pathology*, 170(3):793–804, 2007.

[208] Erica Yada, Satoshi Wada, Shintaro Yoshida, and Tetsuro Sasada. Use of patient-derived xenograft mouse models in cancer research and treatment, 2017.

[209] Samuel Aparicio, Manuel Hidalgo, and Andrew L Kung. Examining the utility of patient-derived xenograft mouse models. *Nature Reviews Cancer*, 15(5):311, 2015.

[210] Rebecca L. Siegel, Kimberly D. Miller, and Ahmedin Jemal. Cancer statistics, 2018. *CA: A Cancer Journal for Clinicians*, 68(1):7–30. doi: 10.3322/caac.21442. URL `https://onlinelibrary.wiley.com/doi/abs/10.3322/caac.21442`.

[211] Yves Hüsemann, Jochen B Geigl, Falk Schubert, Piero Musiani, Manfred Meyer, Elke Burghart, Guido Forni, Roland Eils, Tanja Fehm, Gert Riethmüller, et al. Systemic spread is an early step in breast cancer. *Cancer cell*, 13(1):58–68, 2008.

[212] David G DeNardo and Lisa M Coussens. Inflammation and breast cancer. balancing immune response: crosstalk between adaptive and innate immune cells during breast cancer progression. *Breast cancer research*, 9(4):212, 2007.

[213] Andrew D Rhim, Emily T Mirek, Nicole M Aiello, Anirban Maitra, Jennifer M Bailey, Florencia McAllister, Maximilian Reichert, Gregory L Beatty, Anil K Rustgi, Robert H Vonderheide, et al. Emt and dissemination precede pancreatic tumor formation. *Cell*, 148(1):349–361, 2012.

[214] Andrew D Rhim, Fredrik I Thege, Steven M Santana, Timothy B Lannin, Trisha N Saha, Shannon Tsai, Lara R Maggs, Michael L Kochman, Gregory G Ginsberg, John G Lieb, et al. Detection of circulating pancreas epithelial cells in patients with pancreatic cystic lesions. *Gastroenterology*, 146(3):647–651, 2014.

[215] Suresh T Chari, Kimberly Kelly, Michael A Hollingsworth, Sarah P Thayer, David A Ahlquist, Dana K Andersen, Surinder K Batra, Teresa A Brentnall, Marcia Canto, Deborah F Cleeter, et al. Early detection of sporadic pancreatic cancer: summative review. *Pancreas*, 44(5):693, 2015.

[216] NABIL Hanna and RC Burton. Definitive evidence that natural killer (nk) cells inhibit experimental tumor metastases in vivo. *The Journal of Immunology*, 127 (5):1754–1758, 1981.

[217] Theresa L Whiteside and Ronald B Herberman. The role of natural killer cells in immune surveillance of cancer. *Current opinion in immunology*, 7(5):704–710, 1995.

[218] Camille Guillerey, Nicholas D Huntington, and Mark J Smyth. Targeting natural killer cells in cancer immunotherapy. *Nature immunology*, 17(9):1025, 2016.

[219] Raquel Tarazona, Beatriz Sanchez-Correa, Ignacio Casas-Avilés, Carmen Campos, Alejandra Pera, Sara Morgado, Nelson López-Sejas, Fakhri Hassouneh, Juan M Bergua, Maria Jose Arcos, et al. Immunosenescence: limitations of natural killer cell-based cancer immunotherapy. *Cancer Immunology, Immunotherapy*, 66(2):233–245, 2017.

[220] A. Stathopoulou, I. Vlachonikolis, D. Mavroudis, M. Perraki, Ch Kouroussis, S. Apostolaki, N. Malamos, S. Kakolyris, A. Kotsakis, N. Xenidis, D. Reppa, and V. Georgoulias. Molecular detection of cytokeratin-19-positive cells in the peripheral blood of patients with operable breast cancer: Evaluation of their prognostic significance. *Journal of Clinical Oncology*, 2002. ISSN 0732183X. doi: 10.1200/JCO.2002.08.135.

[221] Anuja Nair, Barry D. Kuban, Nancy Obuchowski, and D. Geoffrey Vince. Assessing spectral algorithms to predict atherosclerotic plaque composition with normalized and raw intravascular ultrasound data. *Ultrasound in Medicine and Biology*, 2001. ISSN 03015629. doi: 10.1016/S0301-5629(01)00436-7.

[222] Ernesl Feleppa, Andrew Kalisz, Joan B. Sokil-Melgar, Frederic L. Lizzi, Tian Liu, Angel L. Rosado, Mary C. Shao, William R. Fair, Yu Wang, Michael S. Cookson, Victor E. Reuter, and Warren D.W. Heston. Typing of prostate tissue by ultrasonic spectrum analysis. *IEEE Transactions on Ultrasonics, Ferroelectrics, and Frequency Control*, 1996. ISSN 08853010. doi: 10.1109/58.503779.

[223] Ronald E. Kumon, Michael J. Pollack, Ashley L. Faulx, Kayode Olowe, Farees T. Farooq, Victor K. Chen, Yun Zhou, Richard C.K. Wong, Gerard A. Isenberg, Michael V. Sivak, Amitabh Chak, and Cheri X. Deng. In vivo characterization of pancreatic and lymph node tissue by using EUS spectrum analysis: a validation study. *Gastrointestinal Endoscopy*, 2010. ISSN 00165107. doi: 10.1016/j.gie.2009.08.027.

[224] Madhu Gudur, Rameshwar R. Rao, Yi-Sing Hsiao, Alexis W. Peterson, Cheri X. Deng, and Jan P. Stegemann. Noninvasive, Quantitative, Spatiotemporal Characterization of Mineralization in Three-Dimensional Collagen Hydrogels Using High-Resolution Spectral Ultrasound Imaging. *Tissue Engineering Part C: Methods*, 2012. ISSN 1937-3384. doi: 10.1089/ten.tec.2012.0180.

[225] Madhu Sudhan Reddy Gudur, Rameshwar R. Rao, Alexis W. Peterson, David J. Caldwell, Jan P. Stegemann, and Cheri X. Deng. Noninvasive quantification of in vitro osteoblastic differentiation in 3D engineered tissue constructs using spectral ultrasound imaging. *PLoS ONE*, 2014. ISSN 19326203. doi: 10.1371/journal.pone.0085749.

[226] Xiaowei Hong, Jan P. Stegemann, and Cheri X. Deng. Microscale characterization of the viscoelastic properties of hydrogel biomaterials using dual-mode ultrasound elastography. *Biomaterials*, 2016. ISSN 18785905. doi: 10.1016/j.biomaterials.2016.02.019.

[227] Jessica Stukel, Monica Goss, Haoyan Zhou, Wenda Zhou, Rebecca Willits, and Agata Exner. Development of a High-Throughput Ultrasound Technique for the Analysis of Tissue Engineering Constructs. 44(3):793–802, 2017. doi: 10.1007/s10439-015-1507-0.Development.

[228] William J Gradishar, Benjamin O Anderson, Ron Balassanian, Sarah L Blair, Harold J Burstein, Amy Cyr, Anthony D Elias, William B Farrar, Andres Forero, Sharon Hermes Giordano, et al. Nccn guidelines insights: breast cancer, version 1.2017. *Journal of the National Comprehensive Cancer Network*, 15(4): 433–451, 2017.

[229] Xiaowei Hong, Ramkumar T Annamalai, Tyler Kemerer, Cheri X Deng, and Jan P Stegemann. Multimode ultrasound viscoelastography for three-dimensional interrogation of microscale mechanical properties in heterogeneous biomaterials. *Biomaterials*, 2018.

[230] Charles Gawad, Winston Koh, and Stephen R Quake. Single-cell genome sequencing: Current state of the science, 2016. ISSN 14710064.

[231] Ja Hye Myung, Cari A Launiere, David T Eddington, and Seungpyo Hong. Enhanced tumor cell isolation by a biomimetic combination of e-selectin and anti-epcam: Implications for the effective separation of circulating tumor cells (CTCs). *Langmuir*, 26(11):8589–8596, 2010. ISSN 07437463. doi: 10.1021/la904678p.

[232] Eric Lin, Lianette Rivera-Báez, Shamileh Fouladdel, Hyeun Joong Yoon, Stephanie Guthrie, Jacob Wieger, Yadwinder Deol, Evan Keller, Vaibhav Sahai, Diane M Simeone, Monika L Burness, Ebrahim Azizi, Max S Wicha, and Sunitha Nagrath. High-Throughput Microfluidic Labyrinth for the Label-free Isolation of Circulating Tumor Cells. *Cell Systems*, 5(3):295—-304.e4, 2017. ISSN 24054720. doi: 10.1016/j.cels.2017.08.012.

[233] Ramdane A Harouaka, Ming Da Zhou, Tim Y Yeh, Waleed J Khan, Jeffery Allerton, and Si Yang Zheng. Viable circulating tumor cell enrichment by flexible micro spring array. In *Proceedings of the Annual International Conference of the IEEE Engineering in Medicine and Biology Society, EMBS*, pages 6269–6272, 2012. ISBN 9781424441198. doi: 10.1109/EMBC.2012.6347427.

[234] Virginia Espina, Julia D Wulfkuhle, Valerie S Calvert, Amy VanMeter, Weidong Zhou, George Coukos, David H Geho, Emanuel F Petricoin, and Lance A Liotta. Laser-capture microdissection. *Nature Protocols*, 1(2):586–603, 2006. ISSN 17542189. doi: 10.1038/nprot.2006.85.

[235] Todd M Gierahn, Marc H Wadsworth, Travis K Hughes, Bryan D Bryson, Andrew Butler, Rahul Satija, Sarah Fortune, J Christopher Love, and Alex K Shalek. Seq-Well: portable, low-cost RNA sequencing of single cells at high throughput. *Nature Methods*, 2017.

[236] H Piccard, R J Muschel, and G Opdenakker. On the dual roles and polarized phenotypes of neutrophils in tumor development and progression, 2012. ISSN 10408428.

[237] Justin A Kenkel, William W Tseng, Matthew G Davidson, Lorna L Tolentino, Okmi Choi, Nupur Bhattacharya, E Scott Seeley, Daniel A Winer, Nathan E Reticker-Flynn, and Edgar G Engleman. An immunosuppressive dendritic cell subset accumulates at secondary sites and promotes metastasis in pancreatic cancer. *Cancer Research*, 77(15):4158–4170, 2017. ISSN 15387445. doi: 10.1158/0008-5472.CAN-16-2212.

[238] Alejandro López-Soto, Segundo Gonzalez, Mark J Smyth, and Lorenzo Galluzzi. Control of Metastasis by NK Cells, 2017. ISSN 18783686.

[239] Muthulekha Swamydas and Michail S Lionakis. Isolation, Purification and Labeling of Mouse Bone Marrow Neutrophils for Functional Studies and Adoptive Transfer Experiments. *Journal of Visualized Experiments*, (77), 2013. ISSN 1940-087X. doi: 10.3791/50586.

[240] Mark Anthony Bray, Shantanu Singh, Han Han, Chadwick T Davis, Blake Borgeson, Cathy Hartland, Maria Kost-Alimova, Sigrun M Gustafsdottir, Christopher C Gibson, and Anne E Carpenter. Cell Painting, a high-content image-based assay for morphological profiling using multiplexed fluorescent dyes. *Nature Protocols*, 11(9):1757–1774, 2016. ISSN 17502799. doi: 10.1038/nprot.2016.105.

[241] Xiaoxu Zhou, Jian Wang, Junye Chen, Yuankai Qi, Di Nan, Luhong Jin, Xiaohan Qian, Xinyi Wang, Qingyong Chen, Xu Liu, and Yingke Xu. Optogenetic control of epithelial-mesenchymal transition in cancer cells. *Scientific Reports*, 8(1), 2018. ISSN 20452322. doi: 10.1038/s41598-018-32539-3.

[242] Jorg A Kruger, Charles D Kaplan, Yunping Luo, He Zhou, Dorothy Markowitz, Rong Xiang, and Ralph A Reisfeld. Characterization of stem cell-like cancer cells in immune-competent mice. *Blood*, 108(12):3906–3912, 2006. ISSN 00064971. doi: 10.1182/blood-2006-05-024687.